TU Braunschweig – Niedersächsisches Forschungszentrum
für Luftfahrt

Berichte aus der Luft- und Raumfahrttechnik

Forschungsbericht 2016-01

Volume-Averaged RANS-Simulation of Turbulent Flow over Porous Media

Michael Mößner

TU Braunschweig

Institut für Strömungsmechanik

Diese Arbeit erscheint gleichzeitig als von der Fakultät für Maschinenbau der Technischen Universität Carolo-Wilhelmina zu Braunschweig zur Erlangung des akademischen Grades eines Doktor-Ingenieurs genehmigte Dissertation.

Diese Arbeit erscheint gleichzeitig als von der Fakultät für Maschinenbau der Technischen Universität Carolo-Wilhelmina zu Braunschweig zur Erlangung des akademischen Grades eines Doktor-Ingenieurs genehmigte Dissertation.

Herausgeber der NFL Forschungsberichte:
TU Braunschweig – Niedersächsisches Forschungszentrum für Luftfahrt
Hermann-Blenk-Straße 27 • 38108 Braunschweig
Tel: 0531-391-9822 • Fax: 0531-391-9804
Mail: nfl@tu-braunschweig.de
Internet: www.tu-braunschweig.de/nfl

VOLUME-AVERAGED RANS-SIMULATION OF TURBULENT FLOW OVER POROUS MEDIA

Von der Fakultät für Maschinenbau
der Technischen Universität Carolo-Wilhelmina zu Braunschweig

zur Erlangung der Würde
eines Doktor-Ingenieurs (Dr.-Ing.)
genehmigte Dissertation

von: Michael Mößner
aus (Geburtsort): Kirchheim unter Teck

eingereicht am: 10. November 2015
mündliche Prüfung am: 8. April 2016

Gutachter: Prof. Dr.-Ing. Rolf Radespiel
Prof. Dr.-Ing. Jan Werner Delfs
Dr.-Ing. Bernhard Eisfeld

2016

Abstract

Recent advances in acoustic research have revealed that making the trailing edges of aircraft wings porous results in significant noise reductions. Such usage of porous media on aerodynamic bodies amongst others requires the development of accurate prediction tools of how the aerodynamics are affected by the presence of porous parts. The present work is a step towards understanding this and demonstrates a complete development process, from the derivation of the theoretical methods over to the integration of the theory into a finite-volume flow solver up to the validation of the methods with DNS-data and experiments.

The derivations of this work are based on the aerodynamic condition of high Reynolds numbers, very fine porous structures and flow velocities up to the range of transonic Mach numbers. These requirements mirror the premise that the porous media are used in civil aviation for noise reduction purposes. The overall strategy to derive the theoretical framework for the simulation of flow over porous media under the given conditions is based on averaging the Navier-Stokes equations in space and time, while always keeping the equations in their compressible form. The unknown terms which occur from the averaging process are modelled with the Darcy and Forchheimer terms which describe the effect of the porous medium on the air. A Reynolds-stress model is used for modelling the turbulent effects.

Special conditions are derived at the surfaces of the porous media such that the flow that penetrates across the so-called nonporous-porous interface continues through the porous regions in a physically correct way. The relationships for the flow variables like velocity, density or pressure are based on the conservation of convective fluxes across the interface where the entropy is also held constant. Further relations for several gradients which are needed for the diffusive fluxes are derived on the basis of the jump conditions of Ochoa-Tapia and Whitaker.

The implementation of the theoretical models into a finite-volume flow solver is briefly presented. After verification with simple test cases, the models are extensively calibrated and validated. The calibration process adjusts the unknown parameters of the models with data from direct numerical simulations in a partly porous channel resulting in good agreement for both velocity and Reynolds-stress profiles. For the final validations, aerodynamic wind-tunnel experiments of a wing with porous trailing edge are performed. Measurements of the lift coefficient and of the flow field over the porous trailing edge compare well with the the numerical results.

Übersicht

Kürzlich durchgeführte akustische Untersuchungen zeigen, dass poröse Tragflügelhinterkanten den Flugzeuglärm deutlich verringern können. Die Simulationsmöglichkeiten für solche Verwendungen von porösen Materialien an Flugzeugen und auch an anderen aerodynamischen Gegenständen sind bisher sehr begrenzt. Die vorliegende Arbeit nimmt sich diesem Problem an und beschreibt den gesamten Entwicklungsprozess einer möglichen Erweiterung für numerische Strömungslöser zur Berechnung turbulenter Strömungen über porösen Materialien, beginnend mit der Herleitung der theoretischen Modelle, über deren Integration in einen Strömungslöser, bis hin zur Validierung der Modelle anhand von DNS-Daten und Experimenten.

Die Randbedingungen der zu simulierenden Strömungen kommen aus der zivilen Luftfahrt und sind unter anderem hohe Reynoldszahlen, sehr feine poröse Strukturen und Geschwindigkeiten im transonischen Machzahlbereich. Um solche Strömungen effektive lösen zu können werden die Navier-Stokes-Gleichungen in ihrer kompressiblen Form räumlich und zeitlich gemittelt. Dadurch entstehen zu modellierende Terme, welche zum einen den Effekt von porösen Materialien auf die Strömung und zum anderen den Effekt der Turbulenz beschreiben. Das verwendete Modell der für die porösen Materialien zuständigen Terme basiert auf den Gesetzen von Darcy- und Forchheimer, und Turbulenzterme werden mit Hilfe eines Reynoldsspannungsmodells modelliert.

An der Übergangsfläche zwischen porösem Medium und freier Strömung werden zusätzliche Bedingungen notwendig. Denn beim Auftreffen der Strömung auf ein poröses Medium muss ihr Zustand so transformiert werden, dass sie ihren Weg im porösen Medium physikalisch sinnvoll fortsetzt. Die Transformation basiert hauptsächlich auf Erhaltungsgleichungen von Masse und Energie. Außerdem wird die Entropie beim Einströmen ins poröse Medium erhalten. Die Berechnung diffusiver Flüsse an der Übergangsfläche erfordert weitere Zusammenhänge für die Gradienten einiger Strömungsvariablen, welche auf den Sprungbedingungen von Ochoa-Tapia und Whitaker basieren.

Nach der Herleitung der benötigten Theorie wird kurz auf deren Implementierung in einen finite-Volumen Strömungslöser eingegangen. Die Funktionsfähigkeit wird anhand von einfachen Testfällen gezeigt, um sich dann der Kalibrierung und Validierung der theoretischen Modelle zu widmen. Kalibriert werden die Modellparameter mit Hilfe von DNS-Daten einer Kanalströmung. Die Lösungen mit den final festgelegten Parameterwerten zeigen gute Übereinstimmung mit DNS-Daten. Für die Validierung werden aerodynamische Windkanaluntersuchungen an dem anfangs beschriebenen Flügel mit poröser Hinterkante durchgeführt. Der Effekt der porösen Hinterkante auf den Auftriebsbeiwert wird durch die numerischen Simulationen gut wiedergegeben. Ein näherer Vergleich zwischen Experiment und Rechnung anhand des Strömungsfelds nahe der porösen Hinterkante zeigt außerdem, dass der Strömungslöser die Strömungsphysik korrekt reproduziert.

Contents

Glossary

Latin Letters

A	Area; flatness factor of Reynolds stresses.
a	Turbulent anisotropy tensor; speed of sound.
A_2	Second invariant of Reynolds-stress anisotropy tensor a, $A_2 = a_{ij}a_{ji}$.
A_3	Third invariant of Reynolds-stress anisotropy tensor a, $A_3 = a_{ij}a_{jk}a_{ki}$.
A_{fs}	Pore surface area of a porous medium which is faces fluid.
c	Chord length.
$c_{d,p}$	Constant in model for turbulent diffusion term D_p.
$c_{d,p,\text{eff}}$	Effective constant in model for turbulent diffusion term D_p.
$c_{\varepsilon,\text{F}}$	Modelling coefficient of gradient diffusion model in Forchheimer term of turbulent dissipation-rate equation.
c_{F}	Forchheimer coefficient.
c_l	Local lift coefficient.
c_μ	Modelling coefficient for computing the eddy viscosity, $c_\mu = 0.09$.
c_p	Heat capacity for constant pressure; pressure coefficient, $c_p = \frac{p-p_\infty}{\frac{\rho}{2}v_\infty^2}$.
c_φ	General constant in gradient diffusion hypothesis.
c_s	Gradient diffusion modelling constant of Daly-Harlow model.
c_t	Gradient diffusion modelling constant of Hanjalić-Launder model.
c_V	Heat capacity for constant volume.
c_{wd}	Model parameter for increasing the effective distance to the porous interface used in the Reynolds-stress redistribution model.
D	Turbulent diffusion term.
d	Distance to porous interface; typical pore dimension.
Da	Darcy number $Da = \frac{\kappa}{L^2}$.
d_{eff}	Effective distance to porous interface.
D_ε	Sum of viscous, turbulent and pressure diffusion term of turbulent dissipation-rate equation.

$D^{(\nu)}$	Viscous diffusion of Reynolds stresses.
D_p	Turbulent diffusion term for modelling extra diffusion inside porous media.
d_{p}	Pore diameter.
$D^{(\mathrm{p})}$	Turbulent pressure diffusion term of Reynolds-stress equation.
E	Total specific fluid energy, $E = e + \frac{v^2}{2}$; flatness factor of turbulent dissipation-rate.
e	Specific inner energy; dissipation anisotropy tensor.
E_2	Second invariant of dissipation anisotropy tensor of Reynolds stresses e, $E_2 = e_{ij}e_{ji}$.
E_3	Third invariant of dissipation anisotropy tensor of Reynolds stresses e, $E_3 = e_{ij}e_{jk}e_{ki}$.
F	Force; flux.
Δg	Functional to describe the magnitude of gradient jumps over nonporous-porous interfaces.
H	Total specific fluid enthalpy, $H = E + \frac{p}{\rho}$; channel height.
h	Specific enthalpy.
k	Turbulent kinetic energy, $k = \frac{1}{2}\widetilde{v_i''v_i''}$.
k_{d}	Heat conduction.
$k_{\mathrm{d}}^{(\mathrm{t})}$	Turbulent heat transport.
L	Characteristic length.
M	Reynolds-stress term which contains the compressibility effects.
Ma	Mach number.
$\mathcal{N}$	Navier-Stokes momentum equation.
n	Normal direction.
P	Turbulent production term.
p	Pressure.
$\mathcal{P}^{(\mathrm{Darcy})}$	Darcy term of Reynolds-stress equation.
$\mathcal{P}_{\varepsilon}^{(\mathrm{Darcy})}$	Darcy term of turbulent dissipation-rate equation.
$\mathcal{P}_{\varepsilon}^{(\mathrm{Forch})}$	Forchheimer term of turbulent dissipation-rate equation.
$\mathcal{P}_{\varepsilon^{\mathrm{h}}}^{(\mathrm{Darcy})}$	Darcy term of homogeneous turbulent dissipation-rate equation.
$\mathcal{P}_{\varepsilon^{\mathrm{h}}}^{(\mathrm{Forch})}$	Forchheimer term of homogeneous turbulent dissipation-rate equation.
P_{ε}	Production term of turbulent dissipation-rate equation.
$\mathcal{P}^{(\mathrm{Forch})}$	Forchheimer term of Reynolds-stress equation.

p^*	Dimensionless pressure, $p^* = \frac{p}{\frac{\rho}{2} v_0^2}$.
R	Flow resistivity.
Re	Reynolds number.
Re_{crit}	Critical Reynolds number where flow starts to become turbulent.
Re_κ	Reynolds number where the length scale is based on the permeability κ, $Re_\kappa = \frac{\rho v \sqrt{\kappa}}{\mu}$.
Re_τ	Reynolds number created with shear stress velocity u_τ, $Re_\tau = \frac{u_\tau L}{\nu}$.
R_s	Specific gas constant.
$S_{\varepsilon 4}$	Pressure gradient term in homogeneous turbulent dissipation-rate equation.
S_l	Length scale limiter of homogeneous turbulent dissipation-rate equation.
T	Temperature; turbulent diffusion; time interval.
t	Time.
T_ε	Turbulent transport term of turbulent dissipation-rate equation.
u_τ	Shear stress velocity.
V	Volume.
v	Velocity.
w	Arbitrary conservative variable.
x	Coordinate direction.
x^*	Dimensionless coordinate, $x^* = \frac{x}{L}$.
Y	Dissipation term of turbulent dissipation-rate equation.
y	Coordinate direction.

Greek Letters

α	Angle of attack; heat transfer coefficient; scaling factor for artificial dissipation.
α^*	Integral value of heat flux coefficient α.
β	Jump coefficient defining jump of velocity gradient at porous interfaces.
β_{t}	Turbulent jump coefficient defining jump of Reynolds-stress gradients at porous interfaces.
ρ	Density.
ϵ	Deviation variable in Taylor expansion.
ε	Turbulent dissipation-rate.
ε^{h}	Homogeneous turbulent dissipation-rate.
$\hat{\varepsilon}^{\mathrm{h}}$	Isotropic part of homogeneous turbulent dissipation-rate.

γ	Isentropic exponent.
κ	Permeability.
κ_2	Blending function for artificial dissipation.
κ_4	Blending function for artificial dissipation.
λ	Thermal conductivity.
λ_{eff}	Effective thermal conductivity.
λ^*	Expansion viscosity, $\lambda^* = -\frac{2}{3}\mu$.
μ	Dynamic viscosity.
μ_{t}	Eddy viscosity.
ν	Kinematic viscosity, $\nu = \frac{\mu}{\rho}$.
ϕ	Porosity.
Φ_ε	Pressure transport term of turbulent dissipation-rate equation.
Π	Pressure-strain correlation.
Π^{w}	Near wall pressure-strain correlation term.
σ	Stress; Prandtl number.
σ_{t}	Turbulent Prandtl number.
τ	Viscous stress tensor.

Operator commands

$\lvert\varphi\rvert$	Absolute value of a arbitrary variable φ; vector length if φ is a vector.
$\widetilde{\varphi}$	Density-weighted time average of arbitrary variable φ.
φ''	Deviation of arbitrary variable φ from its density-weighted time average, $\varphi'' = \varphi - \widetilde{\varphi}$.
∇^2	Laplacian operator.
$\langle\varphi\rangle$	Spatial average of arbitrary variable φ.
$\varphi^{\triangleleft}$	Deviation of arbitrary variable φ from its spatial average, $\varphi^{\triangleleft} = \varphi - \langle\varphi\rangle$.
$\langle\varphi\rangle^{\mathrm{s}}$	Superficial spatial average of arbitrary variable φ.
$\langle\varphi\rangle_{\mathcal{F}}$	Density-weighted spatial average of arbitrary variable φ.
$\varphi^{\diamond}$	Deviation of arbitrary variable φ from its density-weighted spatial average, $\varphi^{\diamond} = \varphi - \langle\varphi\rangle_{\mathcal{F}}$.
$\overline{\varphi}$	Time average of arbitrary variable φ.
φ'	Deviation of arbitrary variable φ from its time average, $\varphi' = \varphi - \overline{\varphi}$.

Typical Indices

0	Reference variable value.

b	Bulk value, this refers to the mean value in the nonporous part of porous-bottom channel computations.
f	Fluid; nonporous side of nonporous-porous interface; fibre.
n	Normal direction.
p	Porous; porous side of nonporous-porous interface; pore.
r	Offset direction, perpendicular to normal and tangential directions.
s	Structure, refers to variables at the solid porous structure; streamline direction; sphere.
t	Tangential direction.
t	Turbulent.
∞	Variable value at farfield.

Abbreviations

DLR	Deutsches Zentrum für Luft- und Raumfahrt (i.e. German Aerospace Center).
DNS	Direct numerical simulations.
JHh-v2	Jakirlić-Hanjalić homogeneous version 2 (Reynolds-stress turbulence model based on homogeneous turbulent dissipation-rate as length scale variable).
PA	Porous aluminum.
PIV	Particle image velocimetry.
RANS	Reynolds-averaged Navier-Stokes.
SBP	Sintered bronze powder.
SFB	Sonderforschungsbereich (i.e. Collaborative Research Center).
SFF	Sintered fibre felt.
VRANS	Volume- and Reynolds-averaged Navier-Stokes.

1. Introduction

The title of this work reads Volume-Averaged RANS-Simulation of Turbulent Flow over Porous Media. In order to clarify this title, the three different terms *Volume-Averaged RANS-Simulations*, *Turbulent Flow* and *Porous Media* must be identified. Beginning with the last, the porous media in this work are understood as rigid materials which contain voids. These voids have to be connected with the outer surface of the rigid material in a way that the fluid can pass through the material with increased efforts (see figure 1.1 to the right). It is of interest to predict the fluid flow over porous media. This prediction is performed with volume-averaged RANS-simulations which will be described further in the theoretical part of this work. The last term *turbulent flow* complicates the simulations since the fluid particles are now allowed to move over time in superimposed small-scale fluctuations.

free flow (can be already simulated)

closed pores (not considerd in this work)

open pores (hard to get through)

Figure 1.1.: Schematic of flow through porous media.

This work is part of the Collaborative Research Center SFB 880 [61] where fundamentals of high-lift for future commercial aircraft are investigated. Part of this collaborative project is the research effort on low-noise take-off and landing [21]. One point of the investigation is aircraft wings with porous trailing edges (see figure 1.2). This specific setup can significantly reduce the trailing edge noise as demonstrated by Herr et al. [33, 34]. However, for the evaluation of the aerodynamic properties of the new quiet wing, there is a lack of reliable tools to simulate the flow in the vicinity of porous media. This provides the motivation for the present work to develop a reliable method for aerodynamic simulations over porous media. For the development of the required theory, several technical challenges must be considered:

1. The Reynolds numbers of the flow around the wing is rather high. Hence, the small-scale structures of the turbulent flow cannot be resolved with to-

days simulations capabilities. This is a well-known problem, which is solved by using the Reynolds-averaged Navier-Stokes equations together with an appropriate turbulence model.

2. The pore sizes of the porous media are very small. This means that the flow inside the pores cannot be resolved with sustainable efforts. This issue can be solved by a volume-averaging procedure. However, models of the integral effect of the porous medium must be developed.

3. High flight speeds and high-lift wing configurations lead to high flight Mach numbers. Thus, compressibility effects must be retained while deriving the theoretical models.

4. High-lift devices also lead to high streamline curvatures which is a critical task for many turbulence models. As a consequence, a high-fidelity Reynolds-stress model is used for the turbulence modelling.

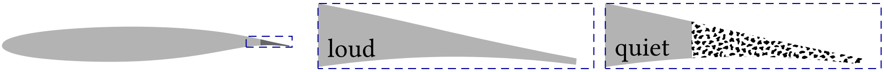

Figure 1.2.: Noise emission of a wing with and without trailing edge.

Even though this work has its direct motivation in aircraft aerodynamics, several other applications can be imagined. Starting with incompressible and laminar flow, there is the filtration of water through sand. This actually led to the development of the law of Darcy [20]. This law was extended by Forchheimer [26] for more general use at higher flow velocities. The given laws (Darcy with Forchheimer extension) are the basis for many other investigations e.g. for flow through heat exchangers as discussed in by Antohe et al. [3]. For even higher velocities, turbulent flow must be considered. This appears in nuclear reactors for example where the fuel rods constitute the porous structure and the cooling water is the fluid (see Chandesris, Serre and Sagaut [17]). In this case, the flow phenomena are already so complex that the complete Navier-Stokes equations have to be solved and turbulence is modelled with the help of additional transport equations. Not only incompressible but also compressible flow applications can be imagined besides the wing with porous trailing edge. One example is the supersonic wind-tunnel design (see Wu [82]) where the flow straighteners can be computed as porous medium.

Many more applications for flow over and through porous media exist. They include the simulation of wind parks close to forests (the trees constitute the porous medium) [57], canopy flow through cities [30] (where the buildings define the structure of the porous medium), flow through catalytic converters [84], delivery of gas from hydraulically fractured gas wells [35] or the tightness of dikes as shortly mentioned in [26].

1.1. State of the art

Under the given conditions of high Reynolds numbers, very fine pore structures and complex applications, the only reasonable flow prediction method is to solve the RANS-equations (Reynolds-averaged Navier Stokes equations) while modelling the effect of the porous media. It is common practice to model the porous media effect as drag forces based on the Darcy and Forchheimer terms. When it comes to turbulence, the most common turbulence model is the k-ε-model. Several variations exist which try to accurately predict the turbulence inside porous media. The most prominent models originate from Nakayama and Kuwahara [52, 51] and from Pedras and Lemos [56]. The main difference can be expressed that the turbulence will decay to zero deep inside the porous medium for the Pedras and Lemos-model while the model of Nakayama and Kuwahara predicts finite values. Especially the model of Pedras and Lemos is adopted by several authors for further investigations, as given in [13, 64, 39, 5] to name a few. On the other side, Guo [29] showed good results for the Nakayama and Kuwahara model. Also, their general idea is adopted in the model given by Chandesris, Serre and Sagaut [17]. Besides of the two main lines, one can find several more variants of the k-ε-model in porous media, e.g. [2, 28, 77]. The large amount of variants without a clear winner already indicates the complexity of the topic.

Some publications state that the two transport equations of the k-ε model are not enough and rather additional transport equations should be introduced. The final set of transport equations allows them to describe the micro-scale turbulence inside the porous structure and the macro-scale turbulence throughout the structure separately. Special terms connect the equations describing the energy transfer between the scales. Kuwata, Suga and Sikurai [42] propose micro-scale k- and ε-equations while Drouin, Grégoire and Simonin [23] use the transport equation of the dispersive kinetic energy and the wake dissipation as additional equations. Note, that the latter model replaces the standard ε-equation by an algebraic relation and thus only has to solve three transport equations.

One further step to increase complexity is to drop the Boussinesq-hypothesis. Rather than solving the k-ε-equations, the Reynolds-stress equations are solved directly. This will mainly decouple the turbulent stresses from viscous stresses allowing to describe more complex flow phenomena. Such a Reynolds-stress model is used by Kuwata and Suga [41, 40] coupled with a micro-scale k-ε-model.

The ideas above concentrate mainly on the existing turbulence modelling strategies inside porous media. However, it should be noted that the present work needs to predict flow *over* porous media and, thus, the transition between nonporous and porous regions have to be also correctly modelled. While the several stated publications mention such scenarios, there are specialized papers on this very topic. The most straightforward procedure is to completely disregard the transition to the porous region but describing the porous models in a way that they automatically fall back to the standard (nonporous) equations in the nonporous regions. Such approach is used by Hang and Li [30]. A more accurate model for the nonporous-porous transition area can be defined by using a smooth blend of the porous properties until they adopt the final value inside the porous regions, as in the work of Kuwata and Suga [41]. Instead of determining the correct smooth behaviour of the porous properties, discrete jump conditions between nonporous and porous media can be defined. The most prominent conditions have their origin in the work of Ochoa-Tapia and Whitaker [55] for non-turbulent flows, and have been adapted to k-ε-models by Silva and Lemos [70, 45, 71] and Chandesris and Jamet [15].

1.2. Necessity and limitations of this work

Section 1.1 demonstrates that a certain amount of research has already been conducted for turbulent flow over porous media. This leads to the question why yet another model for computing flow over porous media is needed. The reasons are manifold. Firstly, to the author's knowledge all developments are completely devoted to incompressible flow whereas the todays aircraft operate at transonic speeds. Hence, models are needed which have the potential to compute compressible flow. This is achieved in this work by using a Reynolds-stress turbulence model which is calibrated to provide reliable results at transonic speeds. In addition to that, the conditions across the nonporous-porous interface are redefined in a way to operate consistently at both, incompressible and compressible flows.

A second reason for the current work is its intention to implement the theory into an established flow solver with the aim to make it accessible for many users. Hence, the theoretical derivations are held very general, valid in 3D-space. And finally, the work focuses on the validation of the theoretical models with realistic applications and, thus, proves its usability.

Despite the intention of this work to provide very general simulation capabilities, some limitations must be defined. The two most restricting ones are:

- The porous media are assumed to be isotropic which means that their properties do not depend on the orientation in space.
- Inside a porous region, the properties of the medium are taken to be constant.

Note that both of these issues are part of the successor project of the Collaborative Research Center SFB 880. Further limitations are

- Only rigid porous media are considered.
- Heat transfer between fluid and porous structure has no effect on the flow.

These two issues are of no interest for this work and are, thus, either ignored or only roughly covered.

1.3. Outline

Chapter 2 begins with a description of the derivation of volume-averaged Navier-Stokes equations which can already be solved for laminar flow. The interface conditions from nonporous to porous flow for laminar flow will also be derived and the rules for computing the integral forces on porous bodies will be set up. The extension from laminar to turbulent flow with the help of time averaging is performed in chapter 3. This chapter is organized similar to the chapter of laminar flow but also writes down the complete *JHh-v2* turbulence model which is needed for determination of the Reynolds stresses.

The subsequent chapter 4 describes a way to implement the theoretical models into a flow solver such as the DLR-TAU-Code. Firstly, this chapter covers the difficulties of implementing the volume treatment of computation grid cells inside the porous media. Then, details about the flux computation over the nonporous-porous interface are explained. The final implementation into the DLR-TAU-Code is verified for porous channel computations in chapter 5.

Chapter 6 describes calibrations for the unknown model parameters with the help of DNS-results of a laminar and a turbulent channel (section 6.1). Afterwards, the code is applied to a realistic application of a wing with porous trailing edge (section 6.2) comparing the lift and demonstrating the detailed flow phenomena.

Finally, chapter 7 concludes the current work and provides an outlook for future work.

2. Laminar Flow in Porous Media

The simulation of flow around complex bodies requires solving the Navier-Stokes equations. Special treatment is needed when porous media are involved, at least when the flow inside the porous structure needs not be resolved. The usual procedure for deriving the suitable equations is by volume averaging the Navier-Stokes equations and then modelling the resulting unknown terms. The primary objective of this chapter is to demonstrate this procedure and present the special treatment at the interface between porous and nonporous regions. Since the final set of equations completely defines laminar flow this chapter is titled “laminar flow in porous media”. In addition, the results of this chapter define the basic infrastructure for developing the models for turbulent flow over porous media which is then covered in chapter 3.

Before starting with the derivation of the governing equations for laminar flow in porous media a short introduction to the principal effects of flow through porous media is given. Later on, this will help to model the unknown terms in the volume-averaged Navier-Stokes equations. But first the definition of the porosity ϕ has to be clarified: It is defined as the void space or rather the entrapped fluid volume inside the porous medium,

$$\phi = \frac{\text{fluid volume}}{\text{total volume}} = \frac{V_\mathrm{f}}{V} \tag{2.1}$$

where V_f is the fluid volume and V is the total volume including also the porous structure (see figure 2.1).

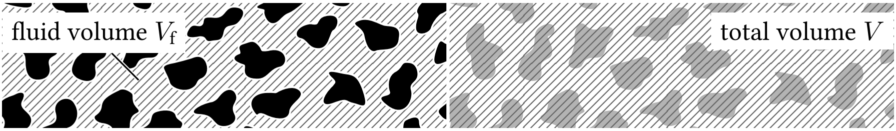

Figure 2.1.: Definition of the fluid volume V_f inside a porous medium and of the total volume V containing also the solid structure.

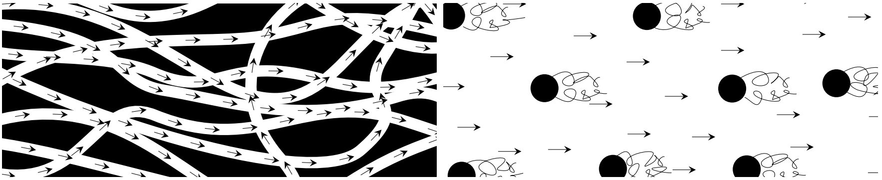

Figure 2.2.: Left hand side: Porous medium composed of many thin channels; right hand side: Porous medium composed of many small particles hindering the flow on its way past the porous medium.

2.1. Effect of porous media on fluid flow

Firstly, assume a porous medium to be a solid structure crossed by several thin channels (see figure 2.2 left). For such kind of channels one can write down the proportionality

$$\frac{\partial p}{\partial x} \propto v \cdot \mu \tag{2.2}$$

as long as the flow in the channel is laminar. In this equation, $\frac{\partial p}{\partial x}$ is the pressure gradient in the porous medium, μ is the dynamic viscosity and v is the fluid's averaged flow velocity. Literally, equation (2.2) states that the drag inside porous media is linearly dependent on the flow velocity v and the dynamic viscosity μ. Though, another perspective for describing a porous medium can be given. This is a medium consisting of several small (connected) particles which hinder the flow on its way through (see figure 2.2 to the right). Flow separation behind the particles leads to pressure drag which is proportional to the square of the flow velocity v and linearly proportional to the density ρ:

$$\frac{\partial p}{\partial x} \propto \rho v^2 \tag{2.3}$$

Combining the two perspectives leads to the law of Darcy with the Forchheimer extension [26],

$$\frac{\partial p}{\partial x} = \underbrace{-\phi \frac{\mu}{\kappa} v}_{\text{Darcy term}} - \underbrace{\phi^2 \frac{c_\mathrm{F}}{\sqrt{\kappa}} \rho v^2}_{\text{Forchheimer term}} \quad , \tag{2.4}$$

where the proportionality constants of this law are constructed with the permeability κ, the Forchheimer coefficient c_F and the porosity ϕ. The three parameters are properties of the porous medium. The permeability κ is generally measured with the help of experiments at very small flow velocities where the Forchheimer term can be neglected. The Forchheimer coefficient c_F itself is determined by either further experiments or by empirical relations (e.g. the Ergun-equation [46]).

Equation (2.4) in its present form can already predict the pressure drop in porous media for a constant velocity. However, in order to solve more complex flow it must be included into the Navier-Stokes equations.

2.2. Navier-Stokes equations

The governing equations for flow in porous media are derived based on the Navier-Stokes equations in their differential form:

$$\frac{\partial \rho}{\partial t} + \frac{\partial \rho v_i}{\partial x_i} = 0 \tag{2.5a}$$

$$\frac{\partial \rho v_i}{\partial t} + \frac{\partial \rho v_i v_j}{\partial x_j} + \frac{\partial p}{\partial x_i} - \frac{\partial \tau_{ij}}{\partial x_j} = 0 \tag{2.5b}$$

$$\frac{\partial \rho E}{\partial t} + \frac{\partial \rho v_i H}{\partial x_i} - \frac{\partial v_i \tau_{ij}}{\partial x_j} + \frac{\partial k_{\mathrm{d},i}}{\partial x_i} = 0 \tag{2.5c}$$

Here, the Einstein notation is used. The nomenclature of the symbols is as follows: ρ is the density, v_i is the velocity component in the coordinate direction x_i, p is the pressure, τ_{ij} is the tensor of viscous stresses and $k_{\mathrm{d},i}$ is the ith component of the heat flux vector. The total energy E[1] consists of internal energy e and the kinetic energy $\frac{v_i v_i}{2}$ ($E = e + \frac{v_i v_i}{2}$). The total enthalpy H is defined as $H = E + \frac{p}{\rho}$.

2.3. Volume-averaging rules

The spatial average of an arbitrary fluid property φ inside the volume V is defined through the integral

$$\langle \varphi \rangle = \frac{1}{V_\mathrm{f}} \int\limits_{V_\mathrm{f}} \varphi \, \mathrm{d}V \quad . \tag{2.6}$$

This is generally referred to as intrinsic average. Furthermore, the superficial average value is defined:

$$\langle \varphi \rangle^\mathrm{s} = \frac{1}{V} \int\limits_{V_\mathrm{f}} \varphi \, \mathrm{d}V \tag{2.7}$$

Both, intrinsic and superficial averages are related by the factor of the porosity:

$$\langle \varphi \rangle^\mathrm{s} = \phi \cdot \langle \varphi \rangle \tag{2.8}$$

---

[1] Strictly speaking, the different energy variables and components E, e, H, h, k_d, $\frac{v_i v_i}{2}$ are *specific* values, i.e. energy components per mass. Note that for convenience, the word *specific* is omitted throughout this work.

Applying one of the averaging operators (2.6) or (2.7) onto the Navier-Stokes equations in their compressible form would lead to several additional complex terms. A simpler derivation can be obtained by using the density-weighted averaging operator which is defined as

$$\langle \varphi \rangle_{\mathcal{F}} = \frac{\langle \rho \varphi \rangle}{\langle \rho \rangle} = \frac{1}{\langle \rho \rangle V_\mathrm{f}} \int\limits_{V_\mathrm{f}} \rho \varphi \, \mathrm{d}V \ . \tag{2.9}$$

In order to derive the volume-averaged Navier-Stokes equations, the treatment of the volume-averaged gradients and the time derivatives must be described. What is needed, is a relationship between the average of a gradient and the gradient of an average. The same applies to the time derivatives. The required relationships are given by Bear and Bachmat [4]. The relation for the time derivative is

$$\left\langle \frac{\partial \varphi}{\partial t} \right\rangle^\mathrm{s} = \frac{\partial \langle \varphi \rangle^\mathrm{s}}{\partial t} - \frac{1}{V} \int\limits_{A_\mathrm{fs}} \varphi v_{\mathrm{s},i} n_i \, \mathrm{d}A \tag{2.10}$$

where n_i is the i-th component of the normal vector $\vec{n}$ and A_fs is the surface area of the porous structure (see figure 2.3). The variable v_s is the velocity of this pore surface. Since the present work only considers rigid porous media, the velocity v_s is always zero and the integral term of equation (2.10) vanishes. Hence, the averaging operator can be pulled into the time derivative without additional concerns. This is different for the spatial gradients where the relation is given as

$$\left\langle \frac{\partial \varphi}{\partial x_i} \right\rangle^\mathrm{s} = \frac{\partial \langle \varphi \rangle^\mathrm{s}}{\partial x_i} + \frac{1}{V} \int\limits_{A_\mathrm{fs}} \varphi n_i \, \mathrm{d}A \ . \tag{2.11}$$

Here, the integral is not always zero. Rather, it describes the effect of porous media onto a fluid inside the volume-averaged Navier-Stokes equations.

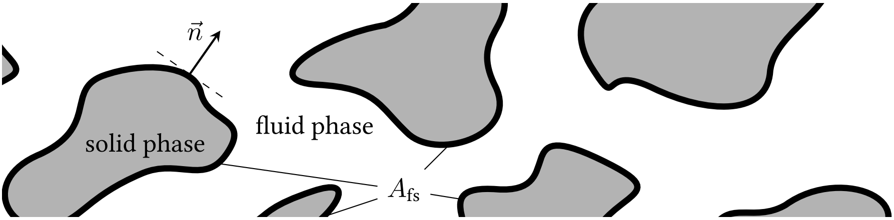

Figure 2.3.: Definition of the pore surface A_fs and its normal vector $\vec{n}$.

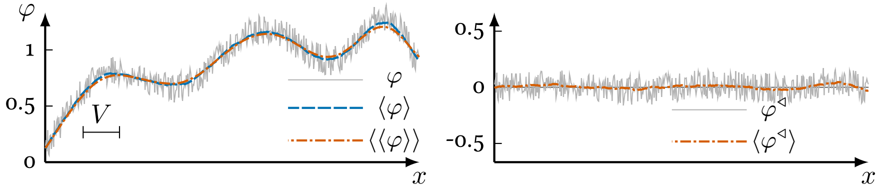

Figure 2.4.: Effect of double averaging the arbitrary variable φ within an averaging volume of size V.

Both relations (2.10) and (2.11) are defined for the superficial volume average. Converting them to the intrinsic counterparts results in additional terms which contain the gradients of the porosity ϕ:

$$\left\langle \frac{\partial \varphi}{\partial t} \right\rangle = \frac{\partial \langle \varphi \rangle}{\partial t} + \langle \varphi \rangle \frac{\partial \phi}{\partial t} + \frac{1}{V_\mathrm{f}} \int\limits_{A_\mathrm{fs}} \varphi v_{\mathrm{s},i} n_i \,\mathrm{d}A \tag{2.12}$$

$$\left\langle \frac{\partial \varphi}{\partial x_i} \right\rangle = \frac{\partial \langle \varphi \rangle}{\partial x_i} + \langle \varphi \rangle \frac{\partial \phi}{\partial x_i} + \frac{1}{V_\mathrm{f}} \int\limits_{A_\mathrm{fs}} \varphi n_i \,\mathrm{d}A \tag{2.13}$$

Additionally, relations of statistical origin will be needed for the derivation of the volume-averaged Navier-Stokes equations. With a given volume-averaged arbitrary flow variable φ its fluctuation value can be defined:

$$\varphi^{\triangleleft} = \varphi - \langle \varphi \rangle \tag{2.14}$$

In the subsequent derivations it is assumed that the rules

$$\langle\langle \varphi \rangle\rangle = \langle \varphi \rangle \quad \text{and} \quad \langle \varphi^{\triangleleft} \rangle = 0 \tag{2.15}$$

are valid. Strictly speaking, this is an approximation which is also presented in figure 2.4 showing the double average for an arbitrary function $\phi(x)$. It can be easily recognized that the double average does not exactly overlap the single average. The figure also shows that the average of the fluctuation value $\phi^{\triangleleft}$ is not identically zero. In terms of "flow in porous media" this implies that the rules (2.15) are only applicable so long as the averaging procedure eliminates the small-scale fluctuations inside the single pores but retains the large-scale flow phenomena.

Besides the fluctuations for the standard volume average (2.6) the fluctuations of the density-weighted average (2.9) can be defined as

$$\varphi^{\diamond} = \varphi - \langle \varphi \rangle_{\mathcal{F}} \quad . \tag{2.16}$$

The same rules applied to the standard volume average are assumed to be valid for the density-weighted averages:

$$\langle \langle \varphi \rangle_{\mathcal{F}} \rangle_{\mathcal{F}} = \langle \varphi \rangle_{\mathcal{F}} \quad \text{and} \quad \langle \varphi^{\diamond} \rangle_{\mathcal{F}} = 0 \tag{2.17}$$

Additional relationships which can be directly obtained from rules (2.15) or (2.17) are

$$\langle \varphi_A + \varphi_B \rangle = \langle \varphi_A \rangle + \langle \varphi_B \rangle \quad ; \quad \langle c\varphi \rangle = c \langle \varphi \rangle \quad ; \quad \langle \varphi^{\triangleleft} \langle \varphi \rangle \rangle = 0 \tag{2.18}$$

where c is an arbitrary spatial constant. The relationships are valid for the density-weighted average as well.

With this the required basic relationships and assumptions are complete and the volume-averaged Navier-Stokes equations (2.5) for flow through porous media can be derived.

2.4. Volume averaging of the Navier-Stokes equations

The starting point for averaging the Navier-Stokes equations (2.5) in space is the averaging operator (2.6). It is applied on the complete set of equations. The volume-averaged mass conservation equation (2.5a) reads

$$\left\langle \frac{\partial \rho}{\partial t} + \frac{\partial \rho v_i}{\partial x_i} \right\rangle = 0 \ .$$

Using the relations (2.18), (2.12) (2.13) this can be stated as

$$\frac{\partial \langle \rho \rangle}{\partial t} + \frac{\partial \langle \rho v_i \rangle}{\partial x_i} + \langle \rho v_i \rangle \frac{\partial \phi}{\partial x_i} + \frac{1}{V_{\mathrm{f}}} \int\limits_{A_{\mathrm{fs}}} \rho v_i n_i \,\mathrm{d}A = 0$$

where the assumptions of a rigid porous structure ($v_{\mathrm{s}} = 0$) as well as the time independence of the porosity ϕ are inherent. Section 1.2 already mentioned that porosity gradients will not be considered in the present work. Consequently, those terms are set to zero. Furthermore, the integral will also vanish since the velocity v_i at the pore surface A_{fs} is zero due to the no-slip condition. Thus, the volume-averaged equation for mass conservation reduces to

$$\frac{\partial \langle \rho \rangle}{\partial t} + \frac{\partial \langle \rho v_i \rangle}{\partial x_i} = 0$$

which can be rewritten by using the definition of the density-weighted average (2.9):

$$\frac{\partial \langle \rho \rangle}{\partial t} + \frac{\partial \langle \rho \rangle \langle v_i \rangle_{\mathcal{F}}}{\partial x_i} = 0 \tag{2.19}$$

The derivation of the remaining conservation equations will be covered quickly applying exactly the same principles used for obtaining the volume-averaged equation for mass conservation. Following similar reductions, the momentum conservation equation (2.5b) becomes

$$\frac{\partial \langle \rho \rangle \langle v_i \rangle_{\mathcal{F}}}{\partial t} + \frac{\partial \langle \rho \rangle \langle v_i v_j \rangle_{\mathcal{F}}}{\partial x_j} + \frac{\partial \langle p \rangle}{\partial x_i} - \frac{\partial \langle \tau_{ij} \rangle}{\partial x_j} + \frac{1}{V_\mathrm{f}} \int\limits_{A_\mathrm{fs}} p n_i - \tau_{ij} n_j \,\mathrm{d}A = 0 \ . \tag{2.20}$$

Here, the integral over the surface A_fs does not vanish completely and the pressure p and the viscous stress tensor τ_{ij} remain in the integral. Both of these variables can further be rewritten in terms of fluctuation values,

$$\begin{aligned}
\int\limits_{A_\mathrm{fs}} p n_i - \tau_{ij} n_j \,\mathrm{d}A &= \int\limits_{A_\mathrm{fs}} \left(\langle p \rangle + p^{\triangleleft}\right) n_i - \left(\langle \tau_{ij} \rangle + \tau_{ij}^{\triangleleft}\right) n_j \,\mathrm{d}A \\
&= \int\limits_{A_\mathrm{fs}} \langle p \rangle\, n_i - \langle \tau_{ij} \rangle\, n_j \,\mathrm{d}A + \int\limits_{A_\mathrm{fs}} p^{\triangleleft} n_i - \tau_{ij}^{\triangleleft} n_j \,\mathrm{d}A \\
&\approx \langle p \rangle \int\limits_{A_\mathrm{fs}} n_i \,\mathrm{d}A - \langle \tau_{ij} \rangle \int\limits_{A_\mathrm{fs}} n_j \,\mathrm{d}A + \int\limits_{A_\mathrm{fs}} p^{\triangleleft} n_i - \tau_{ij}^{\triangleleft} n_j \,\mathrm{d}A \\
&= \int\limits_{A_\mathrm{fs}} p^{\triangleleft} n_i - \tau_{ij}^{\triangleleft} n_j \,\mathrm{d}A
\end{aligned}$$

as the integral $\int_{A_\mathrm{fs}} n_i \,\mathrm{d}A$ is zero for large averaging volumes with constant porosity ϕ.

The second term of equation (2.20) can be split into two by using the averaging rules (2.18):

$$\begin{aligned}
\langle v_i v_j \rangle_{\mathcal{F}} &= \left\langle \left(\langle v_i \rangle_{\mathcal{F}} + v_i^{\diamond}\right) \left(\langle v_j \rangle_{\mathcal{F}} + v_j^{\diamond}\right) \right\rangle_{\mathcal{F}} \\
&= \left\langle \langle v_i \rangle_{\mathcal{F}} \langle v_j \rangle_{\mathcal{F}} \right\rangle_{\mathcal{F}} + \left\langle \langle v_i \rangle_{\mathcal{F}} v_j^{\diamond} \right\rangle_{\mathcal{F}} + \left\langle \langle v_j \rangle_{\mathcal{F}} v_i^{\diamond} \right\rangle_{\mathcal{F}} + \left\langle v_i^{\diamond} v_j^{\diamond} \right\rangle_{\mathcal{F}} \\
&= \langle v_i \rangle_{\mathcal{F}} \langle v_j \rangle_{\mathcal{F}} + \left\langle v_i^{\diamond} v_j^{\diamond} \right\rangle_{\mathcal{F}}
\end{aligned}$$

The term $\left\langle v_i^{\diamond} v_j^{\diamond} \right\rangle_{\mathcal{F}}$ on the right hand side is generally called *subfilter stress* or *dispersion*. Following the given relationships, the final form of the volume-averaged momentum equation reads

$$\begin{aligned}\frac{\partial \langle\rho\rangle \langle v_i\rangle_{\mathcal{F}}}{\partial t} &+ \frac{\partial \langle\rho\rangle \langle v_i\rangle_{\mathcal{F}} \langle v_j\rangle_{\mathcal{F}}}{\partial x_j} + \frac{\partial \langle\rho\rangle \left\langle v_i^{\diamond} v_j^{\diamond}\right\rangle_{\mathcal{F}}}{\partial x_j} \\ &+ \frac{\partial \langle p\rangle}{\partial x_i} - \frac{\partial \langle\tau_{ij}\rangle}{\partial x_j} + \frac{1}{V_{\mathrm{f}}} \int\limits_{A_{\mathrm{fs}}} p^{\triangleleft} n_i - \tau_{ij}^{\triangleleft} n_j \,\mathrm{d}A = 0 \ .\end{aligned} \tag{2.21}$$

Here, the subfilter stresses $\left\langle v_i^{\diamond} v_j^{\diamond}\right\rangle_{\mathcal{F}}$ and the surface integral $\int_{A_{\mathrm{fs}}} p^{\triangleleft} n_i + \tau_{ij}^{\triangleleft} n_j \,\mathrm{d}A$ are unknown and, thus, must be modelled.

Finally, the energy conservation equation (2.5c) is averaged over space:

$$\frac{\partial \langle\rho\rangle \langle E\rangle_{\mathcal{F}}}{\partial t} + \frac{\partial \langle\rho\rangle \langle v_i H\rangle_{\mathcal{F}}}{\partial x_i} - \frac{\partial \langle v_i \tau_{ij}\rangle}{\partial x_j} + \frac{\partial \langle k_{\mathrm{d},i}\rangle}{\partial x_i} + \frac{1}{V_{\mathrm{f}}} \int\limits_{A_{\mathrm{fs}}} k_{\mathrm{d},i} n_i \,\mathrm{d}A = 0$$

which reduces to

$$\begin{aligned}\frac{\partial \langle\rho\rangle \langle E\rangle_{\mathcal{F}}}{\partial t} &+ \frac{\partial \langle\rho\rangle \langle v_i\rangle_{\mathcal{F}} \langle H\rangle_{\mathcal{F}}}{\partial x_i} + \frac{\partial \langle\rho\rangle \langle v_i^{\diamond} H^{\diamond}\rangle_{\mathcal{F}}}{\partial x_i} - \frac{\partial \langle v_i\rangle_{\mathcal{F}} \langle\tau_{ij}\rangle_{\mathcal{F}}}{\partial x_j} \\ &- \frac{\partial \langle v_i\rangle_{\mathcal{F}} \left\langle\tau_{ij}^{\diamond}\right\rangle}{\partial x_j} - \frac{\partial \langle v_i^{\diamond}\rangle \langle\tau_{ij}\rangle_{\mathcal{F}}}{\partial x_j} - \frac{\partial \left\langle v_i^{\diamond} \tau_{ij}^{\diamond}\right\rangle}{\partial x_j} + \frac{\partial \langle k_{\mathrm{d},i}\rangle}{\partial x_i} \\ &+ \frac{1}{V_{\mathrm{f}}} \int\limits_{A_{\mathrm{fs}}} k_{\mathrm{d},i} n_i \,\mathrm{d}A = 0\end{aligned} \tag{2.22}$$

because $\langle\langle\varphi\rangle_{\mathcal{F}}\rangle = \langle\varphi\rangle_{\mathcal{F}}$ is approximately valid (see section A.1). The additional unknowns generated by the volume-averaging procedure are the correlations $\langle v_i^{\diamond} H^{\diamond}\rangle_{\mathcal{F}}$, $\left\langle v_i^{\diamond} \tau_{ij}^{\diamond}\right\rangle$ and the volume-averaged fluctuations $\langle v_i^{\diamond}\rangle$ and $\left\langle\tau_{ij}^{\diamond}\right\rangle$. Besides that, the surface integral over the heat conduction $k_{\mathrm{d},i}$ is unknown. Additionally, note that in the terms representing the average of the total energy E and the total enthalpy H, there exist some hidden fluctuations:

$$\begin{aligned}\langle E\rangle_{\mathcal{F}} &= \langle e\rangle_{\mathcal{F}} + \frac{\langle v_i\rangle_{\mathcal{F}} \langle v_i\rangle_{\mathcal{F}}}{2} + \frac{\langle v_i^{\diamond} v_i^{\diamond}\rangle_{\mathcal{F}}}{2} \\ \langle H\rangle_{\mathcal{F}} &= \langle E\rangle_{\mathcal{F}} + \left\langle \frac{p}{\rho} \right\rangle_{\mathcal{F}} = \langle E\rangle_{\mathcal{F}} + \frac{\langle p\rangle}{\langle\rho\rangle} = \langle e\rangle_{\mathcal{F}} + \frac{\langle v_i\rangle_{\mathcal{F}} \langle v_i\rangle_{\mathcal{F}}}{2} + \frac{\langle v_i^{\diamond} v_i^{\diamond}\rangle_{\mathcal{F}}}{2} + \frac{\langle p\rangle}{\langle\rho\rangle}\end{aligned}$$

At this point all relevant equations are derived in their volume-averaged form. In order to close them, several unknown terms have to be modelled. The following section will reason that several terms can be set to zero and describe models for the unknown terms which remain.

2.5. Closure models for the unknown terms of the volume-averaged equations

The unknown terms of the volume-averaged Navier-Stokes equations can be subdivided into three categories. First, the integrals over the surface A_fs of the porous structure

$$\int\limits_{A_\mathrm{fs}} p^{\triangleleft} n_i - \tau_{ij}^{\triangleleft} n_j \, \mathrm{d}A \quad , \quad \int\limits_{A_\mathrm{fs}} k_{\mathrm{d},i} n_i \, \mathrm{d}A \;\; ,$$

second, the different variances and correlations of fluctuation values

$$\left\langle v_i^{\diamond} v_j^{\diamond} \right\rangle_{\mathcal{F}} \quad , \quad \left\langle v_i^{\diamond} H^{\diamond} \right\rangle_{\mathcal{F}} \quad , \quad \left\langle v_i^{\diamond} \tau_{ij}^{\diamond} \right\rangle$$

and finally, the spatial average of the density weighted fluctuations

$$\left\langle v_i^{\diamond} \right\rangle \quad , \quad \left\langle \tau_{ij}^{\diamond} \right\rangle \;\; .$$

All of the three categories will be briefly discussed in the following sub-sections.

2.5.1. Integrals over the surface of porous structure

In order to get an explicit expression for the surface integrals

$$\int\limits_{A_\mathrm{fs}} p^{\triangleleft} n_i - \tau_{ij}^{\triangleleft} n_j \, \mathrm{d}A$$

of the momentum equations, flow through a channel according to figure 2.5 is assumed. This channel is completely filled with a porous medium and has slip walls. The flow is forced through the channel by a pressure gradient.

For incompressible flow, all gradients of the momentum equations are zero except the pressure gradient $\frac{\partial p}{\partial x}$ along the channel. Hence, the momentum equation (2.21) reduces to

$$\frac{\partial \left\langle p \right\rangle}{\partial x_i} = -\frac{1}{V_\mathrm{f}} \int\limits_{A_\mathrm{fs}} p^{\triangleleft} n_i - \tau_{ij}^{\triangleleft} n_j \, \mathrm{d}A \;\; .$$

This simplified equation can be matched with the empirical laws of Darcy and Forchheimer as discussed in section 2.1. In multidimensional space an appropriate model for the surface integral can be written as (see e.g. [10])

$$\frac{1}{V_\mathrm{f}} \int\limits_{A_\mathrm{fs}} p^{\triangleleft} n_i - \tau_{ij}^{\triangleleft} n_j \, \mathrm{d}A = \phi \frac{\left\langle \mu \right\rangle}{\kappa} \left\langle v_i \right\rangle_{\mathcal{F}} + \phi^2 \frac{c_\mathrm{F}}{\sqrt{\kappa}} \left\langle \rho \right\rangle \left\langle v_i \right\rangle_{\mathcal{F}} \cdot \left| \left\langle \vec{v} \right\rangle_{\mathcal{F}} \right| \;\; . \tag{2.23}$$

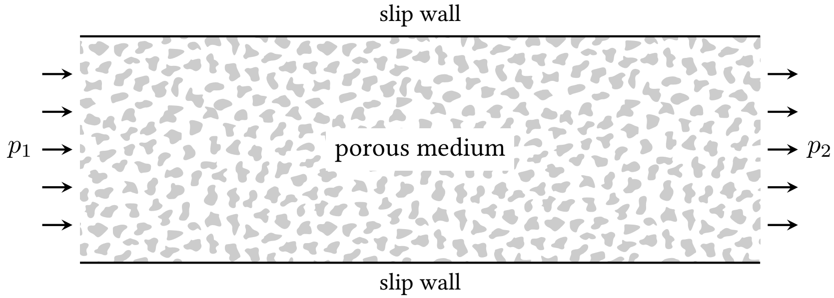

Figure 2.5.: Sketch of a completely porous channel.

The second surface integral

$$\int\limits_{A_{\mathrm{fs}}} k_{\mathrm{d},i} n_i \,\mathrm{d}A \quad , \tag{2.24}$$

which appears in the volume-averaged energy equation is assumed to have a minor influence on the fluid motion and therefore no modelling is required. It would rather influence the heat flux or, in other words, the temperature distribution which, as already stated, is not the focus of the present work. However, for the sake of completeness a short discussion about the term is provided within this section.

The specific heat flux k_{d} from fluid into porous structure can be computed with a heat transfer coefficient α and the temperature difference between the fluid and the porous structure:

$$k_{\mathrm{d},i} = \alpha (T_{\mathrm{s}} - T_{\mathrm{f}}) n_i \tag{2.25}$$

Here, T_{s} is the temperature of the porous structure and T_{f} is the temperature of the fluid. If both of these temperatures are equal at the surface of the porous structure, the integral (2.24) will vanish. This is a valid assumption for flows with small temperature gradients and porous structures which are not externally heated or cooled. Assuming that the temperatures T_{s} and T_{f} differ, the modelling of the integral (2.24) becomes important. Following Nield and Bejan [53] an appropriate model is

$$\frac{1}{V_{\mathrm{f}}} \int\limits_{A_{\mathrm{fs}}} k_{\mathrm{d},i} n_i \,\mathrm{d}A = \frac{\alpha^*}{\phi} \left(\langle T_{\mathrm{s}} \rangle - \langle T_{\mathrm{f}} \rangle \right) \quad . \tag{2.26}$$

The coefficient α^* describes an integral value of the heat flux coefficient α and is dependent on the porous medium. The model (2.26) supplies a source term for the energy equation (2.22) which heats or cools the passing fluid. Typical application candidates for this term would be heat exchangers or the simulation of flow over porous ice agglomerations on airplane wings.

2.5.2. Variance and correlations of fluctuation components

The variances of the velocity fluctuations $\langle v_x^\diamond v_x^\diamond \rangle_\mathcal{F}$, $\left\langle v_y^\diamond v_y^\diamond \right\rangle_\mathcal{F}$ and $\langle v_z^\diamond v_z^\diamond \rangle_\mathcal{F}$ are expected to be in the order of the mean kinetic energy $\frac{1}{2} \langle v_i \rangle_\mathcal{F} \langle v_i \rangle_\mathcal{F}$. This is estimated based on the fact that the actual velocities v_i will range from zero (no-slip at pore surfaces) to values considerably higher than the mean velocity. An effect of high variances can for example be expected in porous ducts where the law of energy conservation would predict an influence of the variances on the pressure distribution (see figure 2.6 where the pressure will drop to lower values in the duct as soon as the variances are considered).

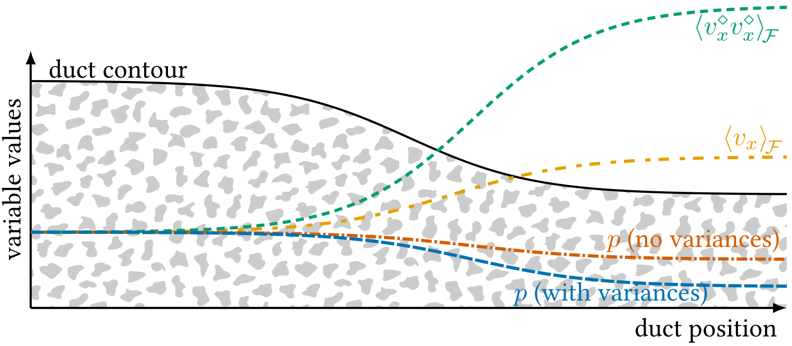

Figure 2.6.: Depiction of flow quantities along a porous duct. All lines are normalized with the values leftmost of the channel. The pressure is plotted for a non-fluctuating velocity (no variances) and for a fluctuating velocity (with variances).

One possible way to model the velocity variances would be

$$\langle v_x^\diamond v_x^\diamond \rangle_\mathcal{F} = \left\langle v_y^\diamond v_y^\diamond \right\rangle_\mathcal{F} = \langle v_z^\diamond v_z^\diamond \rangle_\mathcal{F} = a \cdot \langle v_i \rangle_\mathcal{F} \langle v_i \rangle_\mathcal{F} \tag{2.27}$$

where the parameter a depends on the porous medium. The model is based on the consideration that the fluctuations occur due to the fluid movement around the porous structure. The fluctuation magnitudes in different spatial directions are considered to be equal as long as the structure of the porous medium is isotropic. Such a model is expected to become important in regions with high velocity gradients in stream-wise direction. However, the applications of the present work do not fall into this category. And since no literature was found by the author to further assess the model or the parameter a the variances are neglected in the further derivations.

Furthermore, the unknown correlations $\left\langle v_i^\diamond v_j^\diamond \right\rangle_\mathcal{F}$, $\langle v_i^\diamond H^\diamond \rangle_\mathcal{F}$ and $\left\langle v_i^\diamond \tau_{ij}^\diamond \right\rangle$ or rather their gradients are also set to zero:

$$\frac{\partial \langle \rho \rangle \left\langle v_i^\diamond v_j^\diamond \right\rangle_\mathcal{F}}{\partial x_i} = \frac{\partial \langle \rho \rangle \langle v_i^\diamond H^\diamond \rangle_\mathcal{F}}{\partial x_i} = \frac{\partial \left\langle v_i^\diamond \tau_{ij}^\diamond \right\rangle}{\partial x_i} = 0 \tag{2.28}$$

This can be justified for the gradient of the velocity correlation $\left\langle v_i^\diamond v_j^\diamond \right\rangle_\mathcal{F}$ by the order of magnitude discussions of Whitaker [80] and Breugem [10]. Both suggest that the velocity correlations are small as long as certain conditions are fulfilled. Whitaker provides the conditions

$$d_\mathrm{p} \ll L_v \quad \text{and} \quad \mathit{Re}_\mathrm{p} \cdot \frac{d_\mathrm{p}}{L_v} = \frac{\langle \rho \rangle \langle v \rangle d_\mathrm{p}}{\langle \mu \rangle_\mathcal{F}} \frac{d_\mathrm{p}}{L_v} \ll 1$$

where L_v is the characteristic length scale over which the averaged velocity $\langle v \rangle$ will change. In contrast, Breugem states the conditions than either the Reynolds number Re_p is small or that the representative pore diameter d_p is much smaller than the representative size of a solid particle in the porous structure. The last condition can normally be reduced to the requirement of small porosity values. The given estimations are confirmed by the assumptions of Raupach [63, 62] whose findings are based on experimental data.

Due to a lack of DNS or experimental data, the correlations $\frac{\partial \langle \rho \rangle \langle v_i^\diamond H^\diamond \rangle_\mathcal{F}}{\partial x_i}$ and $\frac{\partial \left\langle v_i^\diamond \tau_{ij}^\diamond \right\rangle}{\partial x_i}$ are assumed to behave in a similar fashion as the velocity correlations and therefore have been set to zero. However, a model for the velocity-temperature correlations given by Saito and de Lemos [65] exists, which could describe parts of the gradient of the velocity-enthalpy correlation $\frac{\partial \langle \rho \rangle \langle v_i^\diamond H^\diamond \rangle_\mathcal{F}}{\partial x_i}$. They suggest a gradient diffusion model which increases the diffusive heat flux inside the porous medium. Since the present work concentrates on the fluid dynamics and not on the heat flux problem it seems reasonable to neglect this term.

2.5.3. Density-weighted fluctuations

The density-weighted fluctuations $\langle v_i^\diamond \rangle$ and $\left\langle \tau_{ij}^\diamond \right\rangle$ which appear in the energy equation (2.22) can be assumed to be responsible for transport of energy due to density fluctuations. As soon as there are no density fluctuations the terms which include $\langle v_i^\diamond \rangle$ or $\left\langle \tau_{ij}^\diamond \right\rangle$ disappear. However, it is anticipated that the terms will be small even for high Mach numbers and the density weighted fluctuations can be set to zero:

$$\langle v_i^\diamond \rangle = \left\langle \tau_{ij}^\diamond \right\rangle = 0$$

This assumption can only be supported from the point of view of turbulence modelling where the density-weighted time fluctuations are considered to be small (see e.g. [72]). Due to the lack of any numerical or experimental data no further assertions can be presented that this is also true for the volume-averaged quantities.

2.6. Summary of closed Navier-Stokes equations in porous media

With all the closure models discussed in the previous sections, a closed set of equations can be written which describes complex flows inside porous media:

$$\frac{\partial \langle \rho \rangle}{\partial t} + \frac{\partial \langle \rho \rangle \langle v_i \rangle_{\mathcal{F}}}{\partial x_i} = 0 \tag{2.29a}$$

$$\begin{aligned} \frac{\partial \langle \rho \rangle \langle v_i \rangle_{\mathcal{F}}}{\partial t} + \frac{\partial \langle \rho \rangle \langle v_i \rangle_{\mathcal{F}} \langle v_j \rangle_{\mathcal{F}}}{\partial x_j} =& -\frac{\partial \langle p \rangle}{\partial x_i} + \frac{\partial \langle \tau_{ij} \rangle}{\partial x_j} \\ & -\phi \frac{\langle \mu \rangle}{\kappa} \langle v_i \rangle_{\mathcal{F}} - \phi^2 \frac{c_{\mathrm{F}}}{\sqrt{\kappa}} \langle \rho \rangle \langle v_i \rangle_{\mathcal{F}} \cdot |\langle \vec{v} \rangle_{\mathcal{F}}| \end{aligned} \tag{2.29b}$$

$$\frac{\partial \langle \rho \rangle \langle E \rangle_{\mathcal{F}}}{\partial t} + \frac{\partial \langle \rho \rangle \langle v_i \rangle_{\mathcal{F}} \langle H \rangle_{\mathcal{F}}}{\partial x_i} = \frac{\partial \langle v_i \rangle_{\mathcal{F}} \langle \tau_{ij} \rangle_{\mathcal{F}}}{\partial x_j} - \frac{\partial \langle k_{\mathrm{d},i} \rangle}{\partial x_i} \tag{2.29c}$$

These equations rely on further relations of the fluid itself. For an ideal gas, the state variables which include pressure p, temperature T and density ρ are connected by

$$p = \rho T R_s \quad \text{or} \quad \langle p \rangle = \langle \rho \rangle \langle T \rangle_{\mathcal{F}} R_s \tag{2.30}$$

where R_s is the specific gas constant with a value of $287\,\mathrm{J\,kg^{-1}\,K^{-1}}$ for air. Further, assuming a calorically perfect gas, the enthalpy h and the inner energy e can be computed from the temperature T:

$$e = c_V T \quad \text{or} \quad \langle e \rangle_{\mathcal{F}} = c_V \langle T \rangle_{\mathcal{F}} \tag{2.31a}$$

$$h = c_p T \quad \text{or} \quad \langle h \rangle_{\mathcal{F}} = c_p \langle T \rangle_{\mathcal{F}} \tag{2.31b}$$

with the heat capacities c_V and c_p for constant volume and constant pressure. The dynamic viscosity μ can be deduced from the temperature T if the Sutherland law is applicable:

$$\mu = \mu_{\mathrm{ref}} T^{1.5} \frac{1 + \frac{110.4\,\mathrm{K}}{T_{\mathrm{ref}}}}{T + \frac{110.4\,\mathrm{K}}{T_{\mathrm{ref}}}} \tag{2.32}$$

where the reference viscosity μ_{ref} for air is $1.716 \times 10^{-5}\,\mathrm{kg\,m^2\,s^{-1}}$ and the reference temperature T_{ref} is 273 K. It is assumed that the law is also valid for the relationship between the averaged viscosity $\langle \mu \rangle$ and the temperature $\langle T \rangle_{\mathcal{F}}$ without any modifications.

Up to now, the tensor of viscous stresses τ_{ij} was used without any comments. In order to define it, a Newtonian fluid is assumed. This leads to the relationship

$$\begin{aligned} \tau_{ij} &= \lambda^* \cdot \delta_{ij} \left(\frac{\partial v_k}{\partial x_k} \right) + \mu \left(\frac{\partial v_i}{\partial x_j} + \frac{\partial v_j}{\partial x_i} \right) \\ \text{or} \quad \langle \tau_{ij} \rangle &= \langle \lambda^* \rangle \, \delta_{ij} \left(\frac{\partial \langle v_k \rangle_{\mathcal{F}}}{\partial x_k} \right) + \langle \mu \rangle \left(\frac{\partial \langle v_i \rangle_{\mathcal{F}}}{\partial x_j} + \frac{\partial \langle v_j \rangle_{\mathcal{F}}}{\partial x_i} \right) \end{aligned} \tag{2.33}$$

where $\lambda^* = -\frac{2}{3}\mu$. The Kronecker delta δ_{ij} will correspond to 1 for $i = j$ and 0 otherwise. The averaged counterpart of the equation is only valid as long as the viscosity μ does not correlate with the velocity gradients and the density-weighted fluctuations are negligible.

In order to define the heat flux $k_{\mathrm{d},i}$ Fourier's law is applied

$$k_{\mathrm{d},i} = -\lambda \frac{\partial T}{\partial x_i} \quad \text{or} \quad \langle k_{\mathrm{d},i} \rangle = -\lambda \frac{\partial \langle T \rangle}{\partial x_i} - \frac{\lambda}{V_{\mathrm{f}}} \int\limits_{A_{\mathrm{fs}}} T n_i \, \mathrm{d}A \tag{2.34}$$

with the thermal conductivity λ. The integral over the pore surfaces can be modelled to be proportional to the gradient of the averaged temperature (consult e.g. d'Hueppe [32]) and therefore expression (2.34) can be reduced to

$$\langle k_{\mathrm{d},i} \rangle = -\lambda_{\mathrm{eff}} \frac{\partial \langle T \rangle}{\partial x_i} \tag{2.35}$$

where λ_{eff} is the effective thermal conductivity inside the porous medium. Note, that this equation requires the volume-averaged temperature T whereas in the preceding equations only the density-weighted volume-averaged form of the temperature T is used. Nevertheless, it is assumed that equation (2.35) is also valid for the density-weighed average of the temperature,

$$\langle k_{\mathrm{d},i} \rangle = -\lambda_{\mathrm{eff}} \frac{\partial \langle T \rangle_{\mathcal{F}}}{\partial x_i} \tag{2.36}$$

inline with the similar case of equation (2.33).

2.7. Demonstration of computations of flow through a porous channel

The effects of the Darcy and Forchheimer term are now quickly demonstrated by a flow through a channel which is completely filled with an arbitrary porous medium.

The channel geometry is shown in figure 2.7. The permeability κ is given in terms of the Darcy number which is defined as

$$Da = \frac{\kappa}{L^2} = 2.5 \times 10^{-6} \tag{2.37}$$

where L is a characteristic length. It is taken to be equal to the channel length. Two cases with different Forchheimer coefficients c_F are computed here. In the first case c_F is set to zero and, thus, it does not consider effects of the Forchheimer term at all. In the second case c_F is 0.1.

The inflow into the channel is an ideal gas with the incoming velocity v_0 and the pressure p_0. The Reynolds number at this point is set to

$$Re = \frac{\rho_0 v_0 L}{\mu_0} = 400\,000 \quad .$$

At the channel outflow the Mach number Ma is fixed to 0.3.

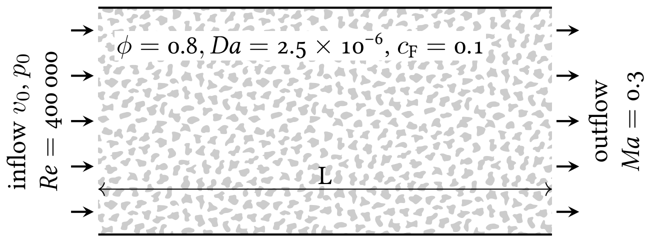

Figure 2.7.: Geometry of channel completely filled with a porous medium.

The results for the velocity $\langle v \rangle_\mathcal{F}$, the pressure $\langle p \rangle$, the density $\langle \rho \rangle$ and the temperature $\langle T \rangle_\mathcal{F}$ are shown in figure 2.8. The pressure and density drop simultaneously along the channel. As a consequence of the decreasing density the velocity increases in a way that the mass flow rate is constant. If the flow had been incompressible the velocity would have to be constant along the whole channel length. The temperature is constant. This implies that the porous drag terms only reduce the pressure but do not influence the inner energy.

2.8. Interface treatment between porous and nonporous regions

In the previous sections only flow inside a porous medium are considered, where the properties of the porous media (porosity ϕ, permeability κ, Forchheimer coefficient c_F) are always held constant. This is a reasonable choice for many applications

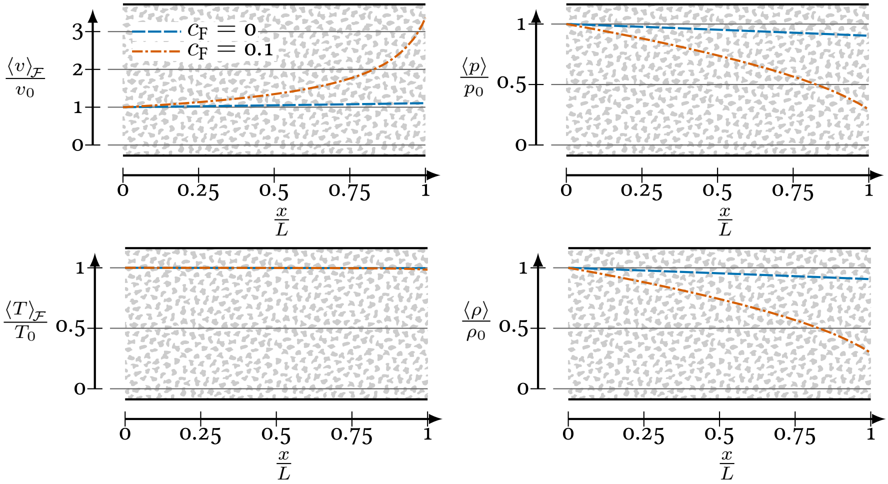

Figure 2.8.: Behaviours of the velocity $\langle v\rangle_{\mathcal{F}}$, the pressure $\langle p\rangle$, the temperature $\langle T\rangle_{\mathcal{F}}$ and the density $\langle \rho\rangle$ for the flow through a channel completely filled with a porous medium.

of flow simulations through porous media. However, the focus of the present work is flow *around* porous media. While the flow outside and inside the porous medium can be solved with the given equations, caution is needed at the outer surface of the porous medium. At this nonporous-porous interface the porosity will jump from the value of $\phi = 1$ in the nonporous region to some value less than one for the porous medium. Similarly, the permeability will change from infinity to some finite value and the Forchheimer coefficient rises from zero to the actual value in the porous region (figure 2.9). Since the changes in the porosity ϕ have been explicitly excluded during the derivation of the equations (2.29) it is not guaranteed that the Darcy and Forchheimer terms will still give valid results for sudden spatial changes of the permeability κ or the Forchheimer coefficient c_F. As a result, the interface requires special treatment.

There are mainly two approaches for addressing the interface problem, stated below:

1. Separate the porous and nonporous regions along the interface and derive explicit relationships between the flow properties of the two regions.

2. Derive equations (2.29) without excluding porosity gradients and model the porosity behaviour at the interface with explicit relationships. Supply this

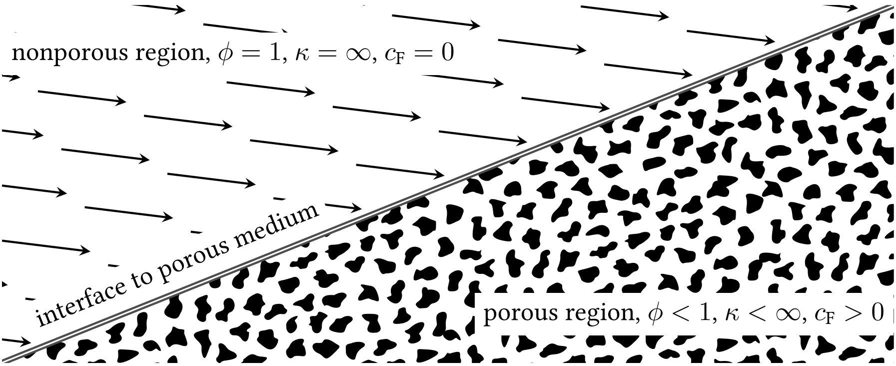

Figure 2.9.: Sketch of fluid which hits a porous medium.

porosity behaviour to the newly emerging terms of the Navier-Stokes equations with porosity gradients.

The most prominent relation for the first approach is given by Ochoa-Tapia and Whitaker [55]. They suggest to hold the flow variables constant over the interface but let the viscous stresses jump. Investigations based on their propositions are conducted in many publications, e.g. [43, 1, 14]. For example, a numerical implementation of this interface condition is given by Silva and Lemos [69]. Breugem [8] also confirms that their interface condition provides comparable results as DNS-simulations.

The second approach where the properties of the porous medium are blended smoothly at the interface region is applied by Breugem [7] and Kuwata and Suga [41]. Here, no sharp interface has to be defined but the flow field is supplied with a porosity, permeability and Forchheimer coefficient distribution. This is attractive for the interface treatment in the numerical solvers in terms of implementation complexity and robustness and it is also favorable for the creation of computation meshes. However, this second method has a drawback that the distributions of the different parameters have to be known. This is especially critical for the permeability as no monotone blending is possible but it will temporarily drop to a small value at the interface before it begins growing again inside the porous region (see Breugem [8]).

The present work sticks to the first method by defining a sharp interface and applying interface conditions very similar to those of Ochoa-Tapia and Whitaker [55]. The conditions are modified in order to also cover compressible flow. Special attention is paid to conserve fluxes which is regarded as an essential requirement to obtain realistic results. Thereby, it is assumed that conservation of convective and diffusive fluxes can be treated separately. Note, that the flux conservation procedure also helps to compute the integral forces which act on the porous medium. This is especially needed for the evaluation of flows around aerodynamic bodies with porous surfaces.

The following derivations are kept as general as possible by defining the interface of two stacked porous media instead of considering an interface between a porous medium and free flow. The special case of an interface between free flow and a porous medium can be recovered by setting the porosity on the nonporous interface side to a value of 1 and the permeability to infinity.

2.8.1. Interface treatment of convective fluxes

Figure 2.10 shows the interface between two different porous media with different properties. Around the interface a very thin control volume is defined. Note, that the convective fluxes can only pass at positions with no solid structure. This is also depicted as “effective flow area A” in figure 2.11. As a result, conservation of mass directly provides

$$\phi_1 \langle \rho_1 \rangle \langle v_{n,1} \rangle_{\mathcal{F}} = \phi_2 \langle \rho_2 \rangle \langle v_{n,2} \rangle_{\mathcal{F}} \tag{2.38}$$

where v_n is the velocity component normal to the interface. Furthermore, conservation of energy reads

$$\begin{aligned} \phi_1 \langle \rho_1 \rangle \langle v_{n,1} \rangle_{\mathcal{F}} & \left(\frac{|\langle \vec{v}_1 \rangle_{\mathcal{F}}|^2}{2} + \langle e_1 \rangle_{\mathcal{F}} + \frac{\langle p_1 \rangle}{\langle \rho_1 \rangle} \right) \\ &= \phi_2 \langle \rho_2 \rangle \langle v_{n,2} \rangle_{\mathcal{F}} \left(\frac{|\langle \vec{v}_2 \rangle_{\mathcal{F}}|^2}{2} + \langle e_2 \rangle_{\mathcal{F}} + \frac{\langle p_2 \rangle}{\langle \rho_2 \rangle} \right) \end{aligned}$$

which reduces to

$$\frac{|\langle \vec{v}_1 \rangle_{\mathcal{F}}|^2}{2} + \langle e_1 \rangle_{\mathcal{F}} + \frac{\langle p_1 \rangle}{\langle \rho_1 \rangle} = \frac{|\langle \vec{v}_2 \rangle_{\mathcal{F}}|^2}{2} + \langle e_2 \rangle_{\mathcal{F}} + \frac{\langle p_2 \rangle}{\langle \rho_2 \rangle} \tag{2.39}$$

when combined with the mass conservation relation (2.38).

Momentum conservation across the interface is not as straightforward as the previous conservation laws since the porous structure at the interface causes additional stresses onto the fluid. One can write the momentum conservation for the stresses σ as

$$\phi_1 \left(\langle \rho_1 \rangle \langle v_{\mathrm{n},1} \rangle_{\mathcal{F}}^2 + \langle p_1 \rangle \right) - \phi_2 \left(\langle \rho_2 \rangle \langle v_{\mathrm{n},2} \rangle_{\mathcal{F}}^2 + \langle p_2 \rangle \right) = \sigma_n \tag{2.40a}$$

$$\phi_1 \left(\langle \rho_1 \rangle \langle v_{\mathrm{n},1} \rangle_{\mathcal{F}} \langle v_{t,1} \rangle_{\mathcal{F}} \right) - \phi_2 \left(\langle \rho_2 \rangle \langle v_{\mathrm{n},2} \rangle_{\mathcal{F}} \langle v_{t,2} \rangle_{\mathcal{F}} \right) = \sigma_t \tag{2.40b}$$

where v_n is the velocity component normal to the interface and v_t is the velocity component tangential to the interface, as sketched in figure 2.11. It can be seen

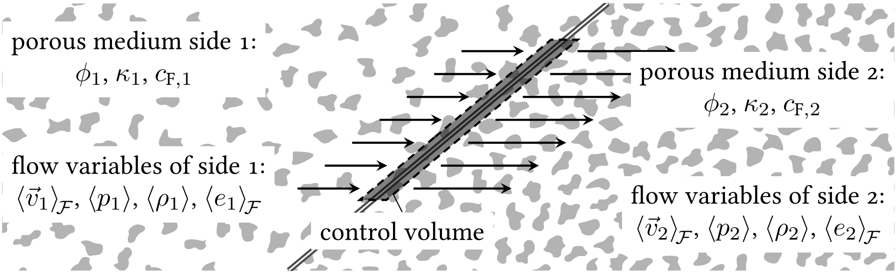

Figure 2.10.: Control volume for calculating the change of flow variables over the interface between different porous regions.

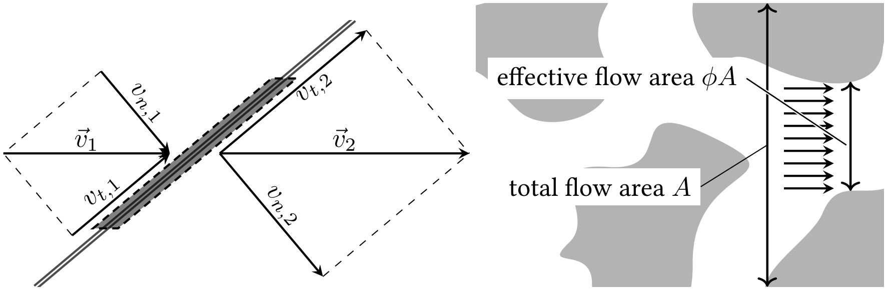

Figure 2.11.: Vector geometry at two sides of the interface between two different porous media (left) and definition of effective flow area (right).

that these conditions bring no direct benefit as they introduce two new unknown stresses σ_n and σ_t. Nevertheless, these conditions are important since they help to define the integral forces acting on the interface.

The three conservation laws (2.38), (2.39) and (2.40) still contain unknown variables in a way that further relations are needed. One assumption in order to gain an additional relation is that the direction of the velocity does not change over the interface:

$$\frac{\langle v_{t,1} \rangle_{\mathcal{F}}}{|\,\langle \vec{v}_1 \rangle_{\mathcal{F}}\,|} = \frac{\langle v_{t,2} \rangle_{\mathcal{F}}}{|\,\langle \vec{v}_2 \rangle_{\mathcal{F}}\,|} \quad \text{or} \quad \frac{\langle v_{n,1} \rangle_{\mathcal{F}}}{|\,\langle \vec{v}_1 \rangle_{\mathcal{F}}\,|} = \frac{\langle v_{n,2} \rangle_{\mathcal{F}}}{|\,\langle \vec{v}_2 \rangle_{\mathcal{F}}\,|} \tag{2.41}$$

This cannot be proven due to a lack of experimental data or resolved computation results. On the other side, it is defined in the same way as the generally accepted conditions of Ochoa-Tapia and Whitaker [55] for incompressible flow. Note, that at this point the incompressible problem is already completely defined as the internal energy e in equation (2.39) is not dependent on the pressure p and the density ρ. Thus, e could be assumed equal on both interface sides. However, in order to solve the compressible interface conditions more relations are needed which can be given by assuming an ideal gas. The internal energy of an ideal gas is directly related to the pressure and the density and the energy conservation (2.39) results in

$$\frac{|\,\langle \vec{v}_1 \rangle_{\mathcal{F}}\,|^2}{2} + \frac{\gamma}{\gamma - 1} \frac{\langle p_1 \rangle}{\langle \rho_1 \rangle} = \frac{|\,\langle \vec{v}_2 \rangle_{\mathcal{F}}\,|^2}{2} + \frac{\gamma}{\gamma - 1} \frac{\langle p_2 \rangle}{\langle \rho_2 \rangle} \tag{2.42}$$

where γ is the isentropic exponent. The last missing information to fully complete the interface conditions is obtained by assuming a reversible flow change over the interface which means that entropy must be constant. For an ideal gas this implies the isentropic condition:

$$\frac{\langle p_1 \rangle}{\langle \rho_1 \rangle^{\gamma}} = \frac{\langle p_2 \rangle}{\langle \rho_2 \rangle^{\gamma}} \tag{2.43}$$

There is no explicit relation to solving the compressible set of interface conditions. However, the problem can be effectively solved for the pressure $\langle p_2 \rangle$ by using a Newton solver. Combining equations (2.38), (2.41), (2.42) and (2.43) in order to eliminate the density $\langle \rho_2 \rangle$ and the velocities $\langle v_{n,2} \rangle_{\mathcal{F}}$ and $\langle \vec{v}_2 \rangle_{\mathcal{F}}$ the implicit function for pressure $\langle p_2 \rangle$ becomes

$$\mathrm{a} \cdot \langle p_2 \rangle^{\mathrm{b}} + \mathrm{c} \cdot \langle p_2 \rangle^{\mathrm{d}} + \mathrm{e} = 0 \tag{2.44}$$

with

$$\mathrm{a} = \frac{\gamma}{\gamma - 1} \frac{\langle p_1 \rangle^{\frac{1}{\gamma}}}{\langle \rho_1 \rangle}; \quad \mathrm{b} = 1 - \frac{1}{\gamma}; \quad \mathrm{c} = \frac{1}{2} \left(|\,\langle \vec{v}_1 \rangle_{\mathcal{F}}\,|\, \langle p_1 \rangle^{\frac{1}{\gamma}} \frac{\phi_1}{\phi_2} \right)^2$$

$$\mathrm{d} = -\frac{2}{\gamma}; \quad \mathrm{e} = -\frac{\gamma}{\gamma - 1} \frac{\langle p_1 \rangle}{\langle \rho_1 \rangle} - \frac{|\,\langle \vec{v}_1 \rangle_{\mathcal{F}}\,|^2}{2} \quad .$$

The Newton iterations can be formulated as follows:

$$\langle p_2\rangle_{i+1} = \langle p_2\rangle_i - \frac{f(\langle p_2\rangle_i)}{f'(\langle p_2\rangle_i)} \tag{2.45}$$

$$\begin{aligned} \langle p_2\rangle_0 &= \langle p_1\rangle \\ \text{with} \qquad f(\langle p_2\rangle_i) &= \mathrm{a}\cdot(\langle p_2\rangle_i)^{\mathrm{b}} + \mathrm{c}\cdot(\langle p_2\rangle_i)^{\mathrm{d}} + \mathrm{e} \\ f'(\langle p_2\rangle_i) &= \mathrm{a}\cdot\mathrm{b}\cdot(\langle p_2\rangle_i)^{\mathrm{b}-1} + \mathrm{c}\cdot\mathrm{d}\cdot(\langle p_2\rangle_i)^{\mathrm{d}-1} \quad . \end{aligned}$$

After solving the equations for the pressure $\langle p_2\rangle$, the density $\langle \rho_2\rangle$ and the velocity vector $\langle \vec{v}_2\rangle_{\mathcal{F}}$ are given by

$$\langle \rho_2\rangle = \langle \rho_1\rangle \left(\frac{\langle p_2\rangle}{\langle p_1\rangle}\right)^{\frac{1}{\gamma}} ; \qquad \langle \vec{v}_2\rangle_{\mathcal{F}} = \langle \vec{v}_1\rangle_{\mathcal{F}} \cdot \frac{\phi_1 \langle \rho_1\rangle}{\phi_2 \langle \rho_2\rangle} \quad . \tag{2.46}$$

If the additional stresses σ acting on the porous interface are required they can now be explicitly computed by following the momentum conservation laws (2.40).

To summarize the present section, relationships between the flow variables on the two interface sides are established. The conditions describe a fluid which undergoes a reversible process. This also means that the flow change can be computed over the interface and back again reaching the original flow state. Note, that the isentropic interface assumption breaks when high Mach numbers come into play. Strictly speaking, no valid solution exists anymore after the Mach number in the porous medium reaches the value of 1. Thus, special conditions would have to be defined which would particularly replace the isentropic condition (2.43). This would result in a higher complexity level since the direction of the flow would appear as an additional variable. Since such kinds of flows are not considered in the present work no further relations are derived at this point.

As an example for the convective interface conditions, figure 2.12 shows a setup of a channel where the flow has to pass through a porous region. The conditions are applied twice: when the fluid enters the porous region and again when leaving it.

In this example, the Reynolds number of the channel is set to 200 000 and is based on the length of the porous region and on the inflow conditions. The porosity ϕ of the porous region is set to 0.5. The permeability κ is given in terms of the Darcy number which is $Da = \frac{\kappa}{L^2} = 1 \times 10^{-5}$. The Forchheimer coefficient c_{F} is set to zero. The computations are accomplished for three different Mach numbers which are fixed at the channel outflow boundary. The computed results for the velocity and the density are shown in figure 2.13. Incompressible flow is represented by the small Mach number Ma of 0.01. This case shows that the velocity v doubles on its way into the porous medium which is a direct consequence of continuity of mass

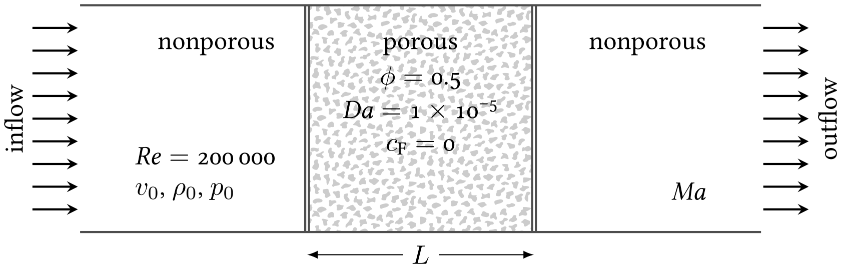

Figure 2.12.: Setup of a channel in which the flow passes through a porous region — an example to visualize the convective jump conditions.

and the constant density ρ. The case with the high Mach number $Ma = 0.3$ displays the need of compressible interface conditions. The density ρ jumps significantly and, thus, leads to a significantly higher velocity inside the porous region compared to the small Mach number case. An intermediate case of $Ma = 0.15$ shows small compressibility effects where the velocity is very similar to the small Mach number case. Obviously, such cases could still be computed with acceptable accuracy by using the incompressible conditions.

2.8.2. Interface treatment of diffusive fluxes

If the fluxes in the Navier-Stokes equations were only of convective nature the treatment of the nonporous-porous interface would be complete by the relationships of the previous section. However, as soon as viscosity comes into play relations for the diffusive fluxes must be found. This leads to the problem that the gradients of the velocity $\vec{v}$ and the temperature T must be related between the two interface sides.

A difference must be made between gradients in direction parallel to the interface and gradients in direction normal to the interface (see also figure 2.14). Gradients in directions parallel to the interface are already defined since they are directly based on the flow variables themselves, which are computed with the relations of section 2.8.1. In contrast, there exists no such relation for the gradients in the direction normal to the interface. Here, further modelling is required.

Before deriving the relations for the gradients, the coordinate systems aligned to the interface must be clarified, as sketched in figure 2.15. It is important to note, that the coordinate axis normal to the interface always points into its own porous region. The other two coordinate axes coincide on both interface sides. They are aligned with the interface area and the coordinate axis x_t points into the direction of

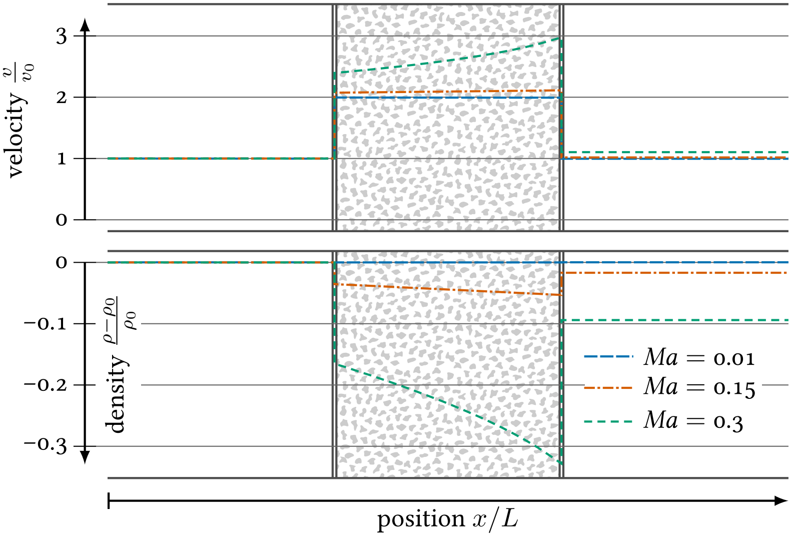

Figure 2.13.: Density and velocity along the length of the channel where the flow passes through a porous region at different Mach numbers.

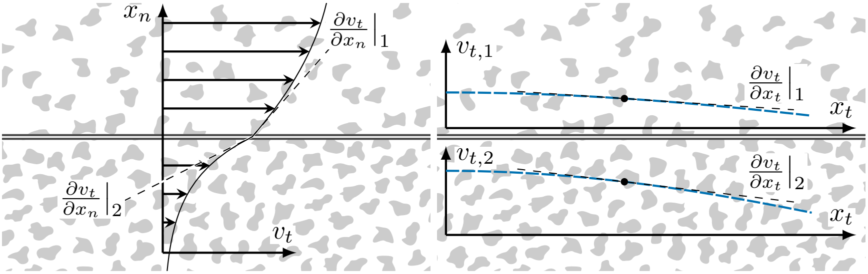

Figure 2.14.: Sketch showing gradients on the adjacent sides of the interface of two different porous media. Right hand side: velocity gradients normal to the interface area; Left hand side: gradients parallel to the interface area.

the velocity vector projected onto the interface[2]. Consequently, the velocity vector component in direction of the third coordinate axis x_r is zero.

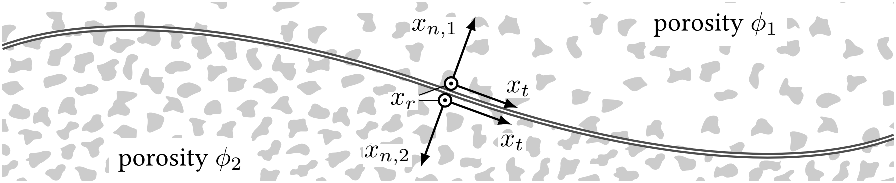

Figure 2.15.: Coordinate systems aligned with the interface between two different porous regions. The normal directions x_n point into the porous regions. The direction x_t is aligned with the interface. The direction x_r is aligned with the interface where at the same time the velocity vector projected onto x_r becomes zero.

With the coordinate systems defined above, relations for the gradients normal to the interface can be given. Literature search reveals several possible relations for the velocity gradients. An overview of most available conditions is given by Alzami and Vafai [1]. It consists of proposals to set the superficial gradients equal [79],

$$\left.\frac{\partial \left\langle v_t \right\rangle^{\mathrm{s}}}{\partial x_n}\right|_{\text{porous}} = -\left.\frac{\partial \left\langle v_t \right\rangle}{\partial x_n}\right|_{\text{nonporous}} \quad \Leftrightarrow \quad \phi\left.\frac{\partial \left\langle v_t \right\rangle}{\partial x_n}\right|_{\text{porous}} = -\left.\frac{\partial \left\langle v_t \right\rangle}{\partial x_n}\right|_{\text{nonporous}}$$

or weighting this relation by an effective viscosity μ_{eff} [58] in the porous region:

$$\phi\mu_{\text{eff}}\left.\frac{\partial \left\langle v_t \right\rangle}{\partial x_n}\right|_{\text{porous}} = -\mu\left.\frac{\partial \left\langle v_t \right\rangle}{\partial x_n}\right|_{\text{nonporous}}$$

As already mentioned, there exists the condition of Ochoa-Tapia and Whitaker [55] who let the gradients of the intrinsic velocities jump over the interface

$$\left.\frac{\partial \left\langle v_t \right\rangle}{\partial x_n}\right|_{\text{porous}} + \left.\frac{\partial \left\langle v_t \right\rangle}{\partial x_n}\right|_{\text{nonporous}} = -\beta\frac{\phi}{\sqrt{\kappa}}\left\langle v_{t,\text{nonporous}} \right\rangle \tag{2.47}$$

with the jump coefficient β that depends on the porous medium. Several different flavours of the condition (2.47) can be found which for example use an effective viscosity [43]

$$\phi\mu_{\text{eff}}\left.\frac{\partial \left\langle v_t \right\rangle}{\partial x_n}\right|_{\text{porous}} + \mu\left.\frac{\partial \left\langle v_t \right\rangle}{\partial x_n}\right|_{\text{nonporous}} = -\beta\frac{\phi\mu}{\sqrt{\kappa}}\left\langle v_{t,\text{nonporous}} \right\rangle$$

---

[2] Note, that the coincidence of the coordinate axis x_t on both interface sides is guaranteed since the direction of the tangential velocity is equal per definition as implied by equation (2.41).

or where the right hand side includes an inertial term [54],

$$\left.\frac{\partial \langle v_t \rangle}{\partial x_n}\right|_{\text{porous}} + \left.\frac{\partial \langle v_t \rangle}{\partial x_n}\right|_{\text{nonporous}} = -\beta_1 \frac{\phi}{\sqrt{\kappa}} \left\langle v_{t,\text{nonporous}} \right\rangle - \beta_2 \phi^2 \frac{\left\langle \rho_{\text{porous}} \right\rangle}{\mu_{\text{porous}}} \cdot \left\langle v_{t,\text{nonporous}} \right\rangle^2$$

with the two jump coefficients β_1 and β_2. Using equation (2.47) as a basis, a more generalized relation can be obtained which should also be applicable if both interface sides face a porous medium.

In terms of viscous fluxes, a fluid which runs along the interface will pass momentum to both, the solid porous structure and to the fluid inside the porous structure. Inside the porous medium, the momentum flux into the porous structure is accounted by the Darcy term but at the interface special treatment is needed. In order to explain this, consider that the porous region is machined from a big porous block. Thus, in the microscopic sense of view, at the outer surface of the porous region (i. e. the interface) additional surface area faces the fluid. This is also illustrated by figure 2.16. In the macroscopic sense of view, this means that at the nonporous-porous interface a locally increased drag force would act on the fluid. For the approach where the interface is treated smoothly (as explained at the beginning of section 2.8) the increased drag can be modelled by a locally decreased permeability κ ([16, 8]). In contrast, at a discontinuous interface as it is used in the present work the additional stresses at the interface must be explicitly modelled.

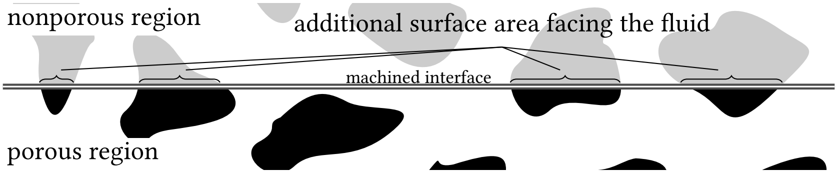

Figure 2.16.: Additional surface area at the nonporous-porous interface which appears by machining the porous region from a big porous block.

In order to define an appropriate model for the jump of velocity gradients, the conservation of viscous fluxes can be written as

$$\left\langle \mu_{\text{nonporous}} \right\rangle \left.\frac{\partial \langle v_i \rangle_{\mathcal{F}}}{\partial x_n}\right|_{\text{nonporous}} = -\left(\phi \left\langle \mu_{\text{porous}} \right\rangle \left.\frac{\partial \langle v_i \rangle_{\mathcal{F}}}{\partial x_n}\right|_{\text{porous}} + (1-\phi) \left\langle \mu_{\text{structure}} \right\rangle \left.\frac{\partial \langle v_i \rangle_{\mathcal{F}}}{\partial x_n}\right|_{\text{structure}} \right) , \tag{2.48}$$

a relation which is also described in figure 2.17[3].

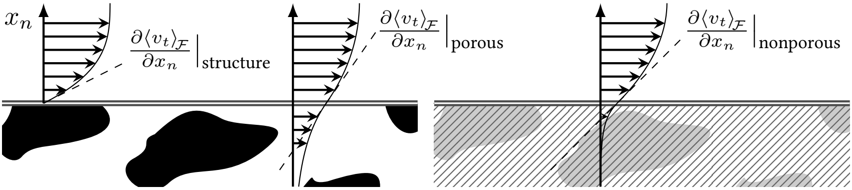

Figure 2.17.: Left hand side: Velocity gradients over the structure and over the fluid regions of a porous medium. Right hand side: Averaged gradient on the non-porous side of the interface.

Relation (2.48) can be generalized if there are porous media on both sides of the interface:

$$\begin{aligned} &\phi_1 \langle \mu_1 \rangle \frac{\partial \langle v_i \rangle_\mathcal{F}}{\partial x_n}\Big|_1 + (1-\phi_1) \langle \mu_{\mathrm{s},1} \rangle \frac{\partial \langle v_i \rangle_\mathcal{F}}{\partial x_n}\Big|_{\mathrm{s},1} \\ &= -\left(\phi_2 \langle \mu_2 \rangle \frac{\partial \langle v_i \rangle_\mathcal{F}}{\partial x_n}\Big|_2 + (1-\phi_2) \langle \mu_{\mathrm{s},2} \rangle \frac{\partial \langle v_i \rangle_\mathcal{F}}{\partial x_n}\Big|_{\mathrm{s},2} \right) \end{aligned} \tag{2.49}$$

where the index s is a shortcut for “structure” and, thus, indicates the different quantities over the porous structure. Since these quantities are unknown a-priori, they have to be modelled, which is achieved by using the quantities of the fluid phase inside the porous medium as an initial value which is then corrected with a newly introduced functional Δg:

$$\left\langle \mu_{\mathrm{s},1/2} \right\rangle \frac{\partial \langle v_i \rangle_\mathcal{F}}{\partial x_n}\Big|_{\mathrm{s},1/2} = \left\langle \mu_{1/2} \right\rangle \frac{\partial \langle v_i \rangle_\mathcal{F}}{\partial x_n}\Big|_{1/2} + \Delta g_{i,1/2} \tag{2.50}$$

Inserting equation (2.50) into (2.49) results in

$$\langle \mu_1 \rangle \frac{\partial \langle v_i \rangle_\mathcal{F}}{\partial x_n}\Big|_1 + (1-\phi_1)\Delta g_{i,1} = -\left(\langle \mu_2 \rangle \frac{\partial \langle v_i \rangle_\mathcal{F}}{\partial x_n}\Big|_2 + (1-\phi_2)\Delta g_{i,2} \right)$$

or, rewritten similar to (2.47)

$$\langle \mu_1 \rangle_\mathcal{F} \frac{\partial \langle v_i \rangle_\mathcal{F}}{\partial x_n}\Big|_1 + \langle \mu_2 \rangle_\mathcal{F} \frac{\partial \langle v_i \rangle_\mathcal{F}}{\partial x_n}\Big|_2 = -(1-\phi_2)\Delta g_{i,2} - (1-\phi_1)\Delta g_{i,1} \ . \tag{2.51}$$

---

[3] Strictly speaking, equation (2.48) will only represent conservation of viscous fluxes if there is no velocity normal to the interface and flow is incompressible. Still, this relation is assumed to be good enough to create a general model for relating the velocity gradients normal to the interface.

Finally, an expression for the functional Δg must be found. It is defined in a way which leads to a relation similar to the condition of Ochoa-Tapia and Whitaker given in equation (2.47):

$$\Delta g_{i,1/2} = \beta_{1/2} \frac{\phi_{1/2} \left\langle \mu_{1/2} \right\rangle}{\sqrt{\kappa_{1/2}}} \left\langle v_{i,1/2} \right\rangle_{\mathcal{F}} \tag{2.52}$$

The appropriateness of this relationship requires further discussion. Recall, that the functional Δg supports the modelling of the unknown viscous stress over the porous structure (equation (2.50)). The stress is modelled by using the stresses of the fluid at the porous interface side (i. e. $\left\langle \mu_{\text{porous}} \right\rangle \frac{\partial \langle v_i \rangle_{\mathcal{F}}}{\partial x_n}\Big|_{\text{porous}}$) as an initial value and correcting it with the functional Δg. The correction can be developed with the help of dimensional analysis by using characteristic values of a velocity, a length scale and a viscosity and adjusting the final term by a modelling constant. As a characteristic velocity serves the velocity $\langle v_i \rangle_{\mathcal{F}}$ at the interface, or rather, its superficial counterpart $\phi \langle v_i \rangle_{\mathcal{F}}$ in order to match the relation of Ochoa-Tapia and Whitaker better. This velocity changes at the interface within the order of a typical length scale which is taken to be the square root of the permeability κ. This seems appropriate because the magnitude of $\sqrt{\kappa}$ is proportional to the pore diameter of the porous medium and, thus, gives a typical value for the range along which the interface affects the flow. The characteristic viscosity is approximated by the viscosity of the fluid inside the pores. The whole expression (2.52) is multiplied by the modelling constant β which is generally called "jump coefficient". It is worth mentioning that the expression (2.52) together with relation (2.51) will lead to the condition of Ochoa-Tapia and Whitaker (2.47), the only difference being that the jump coefficient varies by the factor $(1 - \phi)$.

The equations (2.51) and (2.52) completely define the relation of velocity gradients across the two interface sides. This leaves the relation for the temperature gradient as the final relation which is required for solving the volume-averaged Navier-Stokes equations over the interface between two different porous media. The temperature gradient appears in the energy equation (2.29c) in the form of the heat flux $k_{\mathrm{d},i}$ (equation (2.36)). If it is assumed that energy is not dissipated into the solid porous structure at the interface, the heat flux has to be conserved. However, the energy equation (2.29c) consists of one more flux,

$$\frac{\partial \langle v_i \rangle_{\mathcal{F}} \langle \tau_{ij} \rangle_{\mathcal{F}}}{\partial x_j} \quad ,$$

which is already defined but is not conserved by itself. Therefore, it is assumed that the flux difference of this term will be turned into an additional heat flux. Hence, the temperature gradient normal to the interface is defined by

$$\begin{aligned}\phi_1 \cdot \left(\langle v_{j,1} \rangle_{\mathcal{F}} \langle \tau_{ij,1} \rangle_{\mathcal{F}} n_{1,i} + \lambda_{\text{eff}} \frac{\partial \langle T \rangle_{\mathcal{F}}}{\partial x_n} \bigg|_1 \right) \\ = -\phi_2 \cdot \left(\langle v_{j,2} \rangle_{\mathcal{F}} \langle \tau_{ij,2} \rangle_{\mathcal{F}} n_{1,i} + \lambda_{\text{eff}} \frac{\partial \langle T \rangle_{\mathcal{F}}}{\partial x_n} \bigg|_2 \right)\end{aligned} \tag{2.53}$$

where n_i is the i-th component of the normal vector $\vec{n}$ at the interface.

With all interface conditions for the diffusive fluxes defined an example is shown which demonstrates the effect of the velocity jump given by equation (2.51). The setup is shown in figure 2.18 and consists of a channel in which the lower half is porous. A quasi-1D flow is obtained by applying periodic boundary conditions for inflow and outflow. The fluid is driven through the channel by an artificial forcing term which replaces the pressure gradient.

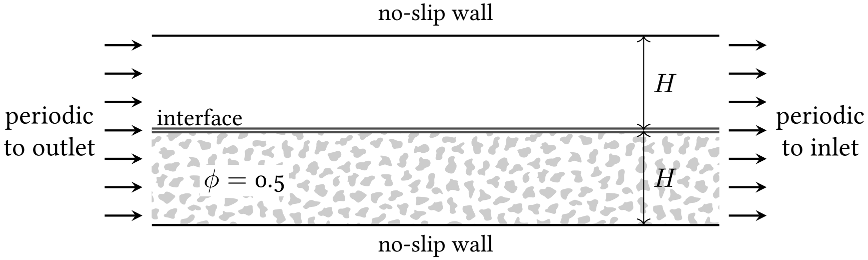

Figure 2.18.: Setup of a laminar channel where the lower half is filled with a porous medium and the upper half is free flow.

The results for three different jump coefficients β are shown in figure 2.19. For all curves, the velocity jumps at the interface. This is a consequence of the interface treatment of convective fluxes as given in section 2.8.1. Note, that for incompressible flows the factor between the velocities at the nonporous side and at the porous side is equal to the porosity ϕ. The velocity profile inside the nonporous region is a parabola and as a consequence the progress of the gradients along the channel height is linear in this region. Inside the porous region the velocity drops exponentially and so do the gradients.

The effect of the jump coefficients β is best visible in the discontinuity of the velocity gradients $\frac{\partial \langle v_x \rangle_{\mathcal{F}}}{\partial y}$ over the interface. A jump coefficient of zero will give a continuous gradient profile. For non-zero values this is not the case. The effect of the jump coefficient onto the velocity profile can be described in a way that a negative coefficient will drag the velocity at the interface to smaller values and correspondingly positive coefficients push the interface velocity to higher values. Finally, it can be recognized that the gradients at the interface always have a kink at the interface i.e. the curvature is always discontinuous. This is an effect of the sudden start of the additional drag forces inside the porous region.

When the upper half of the channel is also filled with a porous media an illustrative result is shown figure 2.20.

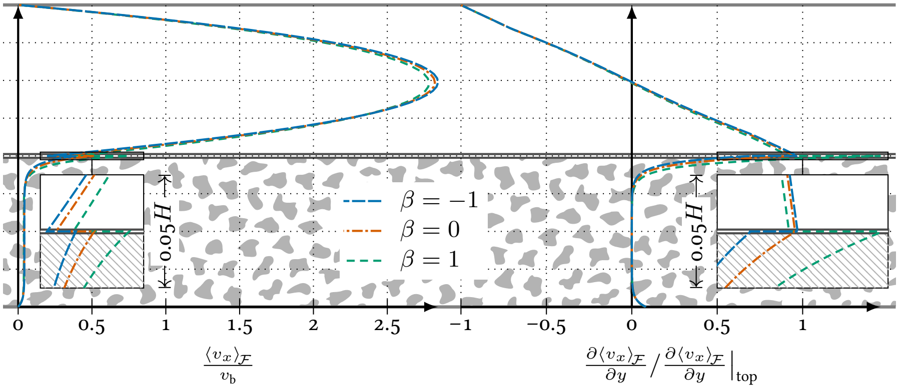

Figure 2.19.: Velocity profile and velocity gradients for varying jump coefficients β for the laminar channel of figure 2.18.

2.8.3. Summary of interface conditions

All the interface conditions defined in the previous sections are summarized in the following. The relations for the flow variables between the two interface sides are defined by conservation of mass

$$\phi_1 \langle \rho_1 \rangle \langle v_{n,1} \rangle_\mathcal{F} = \phi_2 \langle \rho_2 \rangle \langle v_{n,2} \rangle_\mathcal{F} \quad , \tag{2.54}$$

and the conservation of energy

$$\frac{|\langle \vec{v}_1 \rangle_\mathcal{F}|^2}{2} + \langle e_1 \rangle_\mathcal{F} + \frac{\langle p_1 \rangle}{\langle \rho_1 \rangle} = \frac{|\langle \vec{v}_2 \rangle_\mathcal{F}|^2}{2} + \langle e_2 \rangle_\mathcal{F} + \frac{\langle p_2 \rangle}{\langle \rho_2 \rangle} \quad . \tag{2.55}$$

These equations are closed by maintaining the velocity direction constant, i. e.

$$\frac{\langle v_{t,1} \rangle_\mathcal{F}}{|\langle \vec{v}_1 \rangle_\mathcal{F}|} = \frac{\langle v_{t,2} \rangle_\mathcal{F}}{|\langle \vec{v}_2 \rangle_\mathcal{F}|} \quad \text{or, alternatively} \quad \frac{\langle v_{n,1} \rangle_\mathcal{F}}{|\langle \vec{v}_1 \rangle_\mathcal{F}|} = \frac{\langle v_{n,2} \rangle_\mathcal{F}}{|\langle \vec{v}_2 \rangle_\mathcal{F}|} \quad . \tag{2.56}$$

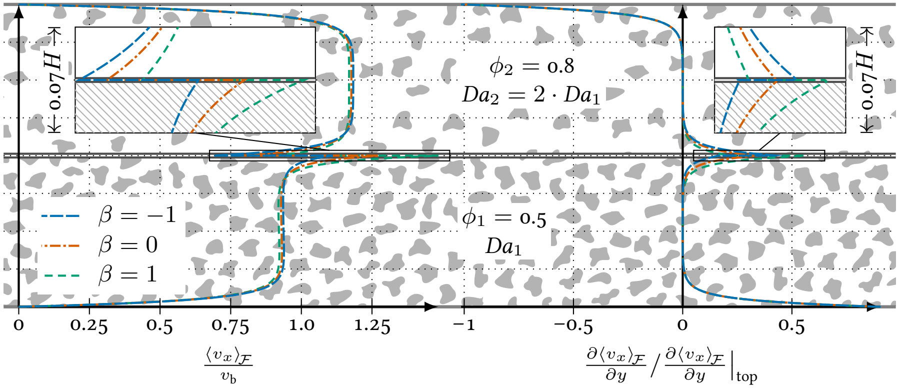

Figure 2.20.: Velocity profile and velocity gradients for varying jump coefficients β in a laminar channel where the lower and upper half are filled with different porous media.

If the fluid was incompressible the equations are already closed as the internal energy e can be removed from the equation (2.55), otherwise it must be defined. Assuming an ideal gas it is

$$e = \frac{1}{\gamma - 1} \frac{\langle p \rangle}{\langle \rho \rangle} \quad . \tag{2.57}$$

An important assumption is the isentropic condition which implies that the flow change over the interface is reversible:

$$\frac{\langle p_1 \rangle}{\langle \rho_1 \rangle^\gamma} = \frac{\langle p_2 \rangle}{\langle \rho_2 \rangle^\gamma} \tag{2.58}$$

The whole set of equations can be solved iteratively by the Newton method. The missing flow quantities like temperature or viscosity can then be explicitly computed by the ideal gas laws and Sutherland's law.

Additional interface conditions have to be defined for the velocity and temperature gradients. They take the final form as

$$\langle \mu_1 \rangle \frac{\partial \langle v_i \rangle_\mathcal{F}}{\partial x_n}\bigg|_1 + \langle \mu_2 \rangle \frac{\partial \langle v_i \rangle_\mathcal{F}}{\partial x_n}\bigg|_2 = -(1 - \phi_2)\Delta g_{i,2} - (1 - \phi_1)\Delta g_{i,1} \tag{2.59}$$

with the stress offset Δg as

$$\Delta g_{i,1/2} = \beta_{1/2} \frac{\phi_{1/2} \langle \mu_{1/2} \rangle}{\sqrt{\kappa_{1/2}}} \langle v_{i,1/2} \rangle_\mathcal{F} \tag{2.60}$$

and

$$\begin{aligned}&\phi_1 \cdot \left(\langle v_{j,1} \rangle_{\mathcal{F}} \langle \tau_{ij,1} \rangle_{\mathcal{F}} n_{1,i} + \lambda_{\text{eff}} \frac{\partial \langle T \rangle_{\mathcal{F}}}{\partial x_n} \bigg|_1 \right) \\ &= -\phi_2 \cdot \left(\langle v_{j,2} \rangle_{\mathcal{F}} \langle \tau_{ij,2} \rangle_{\mathcal{F}} n_{1,i} + \lambda_{\text{eff}} \frac{\partial \langle T \rangle_{\mathcal{F}}}{\partial x_n} \bigg|_2 \right) \quad .\end{aligned} \tag{2.61}$$

There is no need for giving explicit relations for the velocity gradients tangential to the interface as these can be directly computed from the flow variables themselves.

2.9. Computation of integral forces acting on porous media

During his preparation for the next snowball fight Paul is doing his homework for high-precision snowball throws. His basic sketch of the setup is shown in figure 2.21. To enable long-distance shots Paul prepared snowballs which consist of a heavy ice core but are camouflaged with a snow shell (figure 2.22). Paul also successfully performed a CFD computation of the snowball where he modelled the snow shell as a porous medium. The next question of how he can compute the drag coefficient is described in the following paragraphs.

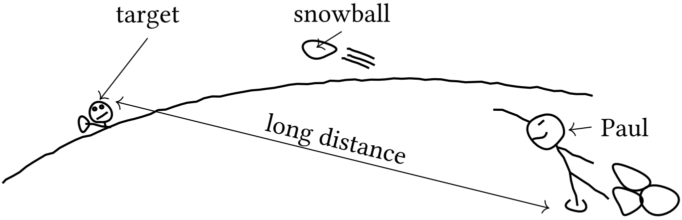

Figure 2.21.: Sketch of snowball fight.

For solid surfaces the computation of the forces is straightforward by calculating the forces which are caused by pressure and by viscous stresses. In contrast, if porous media cover the solid body, additional efforts are required to compute the body forces. Three different issues have to be discussed sketched in figure 2.22:

- Forces originating from the flow inside the porous medium (Darcy and Forchheimer terms)
- Forces acting on the interface between the free flow and the porous medium

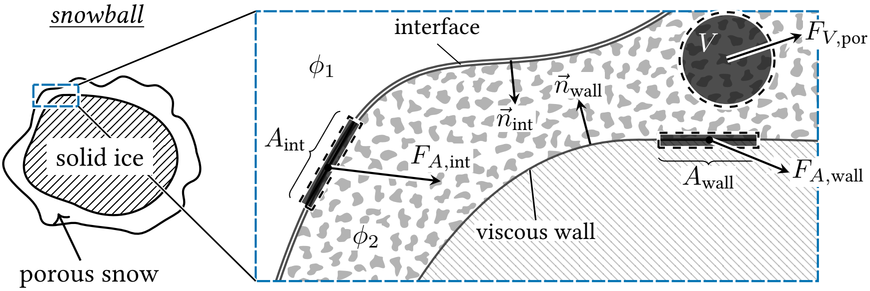

Figure 2.22.: Illustration of forces on a porous structure and on the wall beneath the porous structure.

- Forces acting on solid walls which are covered by a porous medium

The forces acting on the porous structure inside the porous medium are described by the Darcy and Forchheimer terms in the way they appear in the momentum equations. Inside a fixed control volume V, the force integrates to

$$F_{V,\mathrm{por},i} = \int\limits_{V_{\mathrm{f}}} \phi \frac{\langle \mu \rangle}{\kappa} \langle v_i \rangle_{\mathcal{F}} + \phi^2 \frac{c_{\mathrm{F}}}{\sqrt{\kappa}} \langle \rho \rangle \langle v_i \rangle_{\mathcal{F}} \cdot |\langle \vec{v} \rangle_{\mathcal{F}}| \,\mathrm{d}V \quad . \tag{2.62}$$

Note, that the integral is restricted to the fluid volume V_{f} and not to the total volume V which contains the porous structure as well.

The second force to be considered comes from the pressure and stresses onto the interface. This force can be split into two parts: The first is due to the conservation of convective fluxes over the interface and the second part is required to obtain the jump of viscous fluxes over the interface. This can be computed with the momentum conservation (2.40) where σ_n and σ_t are the stresses acting on the interface, leading to

$$\begin{aligned} F_{A,\mathrm{int},i} = \int\limits_{A_{\mathrm{int}}} & \phi_1 \left(\langle \rho_1 \rangle \langle v_{\mathrm{n},1} \rangle_{\mathcal{F}} \langle v_{i,1} \rangle_{\mathcal{F}} + n_i \langle p_1 \rangle \right) \\ & - \phi_2 \left(\langle \rho_2 \rangle \langle v_{\mathrm{n},2} \rangle_{\mathcal{F}} \langle v_{i,2} \rangle_{\mathcal{F}} + n_i \langle p_2 \rangle \right) \mathrm{d}A \quad . \end{aligned} \tag{2.63}$$

The viscous part of the forces acting on the interface can be described by the offset of viscous stresses at the interface as:

$$F_{A,\mathrm{int,visc},i} = \int\limits_{A_{\mathrm{int}}} n_j \left(\phi_2 \langle \tau_{ij,2} \rangle - \phi_1 \langle \tau_{ij,1} \rangle \right) \mathrm{d}A \tag{2.64}$$

An additional force which has to be specially treated is the force acting on a viscous wall that is covered by a porous medium. Such kinds of walls have a reduced area that is affected by the pressure and the viscous stresses. The reduction factor is the porosity ϕ. Hence, the force can be written as:

$$F_{A,\mathrm{wall},i} = \int\limits_{A_{\mathrm{wall}}} \phi \left(n_j \langle \tau_{ij} \rangle - n_i \langle p \rangle \right) \mathrm{d}A \ . \tag{2.65}$$

3. Turbulent Flow in Porous Media

Chapter 2 discusses laminar flow through and over porous media. But for aerodynamics of aircraft the flow is mostly turbulent. The present chapter extends the previous discussions to turbulent flow through and over porous media. It is assumed that the flight Reynolds numbers are high and, consequently, direct numerical simulations or large-eddy simulations are far too expensive. In order to avoid this, the volume-averaged Navier-Stokes equations are averaged in time, a procedure which leads to several additional unknown terms. The modelling of these terms in nonporous regions is commonly performed by one-equation, two-equation or Reynolds-stress models. The present chapter extends the theory of the Reynolds-stress models such that the physics inside porous media is also captured. The choice to use a Reynolds-stress model is motivated by the fact that such models have the potential to predict highly complex flow phenomena where the simpler models would fail. Besides that, the derivation of this type of model is more straightforward than the derivation of one- or two-equation models. Finally, it is assumed that the newly modelled terms can be transferred to the one- and two-equation models much easier.

The present chapter will first shed some light on the expected flow phenomena. Later on, this will help to understand the capabilities of the applied models and where they are expected to fail. Afterwards, the derivation of the turbulent Navier-Stokes equations is performed by time-averaging the volume-averaged equations. This procedure leads to new unknown terms directly resulting in the derivation and modelling of the Reynolds-stress equations. Thereafter, the interface conditions from the previous chapter are extended to be also valid for the turbulent flows.

3.1. Classification of turbulent flow in porous media

For the description of turbulent flow in a porous media the two most obvious types of turbulence are considered. As depicted in figure 3.1, the first type of turbulence is represented by very small eddies which reside inside the porous structure. This kind of turbulence is expected for large pore Reynolds numbers $Re_{d_\mathrm{p}} = \frac{d_\mathrm{p} v}{\nu}$ of about 300 as pointed out by Pedras and Lemos [56]. In terms of the permeability Reynolds

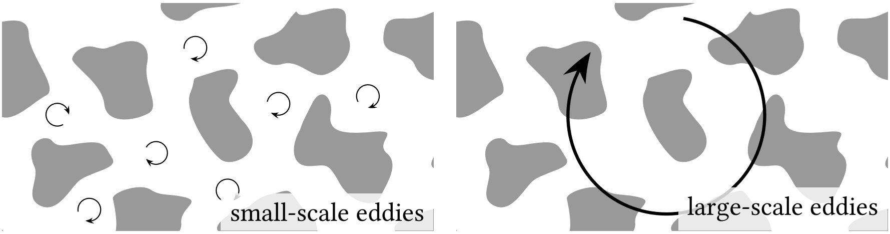

Figure 3.1.: Comparison of small- and large-scale turbulence in a porous structure. The eddies of the small-scale turbulence are smaller than the pore sizes while the eddies of the large-scale turbulence can extend over several pores diameters.

number $Re_\kappa = \frac{\sqrt{\kappa}v}{\nu}$ the critical value would be $Re_{\kappa,\mathrm{crit}} = 10$ or higher (see appendix C.1). The second type of turbulence is defined by the large-scale fluctuations that extend over several pore diameters. These fluctuations are mainly expected when they are transported into the porous media from the outside flow. The life of such large-scale turbulence is limited as it is damped on its way through the porous medium.

The modelling of the first type of turbulence (small-scale eddies) will be quickly discussed at this point. Then, the rest of the chapter will be devoted to the second type of turbulence (large-scale eddies). When modelling the small-scale turbulence one must go back to the previous chapter where the Navier-Stokes equations are averaged in space. Strictly speaking, the space-averaging operator does not only capture the fluctuations which occur from the temporal constant movement of the fluid through the porous structure but also the unsteady small-scale eddies are filtered out. Since the small-scale turbulence stems from the large pore Reynolds number or, rather, from the small viscous stresses, it must also exist in a flow where there are no large-scale velocity gradients. Thus, the volume-averaged momentum equation (2.20) can be used in a strongly simplified version as a starting point for the modelling process:

$$\frac{\partial \langle p \rangle}{\partial x_i} = -\frac{1}{V_\mathrm{f}} \int\limits_{A_\mathrm{fs}} p n_i - \tau_{ij} n_j \, \mathrm{d}A \tag{3.1}$$

In the case of fully laminar flow the integral was modelled with the Darcy and Forchheimer terms (2.23). When it comes to small-scale turbulent flows, the model should be adapted. Two modelling options can be foreseen:

1. By replacing the dynamic viscosity μ in the Darcy term with an effective viscosity μ_eff which takes account of the turbulent stresses. This kind of modelling is used by Nakayama and Kuwahara [51]for modelling the large-scale

turbulence.

2. By exploring the dependency of the permeability κ and the Forchheimer coefficient c_F on the local Reynolds number Re_κ.

After this point the discussion about modelling small-scale turbulence is not pursued any further. The present work will not focus on these small-scale models since the pore Reynolds number for the given applications is small. However, as discussed before the large-scale turbulence is expected to be of high importance and will be discussed in detail in the following sections.

3.2. Reynolds-averaging

Reynolds averaging is commonly known as averaging in time. It is widely applied to avoid the need of simulating the details of the turbulent fluctuations where only the averaged value is of interest. The definition can be found in various works like [6, 81] and can be noted as

$$\overline{\varphi} = \frac{1}{T} \int\limits_T \varphi \, \mathrm{d}t. \tag{3.2}$$

where φ is any arbitrary variable to be averaged over the time t, T is a thoroughly defined time interval which cancels out the time-dependent turbulent fluctuations but not the temporal change of mean variables. Similar to the volume-averaging rules given in section 2.3 a density-weighted average can be defined as

$$\widetilde{\varphi} = \frac{\overline{\rho\varphi}}{\overline{\rho}} = \frac{1}{\overline{\rho} T} \int\limits_T \rho\varphi \, \mathrm{d}t \ . \tag{3.3}$$

The fluctuation values are denoted by one or two primes depending on whether it is standard time averaging or density-weighted time averaging, i. e.

$$\varphi' = \varphi - \overline{\varphi} \quad , \quad \varphi'' = \varphi - \widetilde{\varphi} \ . \tag{3.4}$$

Furthermore, the following relations are considered to be true:

$$\overline{\overline{\varphi}} = \overline{\varphi} \quad , \quad \widetilde{\widetilde{\varphi}} = \widetilde{\varphi} \quad , \quad \overline{\varphi'} = 0 \quad , \quad \widetilde{\varphi''} = 0 \tag{3.5}$$

The Reynolds average of a time derivative and the time derivative of the Reynolds average can be directly exchanged and the same is valid for gradients:

$$\overline{\frac{\partial \varphi}{\partial t}} = \frac{\partial \overline{\varphi}}{\partial t} \quad , \quad \overline{\frac{\partial \varphi}{\partial x_i}} = \frac{\partial \overline{\varphi}}{\partial x_i} \tag{3.6}$$

3.3. Turbulent Navier-Stokes equations

After applying the Reynolds-averaging rule (3.2) onto equations (2.29) and considering the other averaging constraints of section 3.2 the volume-averaged Navier-Stokes equations can be rewritten as

$$\frac{\partial \overline{\rho}}{\partial t} + \frac{\partial \overline{\rho}\, \widetilde{v_i}}{\partial x_i} = 0 \tag{3.7a}$$

$$\frac{\partial \overline{\rho}\, \widetilde{v_i}}{\partial t} + \frac{\partial \overline{\rho}\, \widetilde{v_i}\, \widetilde{v_j}}{\partial x_j} = -\frac{\partial \overline{\rho}\, \widetilde{v_i'' v_j''}}{\partial x_j} - \frac{\partial \overline{p}}{\partial x_i} + \frac{\partial \overline{\tau_{ij}}}{\partial x_j} - \phi \frac{\overline{\mu}}{\kappa} \left(\widetilde{v_i} + \overline{v_i''} \right) - \phi^2 \frac{c_\mathrm{F}}{\sqrt{\kappa}} \overline{\rho}\, \widetilde{v_i\, |\vec{v}|} \tag{3.7b}$$

$$\frac{\partial \overline{\rho}\, \widetilde{E}}{\partial t} + \frac{\partial \overline{\rho}\, \widetilde{v_i}\, \widetilde{H}}{\partial x_i} = -\frac{\partial \overline{\rho}\, \widetilde{v_i'' H''}}{\partial x_i} + \frac{\partial \widetilde{v_i}\, \overline{\tau_{ij}}}{\partial x_j} + \frac{\partial \overline{v_i''}\, \overline{\tau_{ij}}}{\partial x_j} + \frac{\partial \overline{v_i'' \tau_{ij}'}}{\partial x_j} - \frac{\partial \overline{k_{\mathrm{d},i}}}{\partial x_i} \ . \tag{3.7c}$$

Note, that the volume-averaging signs $\langle\rangle$ and $\langle\rangle_\mathcal{F}$ are omitted for the purpose of better readability. Thus, every variable must be taken in its volume-averaged form according as used in section 2.6. Strictly speaking, there would appear additional correlations between velocity fluctuations v_i'' and viscosity fluctuations μ'. Since these correlations are expected to be very small they are neglected in these equations.

The density-weighted average of the total Energy E and the total enthalpy H can be written as

$$\begin{aligned} \widetilde{E} &= \widetilde{e} + \frac{\widetilde{v_i}\, \widetilde{v_i}}{2} + \frac{\widetilde{v_i'' v_i''}}{2} = \widetilde{e} + \frac{\widetilde{v_i}\, \widetilde{v_i}}{2} + k \\ \widetilde{H} &= \widetilde{E} + \widetilde{\left(\frac{p}{\rho} \right)} = \widetilde{E} + \frac{\overline{p}}{\overline{\rho}} = \widetilde{e} + \frac{\widetilde{v_i}\, \widetilde{v_i}}{2} + k + \frac{\overline{p}}{\overline{\rho}} \end{aligned}$$

with the turbulent kinetic energy defined as

$$k = \frac{1}{2} \widetilde{v_i'' v_i''} \ . \tag{3.8}$$

The correlation between the velocity fluctuation v_i'' and the total enthalpy fluctuation H'' can be split into the single terms

$$\widetilde{v_i'' H''} = \widetilde{v_j} \widetilde{v_i'' v_j''} + \frac{1}{2} \widetilde{v_i'' v_j'' v_j''} + \widetilde{v_i'' h''} \ . \tag{3.9}$$

Thus, the unknowns which occur as a result of Reynolds averaging are

$$\widetilde{v_i'' v_j''} \quad , \quad \overline{v_i''} \quad , \quad \widetilde{v_i |\vec{v}|} \quad , \quad \widetilde{v_i'' v_j'' v_j''} \quad , \quad \widetilde{v_i'' h''} \quad \text{and} \quad \overline{v_i'' \tau_{ij}'} \ .$$

The modelling procedure for most of these terms is well-known and summarized by Wilcox in [81]. However, due to the presence of porous media several models have to be modified. The following sections will derive a complete closure by giving models for each of those terms on the basis of Reynolds-stress turbulence models.

3.4. Derivation of closed form of turbulent momentum equations

The unknowns of the momentum equation (3.7b) can be reduced to the average expression of the Forchheimer term $\widetilde{v_i\,|\vec{v}|}$ and to the average of the velocity fluctuations $\overline{v_i''}$. The Reynolds stresses $\widetilde{v_i''v_j''}$ are assumed to be known by solving the Reynolds-stress equations later on. In the following the velocity fluctuation $\overline{v_i''}$ will be neglected which goes along with the publication of Cécora et. al. [12] who neglect the compressibility terms in the Reynolds-stress equations. This leaves the modelling of the Forchheimer term which reads

$$\phi^2 \frac{c_{\mathrm{F}}}{\sqrt{K}} \bar{\rho} \widetilde{v_i|\vec{v}|} \tag{3.10}$$

in which the part $\widetilde{v_i|\vec{v}|} = \widetilde{v_i\sqrt{v_j v_j}}$ has to be modelled. Suggestions for modelling these terms are given in [2, 28] where a power series-expansion is exploited. This approach will also be followed here slightly different. The derivation of the model is borrowed from [49].

The Taylor expansion for a function $f_i(\epsilon)$ is given as

$$f_i(\epsilon) = f_i(\epsilon_0) + \left.\frac{\partial f_i(\epsilon)}{\partial \epsilon}\right|_{\epsilon_0} (\epsilon - \epsilon_0) + \frac{1}{2} \left.\frac{\partial^2 f_i(\epsilon)}{\partial \epsilon^2}\right|_{\epsilon_0} (\epsilon - \epsilon_0)^2 + \ldots$$

where

$$f_i(\epsilon) = \sqrt{v_k v_k}\, v_i \quad \text{and} \quad v_j = \widetilde{v_j} + \epsilon \cdot v_j''$$

with $\epsilon_0 = 0$ being the reference state and $\epsilon = 1$ being the state in which the Taylor expansion is to be evaluated. Therefore, the function $f_i(\epsilon)$ can be written as

$$f_i(\epsilon) = \sqrt{(\widetilde{v_j} + \epsilon v_j'')(\widetilde{v_j} + \epsilon v_j'')} (\widetilde{v_i} + \epsilon v_i'') \ . \tag{3.11}$$

The first derivative $\frac{\partial f_i(\epsilon)}{\partial \epsilon}$ of the function $f_i(\epsilon)$ is

$$\frac{\partial f_i(\epsilon)}{\partial \epsilon} = v_i'' \sqrt{(\widetilde{v_j} + \epsilon v_j'')(\widetilde{v_j} + \epsilon v_j'')} + \frac{v_k''(\widetilde{v_k} + \epsilon v_k'')(\widetilde{v_i} + \epsilon v_i'')}{\sqrt{(\widetilde{v_j} + \epsilon v_j'')(\widetilde{v_j} + \epsilon v_j'')}} \tag{3.12}$$

and the second derivative $\frac{\partial^2 f_i(\epsilon)}{\partial \epsilon^2}$ is

$$\begin{aligned}\frac{\partial^2 f_i(\epsilon)}{\partial \epsilon^2} =& \frac{v_k'' v_k'' (\widetilde{v_i} + \epsilon v_i'')}{\sqrt{(\widetilde{v_j} + \epsilon v_j'')(\widetilde{v_j} + \epsilon v_j'')}} + 2\frac{v_i'' v_k'' (\widetilde{v_k} + \epsilon v_k'')}{\sqrt{(\widetilde{v_j} + \epsilon v_j'')(\widetilde{v_j} + \epsilon v_j'')}} \\ & - \frac{v_l'' v_k'' \widetilde{v_i}\, \widetilde{v_l}\, \widetilde{v_k}}{\sqrt{\left((\widetilde{v_j} + \epsilon v_j'')(\widetilde{v_j} + \epsilon v_j'')\right)^3}} \quad .\end{aligned} \tag{3.13}$$

Performing the second order Taylor expansion for reference point $\epsilon_0 = 0$ at point $\epsilon = 1$ gives

$$f_i(1) \approx (\widetilde{v_i} + v_i'')\sqrt{\widetilde{v_j}\,\widetilde{v_j}} + \frac{v_k'' \widetilde{v_i}\,\widetilde{v_k}}{\sqrt{\widetilde{v_j}\,\widetilde{v_j}}} + \frac{v_i'' v_k'' \widetilde{v_k}}{\sqrt{\widetilde{v_j}\,\widetilde{v_j}}} + \frac{v_k'' v_k'' \widetilde{v_i}}{2\sqrt{\widetilde{v_j}\,\widetilde{v_j}}} - \frac{v_l'' v_k'' \widetilde{v_i}\,\widetilde{v_l}\,\widetilde{v_k}}{2\sqrt{(\widetilde{v_j}\,\widetilde{v_j})^3}} \quad . \tag{3.14}$$

In equation (3.10) the term in question is averaged,

$$\widetilde{f_i(1)} \approx \widetilde{v_i}|\widetilde{\vec{v}}| + \frac{\widetilde{v_i'' v_k''}\,\widetilde{v_k}}{|\widetilde{\vec{v}}|} + \frac{\widetilde{v_k'' v_k''}\,\widetilde{v_i}}{2|\widetilde{\vec{v}}|} - \frac{\widetilde{v_k'' v_l''}\,\widetilde{v_i}\,\widetilde{v_k}\,\widetilde{v_l}}{2|\widetilde{\vec{v}}|^3} \quad ,$$

and hence the Forchheimer term in its second order approximation is

$$\phi^2 \frac{c_{\mathrm{F}}}{\sqrt{\kappa}} \overline{\rho}\, \widetilde{v_i |\vec{v}|} \approx \phi^2 \frac{c_{\mathrm{F}}}{\sqrt{\kappa}} \overline{\rho} \left[\widetilde{v_i}|\widetilde{\vec{v}}| + \frac{1}{2}\frac{\widetilde{v_i}}{|\widetilde{\vec{v}}|}\widetilde{v_k'' v_k''} + \frac{\widetilde{v_k}}{|\widetilde{\vec{v}}|}\widetilde{v_i'' v_k''} - \frac{1}{2}\frac{\widetilde{v_i}\,\widetilde{v_k}\,\widetilde{v_l}}{|\widetilde{\vec{v}}|^3}\widetilde{v_k'' v_l''} \right] \quad . \tag{3.15}$$

Note that if the approximation was reduced to first order, all terms which contain Reynolds stresses would disappear so that the Forchheimer term would have the same form as it does in the laminar equations (2.29b).

The momentum equation in its closed form after including the modelled Forchheimer term reads

$$\begin{aligned}\frac{\partial \overline{\rho}\, \widetilde{v_i}}{\partial t} + \frac{\partial \overline{\rho}\, \widetilde{v_i}\, \widetilde{v_j}}{\partial x_j} =& -\frac{\partial \overline{\rho}\, \widetilde{v_i'' v_j''}}{\partial x_j} - \frac{\partial \overline{p}}{\partial x_i} + \frac{\partial \overline{\tau_{ij}}}{\partial x_j} - \phi \frac{\overline{\mu}}{\kappa}\widetilde{v_i} \\ & - \phi^2 \frac{c_{\mathrm{F}}}{\sqrt{\kappa}} \overline{\rho} \left[\widetilde{v_i}|\widetilde{\vec{v}}| + \frac{1}{2}\frac{\widetilde{v_i}}{|\widetilde{\vec{v}}|}\widetilde{v_k'' v_k''} + \frac{\widetilde{v_k}}{|\widetilde{\vec{v}}|}\widetilde{v_i'' v_k''} - \frac{1}{2}\frac{\widetilde{v_i}\,\widetilde{v_k}\,\widetilde{v_l}}{|\widetilde{\vec{v}}|^3}\widetilde{v_k'' v_l''} \right] \quad .\end{aligned} \tag{3.16}$$

3.5. Derivation of closed form of turbulent energy equation

The unknowns in the energy equation (3.7c) are the triple correlations $\widetilde{v_i'' v_j'' v_j''}$, the velocity-enthalpy correlation $\widetilde{v_i'' h''}$ (see also equation (3.9)) and the velocity-shear-stress correlation $\overline{v_i'' \tau_{ij}'}$. The triple correlation and the velocity-shear-stress correlations will be discussed as part of the modelling of the Reynolds stresses and are described later by equations (3.58), (3.59) and (3.60).

The turbulence model which is used throughout this work borrows the model for the remaining correlation $\widetilde{v_i'' h''}$ from eddy-viscosity models. Strictly speaking, this breaks with the second-moment closure concept used for modelling the Reynolds stresses. Since it is not the intention of this work to create new turbulence models apart from porous media, this inconsistency accepted. With the help of a turbulent eddy viscosity μ_t and a turbulent Prandtl number σ_t the velocity-enthalpy correlation can be modelled as (see [67])

$$\overline{\rho}\,\widetilde{v_i'' h''} = -c_p \frac{\mu_\mathrm{t}}{\sigma_\mathrm{t}} \frac{\partial \widetilde{T}}{\partial x_i} \qquad \text{or} \qquad \overline{\rho}\,\widetilde{v_i'' h''} = -\frac{\mu_\mathrm{t}}{\sigma_\mathrm{t}} \frac{\partial \widetilde{h}}{\partial x_i} \ , \tag{3.17}$$

where c_p is the heat capacity at a constant pressure. The turbulent Prandtl number σ_t is used here as a constant with a typical value of 0.9 ([76]). The eddy viscosity is defined as

$$\mu_\mathrm{t} = c_\mu \rho \frac{k^2}{\varepsilon} \tag{3.18}$$

for the turbulent kinetic energy k and the turbulent dissipation-rate ε. The value of the modelling coefficient c_μ usually is set to 0.09. Both, the turbulent kinetic energy k and the turbulent dissipation-rate ε come from the turbulence model. Note, that if the *JHh-v2*-model is used which is described in section 3.8, the dissipation-rate ε in equation (3.18) is replaced by its homogeneous part ε^h.

The closed form of the turbulent energy equation now reads

$$\begin{aligned} \frac{\partial \overline{\rho}\,\widetilde{E}}{\partial t} + \frac{\partial \overline{\rho}\,\widetilde{v_i}\,\widetilde{H}}{\partial x_i} = -\frac{\partial \overline{\rho}\,\widetilde{v_j}\widetilde{v_i'' v_j''}}{\partial x_i} &+ \frac{1}{2}\left(\overline{\rho} T_{jj} + \overline{\rho} D_{jj}^{(\nu)}\right) \\ &+ \frac{\partial \widetilde{v_i}\,\overline{\tau_{ij}}}{\partial x_j} - \frac{\partial}{\partial x_i}\left(\overline{k_{\mathrm{d},i}} + k_{\mathrm{d},i}^{(\mathrm{t})}\right) \end{aligned} \tag{3.19}$$

where $k_{\mathrm{d},i}^{(\mathrm{t})}$ is the turbulent heat transport

$$k_{\mathrm{d},i}^{(\mathrm{t})} = \overline{\rho}\widetilde{v_i'' h''}$$

as defined in equation (3.17), $\overline{\rho}T_{jj}$ is the turbulent diffusion term as defined in equation (3.59) and $\overline{\rho}D_{jj}^{(\nu)}$ is the viscous diffusion term as defined in equation (3.60).

3.6. Derivation of Reynolds-stress equations for flow in porous media

The present section covers the modelling of the Reynolds stresses. Three different categories of models could be employed which are referred to as one-equation models, two-equation models and Reynolds-stress models. Even though the one- and two-equation models are the most tested and commonly used choices, the present work will concentrate on modelling the turbulent terms with Reynolds-stress models. This model has two main advantages:

- In contrast to one- and two-equation models which rely on the Boussinesq-hypothesis, the direction of Reynolds stresses does not have to be parallel to the viscous stresses [11, 25]. This promises better results especially for complex flow conditions.

- For flow in porous media, there will appear additional terms in the Reynolds-stress and turbulent dissipation-rate equations. If these terms are defined for the Reynolds-stress models it will be easy to transfer them to one- and two-equation models in a straightforward way while the other way round would be more complex.

The theoretical aspects of the derivation of the Reynolds-stress equations are discussed in several books (e.g. by Wilcox [81] or Gersten and Herwig [27]). Thus, the derivation aspects in the present work are only covered in terms of explaining the additional efforts needed for modelling turbulence inside porous media. The derivation is based on the following relation

$$\overline{v_i \mathcal{N}_j + v_j \mathcal{N}_i} - \left(\widetilde{v_i} \overline{\mathcal{N}_j} + \widetilde{v_j} \overline{\mathcal{N}_i} \right) = 0 \tag{3.20}$$

where the expression $\mathcal{N}_i$ represents the momentum equation (2.29b) as

$$\mathcal{N}_i = \frac{\partial \rho v_i}{\partial t} + \frac{\partial \rho v_i v_j}{\partial x_j} + \frac{\partial p}{\partial x_i} - \frac{\partial \tau_{ij}}{\partial x_j} + \phi \frac{\mu}{\kappa} v_i + \phi^2 \frac{c_{\mathrm{F}}}{\sqrt{\kappa}} \rho v_i \cdot |\vec{v}| = 0 \ . \tag{3.21}$$

Several rearrangements lead to the Reynolds-stress equation:

$$
\begin{aligned}
&\frac{\partial \overline{\rho}\widetilde{v_i'' v_j''}}{\partial t} + \frac{\partial \overline{\rho}\widetilde{v}_k \widetilde{v_i'' v_j''}}{\partial x_k} = \\
&\qquad -\overline{\rho}\widetilde{v_i'' v_k''}\frac{\partial \widetilde{v}_j}{\partial x_k} - \overline{\rho}\widetilde{v_j'' v_k''}\frac{\partial \widetilde{v}_i}{\partial x_k} + \overline{p'\left(\frac{\partial v_i''}{\partial x_j} + \frac{\partial v_j''}{\partial x_i}\right)} - \overline{\tau_{ik}'\frac{\partial v_j''}{\partial x_k}} - \overline{\tau_{jk}'\frac{\partial v_i''}{\partial x_k}} \\
&\qquad -\frac{\partial \overline{\rho}\widetilde{v_i'' v_j'' v_k''}}{\partial x_k} + \frac{\partial \overline{\tau_{ik}' v_j''}}{\partial x_k} + \frac{\partial \overline{\tau_{jk}' v_i''}}{\partial x_k} - \frac{\partial \overline{p' v_i''}}{\partial x_j} - \frac{\partial \overline{p' v_j''}}{\partial x_i} \\
&\qquad +\overline{v_i''}\left(-\frac{\partial \overline{p}}{\partial x_j} + \frac{\partial \overline{\tau_{jk}}}{\partial x_k}\right) + \overline{v_j''}\left(-\frac{\partial \overline{p}}{\partial x_i} + \frac{\partial \overline{\tau_{ik}}}{\partial x_k}\right) \\
&\qquad -\phi\frac{\overline{\mu}}{\kappa}\left(\overline{v_i''}\widetilde{v}_j + \overline{v_j''}\widetilde{v}_i + 2\overline{v_i'' v_j''}\right) - \overline{\rho}\phi^2\frac{c_{\mathrm{F}}}{\sqrt{\kappa}}\left(\widetilde{v_i'' v_j |\vec{v}|} + \widetilde{v_j'' v_i |\vec{v}|}\right)
\end{aligned}
\tag{3.22}
$$

Strictly speaking, additional correlation terms would appear as a result of fluctuations of the viscosity μ. They are neglected in agreement with the discussion of the derivation of the time-averaged Navier-Stokes equations (3.7). The different terms are usually named as:

production term: $$\overline{\rho}P_{ij} = -\overline{\rho}\widetilde{v_i'' v_k''}\frac{\partial \widetilde{v}_j}{\partial x_k} - \overline{\rho}\widetilde{v_j'' v_k''}\frac{\partial \widetilde{v}_i}{\partial x_k} \tag{3.23a}$$

pressure-strain correlation: $$\overline{\rho}\Pi_{ij} = \overline{p'\left(\frac{\partial v_i''}{\partial x_j} + \frac{\partial v_j''}{\partial x_i}\right)} \tag{3.23b}$$

dissipation term: $$\overline{\rho}\varepsilon_{ij} = \overline{\tau_{ik}'\frac{\partial v_j''}{\partial x_k}} + \overline{\tau_{jk}'\frac{\partial v_i''}{\partial x_k}} \tag{3.23c}$$

diffusion term: $$\overline{\rho}D_{ij} = -\frac{\partial \overline{\rho}\widetilde{v_i'' v_j'' v_k''}}{\partial x_k} + \frac{\partial \overline{\tau_{ik}' v_j''}}{\partial x_k} + \frac{\partial \overline{\tau_{jk}' v_i''}}{\partial x_k} - \frac{\partial \overline{p' v_i''}}{\partial x_j} - \frac{\partial \overline{p' v_j''}}{\partial x_i} \tag{3.23d}$$

compressibility effects: $$\overline{\rho}M_{ij} = \overline{v_i''}\left(-\frac{\partial \overline{p}}{\partial x_j} + \frac{\partial \overline{\tau_{jk}}}{\partial x_k}\right) + \overline{v_j''}\left(-\frac{\partial \overline{p}}{\partial x_i} + \frac{\partial \overline{\tau_{ik}}}{\partial x_k}\right) \tag{3.23e}$$

Furthermore, the terms which appear particularly due to porous media are assigned to the Darcy and to the Forchheimer term:

Darcy term: $$\mathcal{P}_{ij}^{(\text{Darcy})} = \phi\frac{\overline{\mu}}{\kappa}\left(\overline{v_i''}\widetilde{v}_j + \overline{v_j''}\widetilde{v}_i + 2\overline{v_i'' v_j''}\right) \tag{3.24a}$$

Forchheimer term: $$\mathcal{P}_{ij}^{(\text{Forch})} = \overline{\rho}\phi^2\frac{c_{\mathrm{F}}}{\sqrt{\kappa}}\left(\widetilde{v_i'' v_j |\vec{v}|} + \widetilde{v_j'' v_i |\vec{v}|}\right) \tag{3.24b}$$

Apart from the production term $\overline{\rho}P_{ij}$, all of the remaining terms need modelling. The process for most of these terms can be taken from existing Reynolds-stress models. Special attention must be paid to the Darcy and Forchheimer terms $\mathcal{P}_{ij}^{\text{(Darcy)}}$ and $\mathcal{P}_{ij}^{\text{(Forch)}}$. Besides that, most Reynolds-stress models rely on an additional transport equation to determine a length scale of the turbulent structures. Amongst others, this length scale is used to model the dissipation term $\overline{\rho}\varepsilon_{ij}$. The most frequent transport variable which is used to define the length scale, is the turbulent dissipation-rate ε [44, 18] or subsidiaries directly based on ε like the homogeneous turbulent dissipation-rate ε^{h} [36]. The turbulent dissipation-rate equation will be derived in section 3.7. Before that, the Darcy and Forchheimer terms of the Reynolds-stress equations will be discussed. Another section will focus on the modelling of an extra diffusion term inside porous media.

3.6.1. Modelling of the Darcy term in the Reynolds-stress equations

The Darcy term in the Reynolds-stress equations (3.22) only needs modelling as long as the flow is compressible. In case of incompressible flow the average of the velocity fluctuations v_i'' will vanish. In the present work it is assumed that this is also valid for the compressible flow and, hence, the Darcy term in the Reynolds-stress equations reads

$$\mathcal{P}_{ij}^{\text{(Darcy)}} = 2\phi\frac{\overline{\mu}}{\kappa}\widetilde{v_i''v_j''} \quad . \tag{3.25}$$

This assumption can be based on Morkovin's hypothesis (as e.g. discussed in [72]) which states that the effect of density fluctuations is negligible for high Mach numbers of up to $Ma = 5$ or even more. These assumptions are also basis of the Reynolds-stress model which will be used later in this work.

3.6.2. Modelling of the Forchheimer term in the Reynolds-stress equations

The Forchheimer term which appears in the Reynolds-stress equations presents a similar complexity as the Forchheimer term in the momentum equations that were discussed in section 3.4. Accordingly, it will be approximated by a Taylor expansion in the same way as it was done in section 3.4. The following derivations follow the guidelines given in [49] which again similar to the one stated in [28] but preserves more terms.

The Forchheimer term in the Reynolds-stress equations (3.22) reads

$$\overline{\rho}\phi^2\frac{c_{\text{F}}}{\sqrt{\kappa}}\left(\widetilde{v_i''v_j|\vec{v}|} + \widetilde{v_j''v_i|\vec{v}|}\right) \quad .$$

Here the term to be modelled can be isolated to

$$\widetilde{v_i'' v_j |\vec{v}|} \quad . \tag{3.26}$$

In order to model this term, a Taylor expansion is applied to the function

$$f_{\mathrm{RS}ij}(\epsilon) = v_i'' v_j \sqrt{v_l v_l} = v_i'' f_j(\epsilon) \quad \text{where} \quad v_k = \widetilde{v_k} + \epsilon \cdot v_k'' \quad .$$

The function $f_j(\epsilon)$ comes from equation (3.11) which was used for the approximation procedure of the Forchheimer term in the momentum equation. The velocity fluctuation v_i'' is also scaled with the factor ϵ which leads to

$$f_{\mathrm{RS}ij}(\epsilon) = \epsilon v_i'' f_j(\epsilon) \quad .$$

A third order Taylor expansion for $f_{\mathrm{RS}ij}(\epsilon)$ can be written as

$$\begin{aligned} f_{\mathrm{RS}ij}(\epsilon) \approx f_{\mathrm{RS}ij}(\epsilon_0) + \left.\frac{\partial f_{\mathrm{RS}ij}(\epsilon)}{\partial \epsilon}\right|_{\epsilon_0} (\epsilon - \epsilon_0) + \frac{1}{2} \left.\frac{\partial^2 f_{\mathrm{RS}ij}(\epsilon)}{\partial \epsilon^2}\right|_{\epsilon_0} (\epsilon - \epsilon_0)^2 \\ + \frac{1}{6} \left.\frac{\partial^3 f_{\mathrm{RS}ij}(\epsilon)}{\partial \epsilon^3}\right|_{\epsilon_0} (\epsilon - \epsilon_0)^3 \quad . \end{aligned} \tag{3.27}$$

The first three derivatives of $f_{\mathrm{RS}ij}(\epsilon)$ are

$$\frac{\partial f_{\mathrm{RS}ij}(\epsilon)}{\partial \epsilon} = \epsilon v_i'' \frac{\partial f_j(\epsilon)}{\partial \epsilon} + v_i'' f_j(\epsilon)$$

$$\frac{\partial^2 f_{\mathrm{RS}ij}(\epsilon)}{\partial \epsilon^2} = \epsilon v_i'' \frac{\partial^2 f_j(\epsilon)}{\partial \epsilon^2} + 2 v_i'' \frac{\partial f_j(\epsilon)}{\partial \epsilon}$$

$$\frac{\partial^3 f_{\mathrm{RS}ij}(\epsilon)}{\partial \epsilon^3} = \epsilon v_i'' \frac{\partial^3 f_j(\epsilon)}{\partial \epsilon^3} + 3 v_i'' \frac{\partial^2 f_j(\epsilon)}{\partial \epsilon^2} \quad .$$

The third order Taylor expansion at the reference point $\epsilon_0 = 0$ and evaluated at $\epsilon = 1$ is then

$$f_{\mathrm{RS}ij}(1) \approx v_i'' f_j(0) + v_i'' \left.\frac{\partial f_j(\epsilon)}{\partial \epsilon}\right|_{\epsilon=0} + \frac{1}{2} v_i'' \left.\frac{\partial^2 f_j(0)}{\partial \epsilon^2}\right|_{\epsilon=0} \quad .$$

After inserting the derivatives of $f_j(\epsilon)$ from equations (3.12) and (3.13) and applying the density-weighted average, the function $f_{\mathrm{RS}ij}$ becomes

$$\widetilde{f_{\mathrm{RS}ij}(1)} \approx \widetilde{v_i'' v_j''} |\widetilde{\vec{v}}| + \widetilde{v_i'' v_k''} \frac{\widetilde{v_j} \widetilde{v_k}}{|\widetilde{\vec{v}}|} + \widetilde{v_i'' v_j'' v_k''} \frac{\widetilde{v_k}}{|\widetilde{\vec{v}}|} + \widetilde{v_i'' v_k'' v_k''} \frac{\widetilde{v_j}}{2|\widetilde{\vec{v}}|} - \widetilde{v_i'' v_k'' v_m''} \frac{\widetilde{v_j} \widetilde{v_k} \widetilde{v_m}}{2|\widetilde{\vec{v}}|^3} \quad .$$

With this relation, the complete approximated Forchheimer term now reads

$$\begin{aligned}\mathcal{P}_{ij}^{(\mathrm{Forch})} = \overline{\rho}\phi^2 \frac{c_\mathrm{F}}{\sqrt{K}} \Bigg[& 2\overline{v_i'' v_j''}|\widetilde{\vec{v}}| + \frac{\widetilde{v_j}\,\widetilde{v_k}}{|\widetilde{\vec{v}}|}\overline{v_i'' v_k''} + \frac{\widetilde{v_i}\widetilde{v_k}}{|\widetilde{\vec{v}}|}\overline{v_j'' v_k''} \\ & + 2\frac{\widetilde{v_k}}{|\widetilde{\vec{v}}|}\overline{v_i'' v_j'' v_k''} + \frac{1}{2}\frac{\widetilde{v_j}}{|\widetilde{\vec{v}}|}\overline{v_i'' v_k'' v_k''} + \frac{1}{2}\frac{\widetilde{v_i}}{|\widetilde{\vec{v}}|}\overline{v_j'' v_k'' v_k''} \\ & - \frac{1}{2}\frac{\widetilde{v_j}\widetilde{v_k}\widetilde{v_m}}{|\widetilde{\vec{v}}|^3}\overline{v_i'' v_k'' v_m''} - \frac{1}{2}\frac{\widetilde{v_i}\widetilde{v_k}\widetilde{v_m}}{|\widetilde{\vec{v}}|^3}\overline{v_j'' v_k'' v_m''} \Bigg] \,. \end{aligned} \tag{3.28}$$

This rather complex term contains mean velocities and Reynolds stresses which can be considered to be known. It also consists of triple correlations which have to be modelled. There exist several models for triple correlations since they are needed for modelling the diffusion term D_{ij} in the Reynolds-stress equations. The most commonly used model originates from Daly and Harlow [19] and is defined as

$$\overline{v_i' v_j' v_k'} = -c_s \frac{k}{\varepsilon}\overline{v_k' v_l'}\frac{\partial \overline{v_i' v_j'}}{\partial x_l} \tag{3.29}$$

for the turbulent kinetic energy k and the turbulent dissipation-rate ε. Both variables are considered to be known. The parameter c_s is a modelling constant and its value is normally taken as 0.22. Alternatively, there is another model from Hanjalić and Launder [31] which provides the advantage that it is independent of the index order:

$$\overline{v_i' v_j' v_k'} = -c_t \frac{k}{\varepsilon}\left(\overline{v_i' v_l'}\frac{\partial \overline{v_j' v_k'}}{\partial x_l} + \overline{v_j' v_l'}\frac{\partial \overline{v_i' v_k'}}{\partial x_l} + \overline{v_k' v_l'}\frac{\partial \overline{v_i' v_j'}}{\partial x_l} \right) \tag{3.30}$$

The constant c_t is taken as 0.11.

Both models are described here for the time averages and their related fluctuations. However, in the present work it is assumed that they are also valid for the density-weighted averages and their related fluctuations. Furthermore, it is not clear if the modelling constants c_s or c_t are generally valid for the Forchheimer term. Hence, recalibration of the parameters for the Forchheimer term will have to be investigated.

3.6.3. Modelling of extra diffusion inside porous media

During the procedure of validating the Reynolds-stress models for porous media, it was realized that the Reynolds stresses faded far too fast inside porous media. Breugem already discussed in [10] that the turbulent kinetic energy deep inside porous media are mandatorily driven by the pressure fluctuations close to the interface. The effect, that especially low-frequency pressure fluctuations can travel through porous media was not reproduced during the validation computations. This deficiency of the model is counteracted by an additional diffusion term in the Reynolds-stress equations. Thereby, it is expected that the pressure fluctuations can only cause an enforcement of the normal stresses but will not directly influence the Reynolds shear stresses. As a result, the following diffusion term is proposed:

$$\overline{\rho} D_{p,ij} = \begin{cases} \frac{\partial}{\partial x_k}\left(c_{d,p} \overline{\rho} \frac{k^2}{\varepsilon} \frac{\partial \widetilde{v_i'' v_j''}}{\partial x_k} \right) & \text{if} \quad i = j \\ 0 & \text{else} \end{cases} \tag{3.31}$$

with a new modelling coefficient $c_{d,p}$. The effect of this coefficient on a channel flow similar to the setup of figure 2.18 is shown in figure 3.2. It becomes apparent that the decay of the Reynolds stresses inside the porous medium is much smaller for the case with the new diffusion term. Still, it must be ensured that the additional diffusion is only active inside porous media. Furthermore, in terms of consistency inside extremely permeable porous media where the physics of flow in nonporous regions is dominant, the additional diffusion must vanish. This can be achieved by a switch which compares the turbulent length scale $l_{\text{turbulence}}$ to the square root of the permeability $\sqrt{\kappa}$ which is used as characteristic value of the pore size (see appendix C.1):

$$\text{switch indicator} = \frac{l_{\text{turbulence}}}{\sqrt{\kappa}} \quad \text{with} \quad l_{\text{turbulence}} = 0.09 \cdot \frac{k^{\frac{3}{2}}}{\varepsilon} \tag{3.32}$$

where k is the local turbulent kinetic energy and ε is the local turbulent dissipation-rate. The indicator can be used to replace the modelling coefficient $c_{d,p}$ with an effective value $c_{d,p,\text{eff}}$ which is zero if the turbulent length scale is much smaller than the characteristic pore size. Otherwise $c_{d,p,\text{eff}}$ is equal to $c_{d,p}$. Smooth blending is achieved with the help of a tanh-function as shown in figure 3.3:

$$c_{d,p,\text{eff}} = c_{d,p} \cdot 0.5 \cdot (\tanh(100 \cdot \text{switch indicator} - 5) + 1) \tag{3.33}$$

3.7. Derivation of turbulent dissipation-rate equation inside porous media

As already mentioned in section 3.6, the definition of the length scale is based on an additional transport equation. Inside this work the length scale is based on the turbulent dissipation-rate ε which is defined as

$$\varepsilon = \widetilde{\nu} \overline{\frac{\partial v_i''}{\partial x_j} \frac{\partial v_i''}{\partial x_j}} \tag{3.34}$$

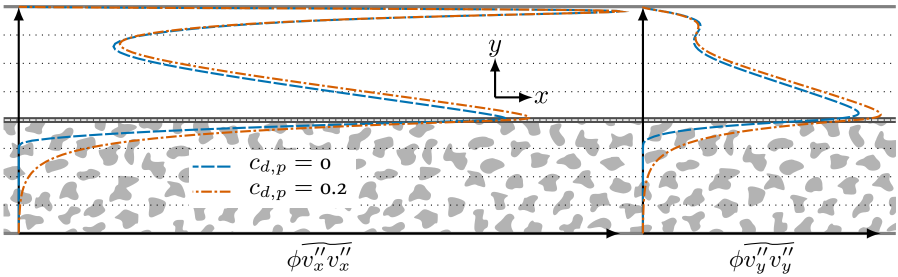

Figure 3.2.: Effect of the additional diffusion inside porous media, where $c_{d,p}$ is the diffusion coefficient.

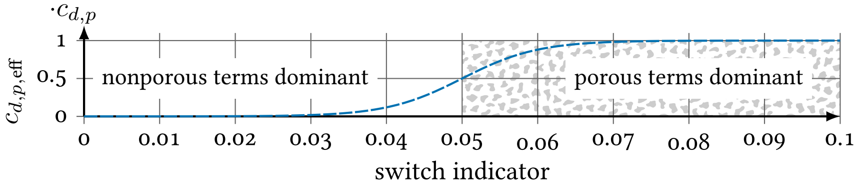

Figure 3.3.: Switch demonstration for the pressure diffusion in porous media.

in which $\nu = \frac{\mu}{\rho}$ is the kinematic viscosity. In order to derive a transport equation for the turbulent dissipation-rate, a rule similar to the one given for the Reynolds-stress transport equations (equation (3.20)) is used. It reads

$$2 \cdot \widetilde{\nu} \left(\overline{\frac{\partial v_i}{\partial x_j} \frac{\partial}{\partial x_j} \left[\frac{1}{\rho} \mathcal{N}_i \right]} - \frac{\partial \widetilde{v_i}}{\partial x_j} \frac{\partial}{\partial x_j} \left[\frac{1}{\overline{\rho}} \overline{\mathcal{N}_i} \right] \right) = 0 \tag{3.35}$$

where $\mathcal{N}_i$ is the momentum equation according to equation (3.21). The application of this rule would lead to a complex equation consisting of many unknown correlations based on density fluctuations. It is observed from the literature that the process of deriving the exact equation for compressible flow is avoided by only presenting the already modelled version of the turbulent dissipation-rate equation (see e.g. [66, 73, 11]) which is based on the incompressible derivation. A justification for this simplification would be that even the incompressible turbulent dissipation-rate equation is strongly modelled since hardly any terms are known. Hence, even for incompressible flow the derivation of the exact dissipation-rate equation can only serve as a guide for modelling a reliable transport equation. Consequently, it also seems sufficient to derive the additional terms inside of porous media on the basis of incompressible equations and then apply them also to compressible flow.

Under incompressible conditions the derivation of the turbulent dissipation-rate can be written in a simplified form:

$$2 \cdot \nu \overline{\frac{\partial v_i'}{\partial x_j} \frac{\partial}{\partial x_j} \left[\mathcal{N}_i \right]} = 0 \tag{3.36}$$

Using the momentum equation $\mathcal{N}_i$ (equation (3.21)) in its incompressible form this leads to a transport equation as follows (see e.g. Wilcox [81] for a detailed derivation):

$$\frac{\partial \rho \varepsilon}{\partial t} + \frac{\partial \rho \overline{v_k} \varepsilon}{\partial x_k} = P_\varepsilon + T_\varepsilon + \Phi_\varepsilon - Y - 2\phi \frac{\mu}{\kappa} \varepsilon - 2\nu \cdot \phi^2 \frac{c_\mathrm{F}}{\sqrt{\kappa}} \overline{\frac{\partial v_i'}{\partial x_j} \frac{\partial v_i |\vec{v}|}{\partial x_j}} \tag{3.37}$$

The designation for the different terms are taken from Mansour et al. [47] and are as follows: P_ε combines several production terms, T_ε is the turbulent transport term, Φ_ε is the pressure transport term, D_ε is the sum of viscous, turbulent and pressure diffusion and Y is the dissipation term. The names of these different terms support basic information about the different mechanisms which take place in the dissipation-rate transport equation. The exact formulation of the terms is of no importance for the present work and is not considered any further. However, a closed form of the homogeneous turbulent dissipation-rate ε^h is presented later on in section 3.8.2. Additional terms appear inside porous media which can be assigned to the Darcy and Forchheimer terms as it has been performed for the Reynolds-stress equations:

$$\text{Darcy term:} \quad \mathcal{P}_\varepsilon^{(\text{Darcy})} = 2\phi\frac{\mu}{\kappa}\varepsilon \tag{3.38a}$$

$$\text{Forchheimer term:} \quad \mathcal{P}_\varepsilon^{(\text{Forch})} = 2\nu \cdot \phi^2 \frac{c_\text{F}}{\sqrt{\kappa}} \overline{\frac{\partial v_i'}{\partial x_j}\frac{\partial v_i|\vec{v}|}{\partial x_j}} \tag{3.38b}$$

The Forchheimer term is unknown and requires modelling. This is conducted corresponding to the modelling of the Forchheimer term in the momentum and Reynolds-stress equation. It is based on [28] or, more precisely, on [49] which keeps more terms from the Taylor expansion. The function which is expanded reads

$$f_\epsilon(\epsilon) = \frac{\partial \epsilon v_i'}{\partial x_j}\frac{\partial v_i|\vec{v}|}{\partial x_j} = \epsilon\frac{\partial v_i'}{\partial x_j}\frac{\partial f_i(\epsilon)}{\partial x_j}$$

where $f_i(\epsilon)$ comes from equation (3.11) which was used for modelling the momentum equation. For a third-order Taylor expansion, as it was used for the Reynolds-stress equations (3.27), the first three derivatives of $f_\varepsilon(\epsilon)$ are needed:

$$\begin{aligned}
\frac{\partial f_\varepsilon(\epsilon)}{\partial \epsilon} &= \frac{\partial v_i'}{\partial x_j}\frac{\partial f_i(\epsilon)}{\partial x_j} + \epsilon\frac{\partial v_i'}{\partial x_j}\frac{\partial}{\partial x_j}\left(\frac{\partial f_i(\epsilon)}{\partial \epsilon}\right) \\
\frac{\partial^2 f_\varepsilon(\epsilon)}{\partial \epsilon^2} &= 2\frac{\partial v_i'}{\partial x_j}\frac{\partial}{\partial x_j}\left(\frac{\partial f_i(\epsilon)}{\partial \epsilon}\right) + \epsilon\frac{\partial v_i'}{\partial x_j}\frac{\partial}{\partial x_j}\left(\frac{\partial^2 f_i(\epsilon)}{\partial \epsilon^2}\right) \\
\frac{\partial^3 f_\varepsilon(\epsilon)}{\partial \epsilon^3} &= 3\frac{\partial v_i'}{\partial x_j}\frac{\partial}{\partial x_j}\left(\frac{\partial^2 f_i(\epsilon)}{\partial \epsilon^2}\right) + \epsilon\frac{\partial v_i'}{\partial x_j}\frac{\partial}{\partial x_j}\left(\frac{\partial^3 f_i(\epsilon)}{\partial \epsilon^3}\right)
\end{aligned}$$

The function f_ε can be approximated as

$$f_\varepsilon(1) \approx \frac{\partial v_i'}{\partial x_j}\frac{\partial f_i(0)}{\partial x_j} + \frac{\partial v_i'}{\partial x_j}\frac{\partial}{\partial x_j}\left(\left.\frac{\partial f_i(\epsilon)}{\partial \epsilon}\right|_{\epsilon=0}\right) + \frac{1}{2}\frac{\partial v_i'}{\partial x_j}\frac{\partial}{\partial x_j}\left(\left.\frac{\partial^2 f_i(\epsilon)}{\partial \epsilon^2}\right|_{\epsilon=0}\right)$$

or after inserting the values of $f_i(0)$ and its derivatives followed by averaging in time

$$\begin{aligned}
\overline{f_\varepsilon(1)} \approx & |\bar{\vec{v}}|\overline{\frac{\partial v_i'}{\partial x_j}\frac{\partial v_i'}{\partial x_j}} + \frac{\partial|\bar{\vec{v}}|}{\partial x_j}\overline{v_i'\frac{\partial v_i'}{\partial x_j}} + \frac{\overline{v_i}\,\overline{v_k}}{|\bar{\vec{v}}|}\overline{\frac{\partial v_i'}{\partial x_j}\frac{\partial v_k'}{\partial x_j}} + \frac{\partial}{\partial x_j}\left(\frac{\overline{v_i}\,\overline{v_k}}{|\bar{\vec{v}}|}\right)\overline{v_k'\frac{\partial v_i'}{\partial x_j}} \\
& + \frac{1}{2}\frac{\overline{v_i}}{|\bar{\vec{v}}|}\overline{\frac{\partial v_i'}{\partial x_j}\frac{\partial v_k'v_k'}{\partial x_j}} + \frac{1}{2}\frac{\partial}{\partial x_j}\left(\frac{\overline{v_i}}{|\bar{\vec{v}}|}\right)\overline{v_k'v_k'\frac{\partial v_i'}{\partial x_j}} \\
& + \frac{\overline{v_k}}{|\bar{\vec{v}}|}\overline{\frac{\partial v_i'}{\partial x_j}\frac{\partial v_i'v_k'}{\partial x_j}} + \frac{\partial}{\partial x_j}\left(\frac{\overline{v_k}}{|\bar{\vec{v}}|}\right)\overline{v_i'v_k'\frac{\partial v_i'}{\partial x_j}} \\
& - \frac{1}{2}\frac{\overline{v_i}\,\overline{v_k}\,\overline{v_l}}{|\bar{\vec{v}}|^3}\overline{\frac{\partial v_i'}{\partial x_j}\frac{\partial v_k'v_l'}{\partial x_j}} - \frac{1}{2}\frac{\partial}{\partial x_j}\left(\frac{\overline{v_i}\,\overline{v_k}\,\overline{v_l}}{|\bar{\vec{v}}|^3}\right)\overline{v_k'v_l'\frac{\partial v_i'}{\partial x_j}} \quad .
\end{aligned}$$

Using the definition of the turbulent dissipation-rate and after several rearrangements, the Forchheimer term of the turbulent dissipation-rate equation reads

$$\begin{aligned}\mathcal{P}_{\varepsilon}^{(\mathrm{Forch})} = \rho\phi^{2}\frac{c_{\mathrm{F}}}{\sqrt{\kappa}}\Bigg[& 2\varepsilon|\overline{\vec{v}}| + \nu\frac{\partial|\overline{\vec{v}}|}{\partial x_j}\frac{\partial\overline{v_i'v_i'}}{\partial x_j} + \nu\frac{\partial}{\partial x_j}\left(\frac{\overline{v_i}\,\overline{v_k}}{|\overline{\vec{v}}|}\right)\frac{\overline{v_i'v_k'}}{x_j} \\ & + 2\nu\frac{\overline{v_k}}{|\overline{\vec{v}}|}\left[\overline{v_k'\frac{\partial v_i'}{\partial x_j}\frac{\partial v_i'}{\partial x_j}} + 2\overline{v_i'\frac{\partial v_i'}{\partial x_j}\frac{\partial v_k'}{\partial x_j}} + \overline{v_i}\,\overline{\frac{\partial v_i'}{\partial x_j}\frac{\partial v_k'}{\partial x_j}}\right] \\ & + \nu\frac{\partial}{\partial x_j}\left(\frac{\overline{v_k}}{|\overline{\vec{v}}|}\right)\left[\overline{2v_i'v_k'\frac{\partial v_i'}{\partial x_j}} + \overline{v_i'v_i'\frac{\partial v_k'}{\partial x_j}}\right] \\ & - 2\nu\frac{\overline{v_i}\,\overline{v_k}\,\overline{v_m}}{|\overline{\vec{v}}|^{3}}\overline{v_k'\frac{\partial v_i'}{\partial x_j}\frac{\partial v_m'}{\partial x_j}} - \frac{1}{3}\nu\frac{\partial}{\partial x_j}\left(\frac{\overline{v_i}\,\overline{v_k}\,\overline{v_m}}{|\overline{\vec{v}}|^{3}}\right)\frac{\partial\overline{v_i'v_k'v_m'}}{\partial x_j}\Bigg] \ . \end{aligned} \tag{3.39}$$

This model of the Forchheimer term in the turbulent dissipation-rate equation contains many unknown correlations. Following [28] some terms can be modelled by employing the gradient diffusion hypothesis ([19]),

$$\overline{v_i'\varphi} = -c_{\varphi}\frac{k}{\varepsilon}\overline{v_i'v_j'}\frac{\partial\overline{\varphi}}{\partial x_j} \quad , \tag{3.40}$$

for an arbitrary variable φ, the modelling coefficient c_{φ}, the turbulent dissipation rate ε and the turbulent kinetic energy k. Additionally, it is assumed that turbulence is locally isotropic:

$$v_i' = v_j' \quad ; \quad \frac{\partial v_i'}{\partial x_k} = \frac{\partial v_j'}{\partial x_k} \quad \text{for} \quad i,j \in 1,2,3 \tag{3.41}$$

Keeping this in mind, at least three terms from equation (3.39) can be modelled:

$$\overline{v_k'\frac{\partial v_i'}{\partial x_j}\frac{\partial v_i'}{\partial x_j}} + 2\overline{v_i'\frac{\partial v_i'}{\partial x_j}\frac{\partial v_k'}{\partial x_j}} = -\frac{c_{\varepsilon,\mathrm{F}}}{\nu}\frac{k}{\varepsilon}\overline{v_k'v_i'}\frac{\partial\varepsilon}{\partial x_i} \tag{3.42}$$

with the modelling coefficient $c_{\varepsilon,\mathrm{F}}$, and

$$\overline{v_i}\,\overline{\frac{\partial v_i'}{\partial x_j}\frac{\partial v_k'}{\partial x_j}} = \overline{v_i}\frac{1}{3\nu}\varepsilon 1_i 1_k \tag{3.43}$$

where the 1_i and 1_k imply that the addition over the indices takes place. In other words

$$1_i = 1 \quad \text{for} \quad i \in 1,2,3 \ .$$

Expression (3.43) is strongly dependent on the orientation of the coordinate system. Excluding the terms which lead to the coordinate system dependency in (3.43) leads to

$$\overline{v_i}\,\overline{\frac{\partial v'_i}{\partial x_j}\frac{\partial v'_k}{\partial x_j}} = \overline{v_k}\frac{1}{3\nu}\varepsilon \ . \tag{3.44}$$

If the factor $2\nu\frac{\overline{v_k}}{|\overline{\vec{v}}|}$ of equation (3.39) is applied to the model (3.44) it will result in

$$2\nu\frac{\overline{v_k}}{|\overline{\vec{v}}|}\overline{v_i}\,\overline{\frac{\partial v'_i}{\partial x_j}\frac{\partial v'_k}{\partial x_j}} = |\overline{\vec{v}}|\frac{2}{3}\varepsilon \ . \tag{3.45}$$

The terms of equation (3.39) which contain $\overline{v'_i v'_k \frac{\partial v'_i}{\partial x_j}}$ or $\overline{v'_i v'_i \frac{\partial v'_k}{\partial x_j}}$ can be reconstructed as gradients of triple correlations as long as the local isotropy according to definition (3.41) is valid:

$$2\overline{v'_i v'_k \frac{\partial v'_i}{\partial x_j}} + \overline{v'_i v'_i \frac{\partial v'_k}{\partial x_j}} = \frac{\partial \overline{v'_i v'_i v'_k}}{\partial x_j} \tag{3.46}$$

The term $\frac{\overline{v_i}\,\overline{v_k}\,\overline{v_m}}{|\overline{\vec{v}}|^3}\overline{v'_k\frac{\partial v'_i}{\partial x_j}\frac{\partial v'_m}{\partial x_j}}$ can be rearranged to coincide with the model (3.42). In this process, the conditions of the gradient diffusion (3.40), local isotropy (3.41) and the assumption that terms which lead to a dependency of the coordinate system are zero are used. The rearrangement leads to

$$\frac{\overline{v_i}\,\overline{v_k}\,\overline{v_m}}{|\overline{\vec{v}}|^3}\overline{v'_k\frac{\partial v'_i}{\partial x_j}\frac{\partial v'_m}{\partial x_j}} = -\frac{\overline{v_k}}{|\overline{\vec{v}}|}\frac{c_{\varepsilon,\mathrm{F},2}}{\nu}\frac{k}{\varepsilon}\overline{v'_k v'_i}\frac{\partial \varepsilon}{\partial x_i} \ . \tag{3.47}$$

If this model and the model from equation (3.42) are plugged into the equation (3.39) they will have the same form and can be summarized to one model with an adapted coefficient $c_{\varepsilon,\mathrm{F}}$.

As a result of the models which are discussed in this section, the Forchheimer term in the turbulent dissipation-rate equation can be written as

$$\begin{aligned}\mathcal{P}_\varepsilon^{(\mathrm{Forch})} = \rho\phi^2\frac{c_\mathrm{F}}{\sqrt{\kappa}}\Bigg[&\frac{8}{3}\varepsilon|\overline{\vec{v}}| + \nu\frac{\partial|\overline{\vec{v}}|}{\partial x_j}\frac{\partial\overline{v'_i v'_i}}{\partial x_j} + \nu\frac{\partial}{\partial x_j}\left(\frac{\partial\overline{v_i}\,\overline{v_k}}{\partial|\overline{\vec{v}}|}\right)\frac{\overline{v'_i v'_k}}{x_j}\\ &- \frac{\overline{v_k}}{|\overline{\vec{v}}|}c_{\varepsilon,\mathrm{F}}\frac{k}{\varepsilon}\overline{v'_k v'_i}\frac{\partial\varepsilon}{\partial x_i} + \nu\frac{\partial}{\partial x_j}\left(\frac{\overline{v_k}}{|\overline{\vec{v}}|}\right)\frac{\partial\overline{v'_i v'_i v'_k}}{\partial x_j}\\ &- \frac{1}{3}\nu\frac{\partial}{\partial x_j}\left(\frac{\overline{v_i}\,\overline{v_k}\,\overline{v_m}}{|\overline{\vec{v}}|^3}\right)\frac{\partial\overline{v'_i v'_k v'_m}}{\partial x_j}\Bigg] \ .\end{aligned} \tag{3.48}$$

There are obvious differences compared to the model of Getachew et al. [28]. The differences are partly due to the different definitions of the turbulent dissipation rate ε and slightly different derivation procedures. As a comparison, Antohe and Lage [2] give a lower order approximation of the Forchheimer term in which at least the term $\frac{8}{3}\varepsilon|\overline{v}|$ coincides with the present model. The rest of the terms are different since the derivation of Antohe and Lage is based on a k-ε-turbulence model and not on Reynolds-stress models.

Assuming that the triple correlations are known from the model (3.30), the closure of the Forchheimer term in the turbulent dissipation-rate equation is complete. However, the resulting model is rather complex. This might not seem appropriate, recalling that the turbulent dissipation-rate equation is very strongly modelled and the original form of Forchheimer term is a model itself. Besides that, validation data for most of the terms do not exist and cannot be validated. Therefore, the Forchheimer term in the dissipation-rate equation should be treated with great care. It seems reasonable to do computations by solely using the lower order terms, only adding higher order terms where they are really needed.

3.8. JHh-v2 Reynolds-stress model inside porous regions

Sections 3.6 and 3.7 presented the procedure for obtaining the contributions of the Darcy and Forchheimer terms to the Reynolds-stress and the turbulent dissipation-rate equations. These derivations are general and independent of the turbulence model. If a specific turbulence model is chosen, several adjustments will be necessary. In the present work, the focus is on the *JHh-v2* Reynolds-stress model. This turbulence model has its origin in the work of Jakirlić and Hanjalić [38, 36, 37]. It has the peculiarity of using the homogeneous turbulent dissipation-rate ε^{h} to define the turbulent length-scale. Jakirlić claims that the standard transport equation which is generally used for the turbulent dissipation-rate ε can only account for its homogeneous part ε^{h}. In other words, by using the homogeneous turbulent dissipation-rate ε^{h} as the additional variable to define the length scale, the correct dissipation-rate profiles for Reynolds stresses can be obtained in a much simpler way. Further terms were added to the homogeneous turbulent dissipation-rate equation by Probst and Radespiel [60] and Probst [59] to take strong pressure gradients and non-equilibrium effects into account. Later, Cécora et al. [11, 12] added quadratic redistribution terms to the Reynolds-stress equations and recalibrated several modelling parameters for better performance in the transonic flow range. This last step leads to the turbulence model which will be introduced in the present section and is called *JHh-v2* (abbreviation for **J**akirlić, **H**anjalić, **h**omogeneous turbulent dissipation-rate, **v**ersion **2**).

The *JHh-v2* turbulence model is used as the standard in the present work for reasons of high expertise in the environment of the author. At the same time the model has also been proven for complex aeronautical flows with flow separations due to high pressure gradients. Such flows are the main applications where the developed models in porous media will be used.

For the sake of completeness, the *JHh-v2* turbulence model as given in [12] is quickly summarized in the following section.

3.8.1. Models for terms in Reynolds-stress equations of JHh-v2 turbulence model

In the following, the single terms of the Reynolds-stress equations, as given in equations (3.23), will be discussed. As already mentioned, the production term $\overline{\rho}P_{ij}$ (3.23a) in the Reynolds-stress equations needs no modelling since all terms are previously known. Proceeding with the pressure-strain correlation $\overline{\rho}\Pi_{ij}$ (3.23b), it is split into four parts:

$$\overline{\rho}\Pi_{ij} = \overline{\rho}\Pi_{ij,1} + \overline{\rho}\Pi_{ij,2} + \overline{\rho}\Pi^{\mathrm{w}}_{ij,1} + \overline{\rho}\Pi^{\mathrm{w}}_{ij,2} \tag{3.49}$$

The first term $\overline{\rho}\Pi_{ij,1}$ is called the slow term and forces turbulence back to isotropy. The second term $\overline{\rho}\Pi_{ij,2}$ is called the rapid term. Its task is the modification of the production term $\overline{\rho}P_{ij}$ to behave more isotropic. The two terms containing the superscript "w" modify the behaviour of the redistribution of Reynolds stresses close to the wall. Basically, they lead to a stronger anisotropy of turbulence. The term $\overline{\rho}\Pi^{\mathrm{w}}_{ij,1}$ can be seen as the near-wall correction of $\overline{\rho}\Pi_{ij}$, and the term $\overline{\rho}\Pi^{\mathrm{w}}_{ij,2}$ as the near-wall correction of $\overline{\rho}\Pi_{ij,2}$. The model states

$$\overline{\rho}\Pi_{ij,1} = -\varepsilon^{\mathrm{h}}\overline{\rho}\left[C_1 a_{ij} + C_1'\left(a_{ik}a_{jk} - \frac{1}{3}\delta_{ij}A_2\right)\right] \tag{3.50a}$$

$$\overline{\rho}\Pi_{ij,2} = -C_2\overline{\rho}\left(P_{ij} - \frac{1}{3}\delta_{ij}P_{kk}\right) \tag{3.50b}$$

$$\overline{\rho}\Pi^{\mathrm{w}}_{ij,1} = C^{\mathrm{w}}_1\overline{\rho}f_{\mathrm{w}}\frac{\varepsilon^{\mathrm{h}}}{k}\left(\delta_{ij}\widetilde{v''_k v''_m}n_k n_m - \frac{3}{2}\widetilde{v''_i v''_k}n_k n_j - \frac{3}{2}\widetilde{v''_j v''_k}n_k n_i\right) \tag{3.50c}$$

$$\overline{\rho}\Pi^{\mathrm{w}}_{ij,2} = C^{\mathrm{w}}_2\overline{\rho}f_{\mathrm{w}}\left(\delta_{ij}\Pi_{km,2}n_k n_m - \frac{3}{2}\Pi_{ik,2}n_k n_j - \frac{3}{2}\Pi_{jk,2}n_k n_i\right) \tag{3.50d}$$

in which k is the turbulent kinetic energy $k = \frac{1}{2}\widetilde{v''_i v''_i}$, the variable a_{ij} is the anisotropy tensor

$$a_{ij} = \frac{\widetilde{v''_i v''_j}}{k} - \frac{2}{3}\delta_{ij} \ , \tag{3.51}$$

P_{ij} is the production term as in equation (3.23a) and n_i are the components along the i-th coordinate direction of the wall normals. The model coefficients are defined as

$$\begin{aligned}
&C_1 = C + \sqrt{A}E^2 \ , \qquad C_1' = -\max(0.7A_2; 0.5)C_1 \ , \qquad C_2 = 0.8\sqrt{A} \ , \\
&C = 2.5A\sqrt[4]{F}f \ , \qquad F = \min(0.6; A_2) \ , \\
&C_1^{\mathrm{w}} = \max\left(1 - 0.7C; 0.3\right) \ , \qquad C_2^{\mathrm{w}} = \min\left(A; 0.3\right) \ , \\
&f = \min\left(\left[\frac{Re_{\mathrm{t}}}{150}\right]^{\frac{3}{2}}; 1\right) \ , \qquad f_{\mathrm{w}} = \min\left(0.4\frac{k^{\frac{3}{2}}}{\varepsilon^{\mathrm{h}}d}; 1.4\right)
\end{aligned} \tag{3.52}$$

with the turbulence Reynolds number

$$Re_{\mathrm{t}} = \frac{k^2}{\widetilde{\nu}\varepsilon^{\mathrm{h}}} \tag{3.53}$$

and the local wall distance d. Regarding the wall distance d, it has to be mentioned that the outer surface of the porous medium will act like a “soft” wall. The definition of this “softness” is part of the discussion in section 3.10.

The variables A, A_2 and A_3 are known as the flatness factors of the Reynolds stresses and the second and third invariant of the Reynolds-stress anisotropy tensor a_{ij}:

$$A = 1 - \frac{9}{8}\left(A_2 - A_3\right) \ , \ A_2 = a_{ij}a_{ji} \ , \ A_3 = a_{ij}a_{jk}a_{ki} \tag{3.54}$$

The flatness factor is also defined for the dissipation rate E which depends on the second and third invariants E_2 and E_3 of the dissipation anisotropy tensor e_{ij}:

$$E = 1 - \frac{9}{8}\left(E_2 - E_3\right) \ , \ E_2 = e_{ij}e_{ji} \ , \ E_3 = e_{ij}e_{jk}e_{ki}$$

Therein, the dissipation anisotropy tensor e_{ij} is defined in a way similar to the anisotropy tensor a_{ij} of the Reynolds stresses:

$$e_{ij} = \frac{\varepsilon_{ij}^{\mathrm{h}}}{\varepsilon^{\mathrm{h}}} - \frac{2}{3}\delta_{ij} \tag{3.55}$$

If the homogeneous turbulent dissipation-rate ε^{h} is assumed to be known this will leave $\varepsilon_{ij}^{\mathrm{h}}$ as the last unknown to compute the pressure-strain correlation (3.49). $\varepsilon_{ij}^{\mathrm{h}}$ is part of the definition of the turbulent dissipation-rate ε_{ij} (3.23c). The dissipation tensor ε_{ij} consists of a homogeneous part and a non-homogeneous part in which the non-homogeneous part is defined in terms of the viscous diffusion term $D_{ij}^{(\nu)}$:

$$\varepsilon_{ij} = \varepsilon_{ij}^{\mathrm{h}} + \frac{1}{2}D_{ij}^{(\nu)} \tag{3.56}$$

In here, $D_{ij}^{(\nu)}$ is the viscous diffusion term which is defined in equation (3.60). The homogeneous turbulent dissipation-rate tensor $\varepsilon_{ij}^{\mathrm{h}}$ depends on the homogeneous turbulent dissipation-rate ε^{h}:

$$\varepsilon_{ij}^{\mathrm{h}} = f_s \widetilde{v_i'' v_j''} \frac{\varepsilon^{\mathrm{h}}}{k} + (1 - f_s) \frac{2}{3} \delta_{ij} \varepsilon^{\mathrm{h}} \quad \text{with} \quad f_s = 1 - \sqrt{A} E^2 \tag{3.57}$$

Note, that this formulation is implicit as the flatness factor E is dependent on the homogeneous turbulent dissipation-rate tensor $\varepsilon_{ij}^{\mathrm{h}}$.

The next term to be modelled is the diffusion term $\overline{\rho} D_{ij}$ (3.23d) of the Reynolds-stress equation. It can be split into three parts: the turbulent transport $\overline{\rho} T_{ij}$, the viscous diffusion $\overline{\rho} D_{ij}^{(\nu)}$ and the pressure diffusion $\overline{\rho} D_{ij}^{(p)}$:

$$\overline{\rho} D_{ij} = \underbrace{-\frac{\partial \overline{\rho} \widetilde{v_i'' v_j'' v_k''}}{\partial x_k}}_{\overline{\rho} T_{ij}} \underbrace{+ \frac{\partial \overline{\tau_{ik}' v_j''}}{\partial x_k} + \frac{\partial \overline{\tau_{jk}' v_i''}}{\partial x_k}}_{\overline{\rho} D_{ij}^{(\nu)}} \underbrace{- \frac{\partial \overline{p' v_i''}}{\partial x_j} - \frac{\partial \overline{p' v_j''}}{\partial x_i}}_{\overline{\rho} D_{ij}^{(p)}} \tag{3.58}$$

The turbulent diffusion is modelled by the generalized gradient diffusion model

$$\overline{\rho} T_{ij} = \frac{\partial}{\partial x_k} \left(D \overline{\rho} \frac{k}{\varepsilon^{\mathrm{h}}} \widetilde{v_k'' v_l''} \frac{\partial \widetilde{v_i'' v_j''}}{\partial x_l} \right) \tag{3.59}$$

with the diffusion coefficient $D = 0.22$. The viscous diffusion is described by

$$\overline{\rho} D_{ij}^{(\nu)} = \frac{\partial}{\partial x_k} \left(\overline{\mu} \frac{\partial \widetilde{v_i'' v_j''}}{\partial x_k} \right) \quad . \tag{3.60}$$

The pressure diffusion term $\overline{\rho} D_{ij}^{(p)}$ is neglected.

The remaining unknown term (3.23e) in the Reynolds-stress equation incorporates the compressibility effects $\overline{\rho} M_{ij}$. The *JHh-v2*-model assumes that this term has minor effects on the numerical solution and, thus, sets it to zero.

Inside porous media, the Darcy and Forchheimer terms have to be added as they are given in the equations (3.25) and (3.28). Also, the additional diffusion given in section 3.6.3 must be considered. Note, that the models (3.29) or (3.30) which define the triple correlations inside the Forchheimer term and contain the dissipation-rate are modified in terms of replacing ε with ε^{h}. The same is valid for the extra diffusion term of equation (3.31).

Having all the terms of the Reynolds-stress equation defined, the closure of the Reynolds-stress equation has to be completed by defining a length scale which is computed by solving the equation of the homogeneous turbulent dissipation-rate ε^{h}. This equation is discussed in detail in the following section.

3.8.2. Definition and modelling of the homogeneous turbulent dissipation-rate equation

The length scale in the *JHh-v2* turbulence model is defined by the transport equation of the homogeneous dissipation-rate ε^{h} as

$$\varepsilon^{\mathrm{h}} = \varepsilon - \frac{1}{2} D_{kk}^{(\nu)} \tag{3.61}$$

in which $D^{(\nu)}$ is the viscous diffusion term defined in equation (3.60). In order to find a transport equation for the homogeneous turbulent dissipation-rate ε^{h} Jakirlić [37] defines the relation

$$\frac{\mathrm{D}\varepsilon^{\mathrm{h}}}{\mathrm{D}t} = \left.\frac{\mathrm{D}\varepsilon}{\mathrm{D}t}\right|_{(\varepsilon=\varepsilon^{\mathrm{h}})} - \frac{1}{2}\frac{\partial}{\partial x_k}\left(\widetilde{\nu}\frac{\partial \varepsilon^{\mathrm{h}}}{\partial x_k}\right)$$

where $\frac{\mathrm{D}}{\mathrm{D}t} = \frac{\partial}{\partial t} + v_k \frac{\partial}{\partial x_k}$ is the total derivative. The expression $\frac{\mathrm{D}\varepsilon}{\mathrm{D}t}|_{(\varepsilon=\varepsilon^{\mathrm{h}})}$ signifies any transport equation for the standard turbulent dissipation-rate ε in which each occurrence of ε is replaced by the homogeneous turbulent dissipation-rate ε^{h}. The final transport equation of the *JHh-v2* model where the terms for porous media have been added then reads

$$\begin{aligned}\frac{\partial \overline{\rho}\varepsilon^{\mathrm{h}}}{\partial t} + \frac{\partial \overline{\rho}\,\widetilde{v_k}\varepsilon^{\mathrm{h}}}{\partial x_k} &= -C_{\varepsilon 1}\overline{\rho}\frac{\varepsilon^{\mathrm{h}}}{k}\widetilde{v_i'' v_j''}\frac{\partial \widetilde{v_i}}{\partial x_j} - C_{\varepsilon 2} f_{\varepsilon}\overline{\rho}\frac{\varepsilon^{\mathrm{h}}\hat{\varepsilon}^{\mathrm{h}}}{k} \\ &+ C_{\varepsilon 3}\overline{\mu}\frac{k}{\varepsilon^{\mathrm{h}}}\widetilde{v_j'' v_k''}\frac{\partial^2 \widetilde{v_i}}{\partial x_j \partial x_l}\frac{\partial^2 \widetilde{v_i}}{\partial x_k \partial x_l} + \frac{\partial}{\partial x_k}\left[\left(\frac{1}{2}\overline{\mu}\delta_{kl} + C_{\varepsilon}\overline{\rho}\frac{k}{\varepsilon^{\mathrm{h}}}\widetilde{v_k'' v_l''}\right)\frac{\partial \varepsilon^{\mathrm{h}}}{\partial x_l}\right] \\ &+ S_l + S_{\varepsilon 4} + \mathcal{P}_{\varepsilon^{\mathrm{h}}}^{(\mathrm{Darcy})} + \mathcal{P}_{\varepsilon^{\mathrm{h}}}^{(\mathrm{Forch})} \quad .\end{aligned} \tag{3.62}$$

The last two terms describe the effect of the porous media and are defined by equations (3.38a) and (3.48) where ε is replaced by ε^{h}. The low-Reynolds damping function f_ε is defined as

$$f_\varepsilon = 1 - \frac{C_{\varepsilon 2} - 1.4}{C_{\varepsilon 2}} e^{\left(-\left[\frac{Re_{\mathrm{t}}}{6}\right]^2\right)}$$

where the turbulence Reynolds number Re_{t} is defined by equation (3.53). The length scale limiter S_l is defined as

$$S_l = \max\left(\left[\frac{1}{C_l^2}\frac{\partial l}{\partial x_k}\frac{\partial l}{\partial x_k} - 1\right]\frac{1}{C_l^2}\frac{\partial l}{\partial x_k}\frac{\partial l}{\partial x_k}; 0\right)\frac{\varepsilon^{\mathrm{h}}\hat{\varepsilon}^{\mathrm{h}}}{k} A$$

with

$$l = \frac{k^{\frac{3}{2}}}{\varepsilon^{\mathrm{h}}}$$

and the flatness factor A of the Reynolds stresses (equation (3.54)).

The pressure-gradient term is

$$S_{\varepsilon 4} = -C^{*}_{\varepsilon 4} \frac{\varepsilon^{\mathrm{h}}}{k} \left(\widetilde{v''_{\mathrm{s}} v''_{\mathrm{s}}} \frac{\partial \widetilde{v_{\mathrm{s}}}}{\partial x_{\mathrm{s}}} + \widetilde{v''_{n1} v''_{n1}} \frac{\partial \widetilde{v_{n1}}}{\partial x_{n1}} + \widetilde{v''_{n2} v''_{n2}} \frac{\partial \widetilde{v_{n2}}}{\partial x_{n2}} \right) \quad .$$

Note, that the term $S_{\varepsilon 4}$ is defined in a streamline-oriented coordinate system which consitutes that the coordinate x_{s} points in the direction of the velocity vector and x_{n1} and x_{n2} are both normal to the velocity vector and normal to each other.

With all the models in the equation of the homogeneous dissipation-rate given, it remains to provide the values for the modelling coefficients. The *JHh-v2* model sets them to

$$C_{\varepsilon 1} = 1.44 \ , \ C_{\varepsilon 2} = 1.85 \ , \ C_{\varepsilon 3} = 0.70 \ , \ C^{*}_{\varepsilon 4} = 0.58 \ , \ C_{\varepsilon} = 0.18 \ , \ C_{l} = 2.5 \quad .$$

Finally, the isotropic part $\hat{\varepsilon}^{\mathrm{h}}$ of the dissipation-rate and its value at viscous walls are defined ([37]):

$$\hat{\varepsilon}^{\mathrm{h}} = \varepsilon^{\mathrm{h}} - \widetilde{\nu} \left(\frac{\partial k^{\frac{1}{2}}}{\partial x_n} \right)^2 \qquad \varepsilon^{\mathrm{h}}\big|_{x_n=0} = \widetilde{\nu} \left(\left. \frac{\partial k^{\frac{1}{2}}}{\partial x_n} \right|_{x_n=0} \right)^2 \tag{3.63}$$

in which x_n is the coordinate direction normal to the wall. These two definitions show that the homogeneous turbulent dissipation-rate ε^{h} is not zero at walls whereas its isotropic part $\hat{\varepsilon}^{\mathrm{h}}$ actually is zero.

3.9. Decay of turbulence in a porous channel: an example

The previous sections define a closed set of equations for turbulent flow inside porous media. In short, the effect of the porous media on turbulence can be described as a sink term. A qualitative example of a channel flow with a porous bump is shown in figure 3.4. It clearly shows how the turbulent kinetic energy k decays inside the porous region.

3.10. Wall distance over porous surfaces

Recall, that the *JHh-v2* turbulence model (section 3.8) requires the distance d of each grid point to its closest wall (equation (3.52)). Now consider the sketch 3.5 with a point in space over a nonporous-porous interface area. For very dense porous media, the interface will behave like a viscous wall. In such cases, the distance to the

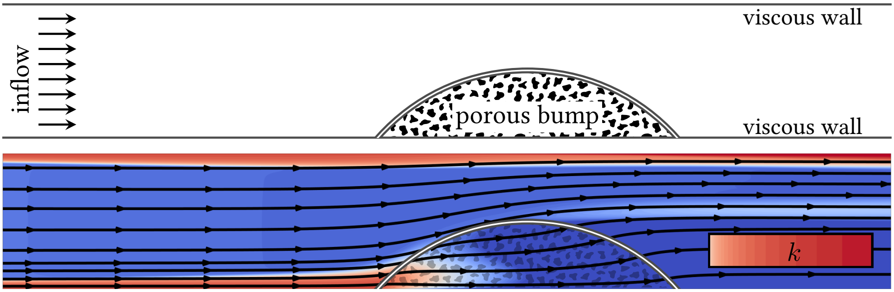

Figure 3.4.: Example for decay of turbulent kinetic energy k inside a porous bump in a turbulent channel flow.

closest solid wall must be replaced by the distance to the interface. In other cases in which the permeability is larger, the interface still affects the flow close by but not as strongly as a viscous wall would do. Consequently, an effective distance d_{eff} over the nonporous-porous interface is computed which is dependent on the properties of the porous medium. In the process, the distance d_{eff} is compared against the distance to the closest viscous wall where the shortest distance is finally passed to the turbulence models. Note, that the distance to the porous medium is only considered if the point in space is positioned inside a nonporous region. Alternatively, if the interface area connects two different kinds of porous media the distance to the interface is only considered if the point is positioned inside the more permeable region.

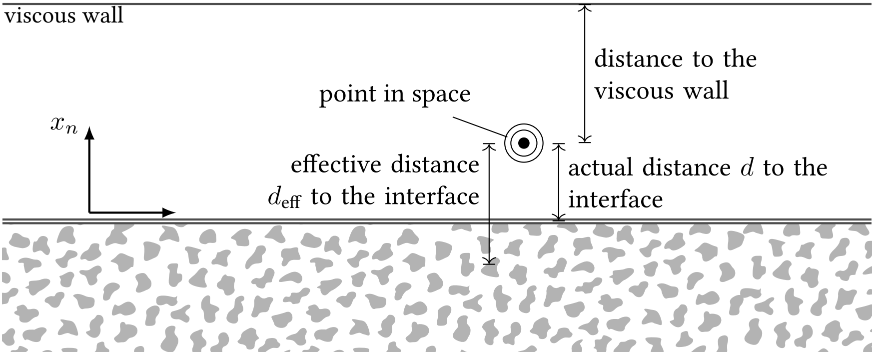

Figure 3.5.: Sketch of wall distance of a point in space over a porous interface.

The computation of the effective wall distance is discussed in [49] and has been reproduced in the following sections. In short, the actual distance d over the nonporous-porous interface is modified by the relation

$$d_{\text{eff}} = d + c_{\text{wd}}\sqrt{\frac{\kappa}{\phi}} \tag{3.64}$$

with the modelling coefficient c_{wd} which has to be calibrated. For very low permeabilities κ, this relation recovers to $d_{\text{eff}} = d$ and the interface will behave like a solid wall.

The derivation of relation (3.64) is based on the observation that for flows tangential to the nonporous-porous interface there is a quick decay of the velocity inside the porous region. It is assumed that the distance along which the velocity drops to very small values can be used as a characteristic length. This length is then added to actual distance to the interface. The theoretical derivation of the characteristic length scale is based a one-dimensional laminar shear flow in which only the Darcy term is active (see figure 3.6). For these kinds of flows the volume-averaged momentum equation (2.29b) reduces to

$$-\mu\frac{\partial^2 v_x}{\partial x_n^2} + \phi\frac{\mu}{\kappa}v_x = 0 \tag{3.65}$$

which can be solved analytically. The solution reads

$$v_x = v_{\text{interface}} \cdot e^{\sqrt{\frac{\phi}{\kappa}}x_n} \quad . \tag{3.66}$$

This implies that the velocity at the interface drops by the factor of e^1 within a distance of $\sqrt{\frac{\kappa}{\phi}}$. This distance scaled with the modelling coefficient c_{wd} leads to equation (3.64), presented at the beginning of the section.

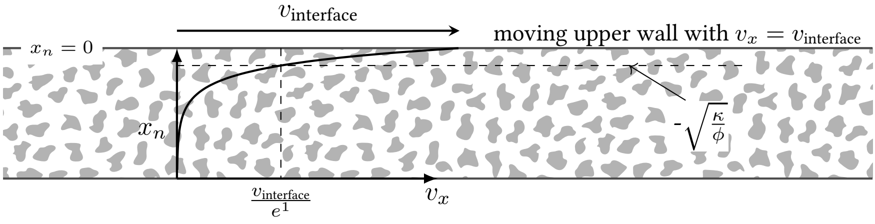

Figure 3.6.: Sketch of shear flow in a porous medium in order to determine the effective wall distance d_{eff} over a porous interface.

The principal effect of the wall distance modification is shown in figure 3.7. Compared to the very high coefficient c_{wd} which simulates a wall very far away, a small value of c_{wd} leads to a strong decrease of the Reynolds stress of the velocity fluctuations normal to the interface $\widetilde{v_y''v_y''}$, while the Reynolds stress of the velocity fluctuations parallel to the interfaces $\widetilde{v_x''v_x''}$ increases.

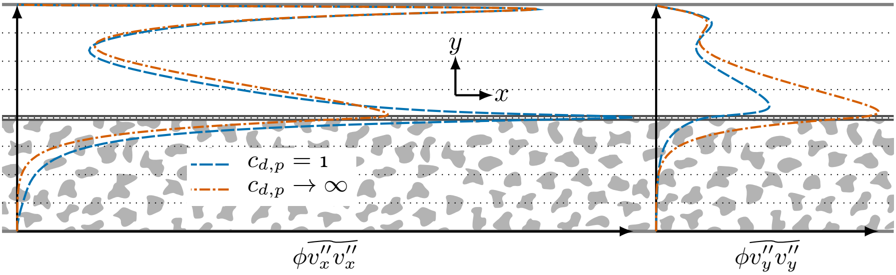

Figure 3.7.: Effect of the wall distance modification parameter c_{wd}.

3.11. Interface treatment in case of turbulent flow

In case of laminar flow, section 2.8 demonstrates how to handle the interface between nonporous and porous regions or, respectively, the interface between two porous regions with different properties. For turbulent flow, these conditions have to be extended to include the turbulence quantities. Besides that, an adaption for the existing conditions of the mean-flow equations must be considered. The strategy is as follows:

1. Review and transfer the laminar interface conditions for turbulent flow. In the course of this, the principles of isentropic flow change and flux conservation will be fulfilled.
2. Define the relations for the turbulent quantities at the interface while making sure that they stay compatible to the conditions of the mean-flow equations.

3.11.1. Interface conditions of flow variables for turbulent flow

For laminar flow, the interface treatment of the mean-flow equations is based on the principles of flux conservation, isentropic flow change and constant velocity direction. Flux conservation is achieved by collecting all the convective fluxes of the transport equations (2.29) and setting them equal on both interface sides. Thereby, the pressure forces which act on the porous structure at the interface are included. If the same procedure is performed for the mean-flow equations for turbulent flow (3.7) the interface conditions will stay unchanged except the condition for energy conservation where the turbulent kinetic energy $k = \frac{1}{2}\widetilde{v_k'' v_k''}$ appears. The result reads

$$\phi_1 \overline{\rho_1}\, \widetilde{v_{n,1}} = \phi_2 \overline{\rho_2}\, \widetilde{v_{n,2}} \tag{3.67a}$$

$$\phi_1 \left(\overline{\rho_1}\, \widetilde{v_{n,1}}^2 + \overline{p_1} \right) - \phi_2 \left(\overline{\rho_2}\, \widetilde{v_{n,2}}^2 + \overline{p_2} \right) = \sigma_n \tag{3.67b}$$

$$\phi_1 \left(\overline{\rho_1}\, \widetilde{v_{n,1}}\, \widetilde{v_{t,1}} \right) - \phi_2 \left(\overline{\rho_2}\, \widetilde{v_{n,2}}\, \widetilde{v_{t,2}} \right) = \sigma_t \tag{3.67c}$$

$$\frac{|\widetilde{v_1}|^2}{2} + k_1 + \widetilde{e_1} + \frac{\overline{p_1}}{\overline{\rho_1}} = \frac{|\widetilde{v_2}|^2}{2} + k_2 + \widetilde{e_2} + \frac{\overline{p_2}}{\overline{\rho_2}} \ . \tag{3.67d}$$

In agreement with the laminar conditions, the remaining unknowns are defined by the isentropic condition

$$\frac{\overline{p_1}}{\overline{\rho_1}^{\gamma}} = \frac{\overline{p_2}}{\overline{\rho_2}^{\gamma}} \ , \tag{3.68}$$

by following the assumption that the flow direction is equal on both sides of the interface

$$\frac{\widetilde{v_{n,1}}}{|\widetilde{\vec{v}_1}|} = \frac{\widetilde{v_{n,2}}}{|\widetilde{\vec{v}_2}|} \qquad \text{or} \qquad \frac{\widetilde{v_{t,1}}}{|\widetilde{\vec{v}_1}|} = \frac{\widetilde{v_{t,2}}}{|\widetilde{\vec{v}_2}|} \ , \tag{3.69}$$

and that the internal energy $\widetilde{e}$ is related to the state variables $\overline{\rho}$ and $\overline{p}$ of the fluid by

$$\widetilde{e} = \frac{1}{\gamma - 1} \frac{\overline{p}}{\overline{\rho}} \tag{3.70}$$

which is only valid for a calorically perfect gas. The now missing condition is a relation between the turbulent energies k_1 and k_2 across the two sides of the interface. From the Reynolds-stress equations (3.22) which are similar to the equation of the turbulent kinetic energy k, it becomes apparent that several source and sink terms exist. Their existence indicates that the conservation of convective fluxes over the interface is not strictly required. This implies freedom to define the relation

$$\phi_1 \overline{\rho_1} \left(\widetilde{v_i'' v_j''} \right)_1 = \phi_2 \overline{\rho_2} \left(\widetilde{v_i'' v_j''} \right)_2 \qquad \text{or} \qquad \phi_1 \overline{\rho_1} k_1 = \phi_2 \overline{\rho_2} k_2 \ . \tag{3.71}$$

Even though there is no direct physical explanation and not enough validation data to confirm this relation, there are reasons which support this condition. First of all, literature gives conditions for incompressible flow which match with the condition (3.71) as can be seen in [70, 71, 45]. Secondly, equation (3.71) is a strict requirement if the interface condition of diffusive momentum fluxes (2.59) should be valid without modification for turbulent flow. Why is that? The interface condition of diffusive momentum fluxes results from collecting all diffusive fluxes of momentum on both sides and manually prescribing an offset (also called jump) between these two fluxes. However, during the derivation of the laminar jump condition (2.59) the Reynolds stresses have not been considered. Since they also have a diffusive effect the jump condition can be true only if the momentum flux due to Reynolds stresses is included in the derivation of the jump condition or, alternatively, if the momentum flux due to Reynolds stresses is constant over the interface. The second option leads to relation (3.71).

Equations (3.67)- (3.71) generate a closed set of equations which can be solved by an iterative procedure. An interface condition for the length scale variable is still missing which is set similar to the interface relationship of Reynolds stresses (3.71):

$$\phi_1 \overline{\rho_1} \varepsilon_1 = \phi_2 \overline{\rho_2} \varepsilon_2 \qquad \text{or} \qquad \phi_1 \overline{\rho_1} \varepsilon_1^{\mathrm{h}} = \phi_2 \overline{\rho_2} \varepsilon_2^{\mathrm{h}} \ . \tag{3.72}$$

The complete system of equations is solved corresponding to the equations for laminar flow as given in section 2.8.1. However, the function (2.44) is now slightly different:

$$\mathrm{a} \cdot (\overline{p_2})^{\mathrm{b}} + \mathrm{c} \cdot (\overline{p_2})^{\mathrm{d}} + \mathrm{e} \cdot (\overline{p_2})^{\mathrm{f}} + \mathrm{g} = 0 \tag{3.73}$$

with

$$\mathrm{a} = \frac{\gamma}{\gamma - 1} \frac{(\overline{p_1})^{\frac{1}{\gamma}}}{\overline{\rho_1}}; \quad \mathrm{b} = 1 - \frac{1}{\gamma}; \quad \mathrm{c} = \frac{1}{2} \left(|\widetilde{\vec{v}_1}| (\overline{p_1})^{\frac{1}{\gamma}} \frac{\phi_1}{\phi_2} \right)^2 ; \quad \mathrm{d} = -\frac{2}{\gamma}$$

$$\mathrm{e} = k_1 (\overline{p_1})^{\frac{1}{\gamma}} \frac{\phi_1}{\phi_2}; \quad \mathrm{f} = -\frac{1}{\gamma}; \quad \mathrm{g} = -\frac{\gamma}{\gamma - 1} \frac{\overline{p_1}}{\overline{\rho_1}} - \frac{|\widetilde{\vec{v}_1}|^2}{2} - k_1$$

An illustration of the jump of turbulent quantities at the nonporous-porous interface of a channel with viscous walls and a porous blockage is shown in figure 3.8.

3.11.2. Interface conditions for the gradients in turbulent flow

The turbulent Navier-Stokes equations (3.7) and the turbulent transport equations (3.22) and (3.37) contain several terms with various gradients which must be defined over the porous interface. For laminar flow, section 2.8.2 discussed that while the gradients in tangential direction of the interface are already defined by computing the change of flow variables over the interface, the gradients in normal direction need to be explicitly defined. For turbulent flow, the gradients in question are

$$\frac{\partial \widetilde{v_i}}{\partial x_n} \ ; \quad \frac{\partial \widetilde{T}}{\partial x_n} \ ; \quad \frac{\partial \widetilde{v_i'' v_j''}}{\partial x_n} \ ; \quad \frac{\partial \varepsilon}{\partial x_n}$$

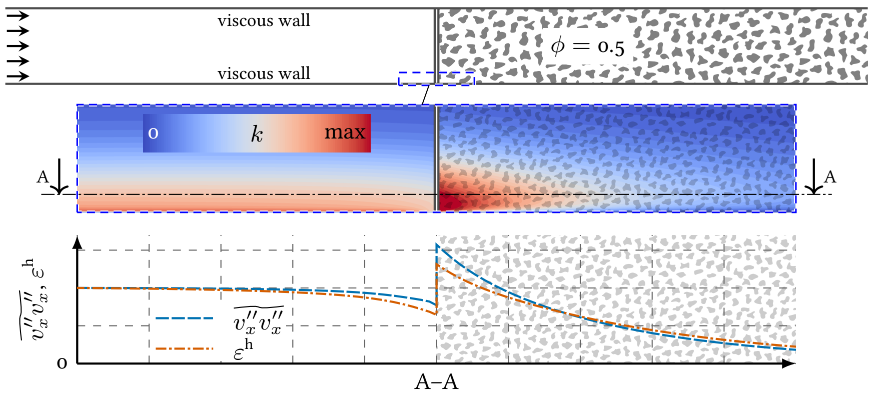

Figure 3.8.: Example of jump in turbulent quantities at a nonporous-porous interface.

where in case of the *JHh-v2* turbulence model the turbulent dissipation-rate ε is replaced by its homogeneous part ε^{h}.

Equation (3.71) from section 3.11.1 already necessitates that the momentum fluxes due to the Reynolds stresses are constant across the interface. Hence, these fluxes do not need reconsideration for the interface condition of diffusive momentum fluxes and the jump condition for the velocity gradients can be adopted from the laminar conditions (2.59):

$$\overline{\mu_1}\frac{\partial \widetilde{v_i}}{\partial x_n}\bigg|_1 + \overline{\mu_2}\frac{\partial \widetilde{v_i}}{\partial x_n}\bigg|_2 = -(1-\phi_2)\Delta g_{i,2} - (1-\phi_1)\Delta g_{i,1} \tag{3.74}$$

with

$$\Delta g_{i,1/2} = \beta_{1/2} \cdot \frac{\phi_{1/2}\overline{\mu_{1/2}}}{\sqrt{\kappa_{1/2}}}\widetilde{v_{i,1/2}} \tag{3.75}$$

where β is the jump coefficient of the porous material and the numbers 1 and 2 are the different sides of the nonporous-porous interface.

A relation for the temperature gradients on the two interface sides for laminar flow is given in (2.61). It assumes that in addition to the convective energy fluxes, the rest of the fluxes are also constant. In case of turbulent flow this includes several more fluxes leading to the relation

$$\begin{aligned} &-\phi_1 \cdot \left(\left[\widetilde{v_{j,1}}\, \overline{\tau_{ij,1}} - \widetilde{v_{j,1}} (\widetilde{v_i'' v_j''})_1 + (\overline{v_i'' \tau_{ij}'})_1 - \frac{1}{2} (\widetilde{v_i'' v_j'' v_j''})_1 \right] n_{1,i} + \lambda_{\text{eff}} \frac{\partial \widetilde{T}}{\partial x_n}\bigg|_1 \right) \\ &= \phi_2 \cdot \left(\left[\widetilde{v_{j,2}}\, \overline{\tau_{ij,2}} - \widetilde{v_{j,2}} (\widetilde{v_i'' v_j''})_2 + (\overline{v_i'' \tau_{ij}'})_2 - \frac{1}{2} (\widetilde{v_i'' v_j'' v_j''})_2 \right] n_{i,2} + \lambda_{\text{eff}} \frac{\partial \widetilde{T}}{\partial x_n}\bigg|_2 \right) \end{aligned} \tag{3.76}$$

with the models for the correlations $\overline{u_i'' \tau_{ij}'}$ and $\widetilde{v_i'' v_j'' v_j''}$ being discussed in section 3.5.

For the relation of the Reynolds-stress gradients $\frac{\partial \widetilde{v_i'' v_j''}}{\partial x_n}$, a similar relation as for the velocity gradients (equation (3.74)) is proposed:

$$\overline{\mu_1} \frac{\partial \widetilde{v_i'' v_j''}}{\partial x_n}\bigg|_1 + \overline{\mu_2} \frac{\partial \widetilde{v_i'' v_j''}}{\partial x_n}\bigg|_2 = -(1-\phi_2)\Delta g_{\text{RS}ij,2} - (1-\phi_1)\Delta g_{\text{RS}ij,1} \tag{3.77}$$

However, some discussion on the definition of the jump function Δg_{RS} is needed.

Literature provides some conditions regarding the kinetic turbulent energy k. In the following paragraphs, these conditions are written in terms of the Reynolds stresses $\widetilde{v_i'' v_j''}$. A widely applied condition in literature [70, 13, 71] reads

$$\left(\overline{\mu_1} + \frac{\mu_{\text{t},1}}{\sigma_{\text{t}}}\right) \frac{\partial \widetilde{v_i'' v_j''}}{\partial x_n}\bigg|_1 + \left(\overline{\mu_2} + \frac{\mu_{\text{t},1}}{\sigma_{\text{t}}}\right) \frac{\partial \widetilde{v_i'' v_j''}}{\partial x_n}\bigg|_2 = 0 \ , \tag{3.78}$$

with μ_{t} being the eddy viscosity according to equation (3.18) and σ_{t} being the turbulent Prandtl number. The right hand side is assumed to be zero. A modification in which the right hand side is nonzero is proposed by Silva and de Lemos [70] and then applied by de Lemos and Silva in [45]:

$$\begin{aligned} &\left(\overline{\mu_1} + \frac{\mu_{\text{t},1}}{\sigma_{\text{t}}}\right) \frac{\partial \widetilde{v_i'' v_j''}}{\partial x_n}\bigg|_1 + \left(\overline{\mu_2} + \frac{\mu_{\text{t},1}}{\sigma_{\text{t}}}\right) \frac{\partial \widetilde{v_i'' v_j''}}{\partial x_n}\bigg|_2 \\ &\qquad = -\left(\overline{\mu} + \mu_{\text{t}}\right) \frac{\beta_{\text{t}}}{\sqrt{\kappa}} \widetilde{v_i'' v_j''} \end{aligned} \tag{3.79}$$

for the turbulent jump coefficient β_{t}. The values of the variables on the right hand side are taken from the nonporous region. Furthermore, Chandesris and Jamet [15] used these conditions but argue that the right hand side of the equation should be linked to production and dissipation of turbulence. However, they do not investigate this proposal any further. Rather, in their computations they set the right hand side to zero resulting in condition (3.78).

At this point a short discussion about the right hand side of the interface jump condition (3.77) is given. Note, that the right hand side of this jump condition can be viewed as a source or sink term. This is, because it directly controls the difference of fluxes which feed into one side of the interface and add up on the other side. The arising task is to define a model which can sufficiently describe this source term. Still assuming the right hand side as a source or sink term, the affected volume can be viewed as a very narrow band around the interface surface. The thickness of the band is estimated to be $\sqrt{\kappa}$ (see figure 3.9) which is used as a characteristic length of the pore geometry. Note, that this point of view reveals that the right hand side of equation (3.79) collapses with the form of the Darcy term $2\phi\frac{\mu}{\kappa}\widetilde{v_i''v_j''}$ multiplied with the "interface thickness" $\sqrt{\kappa}$. Consequently, one would expect that equation (3.79) has a damping effect on the Reynolds stresses, especially if the discussion in section 2.8.2 is considered. There, it is argued that the surface of porous medium leads to a locally increased damping for momentum. However, DNS-data speak against a damping effect of Reynolds stresses close to the nonporous-porous interface. Figure 3.10 shows qualitative DNS-results extracted from the work of Breugem [10] who performed computations with a setup similar to the one given in figure 2.18. The results of Breugem immediately show that the Reynolds stresses are heavily amplified over the nonporous-porous interface compared to the values on the upper wall. This indicates that the dominating effect of the nonporous-porous interface is not the Darcy term as proposed by equation (3.79) but rather the production term (3.23a) of the Reynolds-stress equations. Accordingly, the function $\Delta g_{\mathrm{RS}ij}$ in equation (3.77) is proposed to be

$$\Delta g_{\mathrm{RS}ij} = \sqrt{\kappa}\beta_{\mathrm{t}}\bar{\rho}P_{ij} \tag{3.80}$$

in which P_{ij} is the turbulent production term according to (3.23a). The effect of the function Δg_{RS} on the Reynolds stresses is illustrated in figure 3.11 by showing results while varying the turbulent jump coefficient β_{t}.

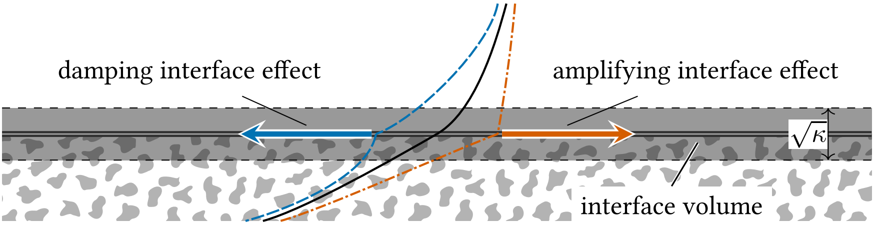

Figure 3.9.: Sketch of possible interface effects onto Reynolds-stress profiles.

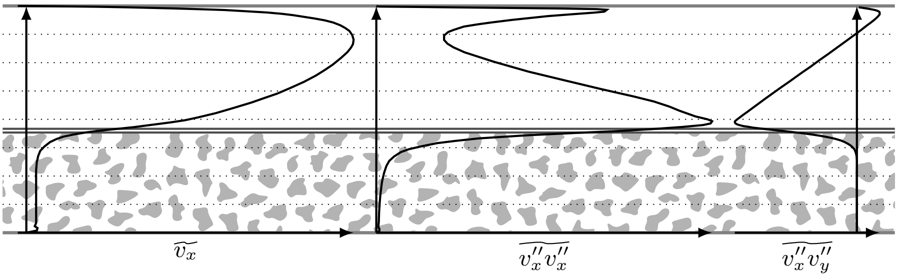

Figure 3.10.: Qualitative DNS-data of velocity and Reynolds stresses of a partially turbulent channel [10].

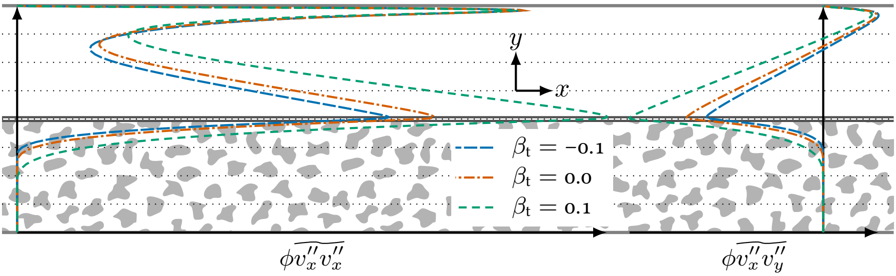

Figure 3.11.: Effect of the turbulent jump coefficient β_t on the Reynolds stresses $\widetilde{v''_x v''_x}$ and $\widetilde{v''_x v''_y}$.

The relation of the gradient of the dissipation rate ε or, respectively its homogeneous part ε^{h} is proposed similar to the relation of Reynolds stresses (3.77):

$$\overline{\mu_1}\frac{\partial \varepsilon}{\partial x_n}\bigg|_1 + \overline{\mu_2}\frac{\partial \varepsilon}{\partial x_n}\bigg|_2 = -(1-\phi_2)\Delta g_{\varepsilon,2} - (1-\phi_1)\Delta g_{\varepsilon,1} \tag{3.81}$$

For the jump function Δg_ε, there are no such DNS-data available as for the Reynolds stresses. Due to lacking more information the function is not modelled and, thus, set to zero:

$$\Delta g_\varepsilon = 0 \tag{3.82}$$

3.12. Computation of integral forces in case of turbulent flow

Recall Paul of section 2.9 where he calculated the drag of a snowball with a core of ice. What happened is shown in figure 3.12. The aerodynamic drag was predicted too high which led to a total overshoot (which was in favour of the target). Paul identified the problem that he only considered laminar flow. He recalculated the flow field around the snowball with a state-of-the-art Reynolds-stress model. Now, he needs slightly adapted equations in order to calculate the drag.

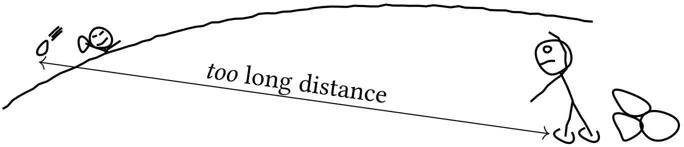

Figure 3.12.: Snowball trajectory after throwing with an overestimated drag.

The adapted forces for turbulent flow in a fixed volume V are

$$\begin{aligned} F_{V,\mathrm{por}} = \int\limits_{V_\mathrm{f}} \phi\frac{\overline{\mu}}{\kappa}\widetilde{v_i} + \phi^2\frac{c_\mathrm{F}}{\sqrt{\kappa}}\overline{\rho}\Bigg[&\widetilde{v_i}|\widetilde{\vec{v}}| + \frac{1}{2}\frac{\widetilde{v_i}}{|\widetilde{\vec{v}}|}\overline{v_k''v_k''} \\ &+ \frac{\widetilde{v_k}}{|\widetilde{\vec{v}}|}\overline{v_i''v_k''} - \frac{1}{2}\frac{\widetilde{v_i}\,\widetilde{v_k}\,\widetilde{v_l}}{|\widetilde{\vec{v}}|^3}\overline{v_k''v_l''}\Bigg]\,\mathrm{d}V \quad . \end{aligned} \tag{3.83}$$

One should note, that the integrals are only over the fluid volume V_f and not over the entire volume V which includes the porous structure.

Compared to the laminar relations, the inviscid forces on the nonporous-porous interface are unchanged:

$$F_{A,\mathrm{int},i} = \int\limits_{A_\mathrm{int}} \phi_1 \left(\overline{\rho_1}\,\widetilde{v_{\mathrm{n},1}}\,\widetilde{v_{i,1}} + n_i\overline{p_1}\right) - \phi_2 \left(\overline{\rho_2}\,\widetilde{v_{\mathrm{n},2}}\,\widetilde{v_{i,2}} + n_i\overline{p_2}\right) \mathrm{d}A \tag{3.84}$$

The same is valid for the viscous forces:

$$F_{A,\mathrm{int,visc},i} = \int\limits_{A_\mathrm{int}} n_j \left(\phi_2\overline{\tau_{ij,2}} - \phi_1\overline{\tau_{ij,1}}\right) \mathrm{d}A \tag{3.85}$$

Theoretically, the forces on the interface which occur as a result of Reynolds stresses would have to be considered:

$$F_{A,\mathrm{int,turb},i} = \int\limits_{A_\mathrm{int}} \phi_1\overline{\rho_1}n_j\widetilde{v_i''v_j''}|_1 - \phi_2\overline{\rho_2}\widetilde{v_i''v_j''}|_2 \,\mathrm{d}A = 0 \tag{3.86}$$

However, since the forces are zero per definition (see equation (3.71)) the equation can be ignored.

Finally the adapted formula for viscous walls in porous regions is needed. It reads

$$F_{A,\mathrm{wall},i} = \int\limits_{A_\mathrm{wall}} \big[\phi \left(n_j\overline{\tau_{ij}} - n_i\overline{p}\right) \mathrm{d}A \ \ . \tag{3.87}$$

4. Implementation of Theoretical Equations into a Flow Solver

The theoretical models for computing flow around bodies with porous surfaces have been described in the previous chapters. The present chapter presents the implementation of these derivations into a finite-volume flow solver. The procedure is explained for the flow solver DLR-TAU-Code [68] which is a well-established unstructured finite-volume code developed at the DLR (Deutsches Zentrum für Luft- und Raumfahrt), Germany.

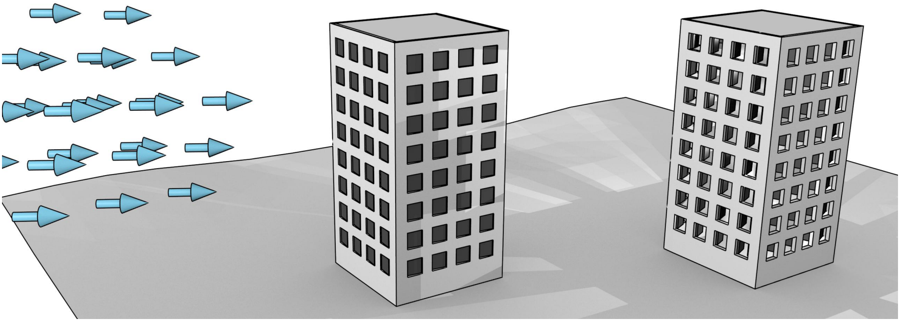

Figure 4.1.: Model of a skyscraper with closed and open windows under aerodynamic load.

For a figurative description of the implementation, consider the case of a skyscraper with closed windows exposed to aerodynamic loads (see figure 4.1). Now assume that all windows and doors of the skyscraper are open, so that the air can pass through the building. How will the aerodynamic loads change compared to the case of the closed windows? The case of closed windows can be solved with a standard flow solver, however the case of open windows is suitable for the new flow solver with porous flow capabilities. Thereby, the rooms of the building represent the pores which are connected by the open doors and windows. Assuming, that the porous properties (like permeability κ and Forchheimer coefficient c_F) of the "porous building" are known, the flow can be solved without any knowledge of the exact room structure.

In contrast to the mesh for the skyscraper with closed windows (figure 4.2 to the left), the case of open windows requires additional grid cells in place of the building (figure 4.2 to the right). Thereby, the outer grid cells of the porous region must match with the nonporous region.

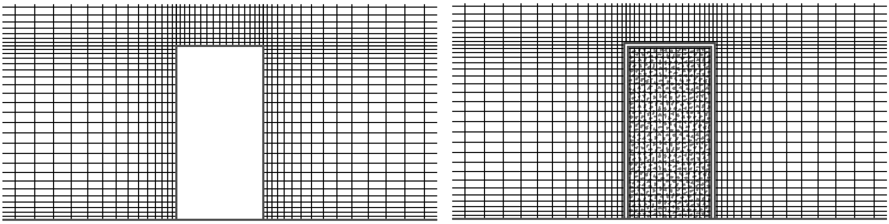

Figure 4.2.: Mesh for a skyscraper with closed windows (nonporous case) and with open windows (porous case).

The tasks of the solver can be split into two major parts (see also figure 4.3):

- Add the effect of the porous medium inside a grid cell to the flux balance.
- Compute the flux over the interface between the porous and nonporous regions.

These two issues will be discussed separately in the following sections. Besides, minor changes have to be carried out: Additional diffusion fluxes have to be added to the Reynolds-stress balances according to section 3.6.3. Finally, when wall distances are required by the turbulence model, the distances over the porous interface must be considered according to section 3.10.

4.1. Implementation of Darcy and Forchheimer term into the flow solver

Let the residual of each grid cell be defined as the fluxes through the cell faces plus the source and the sink terms which act inside the given cell volume. Then, in the porous regions, the contributions from the Darcy and Forchheimer terms have to be added as additional source/sink terms to the residuals of the momentum and the turbulence equations as given in sections 3.4, 3.6.1, 3.6.2 and 3.7. In case of the implicit scheme for time stepping as it is used in TAU [24], the flux Jacobians have to be modified by a contribution of the additional source/sink terms in porous media. Also, when switching to an explicit Runge-Kutta time stepping scheme, the time

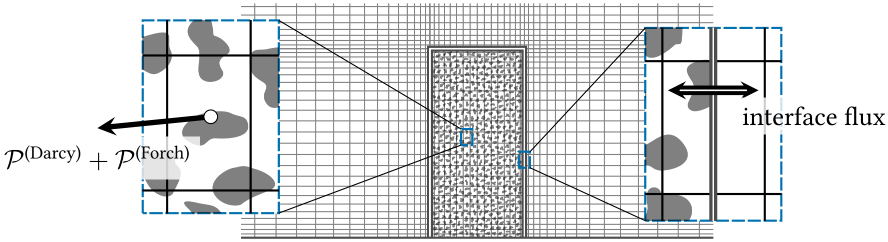

Figure 4.3.: Illustration of the two main tasks of the implementation for the porous-flow solver. In one task, the effect of the porous medium inside a grid cell is added to the flux balance. In the other, the fluxes over the interface between the porous and the nonporous regions are computed.

step is modified on the basis of the Jacobians of the additional terms. The Jacobians are calculated with the assumption that the flux variables are only dependent on themselves while all the other variables and coefficient are independent of the flux variable. In this procedure, the density is also set constant such that the velocity can be multiplied with the density in order to obtain the momentum as flux variable. With the given assumptions, the contributions of the additional terms in porous regions to the important flux Jacobians are as follows: The contribution of the Darcy term to the Jacobian of the momentum equation is:

$$\frac{\partial}{\partial \overline{\rho}\widetilde{v_i}}\left(\phi\frac{\overline{\mu}}{\kappa}\widetilde{v_i}\right) = \frac{\phi}{\overline{\rho}}\frac{\overline{\mu}}{\kappa} \tag{4.1}$$

The contribution of the Forchheimer term (3.15) to the Jacobian is simplified by temporarily replacing each velocity component with the length of the velocity vector. The result is, that only the first term of the Forchheimer term containing the velocity as a variable contributes to the Jacobian. The Forchheimer Jacobian of the momentum equation therefore reads

$$\frac{\partial}{\partial \overline{\rho}|\widetilde{\vec{v}}|}\left(\mathrm{sign}\,(v_i)\phi^2\frac{c_{\mathrm{F}}}{\sqrt{\kappa}}\overline{\rho}|\widetilde{\vec{v}}|^2\right) = 2\cdot\mathrm{sign}\,(v_i)\phi^2\frac{c_{\mathrm{F}}}{\sqrt{\kappa}}|\widetilde{\vec{v}}| \tag{4.2}$$

where sign (v_i) is -1 if v_i is less than zero and 1 if v_i is bigger than zero.

The porous-medium contributions to the Jacobian of the Reynolds stresses are

$$\frac{\partial}{\partial \overline{\rho}\widetilde{v_i''v_j''}}\left(2\phi\frac{\overline{\mu}}{\kappa}\widetilde{v_i''v_j''}\right) = 2\frac{\phi}{\overline{\rho}}\frac{\overline{\mu}}{\kappa} \tag{4.3}$$

for the Darcy term (3.25) and

$$\frac{\partial \mathcal{P}_{ij}^{\text{(Forch)}}}{\partial \overline{\rho}\widetilde{v_i''v_j''}} = \phi^2 \frac{c_{\mathrm{F}}}{\sqrt{\kappa}} \left(2|\widetilde{\vec{v}}| + 2\frac{\widetilde{v_i}\widetilde{v_j}}{|\widetilde{\vec{v}}|} + 2\frac{\widetilde{v_k}}{|\widetilde{\vec{v}}|} \frac{\partial \overline{v_i''v_j''v_k''}}{\partial \widetilde{v_i''v_j''}} + \frac{1}{2}\frac{\widetilde{v_j}}{|\widetilde{\vec{v}}|} \frac{\partial \overline{v_j''v_k''v_k''}}{\partial \widetilde{v_i''v_j''}} \right. \\ + \frac{1}{2}\frac{\widetilde{v_i}}{|\widetilde{\vec{v}}|} \frac{\partial \overline{v_i''v_k''v_k''}}{\partial \widetilde{v_i''v_j''}} - \frac{1}{2}\frac{\widetilde{v_j}\,\widetilde{v_k}\,\widetilde{v_m}}{|\widetilde{\vec{v}}|^3} \frac{\partial \overline{v_i''v_k''v_m''}}{\partial \widetilde{v_i''v_j''}} \\ \left. - \frac{1}{2}\frac{\widetilde{v_i}\,\widetilde{v_k}\,\widetilde{v_m}}{|\widetilde{\vec{v}}|^3} \frac{\partial \overline{v_j''v_k''v_m''}}{\partial \widetilde{v_i''v_j''}} \right) \tag{4.4}$$

for the Forchheimer term, where the derivatives $\frac{\partial \overline{v_l''v_m''v_n''}}{\partial \widetilde{v_i''v_j''}}$ are given by

$$\frac{\partial \overline{v_l''v_m''v_n''}}{\partial \widetilde{v_i''v_j''}} = \frac{c_t}{\varepsilon} \cdot \left[\underbrace{\frac{1}{2} \left(\widetilde{v_l''v_k''} \frac{\partial \widetilde{v_m''v_n''}}{\partial x_k} + \widetilde{v_m''v_k''} \frac{\partial \widetilde{v_n''v_l''}}{\partial x_k} + \widetilde{v_n''v_k''} \frac{\partial \widetilde{v_l''v_m''}}{\partial x_k} \right)}_{\text{if } i=j} \right. \\ \left. + k \cdot \left(\underbrace{\frac{\partial \widetilde{v_m''v_n''}}{\partial x_k}}_{\substack{\text{if} \\ l=i\wedge k=j \\ l=j\wedge k=i}} + \underbrace{\frac{\partial \widetilde{v_l''v_n''}}{\partial x_k}}_{\substack{\text{if} \\ m=i\wedge k=j \\ m=j\wedge k=i}} + \underbrace{\frac{\partial \widetilde{v_l''v_m''}}{\partial x_k}}_{\substack{\text{if} \\ n=i\wedge k=j \\ n=j\wedge k=i}} \right) \right] \tag{4.5}$$

if the model by Hanjalić and Launder [31] is used for computing the triple correlations (3.30). See appendix A.2 for the details of the derivation.

Finally, a contribution to the Jacobian of the turbulent dissipation-rate ε is needed. It is

$$\frac{\partial \mathcal{P}_{\varepsilon}^{\text{(Darcy)}}}{\partial \varepsilon} + \frac{\partial \mathcal{P}_{\varepsilon}^{\text{(Forch)}}}{\partial \varepsilon} = 2\phi\frac{\mu}{\kappa} + \phi^2 \frac{c_{\mathrm{F}}}{\sqrt{\kappa}} \left[\frac{8}{3}|\widetilde{\vec{v}}| + \frac{\widetilde{v_k}}{|\widetilde{\vec{v}}|} c_{\varepsilon,\mathrm{F}} \frac{k}{\varepsilon^2} \widetilde{v_k''v_i''} \frac{\partial \varepsilon}{\partial x_i} \right] \tag{4.6}$$

in which $\mathcal{P}_{\varepsilon}^{\text{(Darcy)}}$ and $\mathcal{P}_{\varepsilon}^{\text{(Forch)}}$ are taken from equations (3.38a) and (3.48).

4.2. Flux computation across nonporous-porous interface area

The flux computations across the interface are accomplished by a central scheme. However, a direct application of this scheme to the adjoining cells on the porous and the nonporous interface sides is not possible because the interface acts as sink or source for several fluxes. Thus, the flux computation is split into two parts, computing the flux into the porous region and computing the flux into the nonporous region separately. For each flux computation a ghost cell is introduced as illustrated in figure 4.4. The procedure for computing the flux into the porous region is as follows:

1. Transform the flow state of the nonporous cell into a porous ghost cell by using the interface conditions described in section 3.11.
2. Compute the flux into the cell of the porous region by applying a central scheme between the porous ghost cell and the cell of the porous region.

The same procedure is processed for computing the flux into the nonporous cell. However, the following difficulties are observed:

- The just described scheme does not strictly provide conservation of fluxes over the interface. However, this would be favourable especially to ensure mass and energy conservation. Thus, an extension of the given scheme is presented which restores the flux conservation.
- Computation of artificial dissipation fluxes over the interface is needed to stabilize the central scheme.
- Meshes with low resolutions would quickly lead to a wrong behaviour of the turbulent dissipation-rate ε. This is counteracted by a correction of the interface conditions.
- Transformation rules between xyz-coordinate system and coordinate system aligned with the interface normals are needed for the computation of the flow state in the ghost cells.

All of the given points will be discussed in the following sections.

4.2.1. Restoring of the conservation of the fluxes at the interface

The fact that the fluxes are strictly conserved is one of the strengths of the finite-volume methods. However, the previously described flux-computation procedure over the interface breaks the conservation of fluxes. This is restored by applying the following steps:

The general flux F_{average} over the two interface sides 1 and 2 is computed by

$$\begin{aligned} F_{1,\text{average}} &= \frac{1}{2}\left(F_1 - F_{1,\text{ghost}}\right) \\ F_{2,\text{average}} &= \frac{1}{2}\left(F_2 - F_{2,\text{ghost}}\right) \end{aligned} \tag{4.7}$$

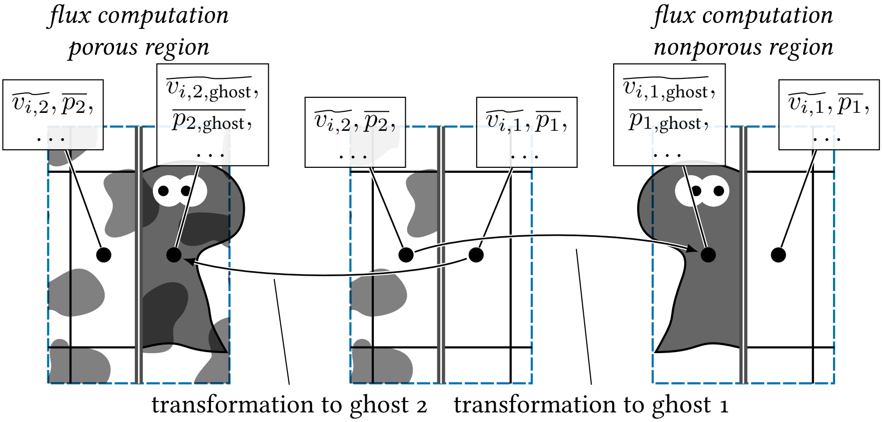

Figure 4.4.: Illustration of ghost cells in order to compute fluxes over the nonporous-porous interfaces.

where $F_{1/2}$ is the flux determined with the flow state at the interface side 1/2 and where $F_{1/2,\text{ghost}}$ are the fluxes calculated with the flow states of the ghost cells.

Next, the fluxes of the ghost cells are split into two parts where the first part $F_{1/2}$ embodies the flux of a non-ghost cell and the second part ΔF_{ghost} is the deviation from this non-ghost flux:

$$\begin{aligned} F_{1,\text{ghost}} &= F_2 + \Delta F_{1,\text{ghost}} \\ F_{2,\text{ghost}} &= F_1 + \Delta F_{2,\text{ghost}} \end{aligned} \tag{4.8}$$

It is expected that for a perfectly converged solution, the deviations ΔF_{ghost} would be the same on both sides,

$$\Delta F_{1,\text{ghost}} = \Delta F_{2,\text{ghost}} \quad , \tag{4.9}$$

as the fluxes for a converged solution must become

$$\begin{aligned} F_1 &= -F_{1,\text{ghost}} \\ F_2 &= -F_{2,\text{ghost}} \quad . \end{aligned}$$

This allows to determine an average deviation:

$$\Delta F_{\text{average, ghost}} = \frac{1}{2}\left(\Delta F_{1,\text{ghost}} + \Delta F_{2,\text{ghost}}\right) \tag{4.10}$$

Using these definitions as a replacement of the deviations $\Delta F_{1/2,\text{ghost}}$ the equations (4.8) become

$$\begin{aligned} F_{1,\text{ghost, conservative}} &= F_2 + \Delta F_{\text{average, ghost}} \\ F_{2,\text{ghost, conservative}} &= F_1 + \Delta F_{\text{average, ghost}} \end{aligned} \tag{4.11}$$

and plugging these "conservative" ghost fluxes back into the starting equation (4.7) gives the conservative fluxes

$$\begin{aligned} F_{1,\text{average, conservative}} &= \frac{1}{2}\left(F_1 - F_2 - \Delta F_{\text{average, ghost}}\right) \\ F_{2,\text{average, conservative}} &= -\frac{1}{2}\left(F_1 - F_2 + \Delta F_{\text{average, ghost}}\right) \quad . \end{aligned} \tag{4.12}$$

The conservative nature of equations (4.12) becomes directly apparent for flow properties where $\Delta F_{\text{average,ghost}}$ is zero. This is for example always the case for mass fluxes. For other properties like momentum fluxes, conservation is still valid since the interface acts as a source or sink term with the magnitude of $2\Delta F_{\text{average, ghost}}$.

4.2.2. Computation of artificial dissipation fluxes across the interface

In order to stabilize the numerical solution process with the central scheme, artificial dissipation fluxes are added. The flow solver TAU uses the form given in [48]. Suited for the differential notation of the Navier-Stokes equations it reads

$$D_{\text{artifical}} = \alpha\left(\kappa_2 \nabla^2 w + \kappa_4 \nabla^2(\nabla^2 w)\right) \quad . \tag{4.13}$$

Here, ∇^2 is the Laplacian operator, w is an arbitrary conservative variable (ρ, ρv_i, ...), α is a scaling factor dependent on the Eigenvalues of the Navier-Stokes equations, and κ_2 and κ_4 are functions to blend between the contributions of second and fourth gradients.

Equation (4.13) implies that inside two neighboring cells, the first gradients as well as third gradients of the conservative variables can be computed. However, at the interface cells third gradients can not be computed as this would require interface conditions for second gradients. Hence, at the interface, the blending in equation (4.13) is adjusted in a way that the second gradient term $\kappa_2 \nabla^2 w$ is fully active and the fourth gradient term $\kappa_4 \nabla^2(\nabla^2 w)$ is disabled. This results in an accuracy reduction from second to first order close to the interface.

4.2.3. Correction of turbulent dissipation-rate for low-resolution meshes

Consider an extremely low permeable medium where the surface is so impenetrable that it will behave like a viscous wall. For such a medium the Darcy and Forchheimer terms in the momentum and in the turbulence equations will lead all the relating conservative variables to zero. While this is the correct behaviour for the momentum and Reynolds stresses this is not the case for the turbulent homogeneous dissipation-rate ε^{h}. Its value should tend to the value given in equation (3.63). For the nonporous interface side, ε^{h} would be

$$\varepsilon^{\mathrm{h}}\big|_{x_n=0,\text{nonporous}} = \widetilde{\nu}\left(\left.\frac{\partial k^{\frac{1}{2}}}{\partial x_n}\right|_{x_n=0,\text{nonporous}}\right)^2 \quad . \tag{4.14}$$

This condition is different than the required value on the porous interface side

$$\varepsilon^{\mathrm{h}}\big|_{x_n=0,\text{porous}} = \widetilde{\nu}\left(\left.\frac{\partial k^{\frac{1}{2}}}{\partial x_n}\right|_{x_n=0,\text{porous}}\right)^2 = 0 \tag{4.15}$$

since the turbulent kinetic energy k inside the nearly impenetrable porous medium will constantly be zero. Note, that equation (4.15) is also consistent with the fact that the Darcy and Forchheimer terms will drag the homogeneous turbulent dissipation-rate ε^{h} to zero. Typical profiles of the dissipation-rate and the square root of the turbulent kinetic energy which are expected at the nonporous-porous interface are sketched in figure 4.5.

The above stated limiting conditions (4.14) and (4.15) for very dense porous media clearly diverge from the interface condition given by (3.72), that

$$\phi_1\overline{\rho_1}\varepsilon_1^{\mathrm{h}} = \phi_2\overline{\rho_2}\varepsilon_2^{\mathrm{h}} \quad . \tag{4.16}$$

One option to overcome this contradiction is to make the mesh spacing extremely small such that the drop of the homogeneous turbulent dissipation-rate ε^{h} is resolved. However, in this case the mesh resolution for a correct solution is expected to be magnitudes higher than the required mesh spacing near a viscous wall. Therefore, as an alternative, inside the solver the interface condition for the homogeneous turbulent dissipation-rate ε^{h} is adapted as:

$$\begin{aligned}\varepsilon^{\mathrm{h}}_{2,\text{ghost}} &= \frac{\phi_1\overline{\rho_1}}{\phi_2\overline{\rho_{2,\text{ghost}}}}\left(\varepsilon^{\mathrm{h}}_1 - \varepsilon^{\mathrm{h}}_{\text{low-resolution-correction}}\right)\\ \varepsilon^{\mathrm{h}}_{1,\text{ghost}} &= \frac{\phi_2\overline{\rho_2}}{\phi_1\overline{\rho_{1,\text{ghost}}}}\varepsilon^{\mathrm{h}}_2 + \varepsilon^{\mathrm{h}}_{\text{low-resolution-correction}}\end{aligned} \tag{4.17}$$

where

$$\varepsilon^{\mathrm{h}}_{\text{low-resolution-correction}} = \widetilde{\nu_1} \left.\frac{\partial k^{\frac{1}{2}}}{\partial x_i}\right|_1 \left.\frac{\partial k^{\frac{1}{2}}}{\partial x_i}\right|_1 - \widetilde{\nu_{1,\text{ghost}}} \left.\frac{\partial k^{\frac{1}{2}}}{\partial x_i}\right|_{1,\text{ghost}} \left.\frac{\partial k^{\frac{1}{2}}}{\partial x_i}\right|_{1,\text{ghost}} .$$

Here, the quantities with index 1 are at the nonporous side. In case both sides of the interface have a porous medium, the index 1 refers to the side with the higher permeability. The numerical value of the gradients $\frac{\partial k^{\frac{1}{2}}}{\partial x_i}$ at the ghost cells has to be obtained from the jump condition (3.77) and reads

$$\begin{aligned} &2\mu_1 k_1^{\frac{1}{2}} \left.\frac{\partial k}{\partial x_n}\right|_1 - 2\mu_{1,\text{ghost}} k_{1,\text{ghost}}^{\frac{1}{2}} \left.\frac{\partial k}{\partial x_n}\right|_{1,\text{ghost}} \\ &\qquad =(1-\phi_2)\frac{\Delta g_{\mathrm{RS}ij,1,\text{ghost}}}{2} - (1-\phi_1)\frac{\Delta g_{\mathrm{RS}ij,1}}{2} . \end{aligned}$$

The modified relation (4.17) coincides with the original relation (4.16) for converged solution with sufficiently high mesh resolutions as the low-resolution correction tends to zero.

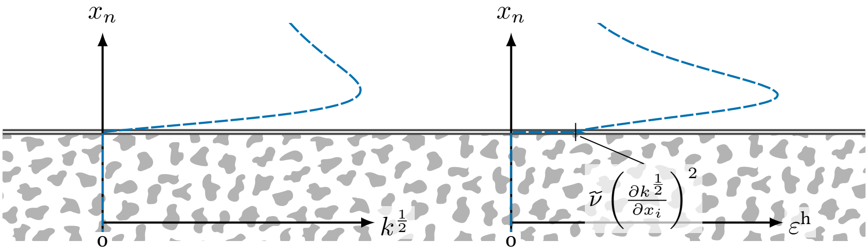

Figure 4.5.: Interface behaviour of the square root of the turbulent kinetic energy k and the turbulent homogeneous dissipation-rate ε^{h} for a very dense porous medium [49].

An exemplary computation result for two under-resolved meshes and one fully resolved mesh is shown in figure 4.6. The case with the strongly under-resolved mesh ($y = 5 \times 10^{-4} H$) shows an abrupt change of the gradient of the Reynolds stress $\widetilde{v_x v_x}$ at the interface. This causes the low-resolution correction to let the homogeneous dissipation-rate ε^{h} jump at the interface. On the contrary, the case with the fully resolved mesh ($y = 2 \times 10^{-5} H$) does not show such a jump of Reynolds-stress gradients and, hence, the homogeneous dissipation-rate will also not jump at the interface. Besides that, it becomes visible that the results of the different meshes do not perfectly match. It seems, that the fully resolved mesh under-predicts the homogeneous dissipation-rate. However, this drawback is independent of the low-resolution correction but must be credited to the theory of the interface conditions (3.81) and (3.82) which could be improved in future.

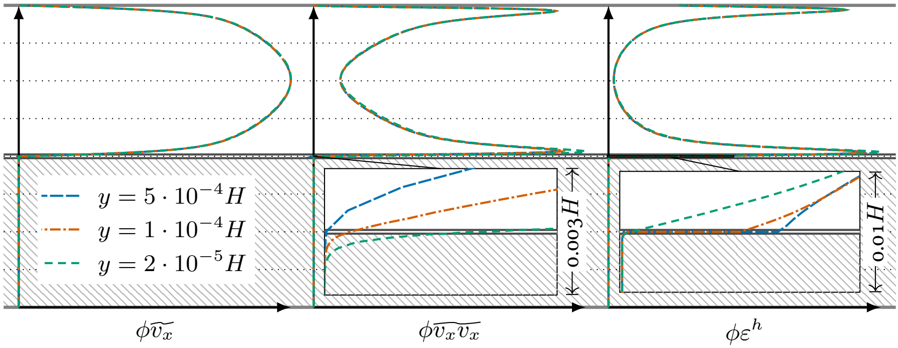

Figure 4.6.: Effect of the grid resolution at the nonporous–porous interface on the simulation result of a channel with a hardly permeable lower porous part. H is the height of the nonporous channel part. y defines the spacing of the first grid point over and below the porous interface.

4.2.4. Computation of the numerical gradients at the ghost cells

The computation of the gradients in the ghost cells is described in section 2.8 (laminar flow) and in section 3.11.2 (turbulent flow). In section 2.8 it is remarked that only gradients normal to the interface require special interface treatment since the gradients in tangential direction are already defined by the variable values of the ghost cells.

Figure 4.7 shows the procedure which is performed by the flow solver for a porous ghost cell:

1. The gradients in the tangential direction are directly copied from the porous interface side to the porous ghost cell.
2. The gradients in the normal direction are taken from the nonporous interface cell but before copying them to the ghost cell they are transformed according to section 3.11.2.

The procedure is applied in the same manner for the nonporous ghost cells. The procedure in mathematical language reads

$$\left.\frac{\partial\varphi}{\partial x_i}\right|_{2,\text{ghost}} = \left.\frac{\partial\varphi}{\partial x_i}\right|_2 - n_i\left(\left.\frac{\partial\varphi}{\partial x_n}\right|_2 - \left.\frac{\partial\varphi}{\partial x_n}\right|_{2,\text{ghost}}\right)$$

with

$$\frac{\partial\varphi}{\partial x_n} = n_j\frac{\partial\varphi}{\partial x_j}$$

where n_i is the i-th coordinate component of the interface normal vector, $\frac{\partial}{\partial x_n}$ is the gradient in the direction of the normal vector and φ is the considered flow variable.

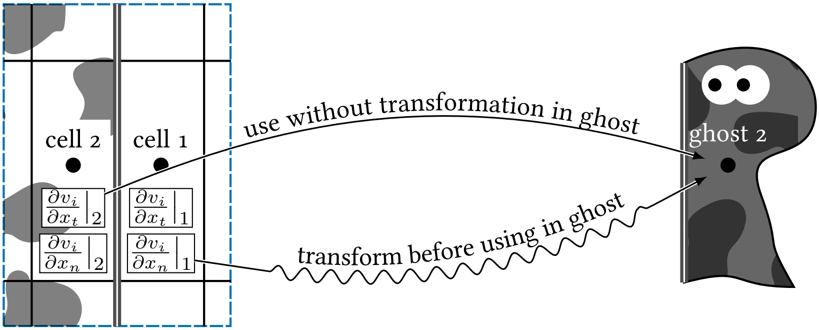

Figure 4.7.: Computation of the gradients at the porous ghost cells.

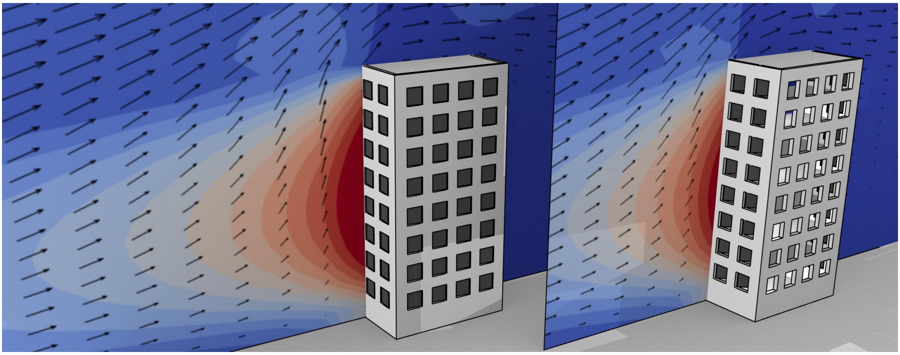

Figure 4.8.: Artistic solution of flow field around skyscraper with closed (left) and open (right) windows including the 2D-velocity vectors and the pressure field.

5. Verification of the Theory and the Solver Implementation

In the course of the theoretical chapters, several examples of computational results were given which served as qualitative illustrations of the different aspects for the described theoretical models. The current verification section takes some of these setups and converts them to cases of which the ideal solution is known – either by analytical results or by limiting conditions which must coincide with nonporous cases. All of these cases serve as a verification of the solver implementation and also, to a very limited amount, verify the theoretical developments. The correct reproduction of the ideal results is a necessary condition for the validity of more complex cases.

5.1. Pressure drop and jump of flow quantities in a channel with porous blockage

The setup of figure 5.1 can serve as a test case to verify the Darcy and Forchheimer term in the porous region and also for the isentropic flow change over the nonporous-porous boundary.

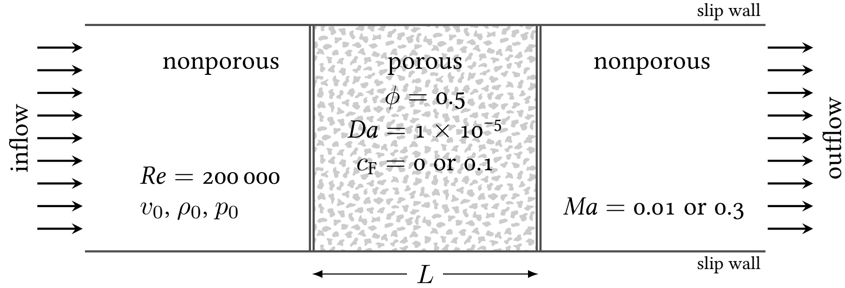

Figure 5.1.: Channel with porous blockage for the verification for the pressure drop in a porous region and the isentropic flow change over the nonporous-porous interfaces.

The contributions of Darcy and Forchheimer terms is verified for a very small Mach number of $Ma = 0.01$ which imitates incompressible flow. This case allows to analytically solve the pressure drop inside the porous region. It it presented in a way similar to Mößner and Radespiel [49]. The governing equation reads

$$\frac{\partial \overline{p}}{\partial x} = -\phi \frac{\mu}{\kappa} \widetilde{v_x} - \overline{\rho} \frac{\phi^2 c_\mathrm{F}}{\sqrt{\kappa}} \widetilde{v_x}^2 \ , \tag{5.1}$$

or, in its dimensionless form:

$$\frac{\partial \overline{p^*}}{\partial x^*} = -\phi \frac{2}{Da\,Re} \frac{\widetilde{v_x}}{v_0} - \frac{\rho}{\rho_0} \frac{2\phi^2 c_\mathrm{F}}{\sqrt{Da}} \left(\frac{\widetilde{v_x}}{v_0} \right)^2 \tag{5.2}$$

with $p^* = \frac{p}{\frac{\rho}{2} v_0^2}$, $x^* = \frac{x}{L}$ and $Re = \frac{\rho L v_0}{\mu}$. The reference velocity v_0 is taken at the inflow of the channel. The density ρ and the viscosity μ are taken to be constant, therefore any averaging indicators are omitted. The right hand side of equation (5.2) is constant for incompressible flow and, thus, the dimensionless pressure drop $\Delta\overline{p^*}$ along the distance Δx^* inside the porous region has to be

$$\Delta \overline{p^*} = -\phi \frac{2}{Da\,Re} \frac{\widetilde{v_x}}{v_0} - \frac{\rho}{\rho_0} \frac{2\phi^2 c_\mathrm{F}}{\sqrt{Da}} \left(\frac{\widetilde{v_x}}{v_0} \right)^2 \Delta x^* \ . \tag{5.3}$$

The numerical result on a mesh which has 60 equally distributed cells along the channel is plotted in figure 5.2. For comparison, equation (5.3) is evaluated inside the porous region. The solutions from the two methods match. Note, that the velocity profile of the numerical solution is only shown for $c_\mathrm{F} = 0$ as it is equal for both Forchheimer coefficients. This is expected since the flow is incompressible.

Still considering the incompressible flow, according to equation (3.67) the interface conditions read

$$\rho \widetilde{v_\text{nonporous region}} = \rho \phi \widetilde{v_\text{porous region}}$$

which implies that for a porosity of $\phi = 0.5$ the velocity must double inside the porous region.

With the incompressible interface condition of the velocity satisfied, the more sophisticated case of compressible flow is considered. Therefore, the Mach number is increased to a value of $Ma = 0.3$ for the case with $c_\mathrm{F} = 0$. Flow is still regarded as laminar. Now, the results must fulfill the interface conditions of section 3.11.1.

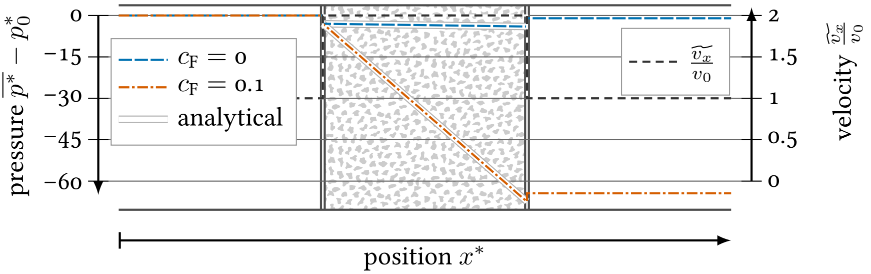

Figure 5.2.: Comparison of the numerical results with the analytical solution of the pressure progress along a channel with and without Forchheimer term at *Ma* = 0.01. Additionally, the velocity profile from the numerical solution ($c_F = 0$) is shown.

The three necessary conditions are written in their dimensionless forms:

$$\text{Isentropic condition:} \quad \frac{\overline{p^*}}{\left(\frac{\overline{\rho}}{\rho_0}\right)^{\gamma}} = \text{constant}$$

$$\text{Conservation of Mass:} \quad \frac{\overline{\rho}}{\rho_0}\frac{\widetilde{v_x}}{v_0}\phi = \text{constant}$$

$$\text{Conservation of Energy:} \quad \left(\frac{\widetilde{v_x}}{v_0}\right)^2 + \frac{\gamma}{\gamma-1}\frac{\overline{p^*}}{\frac{\overline{\rho}}{\rho_0}} = \text{constant}$$

The numerical results are shown in figure 5.3. With this data, the necessary conditions can be calculated at both interfaces (inflow and outflow of the porous region). Without being shown, it is emphasized that the results are correct. This verifies the proper implementation of the interface conditions at least for laminar flow.

5.2. Velocity profile in laminar channel with porous bottom

Boundary layers over porous media can be verified with a channel flow in which the lower part of the channel is filled with a porous medium (see figure 5.4). Under the assumption of incompressible flow and that the Forchheimer term has no contribution ($c_F = 0$), the flow quantities only change along the channel height (except the pressure). Thus, the only equation to solve is an ordinary differential equation

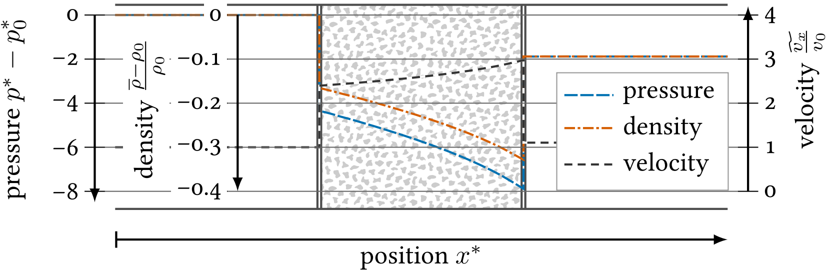

Figure 5.3.: Numerical solution for channel with porous blockage for compressible flow ($Ma = 0.3$, $c_F = 0$, the dimensionless inflow pressure is $p_0^* = \frac{p_0}{\frac{\rho_0}{2} v_0^2} = 19.420$).

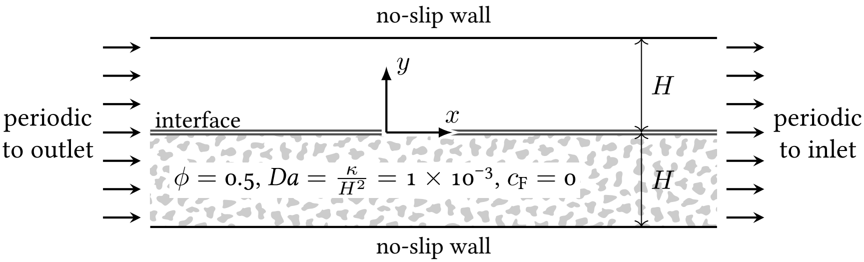

Figure 5.4.: Channel flow in which the lower part is filled with a porous medium. The setup is used for the verification of boundary layers over porous media.

of second order:

$$\overline{\mu}\frac{\partial^2 \widetilde{v_x}}{\partial y^2} - \phi\frac{\overline{\mu}}{\kappa}\widetilde{v_x} = \frac{\partial \overline{p}}{\partial x} \tag{5.4}$$

where the pressure gradient $\frac{\partial \overline{p}}{\partial x}$ can be considered as a constant. The boundary conditions are defined through no-slip conditions on the walls and the interface conditions (3.67a), (3.69) and (3.74):

$$\begin{aligned} \widetilde{v_x}|_{y=H} &= \widetilde{v_x}|_{y=-H} = 0 \\ \widetilde{v_x}|_{y=0,\text{nonporous}} &= \phi\widetilde{v_x}|_{y=0,\text{porous}} \\ \left.\frac{\partial v_x}{\partial y}\right|_{y=0,\text{nonporous}} - \left.\frac{\partial v_x}{\partial y}\right|_{y=0,\text{porous}} &= (1-\phi)\beta\frac{\phi}{\sqrt{\kappa}}\widetilde{v_x}|_{y=0,\text{porous}} \end{aligned} \tag{5.5}$$

Equation (5.4) is generalized by substituting the velocity $\widetilde{v_x}$ and the y-coordinate by

$$y^* = \frac{y}{H} \qquad ; \qquad \widetilde{v_x^*} = \frac{\widetilde{v_x}}{\frac{H^2}{\overline{\mu}}\frac{\partial p}{\partial x}} \tag{5.6}$$

leading to

$$\frac{\partial^2 \widetilde{v_x^*}}{\partial (y^*)^2} - \frac{\phi}{Da}\widetilde{v_x^*} = 1 \tag{5.7}$$

where the Darcy number is defined by $Da = \frac{\kappa}{H^2}$. Accordingly, the new boundary conditions are

$$\begin{aligned} \widetilde{v_x^*}|_{y^*=1} &= \widetilde{v_x^*}|_{y^*=-1} = 0 \\ \widetilde{v_x^*}|_{y^*=0,\text{nonporous}} &= \phi\widetilde{v_x^*}|_{y^*=0,\text{porous}} \\ \left.\frac{\partial v_x^*}{\partial y^*}\right|_{y^*=0,\text{nonporous}} - \left.\frac{\partial v_x^*}{\partial y^*}\right|_{y^*=0,\text{porous}} &= (1-\phi)\beta\frac{\phi}{\sqrt{Da}}\widetilde{v_x^*}|_{y^*=0,\text{porous}} \end{aligned} \tag{5.8}$$

The solution in the nonporous region of the channel is achieved by solving equation (5.7) without the Darcy term. After solving the equations inside and outside the porous region the velocity profile reads

$$\widetilde{v_x^*} = \begin{cases} \frac{(y^*)^2}{2} + c_1 y^* + c_2 & \text{for} \quad y^* > 0 \\ c_3 e^{\sqrt{\frac{\phi}{Da}}y^*} + c_4 e^{-\sqrt{\frac{\phi}{Da}}y^*} - \frac{Da}{\phi} & \text{for} \quad y^* < 0 \end{cases} . \tag{5.9}$$

The constants $c_1 - c_4$ are determined through the boundary conditions:

$$\begin{aligned} c_1 + c_2 &= -\frac{1}{2} \\ c_3 e^{-\sqrt{\frac{\phi}{Da}}} + c_4 e^{\sqrt{\frac{\phi}{Da}}} &= \frac{Da}{\phi} \\ c_2 - \phi c_3 - \phi c_4 &= -Da \\ c_1 - (1-\phi)\frac{\beta}{\sqrt{Da}} c_2 - \sqrt{\frac{\phi}{Da}} c_3 + \sqrt{\frac{\phi}{Da}} c_4 &= 0 \end{aligned} \tag{5.10}$$

This constitutes a linear set of equations, the explicit solution is not being shown here. Rather, it is solved after inserting the actual values of the flow parameters β, ϕ, Da.

The numerical setup uses a mesh with 380 grid points along the channel height. The outflow of the channel is fed into the inflow as periodic boundaries. The pressure gradient is replaced by a volume force which drives the fluid through the channel. The Mach number inside the channel is of the order $Ma \approx 0.1$ to ensure both incompressible flow behaviour and a reasonable convergence rate for the compressible solver.

Figure 5.5 compares the numerical solution against the analytical solution for three different jump coefficients. The velocities are made dimensionless with the bulk velocity v_b in the free flow,

$$v_\mathrm{b} = \frac{1}{H} \int_0^H v \,\mathrm{d}y$$

in which v refers to the analytically solved velocity $\widetilde{v_x^*}$ or the solution of the numerical solution $\widetilde{v_x}$, respectively. Analytical and numerical solutions match very well verifying the correct implementation of the equations into the numerical flow solver.

5.3. Limiting cases for the turbulent channel with porous bottom

There are no such analytical solutions for turbulent cases as they exist for laminar cases. However, the solution for two limiting cases, as described below, can be obtained from the original flow solver which does not have porous flow capabilities. The setup and computational results are already presented [49] and will be reviewed here.

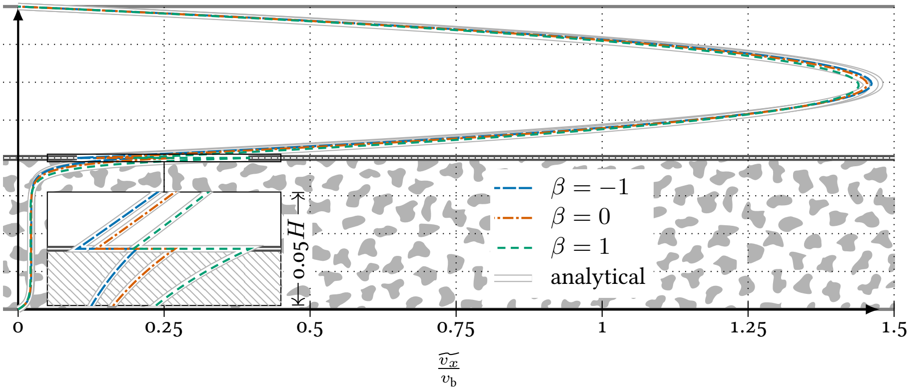

Figure 5.5.: Comparison of the numerical results with the analytical solution for a laminar channel where the lower part is filled with a porous medium.

The two limiting cases are based on the channel with a porous bottom part in figure 5.4 which is already used for the verification of the laminar boundary layer profiles. In this channel, the properties of the porous medium are set, firstly, to a very high permeability κ and the porosity $\phi = 1$ and, secondly, to a very low permeability κ. The first case has to match a channel flow where the porous media is removed. The second case must be equal to a channel flow in which the lower wall is shifted to the position of the interface. The principle is also displayed in figure 5.6.

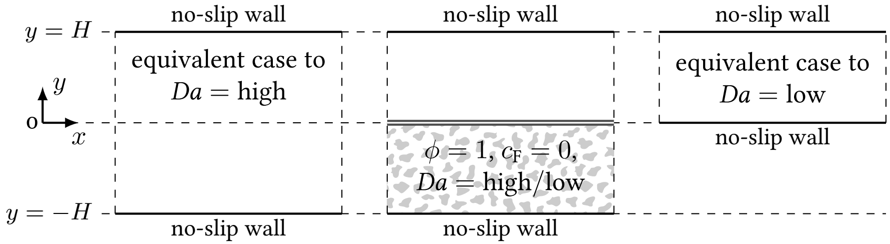

Figure 5.6.: Principal sketch for verifying porous media computations with limiting properties. The high-permeability case (Da = high) has to behave like the channel where the porous medium is removed. The low-permeability case (Da = small) must behave like the case where the lower channel wall moves up to the nonporous-porous interface.

The mesh for the case with porous medium has 180 points along the complete channel height. The nonporous meshes which serve as reference are obtained by either using the same mesh but redefining the porous region to nonporous or by deleting the whole porous region. The Reynolds number in the channel is defined as

$$Re = \frac{\overline{\rho} v_\mathrm{b} 2H}{\overline{\mu}}$$

for the extremely permeable case and as

$$Re = \frac{\overline{\rho} v_\mathrm{b} H}{\overline{\mu}}$$

for the case with an extremely low permeable medium. The bulk velocity v_b is the mean velocity in the complete channel for the extremely permeable case and the mean velocity in the nonporous region for the case with low permeability. The Reynolds number is set to a value of $Re \approx 6000$, which ensures turbulent flow in channels. The Mach number is of the order $Ma = 0.1$. The turbulence model which is used is the *JHh-v2* Reynolds-stress model presented in section 3.8.

The computational strategy is similar to the description given for the laminar case (section 5.2) with periodic inflow/outflow and forcing terms which replace the pressure gradients. The final result which is demonstrated in figure 5.7 shows that the computational results match with the reference cases without porous medium. Note, that the Reynolds stresses $\widetilde{v_x''v_x''}$ and $\widetilde{v_x''v_y''}$ and also the homogeneous turbulent dissipation rate ε^h are made dimensionless with the shear stress velocity u_τ at the top wall

$$u_\tau = \sqrt{\left(\widetilde{\nu} \left| \frac{\partial \widetilde{v_x}}{\partial y} \right| \right)_{y=H}} \ .$$

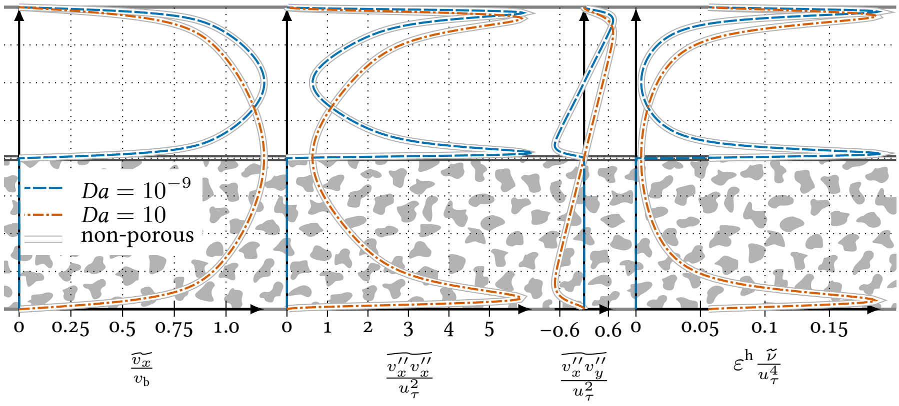

Figure 5.7.: Numerical solutions of a channel with porous lower part where the porous medium is, in one case, extremely permeable and, in the other, very dense. The solution is compared to the numerical results of channels without porous media. The channel Reynolds number $Re \approx 6000$ is based on the height and bulk velocities of the nonporous computations. The Mach number in the channel is of the order $Ma \approx 0.1$.

6. Calibration and Validation of Models for Flow over Porous Media

The previous chapters presented the theory and implementation for simulating flow over and through porous media with a volume- and time-averaging approach. Also, it was verified that the modified flow solver DLR TAU-Code works correctly. This chapter shows that given theoretical aspects can reflect flow phenomena in the real world. Two questions will be answered:

- During the progress of developing the porous simulation model, several parameters have been introduced. This asks for understanding the effects and sensitivities of those parameters. Is it possible to find a general set of fixed values?
- Are the given models able to reflect the physical flow phenomena in sufficient accuracy?

For answering these questions direct numerical simulations (DNS) of Breugem [10] are consulted who solved the flow through a simple channel with a porous bottom. Breugem supplies high precision data of several flow quantities also inside the porous medium which helps to calibrate the modelling parameters. Afterwards, computations of an airfoil with a porous trailing edge are compared with wind-tunnel experiments.

6.1. Channel with porous bottom

Breugem [8, 7, 10, 9] accomplished DNS-computations for a channel where the lower part is filled with a porous medium (see figure 6.1). In his publications Breugem used two kinds of porous media. The first one is a rather simple artificial structure consisting of a 3-dimensional grid of cubes. In contrast, the structure of the second kind of porous media is unknown but only the integral properties (porosity ϕ, permeability κ, Forchheimer coefficient c_F) are defined. While the flow through the grid of cubes can be computed with resolved DNS-computations the cases with

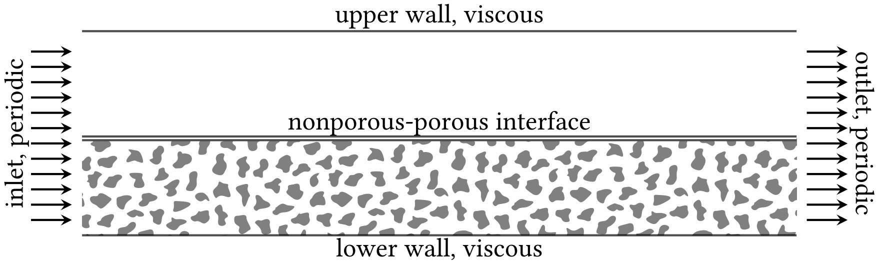

Figure 6.1.: General sketch of Breugem's DNS-computation cases of channel with porous bottom.

unknown porous structure require a volume-averaging approach. Thanks to the extensive documentation of Breugem for all his computations, they make them to the ideal validation candidates which also help to calibrate the unknown parameters of the models given in the present work. Note, that the solutions which are obtained with the models of the present work are from now on called "VRANS" which stands for volume- and time-averaged Navier-Stokes equations.

In principal, the VRANS-model consists of six unknown parameters which appear during the modelling procedure of the flow through porous media:

- The jump coefficient β which controls the jump of velocity-gradients of the nonporous-porous interface (see equation (3.75)),
- The turbulent jump coefficient β_t which controls the jump of gradients of Reynolds stresses over the nonporous-porous interface (see equation (3.80)),
- The wall distance offset parameter c_wd for increasing the effective distance of a point in space from the nonporous-porous interface (see equation (3.64)),
- The diffusion parameter $c_{d,p}$ for modelling additional diffusion of Reynolds normal stresses in porous media (see equation (3.31)),
- The gradient diffusion parameter c_t for modelling velocity fluctuation triple correlations (see equation (3.30)),
- The gradient diffusion parameter $c_{\varepsilon,\mathrm{F}}$ for modelling velocity gradient correlations (see equation (3.42)).

In order to find a suitable parameter set three DNS-cases of Breugem have been chosen to serve as references. They include a resolved laminar case (CUB-LAM), a resolved turbulent case (CUB) where the porous medium consists of a grid of cubes and one volume-averaged turbulent case (E80). The case CUB-LAM can serve to adjust the jump coefficient β independently from the other parameters which only affect turbulent flow. These remaining parameters are calibrated with the cases CUB and E80. While the permeability κ of the porous medium of the CUB-case is rather high, the E80-case is representative for small permeabilities. The properties of the porous media for the different channel cases are given in table 6.1.

		CUB-LAM	CUB	E80
Porosity	ϕ	0.875	0.875	0.8
Darcy number	$Da = \frac{\kappa}{H^2}$	5.2×10^{-4}	3.4×10^{-4}	7.1×10^{-6}
Forchheimer coefficient	c_F	0	0.026	0.19

Table 6.1.: Properties of the porous media for the channel cases with a porous bottom.

Before the detailed description of the individual cases is given, a suitable parameter set is suggested:

$$\beta = -5; \quad \beta_\mathrm{t} = 0.7; \quad c_\mathrm{wd} = 5; \quad c_{d,p} = 0.2; \quad c_t = 0.11; \quad c_{\varepsilon,\mathrm{F}} = 0 \qquad (6.1)$$

The values of the parameters have been manually adjusted during many computations. The procedure revealed that varying the parameter c_t can help improving the solution but its not essential to set it to a specific value at least for the computation cases of this work. Rather, it is sufficient to maintain the standard value of $c_t = 0.11$ of Hanjalić and Launder [31]. Besides, the DNS-validation data do not supply sufficient data to get a detailed insight into the dissipation-rate equation. In consequence, the parameter $c_{\varepsilon,\mathrm{F}}$ is set to zero.

6.1.1. General numerical setup

The DNS-channels are infinitely long and wide. This is emulated by making the inflow area periodic to the outflow and the right channel side periodic to the left channel side. In this context, periodic denotes that the flow data of one periodic plane is fed into its partner. The flow is driven through the channel by an artificial forcing term, a term which replaces the effect of the pressure gradient in a non-periodic channel. The driving force is adjusted in a way that the Reynolds number results in a value of $Re = \frac{v_\mathrm{b} H}{\nu_\mathrm{b}} = 5500$. Herein, the bulk velocity v_b is the mean velocity in the nonporous region and the bulk viscosity ν_b is the mean viscosity.

The setup of the VRANS-computation will be exemplarily shown for the case CUB. The grid and the boundary conditions are shown in figure 6.2. It is principally similar to the DNS-setup: Inflow and outflow are periodic to each other and a forcing term takes the role of the pressure gradient to drive the fluid through the channel. The definition of the left and right side of the channel differs in respect that they are defined as symmetry planes. This given setup leads to a quasi-1-dimensional problem where the flow quantities only change along the channel height. It is also visible that the interface between nonporous and porous medium is not exactly centered in the channel but aligned with the top row of the grid of cubes. Since this alignment is not possible for the case E80 it is adjusted manually to fit best with the DNS-results[1].

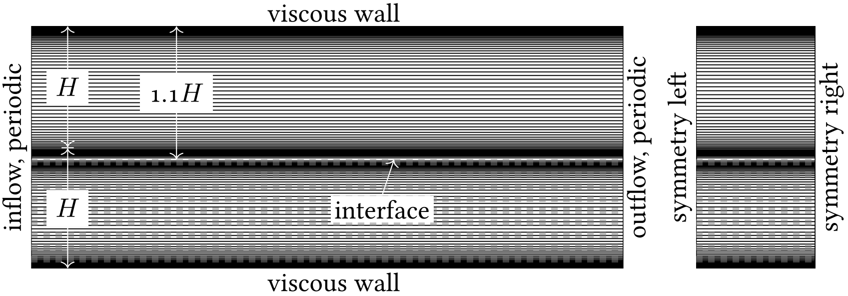

Figure 6.2.: Computational grid for case CUB including the definition of the boundaries and the position of the nonporous-porous interface.

The setup of the numerical solver is as follows: The mean-flow inviscid fluxes are obtained with a second-order central scheme with scalar dissipation. The convective turbulent fluxes are computed with a first-order upwind Roe scheme. The integration between the iteration steps is performed with a Backward-Euler scheme. In contrast to the DNS-computations the equations are solved for compressible air. The averaged Mach number in the upper half of the channel is set to about $Ma \approx 0.15$ which is a compromise between obtaining a good convergence rate and preserving an incompressible flow behaviour. The porous region increases the duration per iteration step by a factor of about 1.6 if compared to a channel with the same grid but without the porous material. This factor depends on the number of porous cells. It is expected that if the number of cells in the porous region was smaller the time overhead would be less.

Figure 6.3 shows a typical residual progress for the case CUB. The results are sufficiently converged such that there are no more visible changes of the flow variables. All cases are tested for grid convergence for at least one parameter set. An example

---

[1] The most obvious choice for the interface position of case E80 would of course be the same position as used for the DNS-computations. However, VRANS-computations showed that this position is not appropriate because of the different interface treatments.

is given for case CUB in figure 6.4. The results of the three different grids change only marginally. Therefore, the coarsest grid with 270 cells along the channel height is used for further computations.

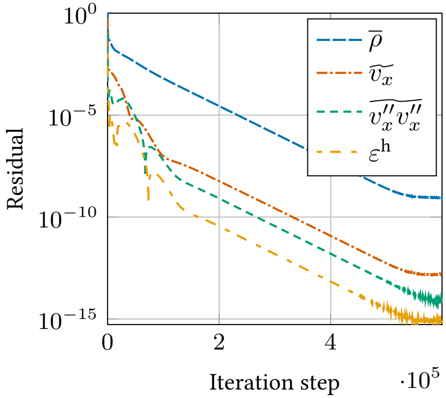

Figure 6.3.: Residual progress of channel case CUB for obtaining the result in figure 6.9.

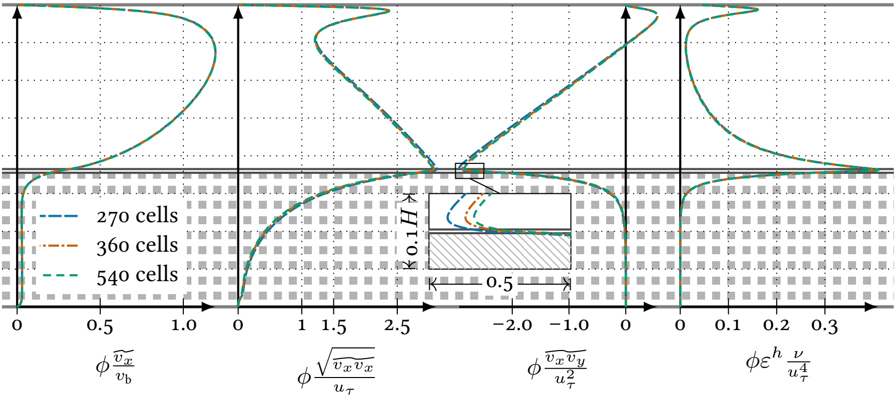

Figure 6.4.: Demonstration of grid convergence for the computation of the channel with cubes. The given cell number is the number of cells along the channel height.

6.1.2. Setup and results of the laminar channel case CUB-LAM

The laminar DNS-computations of Breugem can help to estimate the magnitude of the jump coefficient β. There is also the big advantage that the VRANS-implementation was verified in section 5.2 for these kinds of setups.

The channel geometry with the grid of cubes which was used by Breugem is displayed in figure 6.5. Besides that, it is shown that the interface for the VRANS-computation is positioned at the upper bound of the cubes. This is not self-evident. Breugem discussed in [8] that the position of the interface strongly influences the value of β. However, the present work aims to compute real-life applications where the user should not be confronted with the problem where exactly the interface has to be. This is why the position of the interface is fixed at the most natural place – which is the outer bound of the porous medium. While detailed studies of the interface position are not needed, the sensitivities of the jump coefficient β must be studied.

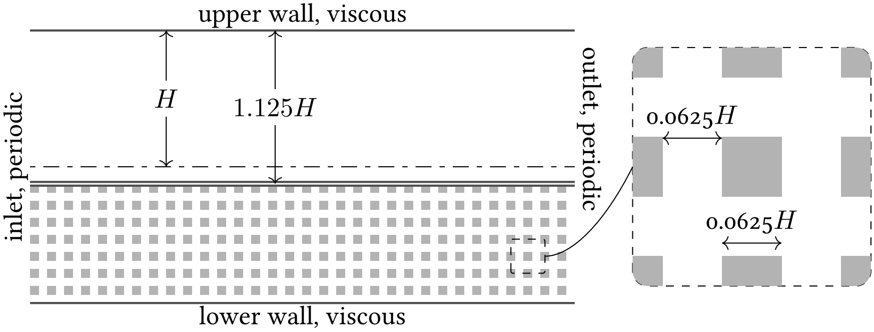

Figure 6.5.: Channel setup and geometry of the porous medium for the laminar channel case CUB-LAM.

The results for three different jump coefficients β is shown in figure 6.6. They are computed with a mesh resolution of 270 points along the channel height. While Breugem performed the DNS-computations at a bulk Reynolds number of $Re = \frac{v_b H}{\nu_b} = 1$ to ensure laminar flow, the present computations were accomplished at the same Reynolds number as the other channel cases CUB and E80 of $Re = 5500$. Laminar flow is ensured by switching off the turbulent terms in the VRANS-equations. The choice not to match the Reynolds number is valid because the laminar flow solution is independent of the Reynolds number (see the analytical solution (5.9) and (5.10)). However, for the Reynolds-number independency exists the one restriction that the Forchheimer term is negligible. Since this is true for the flow setup of the DNS-computations, the Forchheimer term is switched off in the VRANS-computations by setting c_F to zero.

Note that due to the weighting with the porosity ϕ, the velocity profiles are continuous across the interface. This porosity-weighted velocity is also called superficial velocity. The results show that the peak value of the velocity profile agrees best with the DNS-results for a negative jump coefficient of $\beta = -5$. On the other hand, at the position of the interface, the solution of a jump coefficient of zero is closest to the DNS-data and it appears that slightly positive jump coefficients would bring the results even closer.

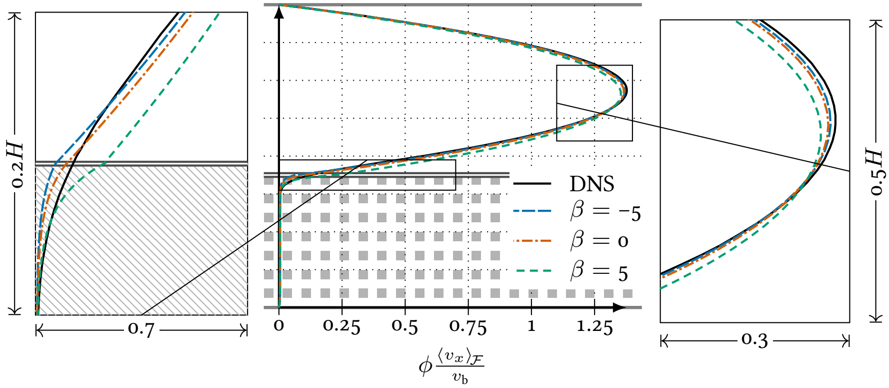

Figure 6.6.: Comparison of laminar DNS-results for case CUB-LAM against VRANS-computations with different jump coefficients β.

At this point the spatial averaging procedure of Breugem must be discussed. The averaging volume of Breugem ranges over a span of two cubes and two clearances. This is a total length of $0.25H$. Inside the averaging volume Breugem uses a weighting function where the weighting value grows linearly from zero at the volume bounds to its maximum value at the volume center. The same averaging procedure is now applied to the VRANS-computations. The averaging filter for an arbitrary flow quantity φ reads

$$\varphi_{\text{filtered}}(y) = \int_{-0.125H}^{0.125H} m(r)\varphi(y+r)\,\mathrm{d}r \tag{6.2}$$

with the definition of the weight:

$$m(r) = \begin{cases} \frac{16}{H} \cdot (0.125H - |r|) & \text{if} \quad |r| < 0.125H \\ 0 & \text{if} \quad |r| > 0.125H \end{cases} . \tag{6.3}$$

Figure 6.7 shows the filtered and unfiltered result for a jump coefficient of $\beta = -5$ compared to the DNS-data. It becomes clear that after filtering the VRANS-solution almost exactly matches the DNS-results. The reason for the growing difference at the peak value of the velocity in the nonporous region comes from the fact that Breugem did not use the filter in the upper half of the channel.

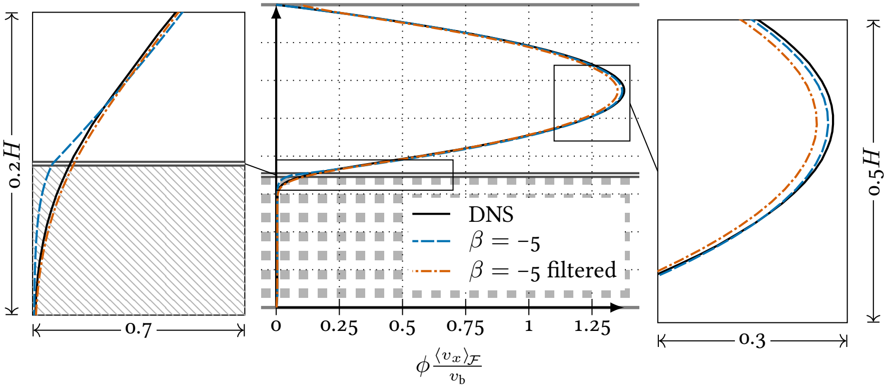

Figure 6.7.: Effect of a spatial filter on the VRANS-data for the laminar channel case CUB-LAM at a jump coefficient of $\beta = -5$. The same filter has been used by Breugem on his DNS-data in [8].

Finally, a summary for the validation with case CUB-LAM is given. Firstly, it is shown that the jump coefficient of $\beta = -5$ leads to a very good match between VRANS- and DNS-results. The negative sign of the jump coefficient means that the porous-medium drag at the nonporous-porous interface is locally increased. In other words, the velocity at the interface decreases together with the jump coefficient. This coincides with the discussion of theoretical section 2.8.1 which states that the permeability κ should increase locally. There, it is argued that by creating the interface area through cutting the porous medium, additional porous surface area is unveiled in a microscopic sense of view. And this additional structure area means more viscous drag. The second important point of this summary is, that the spatial filtering of DNS-data strongly influences the velocity profile close to the interface. As a consequence, the same spatial filter should be applied to the VRANS-data if a detailed comparison is demanded.

6.1.3. Numerical setup and results of the turbulent channel with cubes (case CUB)

The exact geometry of the case CUB is slightly different than the case CUB-LAM. The cubes are smaller which effectively results in a slightly upwards shifted interface area. The setup of Breugem's DNS-computations is shown in figure 6.8. The properties of the cubes representing the porous medium are given by Breugem and listed in table 6.1.

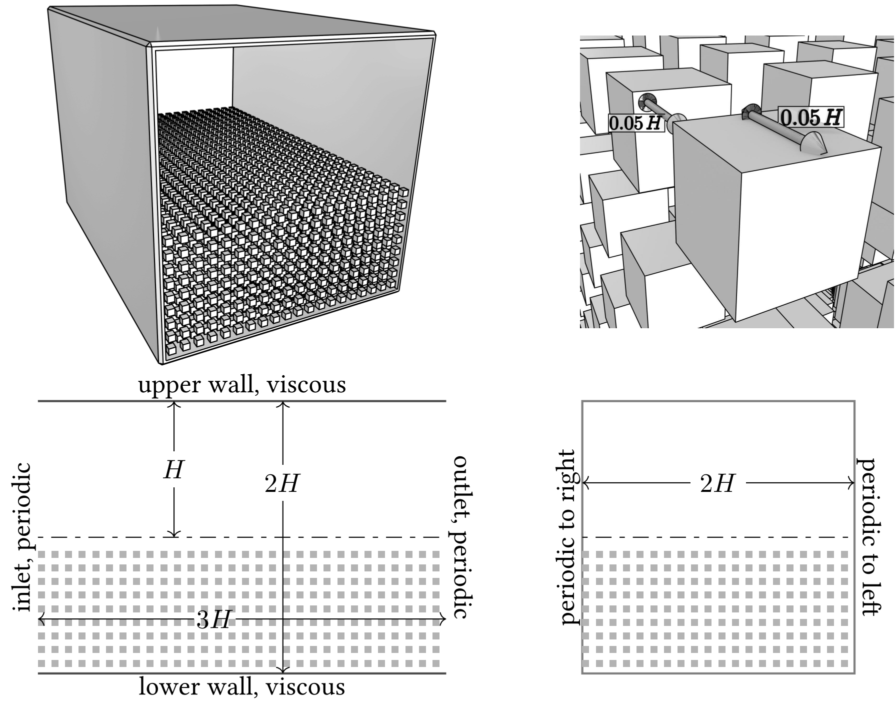

Figure 6.8.: DNS-computation domain of Breugem for the case CUB with an additional view on the detailed porous structure. The size and spacing of the cubes is based on half the channel height H.

The VRANS-mesh resolves the channel height with 270 cells. The cell spacing at the upper wall and at the interface is $\Delta y^{\text{(upper wall/interface)}} = 3 \times 10^{-4}\,H$. At the lower wall the spacing is $\Delta y^{\text{(lower wall)}} = 6 \times 10^{-4}\,H$. In terms of inner coordinates y^+,

$$y^+ = y \cdot \frac{u_\tau}{\tilde{\nu}} = \frac{y}{H} Re_\tau \quad \text{with} \quad Re_\tau = \frac{u_\tau H}{\tilde{\nu}} \ , \tag{6.4}$$

the wall spacing $\Delta y^{+,\text{(upper wall)}}$ at the upper wall is

$$\Delta y^{+,\text{(upper wall)}} = \frac{\Delta y^{\text{(upper wall)}}}{H} Re_\tau^{\text{(upper wall)}} = 0.12$$

and the wall spacing $\Delta y^{+,\text{(interface)}}$ at the interface is

$$\Delta y^{+,\text{(interface)}} = \frac{\Delta y^{\text{(interface)}}}{H} Re_\tau^{\text{(interface)}} = 0.2 \quad .$$

The Reynolds numbers in these definitions are used according to Breugem who computed the values to be

$$Re_\tau^{\text{(upper wall)}} = 394 \quad \text{and} \quad Re_\tau^{\text{(interface)}} = 669 \quad .$$

The definition of the shear-stress velocity u_τ which is used by Breugem is

$$u_\tau = \sqrt{\left| -\overline{\langle v'_x v'_y \rangle} + \nu \frac{\partial \overline{v_x}}{\partial y} \right|}$$

where the fluctuation values v'_x and v'_y are computed from the velocity field before it is averaged in space. The interface between the porous and nonporous region is placed at the upper surface of the top row of cubes which measures 1.1 H below the upper wall.

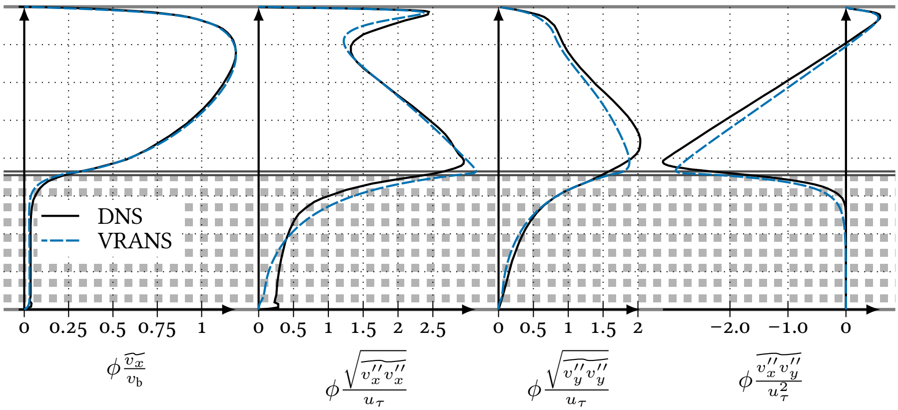

Figure 6.9.: Comparison of DNS- and VRANS-Computations of channel with cubes. VRANS (Volume- and Reynolds-averaged Navier-Stokes) are the computation with the newly developed code while the DNS-data are taken from Breugem [10]. (Applied parameter set: $\beta = -5$; $\beta_\text{t} = 0.7$; $c_\text{wd} = 5$; $c_{d,p} = 0.2$; $c_t = 0.11$; $c_{\varepsilon,\text{F}} = 0$)

The result which is obtained with the parameter set 6.1 is shown in figure 6.9. DNS- and VRANS-results agree well, especially the velocity profile. Also the local Reynolds numbers of the VRANS-computations, which obtain a value of

$$Re_\tau^{\text{(upper wall)}} = 372 \quad \text{and} \quad Re_\tau^{\text{(interface)}} = 619$$

agree well with the DNS results given above. There remain small differences especiall for the Reynolds stresses close to the interface. This has various reasons:

- The applied parameter set is a compromise between the three cases CUB-LAM, CUB and E80. However, there is no strict reason why the parameters should be independent of the porous medium.
- The modelling of turbulence in the porous media is based on many assumptions and simplifications. Obviously, the models are not capable to reproduce the exact results.
- The spatial filtering as given for the case CUB-LAM (equations (6.2) and (6.3)) is not performed for the present case. Such a filtering would slightly decrease the strong local curvatures of the VRANS-results below the porous interface. However, since the expected effect is very small, it is not investigated any further here.

With this in mind, a preliminary conclusion should be given:

- The agreement between DNS- and VRANS-results is good enough to give confidence that the VRANS-models have the potential for reliable predictions of more complex flow cases.
- The final parameter set of the channel cases must be understood as a first suggestion but must not be generalized. A generalization would need more detailed studies with different porous media.

Besides this first conclusion, the CUB channel case is ideal to understand the effect of the single modelling parameters. This will be the content of the following discussions.

Effect of the jump coefficient β

Variations of the jump coefficient β are already shown for the laminar case CUB-LAM in section 6.1.2. The effect is further evaluated in figure 6.10. The slight changes of the velocity at the interface show the primary effect of this parameter: A more negative jump coefficient pulls the velocity at the interface to smaller values whereas a less negative jump coefficient releases the velocity to higher values. Another interpretation is that the most negative jump coefficient leads to the largest gradient jump over the interface. However, this effect can hardly be recognized in the plot.

The secondary effect on the turbulent shear stress is much more visible. The modification of the velocity gradient significantly influences the turbulent production (3.23a) which has a strong effect on the Reynolds-stress profiles and also on the gradient jump of the Reynolds stresses (equation (3.80)).

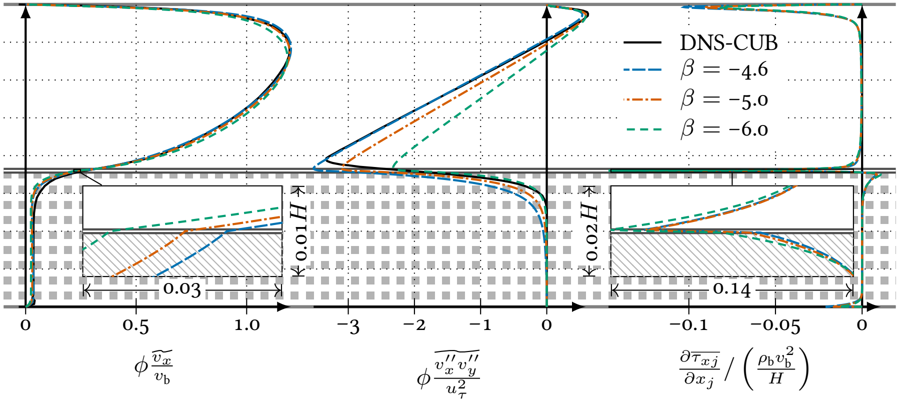

Figure 6.10.: Effect of the jump coefficient β on the velocity $\widetilde{v_x}$, the Reynolds shear stress $\widetilde{v''_x v''_y}$ and the viscous stress $\frac{\partial \tau_{xj}}{\partial x_j}$ for the channel case CUB. (Applied parameter set: $\beta_t = 0.7$; $c_{wd} = 5$; $c_{d,p} = 0.2$; $c_t = 0.11$; $c_{\varepsilon,F} = 0$)

The viscous contributions τ_{ij} to the momentum equations are shown as a final graph in figure 6.10. The rather small variations of the jump coefficients also lead to very small effects on these profiles. However, all shear stress profiles show a sudden jump over the porous interface originating from the suddenly changing curvature of the velocity profiles. This is the effect of the abruptly starting Darcy and Forchheimer contributions in the porous region.

Lastly, it should be mentioned that when the jump coefficient grows to more positive values the computations start to become instable. This problem is associated with the Reynolds stresses which start growing very quickly when the jump coefficient approaches zero. And as soon a certain margin is exceeded the Reynolds stresses start an infinite growth blowing up the computation. This behaviour can be counteracted by reducing the turbulent jump coefficient β_t.

Effect of the turbulent jump coefficient β_t

The effect of the turbulent jump coefficient β_t on the Reynolds stresses is similar to the effect of the jump coefficient β on the velocity. For a growing value of β_t the Reynolds stresses are pulled to higher values as clearly shown in figure 6.11. It is interesting to see that for very small β_t-values the different graphs begin to completely change their behaviour. This is especially visible in the profile of the turbulent production P_{xx}. Obviously, the different governing equations are strongly coupled which results in a very sensitive balance between the different models and

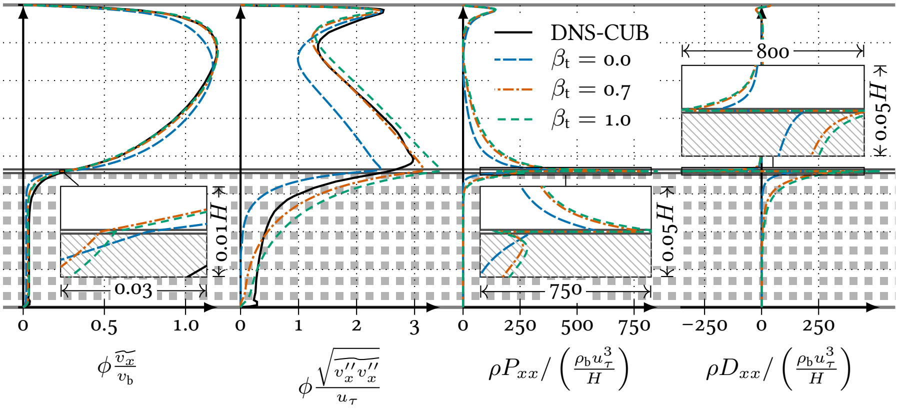

Figure 6.11.: Effect of the turbulent jump coefficient β_t on the velocity $\widetilde{v_x}$, the Reynolds normal stress $\widetilde{v_x''v_x''}$ (represented by root mean square of the x-velocity), the turbulent production P_{xx} and the diffusion D_{xx} (including viscous diffusion (3.60), turbulent diffusion (3.59) and pressure diffusion (3.31)) for the channel case CUB. (Applied parameter set: $\beta = -5$; $c_{\mathrm{wd}} = 5$; $c_{d,p} = 0.2$; $c_t = 0.11$; $c_{\varepsilon,\mathrm{F}} = 0$)

terms.

As a last comment, note that the standard value of $\beta_t = 0.7$ is rather high. It is needed for matching the Reynolds-stress profiles with the DNS-data. The downside is that the margin to an unbounded growth of the Reynolds stresses is very small. The strong coupling of the different equations and terms also means that all the other parameters (β, c_{wd}, $c_{d,p}$, c_t, $c_{\varepsilon,\mathrm{F}}$) have very limited value ranges.

Effect of the wall distance offset parameter c_{wd}

The redistribution term of the applied *JHh-v2* turbulence model contains near-wall terms. These terms make sure that close to walls the wall-normal velocity fluctuations are damped. At the same time this means that the fluctuation values tangential to the wall cannot transfer as much energy to the wall-normal fluctuations. The described effect appears also close to porous surfaces. The parameter c_{wd} influences the magnitude of the offset distance which is added to the actual distance between the considered point in space and the next porous surface. The effect is shown in figure 6.12. Small offset values (e.g. $c_{\mathrm{wd}} = 4$) lead to decreased wall-normal fluctuations which are represented by $\sqrt{\widetilde{v_y''v_y''}}$. Simultaneously, the tangential fluctuation

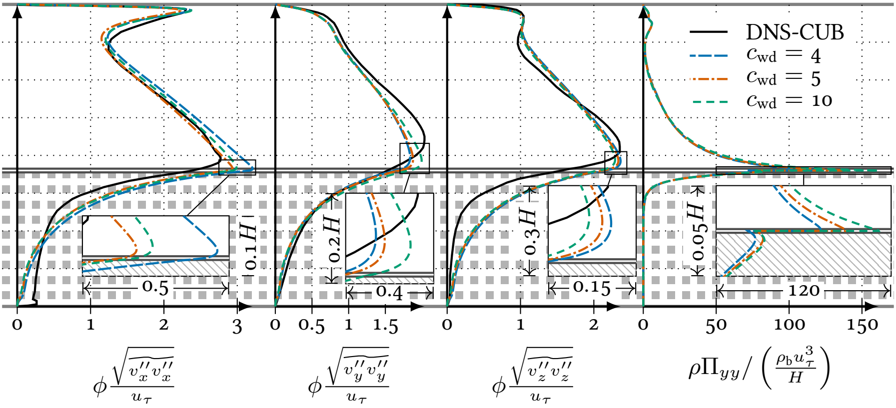

Figure 6.12.: Effect of the wall distance offset parameter c_{wd} on the Reynolds normal stresses $\widetilde{v_x'' v_x''}$, $\widetilde{v_y'' v_y''}$ and $\widetilde{v_z'' v_z''}$ (represented by root mean squares of velocity components) and pressure-strain correlation Π_{yy} for the channel case CUB. (Applied parameter set: $\beta = -5$; $\beta_{\mathrm{t}} = 0.7$; $c_{d,p} = 0.2$; $c_t = 0.11$; $c_{\varepsilon,\mathrm{F}} = 0$)

components $\sqrt{\widetilde{v_x'' v_x''}}$ and $\sqrt{\widetilde{v_z'' v_z''}}$ increase. The same behaviour can be identified in the redistribution term Π_{yy} of the wall-normal Reynolds-stress equation. It decreases with a decreasing parameter c_{wd} which means that less energy is transferred to the other Reynolds stresses. For very high factors of about $c_{\mathrm{wd}} = 50$ to $c_{\mathrm{wd}} = 100$ the offset distance is so large that no wall damping will take place anymore and the solution stops changing. A value of $c_{\mathrm{wd}} = 0$ would lead to a damping of wall-normal Reynolds stresses similar to a solid wall. However, the given parameter set with the high turbulent jump coefficient β_{t} will lead to an unstable solution for such small values of c_{wd}.

Effect of the pressure diffusion parameter $c_{d,p}$

Several tests without the parameter $c_{d,p}$ showed that the very high Reynolds stresses inside the porous region of the channel can not be reached with reasonable parameter sets. Here, the findings of Breugem [10] are pointed out, who argues that the high Reynolds stresses are caused by pressure fluctuations at the porous interface. Therefore, the choice was made to include an additional diffusion term for the Reynolds normal stresses inside the porous region controlled by the parameter $c_{d,p}$. The effect is shown in figure 6.13. The Reynolds stresses begin to detach from the zero line for the parameter values bigger than zero. Note, that the coupling between the different equations also leads to an increased shear stress $\widetilde{v_x'' v_y''}$ which does not

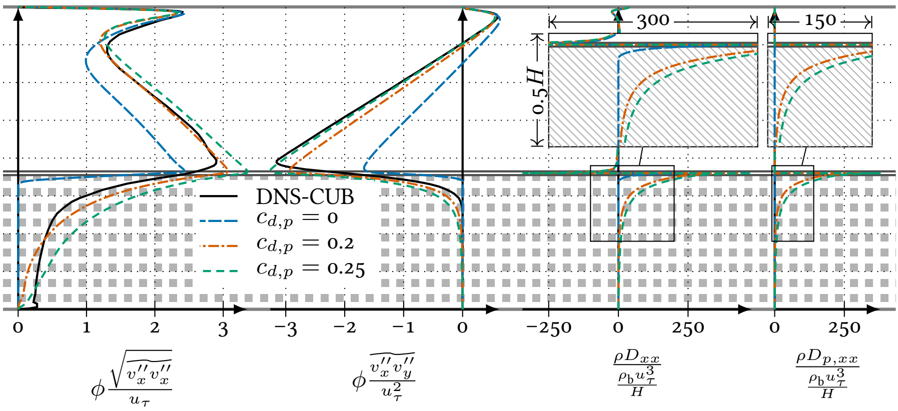

Figure 6.13.: Effect of the extra diffusion parameter $c_{d,p}$ on the Reynolds stresses $\widetilde{v''_x v''_x}$ (represented by root mean square of x-velocity component) and $\widetilde{v''_x v''_y}$, the diffusion term D_{xx} (including viscous diffusion (3.60), turbulent diffusion (3.59) and pressure diffusion (3.31)) and the isolated pressure diffusion term $D_{p,xx}$ (3.31) for the channel case CUB. (Applied parameter set: $\beta = -5$; $\beta_\mathrm{t} = 0.7$; $c_\mathrm{wd} = 5$; $c_t = 0.11$; $c_{\varepsilon,\mathrm{F}} = 0$)

experience the additional diffusion.

Figure 6.13 also shows the contribution of the complete diffusion D_{xx} (including the viscous, the turbulent and the new pressure diffusion term) and the isolated new pressure diffusion term $D_{p,xx}$. It can be recognized that the diffusion is now dominated by the newly introduced diffusion term.

Effect of the gradient diffusion constant c_t

The parameter c_t controls the gradient diffusion model for the velocity-fluctuation triple correlations in the Forchheimer term. Its effect is somehow similar to the previously described parameter $c_{d,p}$ even though the triple correlations do not appear inside gradients and, hence, the modelled triple correlations are no real diffusion. It should rather be understood as a term which enhances the convective transport of Reynolds stresses based on the velocity fluctuations. It was tried to replace the parameter $c_{d,p}$ by turning up the parameter c_t to very high values. However, this would firstly require values of the order of 1 which is unphysical if compared to the proposed values in literature (around $c_t = 0.1$) and secondly this further destabilizes the solution.

Up to now a validation of a suitable value is difficult as no DNS-data are available

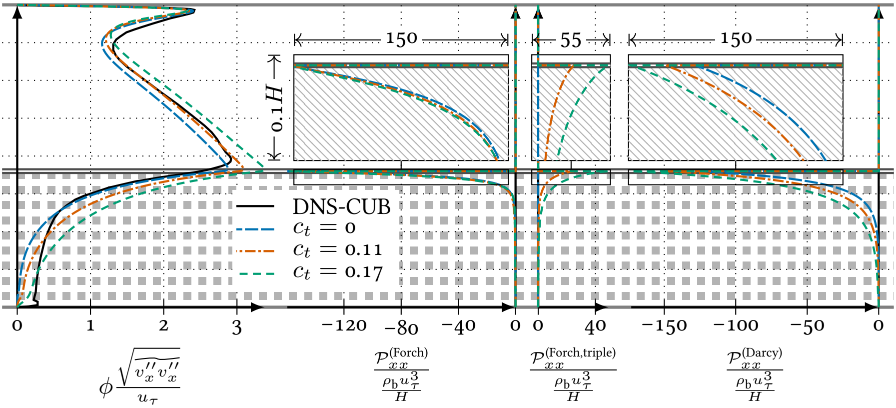

Figure 6.14.: Effect of the gradient diffusion constant c_t for modelling the triple correlations of equation (3.30) on the Reynolds normal stress $\widetilde{v_x''v_x''}$ (represented by root mean square of x-velocity component), the complete Forchheimer term $\mathcal{P}_{xx}^{\text{(Forch)}}$ (3.28), the part of the Forchheimer term which only consists of terms with velocity-fluctuation triple correlations $\mathcal{P}_{xx}^{\text{(Forch, triple)}}$ and on the Darcy term $\mathcal{P}_{xx}^{\text{(Darcy)}}$ for the channel case CUB. (Applied parameter set: $\beta = -5; \beta_\text{t} = 0.7; c_\text{wd} = 5; c_{d,p} = 0.2; c_{\varepsilon,\text{F}} = 0$)

for the velocity triple correlations. Hence, the final value is taken from the original paper [31] which is $c_t = 0.11$.

The effect of the parameter is shown in figure 6.14. According to the previous paragraphs the effect is similar to $c_{d,p}$ as it increases the Reynolds stresses inside the porous region while reducing the curvature. This consequently leads to an increase of the Darcy term $\mathcal{P}_{xx}^{(\mathrm{Darcy})}$ which is proportional to the Reynolds stresses. It can also be seen that the Forchheimer contributions of the triple correlations $\mathcal{P}_{xx}^{\mathrm{Forch,triple}}$ is positive. Thus, it counteracts the general damping effect of the Darcy- and Forchheimer terms. Finally, note that the total Forchheimer term $\mathcal{P}_{xx}^{(\mathrm{Forch})}$ is mostly unaffected by the parameter c_t. However, as there is no known reason why this should be generally valid, it is regarded as a coincidence.

Effect of the gradient diffusion constant $c_{\varepsilon,\mathrm{F}}$

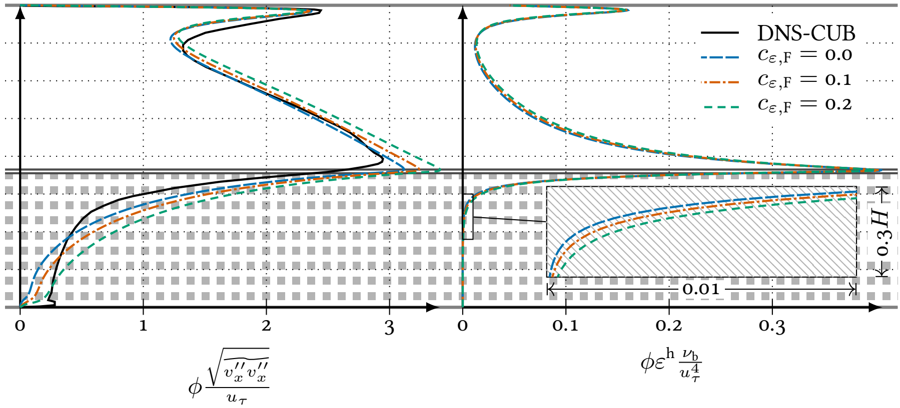

Figure 6.15.: Effect of the gradient diffusion constant $c_{\varepsilon,\mathrm{F}}$ for modelling the triple correlations of two velocity-fluctuation gradients and one velocity fluctuation according to equation (3.42). The effect is shown in terms of the Reynolds normal stress $\widetilde{v''_x v''_x}$ (represented by root mean square of the x-velocity component) and the homogeneous turbulent dissipation-rate ε^{h} for the channel case CUB. (Applied parameter set: $\beta = -5$; $\beta_{\mathrm{t}} = 0.7$; $c_{\mathrm{wd}} = 5$; $c_{d,p} = 0.2$; $c_t = 0.11$)

The last parameter $c_{\varepsilon,\mathrm{F}}$ is the most uncertain parameter since there is hardly any validation basis and its effect on the turbulent dissipation-rate equation leads to a very coupled response of the Reynolds-stress equations. The parameter itself can be regarded as the dissipation-rate analogon to the parameter c_t in the Reynolds-stress equations. It therefore is assumed to have a similar effect on the turbulent dissipation-rate ε than the parameter c_t has on the Reynolds stresses. This can actually be observed in figure 6.15. In contrast, one would expect decreasing Reynolds stresses for an increasing dissipation rate which is obviously not the case. In fact, this indicates a very strong coupling between the different governing equations in a way that the given observations cannot provide any information about cause and effect. Rather, a much more detailed insight into the different terms of the dissipation-rate equation is needed. Since this cannot be accomplished with the available data, the parameter $c_{\varepsilon,\mathrm{F}}$ is set to zero.

6.1.4. Numerical setup and results of volume-averaged DNS channel case E80

The last channel case which is presented now incorporates a rather small permeability κ of two orders of magnitude smaller than the case CUB. This case E80 is shown in order to emphasize the generality of the theoretical models. The properties of the applied porous medium are given in table 6.1.

The mesh resolution of the case E80 is 300 cells along the channel height. The grid spacing at the upper wall is

$$\Delta y^{\text{(upper wall)}} = 5 \times 10^{-4} \quad ,$$

at the interface it is

$$\Delta y^{\text{(interface)}} = 1 \times 10^{-5}$$

and at the bottom it is

$$\Delta y^{\text{(lower wall)}} = 1 \times 10^{-3} \quad .$$

In terms of inner coordinates these distances correspond to

$$\Delta y^{+,\text{(upper wall)}} = 0.20 \quad \text{and} \quad \Delta y^{+,\text{(interface)}} = 0.004 \quad .$$

In here, the definitions of equation (6.4) are used together with the Reynolds numbers

$$Re_\tau^{\text{(upper wall)}} = 354 \quad \text{and} \quad Re_\tau^{\text{(interface)}} = 398$$

taken from [10]. Compared to the case CUB the resolution at the interface is significantly increased to get a better resolution of the velocity decay inside the porous medium. Since there is no explicit interface position as it existed for the CUB-case it is set by trial and error to $0.01H$ below the channel center.

The results for the same parameter set as it is used for case CUB are shown in figure 6.16. If the Reynolds shear stress $\widetilde{v_x'' v_y''}$ is compared to the case CUB (figure 6.9) it can be recognized that it is now over-predicted instead of under-predicted. This could be improved if the value of the wall distance offset parameter c_{wd} was chosen individually for both cases. However, as a general value is preferred a compromise has been made at that point.

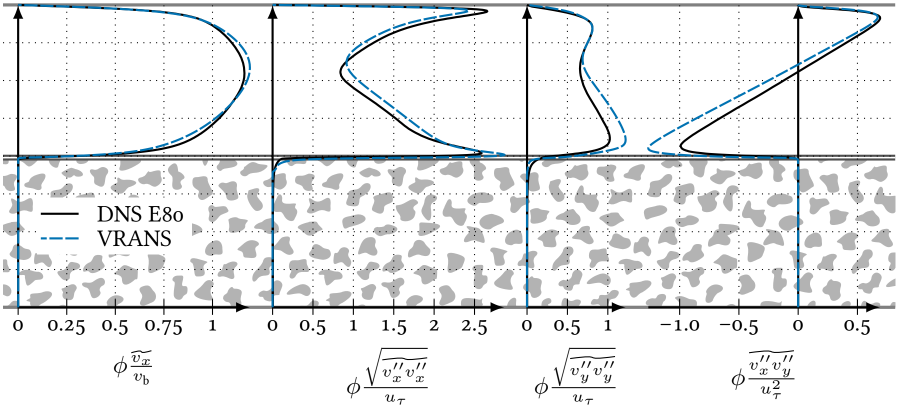

Figure 6.16.: Comparison of DNS- and VRANS-computations for the channel case E80. The VRANS are the computation with the newly developed code while the DNS-data are taken from Breugem [10]. (Applied parameter set: $\beta = -5; \beta_\mathrm{t} = 0.7; c_\mathrm{wd} = 5; c_{d,p} = 0.2; c_t = 0.11; c_{\varepsilon,\mathrm{F}} = 0$)

6.2. DLR-F16 airfoil with a porous trailing edge

The last and most interesting validation case is a wing with a porous trailing edge (figure 6.17). In contrast to the previous case it is directly connected to a real-life application. The motivation of replacing the solid trailing edge with a porous material originates from the field of acoustics. In [33], Herr showed for a NACA0012-like airfoil that noise can be reduced by a significant amount if the trailing edge is made porous. Amongst others, this research was continued in the framework of the collaborative research center SFB880 [61] for a wing with the non-symmetrical airfoil DLR-F16. Several acoustic results for this wing have been published in [34]. The identical wind-tunnel model of the DLR-F16 wing has also been investigated in respect of its aerodynamic performance for the present work. The present section describes the conducted experiments and compares the results against numerical computations. The section is a revised version of [50].

6.2.1. Experimental setup

The experiments are performed on a 2D-wing with 1.3 m wingspan and 0.3 m chord length. The geometry is shown in figure 6.18. The cross section of the model is defined as the DLR-F16 airfoil. The trailing edge of the model can be replaced with various porous inlays. The inlays occupy 10 % of the chord length (0.03 m) and are

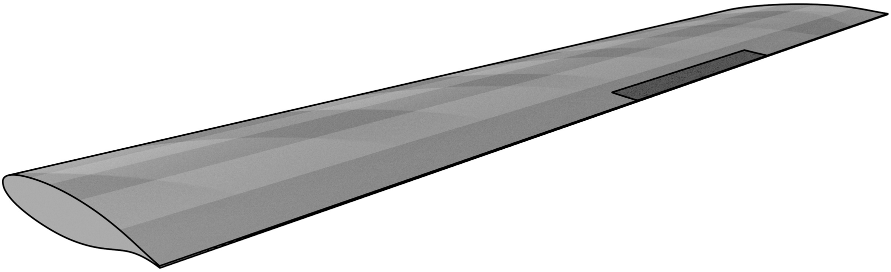

Figure 6.17.: 3D-Drawing of a wing with porous trailing edge used for comparison of wind-tunnel experiments against numerical simulations.

0.3 m wide. The employed porous media include porous aluminum (PA), sintered fibre felts (SFF) and sintered bronze powder (SBP). Turbulent flow is ensured by tripping with a zig-zag-tape. The tape is located at 5 % chord on the upper wing surface and at 10 % chord on the lower wing surface. The effectiveness of the tripping procedure was checked by using a stethoscope with an attached Prandtl probe.

In order to get a comprehensive insight into the aerodynamics of the wing with porous trailing edge both pressure and particle image velocimetry (PIV) measurements are performed. The pressure measurements mainly supply the integral lift coefficient c_l while the PIV-measurements give deeper information about the flow physics which occurs at the trailing edge.

All experiments are conducted in the low-speed wind-tunnel MUB of the Technische Universität Braunschweig. It is a closed-return wind-tunnel with a closed test section of 1.3×1.3 m cross section.

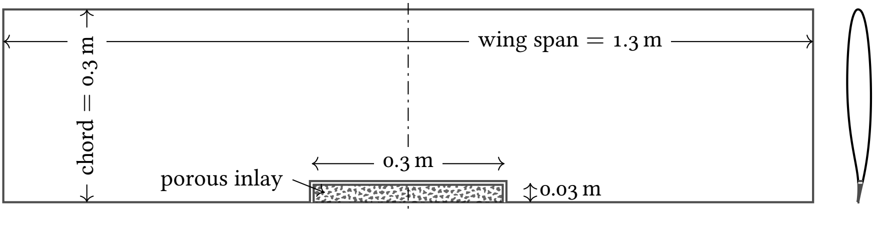

Figure 6.18.: Geometry of DLR-F16 wind-tunnel model with porous trailing edge.

Characterization of porous inlays

Since the theoretical closure model of this work is limited to isotropic porous media, only such materials will be discussed here. Two types of constructions are investigated. The first type uses the porous media only as sheets on a rib structure. The second type are porous media where the trailing edges are directly cut from a solid block according to the airfoil shape (see figure 6.19).

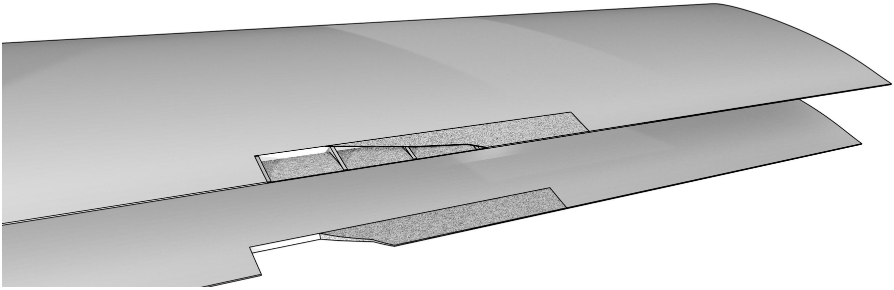

Figure 6.19.: Construction details of porous trailing edge. The upper wing shows the construction where the porous medium was used as a sheet, whereas the lower wing shows the porous trailing edge cut from a solid porous block.

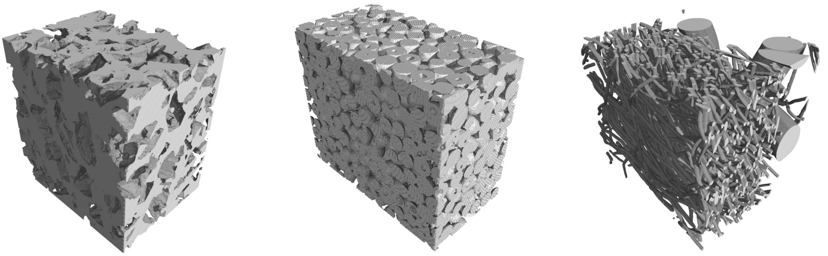

Figure 6.20.: Computer-tomography-data from left to right for porous aluminum (PA), sintered bronze powder (SBP) and sintered fibre felts (SFF).

The materials under investigation are porous aluminum and sintered bronze powder representing solid trailing edges and sintered fibre felts which are used as sheet material. The structure of these media is visualized in figure 6.20. The procedure for obtaining the characteristic data of the different porous media is described by Uphoff et al. in [78]. In short, the geometry of the porous structure is identified

material name	typical pore dimension [µm]	sheet thickness [mm]	porosity ϕ	permeability κ [m²]
PA 80-110	$d_\mathrm{p} \approx 700$	solid	0.46	1.24×10^{-10}
SBP 60	$d_\mathrm{s} = 278$	solid	0.37	6.52×10^{-11}
SBP 120	$d_\mathrm{s} = 590$	solid	0.36	2.80×10^{-10}
SFF 50	$d_\mathrm{f} = 25$	0.6	0.86	2.28×10^{-10}
SFF 120	$d_\mathrm{f} = 26$	0.3	0.89	1.91×10^{-10}

Table 6.2.: Properties of the different porous media used as trailing edges of the wind-tunnel model. d_p is pore size, d_s is sphere size and d_f is fibre diameter. The material abbreviations are as follows: PA is porous aluminum, SBP is sintered bronze powder and SFF are sintered fibre felts.

by 3D-computer tomography and 2D-light microscopy. The value of the flow resistivity R is determined at the Physikalisch Technische Bundesanstalt Braunschweig using the alternating airflow method (Method B DIN EN 29053, ISO 9053). The conversion of the flow resistivity R to the required permeability κ is accomplished by the rule

$$\kappa = \frac{\mu_0}{R} \qquad \text{with} \qquad \mu_0 = 1.81 \times 10^{-5}\,\mathrm{kg\,m^{-1}\,s^{-1}} \tag{6.5}$$

where the value of the dynamic viscosity μ_0 corresponds to viscosity of air at a temperature of 293 K. All important properties of the different porous media are summarized in table 6.2. The data are equal to the values given in [34].

The Forchheimer coefficient c_F has not been measured. Hence, it is set to an approximate value of $c_\mathrm{F} = 0.1$ for all porous media. This approximation is obtained with the help of the Ergun equation described e.g. in [46]. The jump coefficients β and β_t of equations (3.75) and (3.80) are presently unknown and initially set to zero. Nevertheless, a discussion about their effect is given in section 6.2.6.

Setup of pressure measurements

The model is instrumented with 45 static pressure measurement taps along a plane parallel to the mid section of the wing. Close to the leading edge the taps are clustered for capturing the suction peak. The exact distribution is shown in figure 6.21.

The pressure measurements were accomplished at a variety of angles of attack in increasing and decreasing direction to identify the hysteresis effect when the flow separates. For each measurement point 50 samples were taken and averaged in order to get the mean pressure distribution. The measurements were taken at a

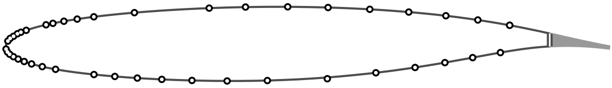

Figure 6.21.: Position of pressure taps around airfoil.

Reynolds number of

$$Re = \frac{\rho v_\infty c}{\mu} = 1\,000\,000$$

with the chord length c. The Mach number was set to

$$Ma = \frac{v_\infty}{a} = 0.15$$

with the speed of sound a. For the atmospheric conditions at the wind-tunnel the given Mach number corresponds to an inflow velocity of about $v_\infty = 55\,\mathrm{m\,s^{-1}}$.

PIV setup

Besides the pressure measurements, PIV-measurements were accomplished to resolve the flow field at the trailing edge of the airfoil. These investigations promise detailed information about the flow close to the porous trailing edge and the behaviour of turbulence. The Reynolds number and Mach number for the PIV-experiments were equal to those of the pressure measurements ($Re = 1\,000\,000$, $Ma = 0.15$). Due to the higher experimental efforts of PIV-measurements only a limited set of porous materials were investigated at two angles of attack each.

The PIV-system employed is a 2D-setup measuring the flow field at the symmetry plane of the wing. The captured image window is restricted to the area over the porous trailing edge.

The big challenge of the setup is that the surface of the porous media leads to diffusive reflections of the laser beam corrupting the image quality. In order to counteract this effect a tangential laser sheet was used which was directed from downstream over the airfoil and, thus, hardly touches the porous material. The principal setup with the lenses and mirrors is shown in figure 6.22.

The PIV-setup includes a ImagerProX11M camera with a CCD image sensor with a resolution of 4032×2688 pixels. The tracer particles are lightened by a Quantel Twin Nd:YAG laser with two Brilliant optical heads. This double pulsed laser has a maximum pulse energy of 200 mJ. The output wave length of 1064 nm is halved inside a frequency-doubling unit in order to get human visible green light with a wave length of 532 nm. Di-Ethyl-Hexyl-Sebacat (DEHS) droplets with a typical size of 1 µm were used as tracer particles. They were added upstream of the wind-tunnel settling chamber.

The resulting images were processed with the software LaVision Davis 7.2 utilizing a multi-pass algorithm. The resulting window size was adjusted depending on the image quality and comprises a range between 16×16 pixels and 128×128 for obtaining one vector. The window overlap for obtaining a neighboring vector was set to 50 %. In order to get information about the mean-flow data and the Reynolds stresses 1500 double pictures were taken for each flow case.

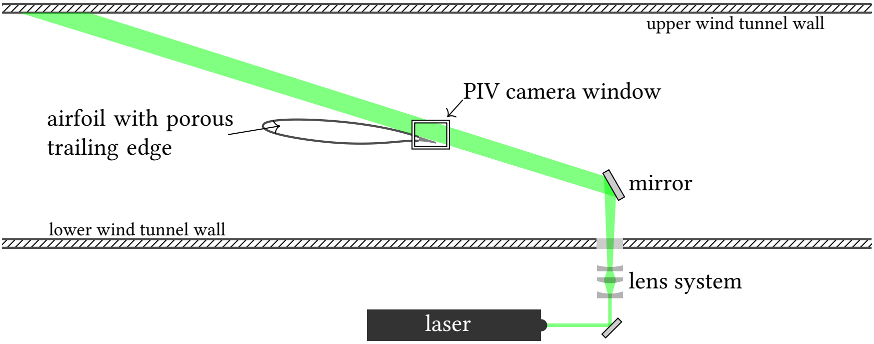

Figure 6.22.: Sketch of PIV-setup in wind-tunnel experiment of DLR-F16 wing.

6.2.2. Evaluation of experiments

The evaluation of the experiments is basically split into the evaluation of the pressure data and the evaluation of the PIV-data. Firstly, the pressure data supply information about the effect of the porous trailing edges on the lift coefficient c_l of the airfoil. Then, the PIV-data are used in order to give a more detailed insight into the effects of the porous trailing edge on the velocity field and the turbulence quantities.

Details about the computation of the lift coefficient $\mathbf{c_l}$

The lift coefficient c_l is computed by integration of the pressure coefficients c_p around the airfoil. The two coefficients are defined as follows:

$$c_p = \frac{p - p_\infty}{\frac{\rho}{2} v_\infty^2} \qquad\qquad c_l = \frac{1}{c} \oint c_p \, \mathrm{d}x \tag{6.6}$$

where p_∞ and v_∞ are the static pressure and velocity far away from the airfoil and c is the airfoil chord length.

Figure 6.21 indicates that there are no pressure taps positioned along the last 20 % of the airfoil. This is a consequence of the design. In order to obtain meaningful lift coefficients the pressure behaviour is linearly approximated at the last 20 % by setting the pressure coefficient at the trailing edge to the last available value of the lower airfoil side (see figure 6.23 left). The error made regarding the lift coefficient c_l is estimated by the panel code XFOIL [22] where the lift coefficient was computed for both the resolved and the not resolved trailing edge (figure 6.23 right). It shows that independent of the angle of attack the error of the lift coefficient c_l is approximately 0.015. These significant values will of course distort the α-c_l curves. But as the error occurs for all different porous trailing edges it can at least be expected that the differences between the lift curves have the correct magnitude.

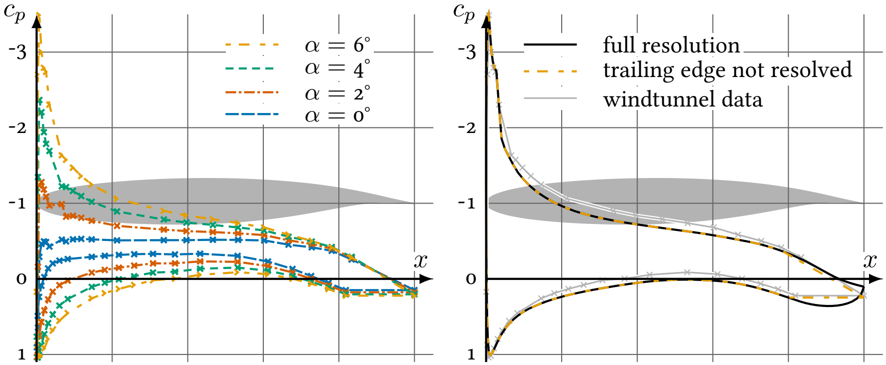

Figure 6.23.: Left: c_p-distributions from wind-tunnel measurements of DLR-F16 airfoil with solid trailing edge at $Re = 1\,000\,000$. Right: c_p-distribution from XFOIL for $\alpha = 6°$ with and without resolved trailing edge.

Effect of the porous trailing edges on the pressure distributions

The main effect of the porous trailing edge on the flow can be assigned to a relaxation flow between the upper low-pressure side and the lower high-pressure side. This flow through the trailing edge leads to smaller pressure differences which can primarily be recognized at the upper side as can be seen in figures 6.24 and 6.25. Regarding the trailing edges made of sintered bronze powder (SBP 60 and SBP 120) it becomes apparent that a higher permeability leads to a stronger effect. The porous aluminum PA 80-110 does not fit into this scheme as its permeability lies in between the two sintered bronze powders but the pressure distribution is at a slightly lower level. However, a later evaluation of the lift coefficients (see figure 6.26) will show that the porous aluminum PA 80-110 is nevertheless in between the sintered bronze powders which indicates the wind-tunnel reference pressure for the porous aluminum was slightly wrong so that the whole pressure curve is shifted to smaller c_p-values.

The effect of sheeted trailing edges — the sintered fibre felts — on the pressure distribution is much higher. This is obvious since the thickness of the sheetings is smaller whereas the permeability of the fibre felts are similar to the permeabilities of the trailing edges cut from solid blocks. The consequence is a much higher effective permeability leading to significantly increased relaxation flows through the trailing edges.

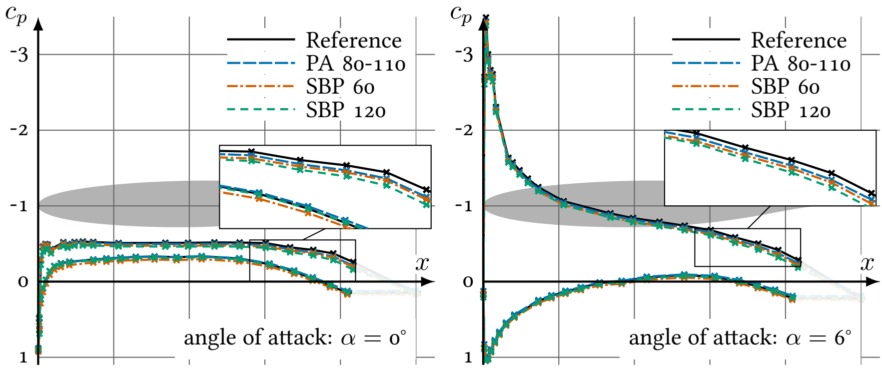

Figure 6.24.: Measured pressure distributions of the DLR-F16 airfoil at $Re = 1\,000\,000$ for trailing edges cut from solid blocks at $\alpha = 0°$ and $6°$.

Comparison of lift for different porous trailing edges

An idea of the behaviour of the lift curves for the different porous trailing edges is already given in the discussion of the pressure distributions. It turns out that the permeability has a direct impact on the loss of lift. This can be recognized in figure 6.26 to the left where the usage of sintered bronze powder SBP 120 with the highest permeability leads to the highest loss of lift. On the contrary, the sintered bronze powder SBP 60 with the lowest permeability leads to the smallest loss of lift.

The effect of the different sheet materials appears to be very similar if the total permeability was considered which is defined as the permeability divided by the sheet thickness.

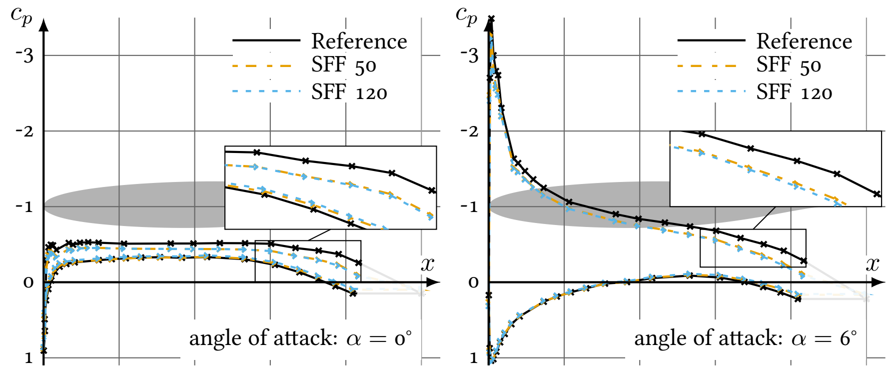

Figure 6.25.: Measured pressure distributions of the DLR-F16 airfoil at $Re = 1\,000\,000$ for sheeted porous trailing edges at $\alpha = 0°$ and $6°$.

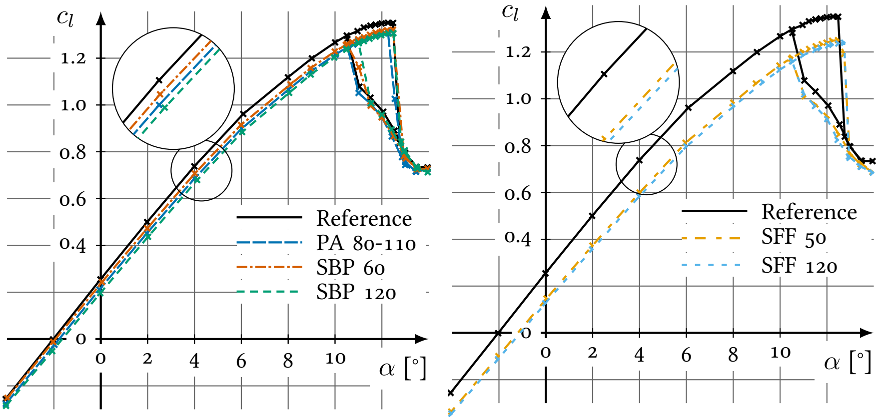

Figure 6.26.: Lift coefficients c_l at the mid-section of the wing over the angle of attack α for different porous trailing edges. The ambiguous lift coefficients at high angles of attack are a hysteresis effect, originating from measuring rising and declining angles of attack.

3D-corrections for angle of attack

The rather small span of the porous trailing edge which is equal to the chord length (see figure 6.18) indicates the results underlie 3D-effects. These effects are mainly based on the circulation distribution along the complete wing. The outer wing sections without porous trailing edges generate more circulation than mid-section with porous trailing edge. However, the exchange of circulation information between the different wing sections leads to a smooth circulation curve along the complete wing. Thus, the lift is increased at the wing section with porous trailing edge compared to a 2D-wing. In order to make the experiments comparable to 2D-cases corrected lift curves are constructed by computing a modified angle of attack. The magnitude of the 3D-effect can be approximated by the panel code XFLR5 [83] through imitating the loss of lift at the porous wing section with a deflected flap. The result of such a computation with 2° flap upwards deflection is shown in figure 6.27. It immediately becomes clear that at the mid-section of the wing ($x = 0$), the loss of lift for the 3D-case is much less compared with the 2D-case.

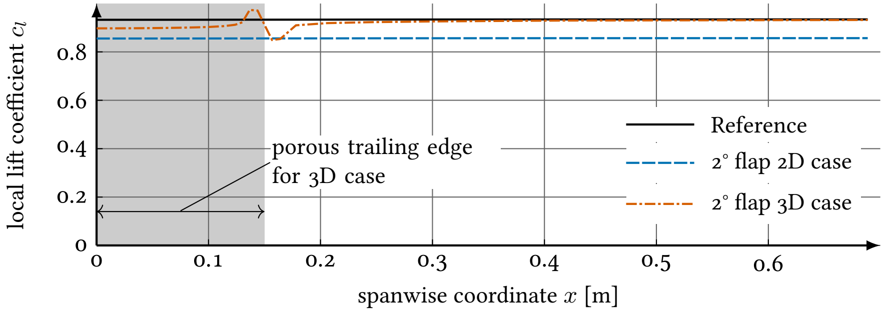

Figure 6.27.: 3D-effect on the lift distribution for a porous trailing edge with limited width.

With the help of several XFLR5 evaluations at different angles of attack it turns out that a suitable relation for a corrected angle of attack is

$$\alpha_{\text{corrected}} = \alpha + C \cdot \left(c_{l,\text{ref}}(\alpha) - c_{l,\text{por}}(\alpha)\right) \tag{6.7}$$

where $c_{l,\text{ref}}(\alpha)$ and $c_{l,\text{por}}(\alpha)$ are the local lift coefficients for the nonporous and the porous trailing edge at the uncorrected angle of attack α. The constant C is set to $C = 10.5°$. The corrected curves originating from figure 6.26 are shown in figure 6.28. Since the correction is expected to fail after the wing stalls it is limited to smaller angles of attack.

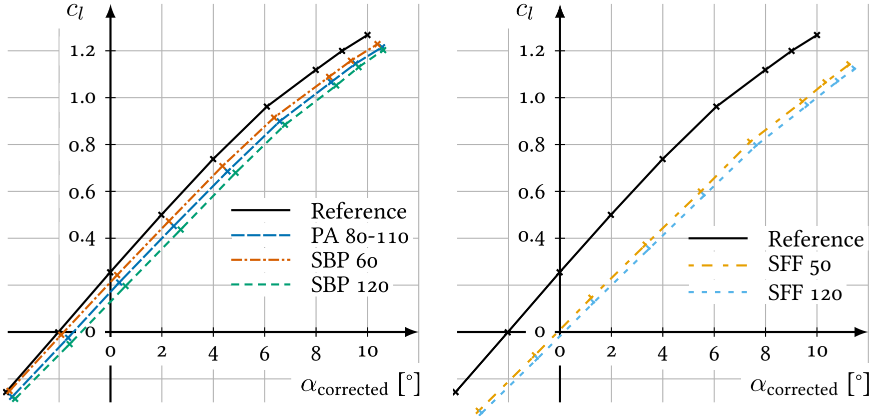

Figure 6.28.: Measured lift coefficients c_l at the mid-section of the wing using 3D-corrected angles of attack according to equation (6.7)

Effect of porous trailing edge on flow field

To gain a more detailed understanding of the flow the PIV-data are evaluated for two different angles of attack. Figure 6.29 shows the flow at the trailing edge over different porous regions for an angle of attack $\alpha = -0.5°$. Figure 6.30 displays the same picture at a modified angle of attack of $\alpha = 6°$. The most visible effect compared to the nonporous reference can be recognized for the sintered fibre felt SFF 120 which also experiences the highest loss of lift. The turbulence (which is represented by $\overline{v'_x v'_x} + \overline{v'_z v'_z}$) appears to be strongly effected by the porous trailing edge. Closely above the trailing edge turbulence is reduced (especially for the case SFF 120) which indicates that the turbulent kinetic energy is strongly damped while the air passes through the trailing edge from the lower to the upper side of the airfoil. But still, the turbulence in the wake is increased in case of the porous trailing edges. This is mainly caused by the increased velocity gradients in the flow field which yield a higher production rate of turbulence. The effect can be clearly recognized in the picture of the sintered fibre felt (SFF 120) where the peak of the turbulence follows the regions of highest velocity gradients.

The two figures 6.31 and 6.32 show the velocity profiles of the different porous trailing edges in more detail. Analyzing the velocity profile of the porous aluminum PA 80-110 shows that the velocity is only influenced above and downstream of the trailing edge but not upstream. In case of the very permeable trailing edge which is only covered with a thin layer of sintered fibre felt SFF 120 the boundary layers are completely different. Here, an effect is also visible upstream. With the help of the

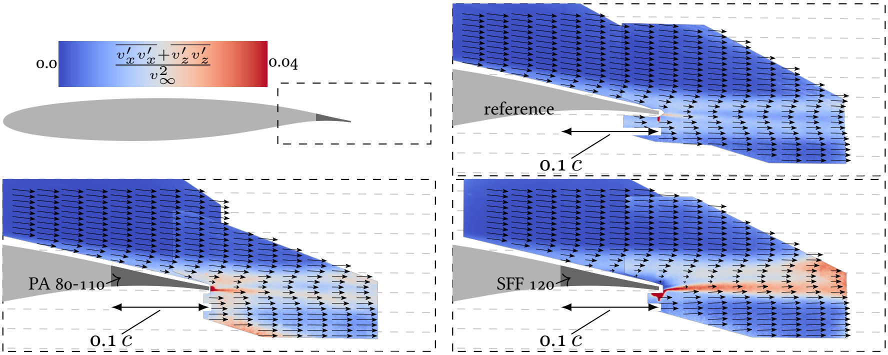

Figure 6.29.: Flow field at various porous trailing edges of the DLR-F16 airfoil at an angle of attack $\alpha = -0.5°$. The vectors are interpolated data inside the PIV-images. The dashed lines in the background show the direction of the farfield velocity. The Reynolds number is $Re = 1\,000\,000$.

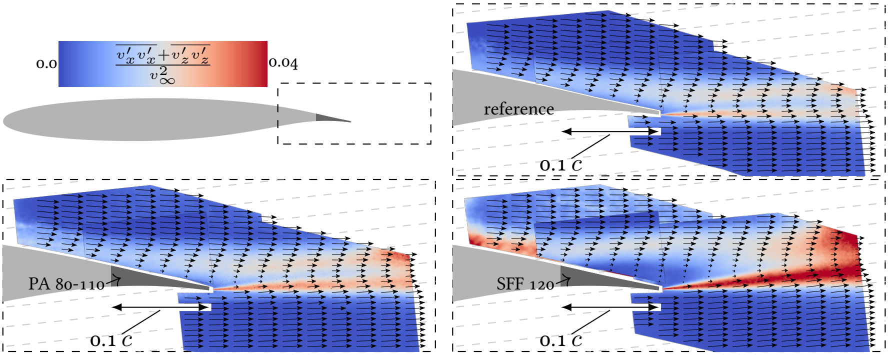

Figure 6.30.: Flow field at various porous trailing edges of the DLR-F16 airfoil at an angle of attack $\alpha = 6°$. The vectors are interpolated data inside the PIV-images. The dashed lines in the background show the direction of the farfield velocity. The Reynolds number is $Re = 1\,000\,000$.

point of the smallest velocity in the wake one can learn that the down-deflection of the fluid is significantly weakened for the porous media. As a result, a decrease of lift can be expected which is already visualized in figure 6.26.

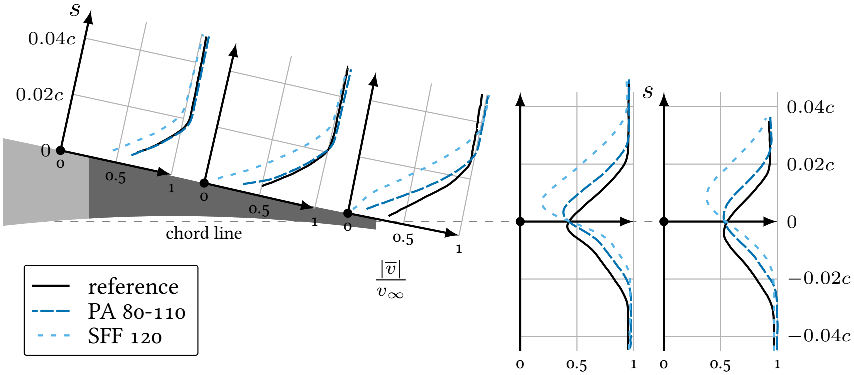

Figure 6.31.: Velocity plots along the trailing edge and in the wake of the airfoil at an angle of attack of $\alpha = -0.5^\circ$ and a Reynolds number of $Re = 1\,000\,000$. The nonporous reference is compared against two different porous trailing edges (porous aluminum PA 80-110 and sintered fibre felt SFF 120).

6.2.3. Numerical setup

The numerical computations are performed on 2D-grids which are constructed on basis of the geometry at the mid-section of the wind-tunnel model. Transition is either set at the location of the transition tape in the experiment or at the position of the pressure suction peak for high angles of attack (see figure 6.33). O-type meshes are used leading to a rather high resolution at the trailing edge. The mesh of the nonporous reference case is equal to the mesh of the cases with solid porous trailing edges (porous aluminum and sintered bronze powder) with the exception that the porous trailing edge is also filled with mesh points. The mesh construction of the sheeted trailing edges (sintered fibre felt) is more sophisticated leading to a slightly different mesh. All three meshes have a point number of about 40 000 and are shown in figure 6.34. The mesh spacing at the viscous walls is about 1×10^{-5} of the airfoil's chord length c. This corresponds to an average spacing of 0.5 in inner y^+-coordinates. Very close to the nose the spacing increases to a maximum value of $\Delta y^+ = 1.5$ for the $\alpha = 8^\circ$ case.

Mesh convergence has been checked on basis of the mesh for the wing where the trailing edge is made of porous aluminum PA 80-110. Three different mesh levels

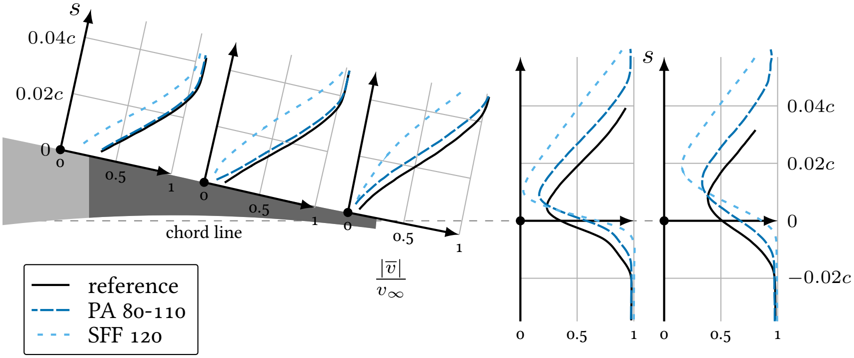

Figure 6.32.: Velocity plots along the trailing edge and in the wake of the airfoil at an angle of attack of $\alpha = 6°$ and a Reynolds number of $Re = 1\,000\,000$. The non-porous reference is compared against two different porous trailing edges (porous aluminum PA 80-110 and sintered fibre felt SFF 120).

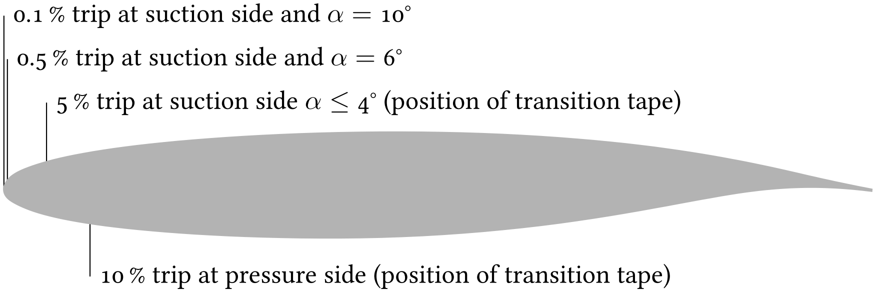

Figure 6.33.: Position of tripping to enforce transition for numerical computations. The positions are either set close to the pressure minimum for high angles of attack or at the location of the transition tape as it was used in the experiment.

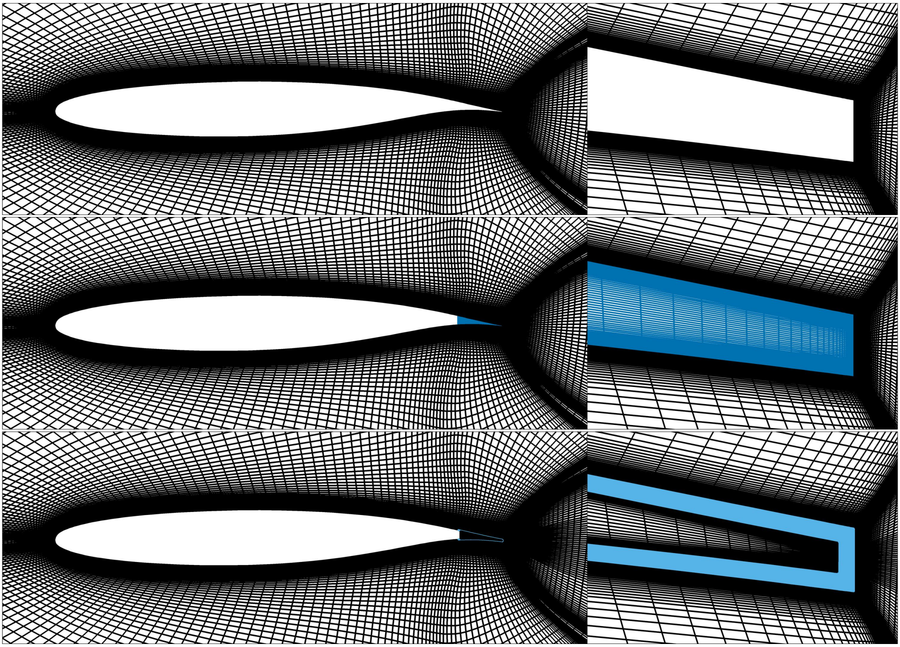

Figure 6.34.: Meshes for the DLR-F16 airfoil without porous trailing edge (top), for solid porous trailing edges (middle) and for the SFF 120-sheeted trailing edge (bottom). The porous regions are emphasized by a different color.

have been tested with about 20 000, 40 000 and 100 000 points (see figure 6.35). The comparison of the lift curves in figure 6.36 shows no visible difference between the two finer meshes. This observation justifies the use of the 40 000 point meshes.

Steady state simulations were accomplished for all cases. Typical residual progresses for density, momentum, Reynolds stress and homogeneous turbulent dissipation-rate are shown in figure 6.37. Each 1000 iterations an averaged lift coefficient is computed from the last 1000 values. The solver is stopped as soon as the change of two averaged lift coefficients c_l goes below 1×10^{-6}. The averaging procedure is required as the blunt trailing edge tends to make the velocity field unsteady such that for some cases the lift coefficient would not always converge to a completely steady value.

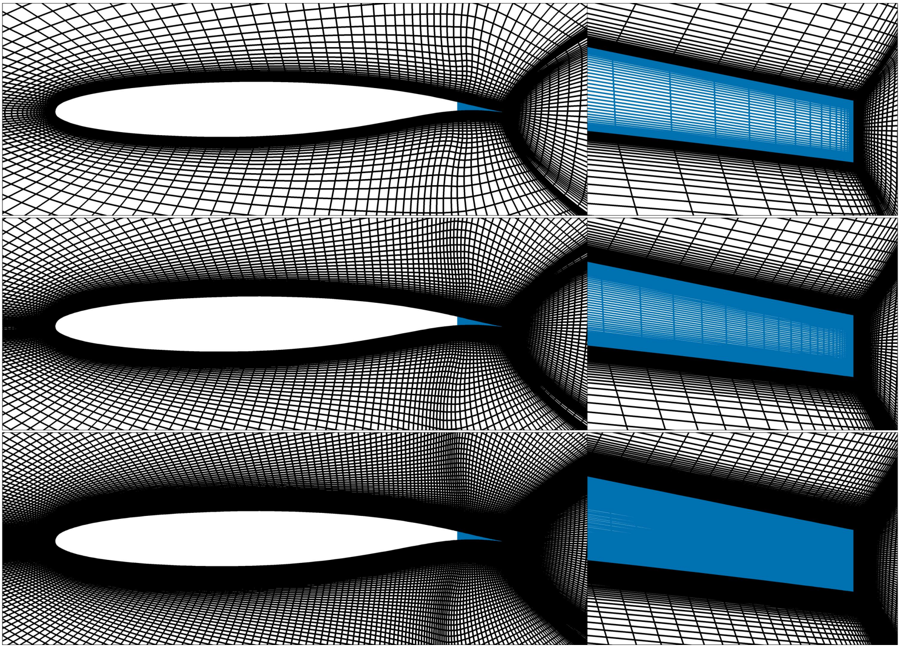

Figure 6.35.: Meshes for the DLR-F16 airfoil with porous trailing edge for different fineness levels used for the mesh convergence study. The porous region (i.e. the trailing edge) is emphasized by a different color.

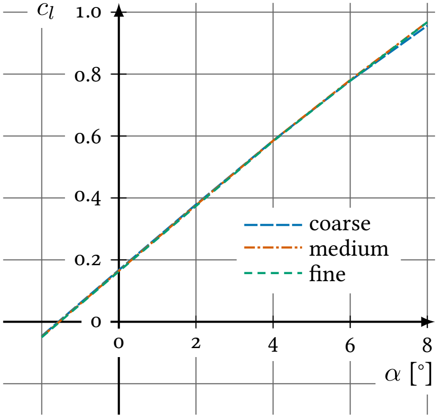

Figure 6.36.: Demonstration of mesh convergence for the DLR-F16 airfoil with porous trailing edge (PA 80-110) with the help of the lift curves. The results are obtained with the meshes shown in figure 6.35.

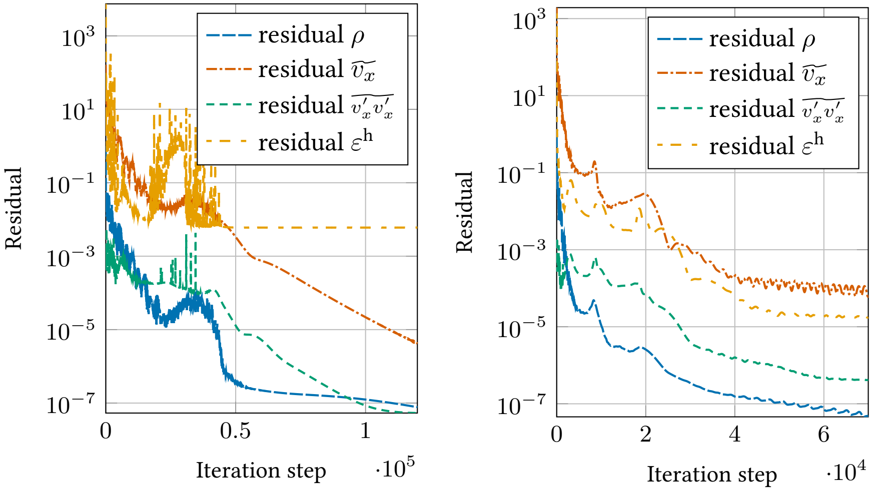

Figure 6.37.: Residual progress of DLR-F16 airfoil simulations with nonporous edge (left) and with the porous trailing edge PA80-110 (right). (Angle of attack: $\alpha = 4°$)

6.2.4. Numerical results

Before comparing and evaluating the quality of the simulations with the help of the experiments the simulation data are used to provide a more detailed insight into the flow physics for wings with porous trailing edges. In contrast to the experiments the flow field is fully known and can be analyzed much better.

Figure 6.38 identifies the main mechanism of the flow through the porous trailing edge. The air passes through the porous medium from the airfoil pressure to the airfoil suction side where the driving force is the pressure gradient. The main effect of this relaxing flow through the trailing edge is a decambering of streamlines leading to a smaller pressure difference between upper and lower airfoil side which means reduced lift.

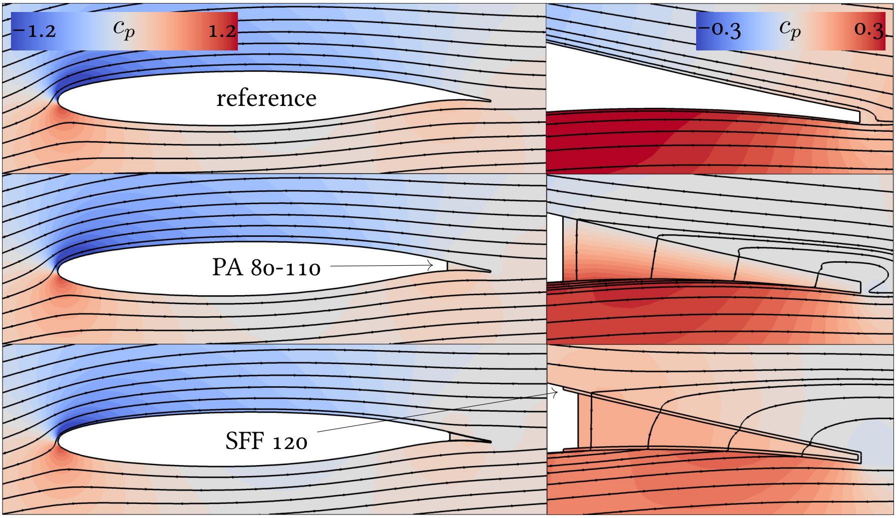

Figure 6.38.: Pressure distributions around DLR-F16-airfoils with different trailing edges at an angle of attack of $\alpha = 6°$.

A contour plot of the turbulence shows figure 6.39. If compared to experimental result in figure 6.30 it becomes visible that the basic behaviour of turbulence above the wing is similar but the lower edge of the blunt trailing edge induces much more turbulence in the experiments. It is also apparent that practically no turbulence exists inside the porous trailing edge which is an effect of the strong Darcy and Forchheimer damping terms in the turbulence equations.

Figure 6.40 shows a more detailed view onto the progress of the boundary layers over the trailing edge. The effect of the air passing the trailing edge is mirrored in

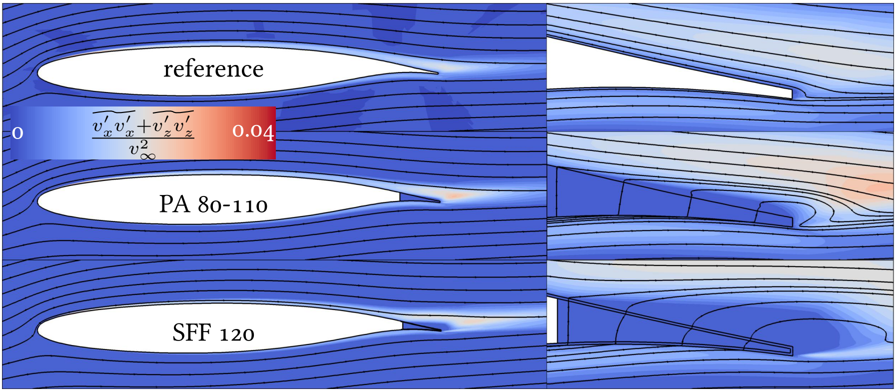

Figure 6.39.: Turbulence distributions around DLR-F16-airfoils with different trailing edges at an angle of attack of $\alpha = 6°$.

the boundary layer thicknesses. While the thickness for the porous trailing edges on the suction side grows it decreases on the pressure side. Especially the turbulence profiles show that the wake runs at a higher position indicating the decambering of the streamlines.

6.2.5. Comparison of simulations and experiments

The previous sections discussed experiments and numerical results for the DLR-F16 airfoil with porous trailing edges separately. The simulations show consistent results reflecting the expected flow phenomena. However, knowledge of the accuracy of the simulations is needed for using them in other applications. The following sections compare the experiments with the numerical results in order to obtain insight into the quality of the VRANS-implementation.

Comparisons of lift curves

Figure 6.41 displays the lift coefficients c_l of experimental and numerical results. The curves are not exactly reproduced even for the reference case. This indicates that there is a wind-tunnel wall interference in the experiments leading to the deviation in lift. However, the focus of the validation computations concentrates on the effect of the porous trailing edges. It can be seen in the figures that the loss of lift is well-predicted. Still, there is one flaw in the results: The numerical lift curve of the sintered bronze powder SBP 120 shows less lift losses than the porous aluminum PA 80-110 even though the permeability is higher. This seems to be a shortcoming

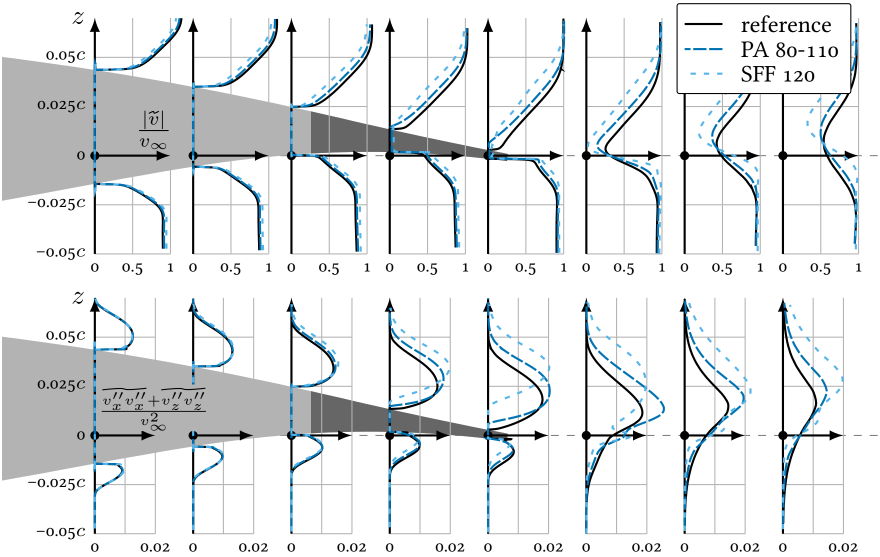

Figure 6.40.: Comparison of boundary layers close to the trailing edge of the DLR-F16 airfoil for different porous trailing edges. (Angle of attack: 6°)

of the theoretical model which occurs for small porosities and high permeabilities. This case will be investigated in more detail later in section 6.2.6.

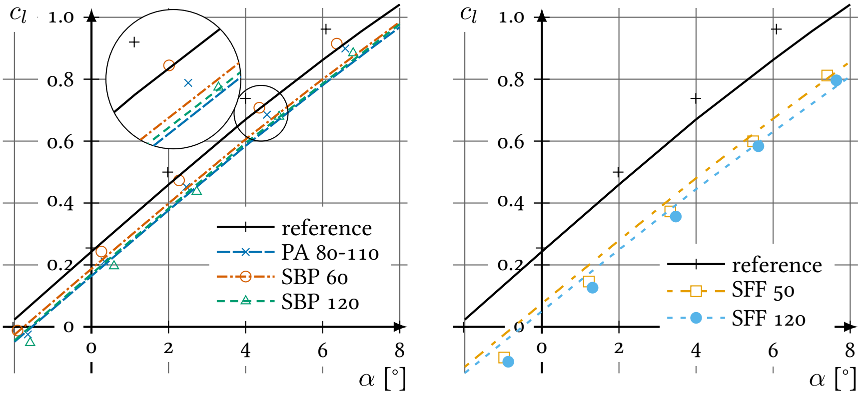

Figure 6.41.: Lift curves of different trailing edges where experimental (symbols) data are compared against numerical (lines) results. The left diagram shows the solid porous trailing edges and the right plot presents the sheeted trailing edges.

Comparison of boundary layers

Even though the lift curves for the nonporous and porous trailing edge match well with the experiments it is of importance that the changes are also reflected in the flow physics. Otherwise, reliable solutions cannot be guaranteed. Deeper insight into the flow phenomena is obtained with the help of the PIV-measurements. These are available for the angles of attack of $\alpha = -0.5^\circ$ and $\alpha = 6^\circ$. They are compared with VRANS-computations at equal lift coefficients. The corresponding angles of attack are listed in table 6.3.

	reference		PA 80-110		SFF 120	
c_l	0.193	0.953	0.157	0.898	0.070	0.796
experimental α	-0.5°	6.0°	-0.5°	6.0°	-0.5°	6.0°
numerical α	-0.5°	7.0°	-0.1°	7.3°	0.2°	7.9°

Table 6.3.: Lift coefficients c_l and angles of attack α for the comparison of experimental PIV-data with numerical results.

Starting with the angle of attack $\alpha = -0.5^\circ$ the boundary layers of the velocity $|\widetilde{v}|$ and the turbulence in terms of $\frac{\widetilde{v'_x v'_x} + \widetilde{v'_z v'_z}}{v_\infty^2}$ are plotted at different positions for different trailing edges in figures 6.42 and 6.43. Note, that the turbulence quantity $\widetilde{v'_x v'_x} + \widetilde{v'_z v'_z}$ in the experiments is computed with the time-averaged Reynolds stresses whereas the simulation uses the density-weighted time-averaged values. Since the comparisons in this paper are carried out at small Mach numbers compresibility effects are small and therefore the time average is equal to its density-weighted counterpart.

The computed boundary layer profiles of the velocity $|\widetilde{v}|$ over the trailing edge match very well with the experiments. The velocity profiles are affected by turbulence and therefore, the turbulence profiles should also agree. They do indeed, even though the differences are larger. It is assumed, that these differences originate from the much more sensitive determination of the turbulent kinetic energy: Firstly, a typical value of a velocity fluctuation v' is about 5-10 times smaller than the mean velocity and hence, is much harder to capture accurately. Secondly, each erroneous velocity vector which has not been filtered in the PIV-velocity field contributes to the turbulent kinetic energy. The second issue asks for very strict filters which can even lead to under-predicted turbulence values. However the rather big deviations of the turbulence quantity for the sintered fibre felt SFF 120 are not expected to be due to measurement errors. This assertion is underlined by figure 6.45 which shows the results at a high angle of attack of $\alpha = 6^\circ$. In this figure the turbulence is over-predicted by about 20 % by the numerical code leading to a slightly thicker boundary layer. Since this is a known phenomenon of the *JHh-v2* turbulence model for cases that are close to separation the deviations are accepted to be small enough.

The differences of the turbulence are much higher in the wake. Only the upper peak value at the first wake position is rather well reproduced by the numerical computations. In the downstream wake position this upper peak dissipated much more than it did in the experiments. It is assumed that this is a consequence of the quickly decreasing mesh density. No further investigation is spent to this issue as the far wake is of minor interest for predicting the integral force coefficients of the wing. The lower turbulence peak is very high for the experimental data while it is hardly visible for most the numerical data. In figure 6.30 one can see that the turbulence peak of the experiments starts at the lower corner of the blunt trailing edge. It can be assumed that due to the bluntness there is a local instationary flow which induces turbulent fluctuations. Obviously, the numerical computation do not reproduce this behaviour, either because of a lacking mesh resolution or because of the nature of the steady state simulations.

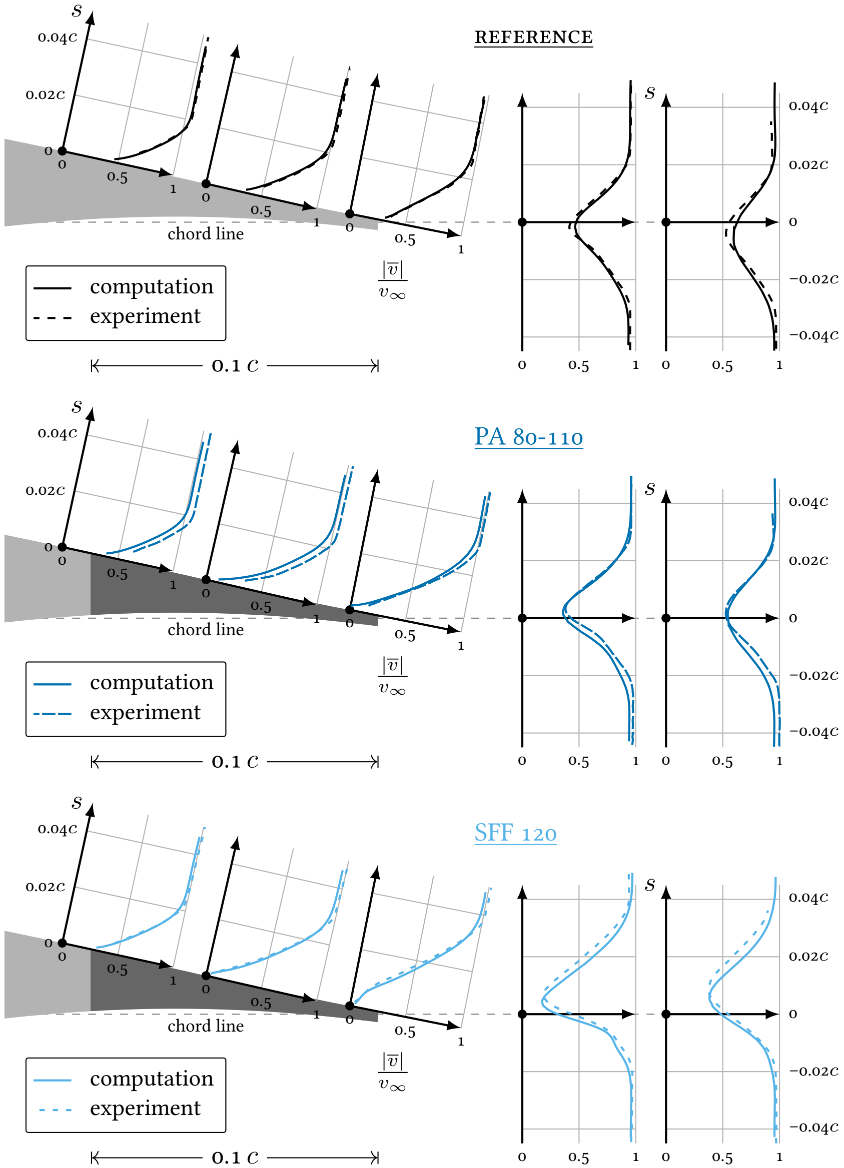

Figure 6.42.: Velocity profiles over different trailing edges of the DLR-F16 airfoil. The angle of attack for the experiments is $\alpha = -0.5^\circ$. The computation results are shown at an angle of attack at equal lift coefficients c_l as given in table 6.3.

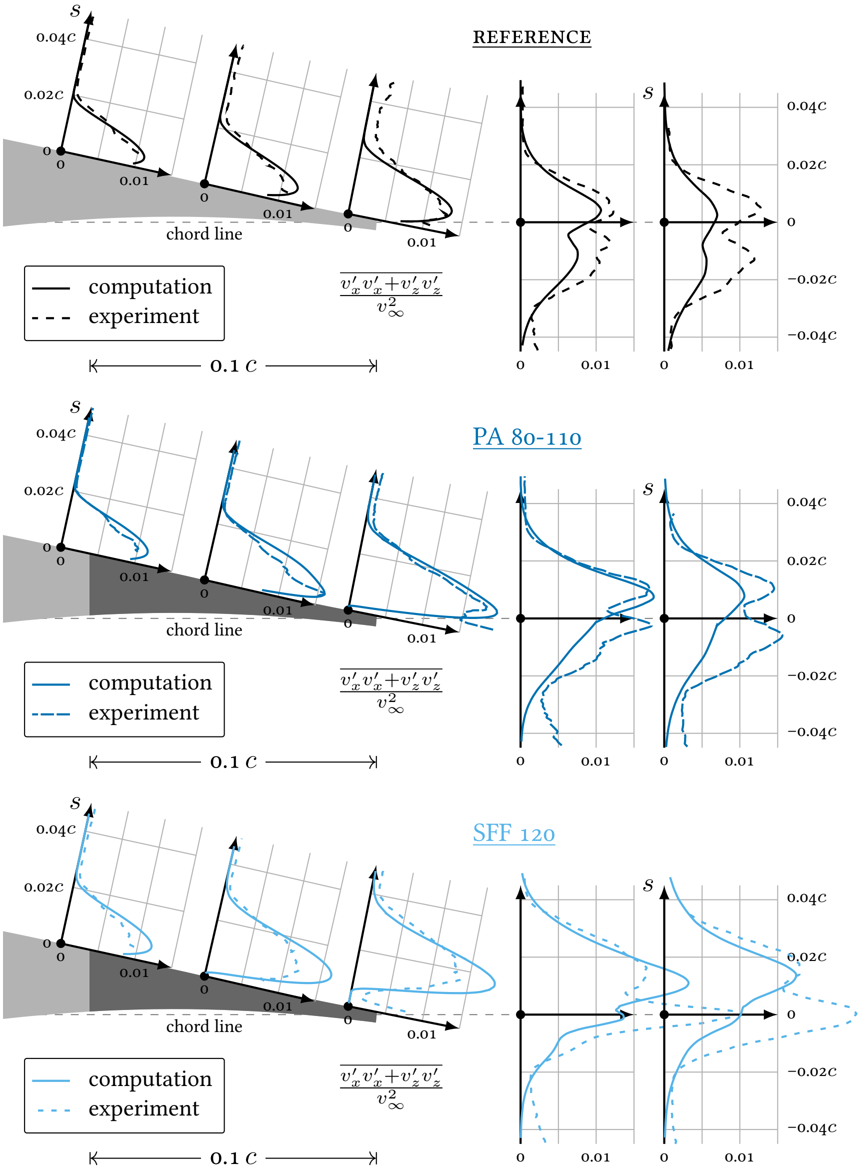

Figure 6.43.: Turbulence profiles $\overline{v'_x v'_x + v'_z v'_z}$ over different trailing edges of the DLR-F16 airfoil. The angle of attack for the experiments is $\alpha = -0.5^\circ$. The computation results are shown at an angle of attack at equal lift coefficients c_l as given in table 6.3.

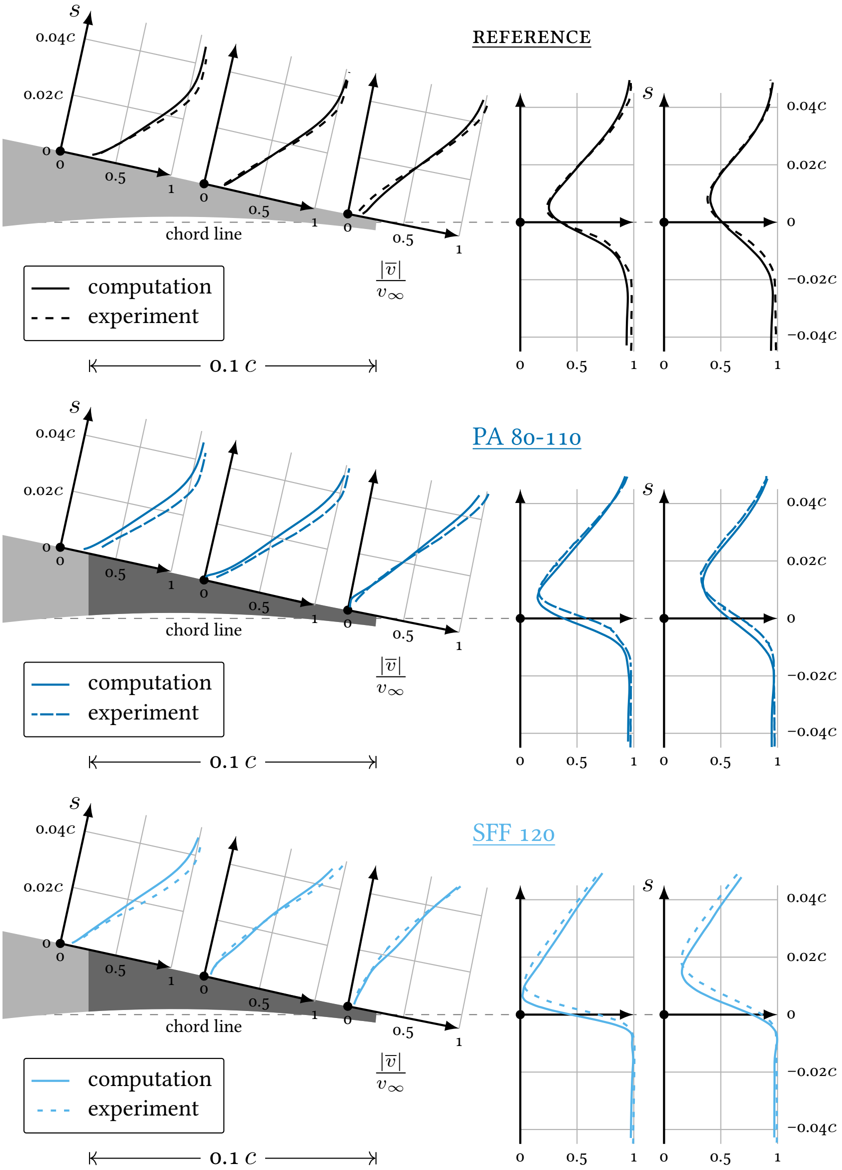

Figure 6.44.: Velocity profiles over different trailing edges of the DLR-F16 airfoil. The angle of attack for the experiments is $\alpha = 6°$. The computation results are shown at an angle of attack at equal lift coefficients c_l as given in table 6.3.

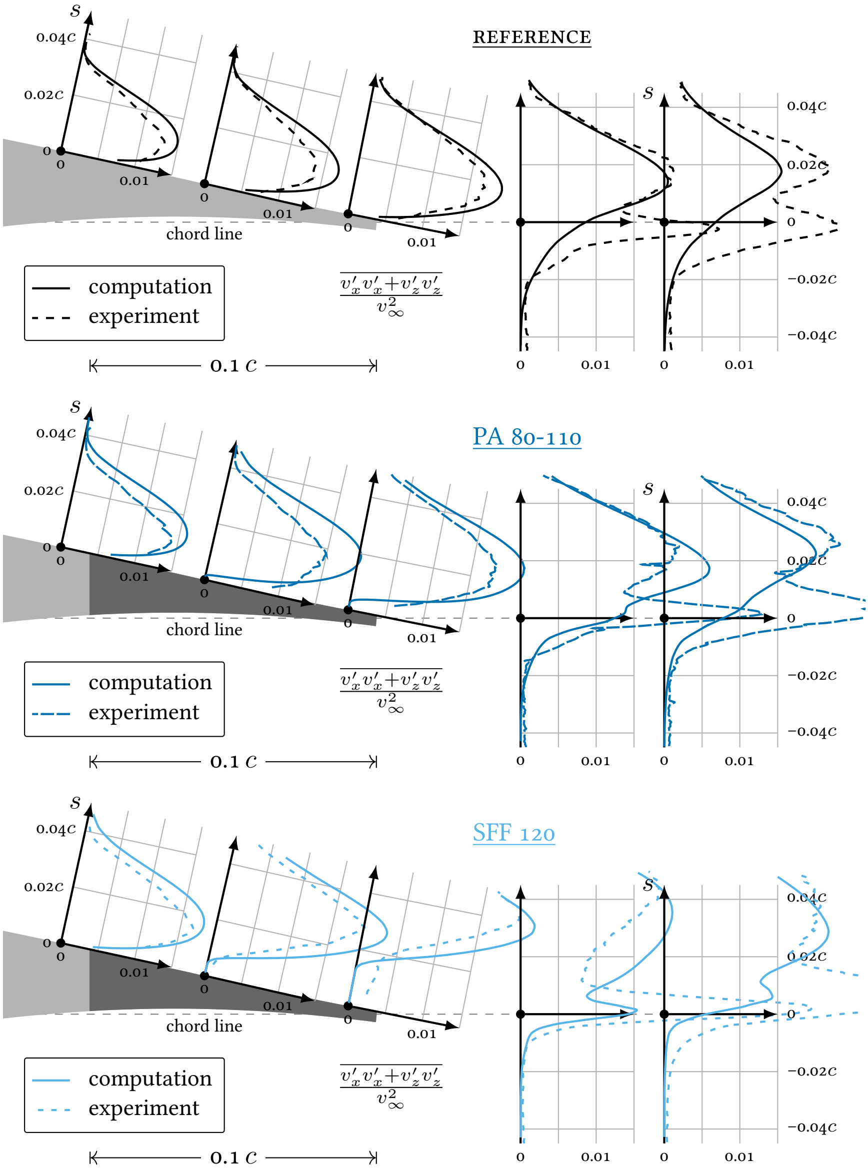

Figure 6.45.: Turbulence profiles $\overline{v_x'v_x' + v_z'v_z'}$ over different trailing edges of the DLR-F16 airfoil. The angle of attack for the experiments is $\alpha = 6°$. The computation results are shown at an angle of attack at equal lift coefficients c_l as given in table 6.3.

6.2.6. Parameter sensitivities for numerical computations

Finally, some parameter sensitivities on the results of the numerical computations will be given. These include the jump coefficients β and β_t and the porosity ϕ. In the previous sections the jump coefficients had been set to zero as they are expected to be material dependent but no explicit value has been computed yet. The sensitivities can help to classify their importance in the airfoil computations. The investigation of the porosity ϕ is presented since it plays a significant role in the interface conditions (3.67) to (3.69) and its behaviour is important to explain the trends of the lift curves in figure 6.41.

The effect of the porosity

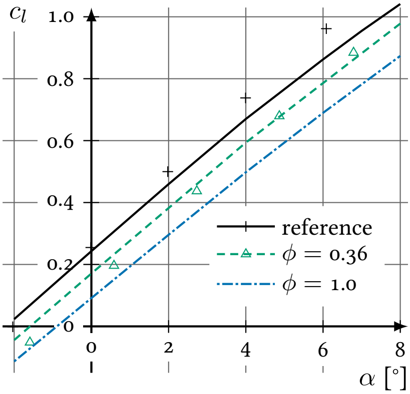

Figure 6.46.: Lift coefficient c_l over angle of attack α for the case SBP 120 with the real porosity of $\phi = 0.36$ and a very high porosity of $\phi = 1.0$. Additionally, the experimental data are shown as symbols.

Recall figure 6.41 where the numerical computations of the sintered bronze powder SBP 120 shows higher lift coefficients than the porous aluminum PA 80-110 even though the permeability κ is higher for the sintered bronze powder. Also, the experimental data contradict the numerical behaviour. The reason for this lies in the effect of the porosity ϕ. Figure 6.46 shows the sintered bronze powder SBP 120 recomputed with a fictive porosity of $\phi = 1.0$. Obviously, the reduction of lift compared to the nonporous reference is about twice the lift reduction of the computations with the real porosity of $\phi = 0.36$. If compared to the experiments the case with high porosity does match better.

The reason for the big differences can be explained with the pressure distributions in figure 6.47. At the lower side of the porous trailing edge the pressure at both sides of the nonporous-porous interface is equal for the porosity $\phi = 1.0$ whereas the small porosity case shows a pressure jump. For the high porosity values, this leads to much higher pressure gradients inside the porous media which drives the air through the trailing edge.

One question remains: Wherein lies the origin of the pressure jump for the small porosity values? Besides others, the nonporous-porous interface condition given by equation (3.69) is based on the assumption that the velocity multiplied with the porosity at the porous interface side is equal to the velocity at the nonporous interface side. This is widely accepted in literature of incompressible flow, e.g. [55] or [10] and has been maintained here with minor modifications to yield in the compressible interface conditions (3.67) to (3.69). However, in order to fulfill energy conservation across the interface the pressure must jump when the velocity jumps. This is clearly shown in figure 6.47. Thus, in summary, the pressure jump is the result of the combination of energy conservation and the definition of the velocity jump across the interface.

In order to obtain a better match with the experiments the interface conditions could be modified by holding the velocity component tangential to the nonporous-porous interface constant. However, this would mean to depart from existing literature. Alternatively, the pressure jump can be circumvented by setting the porosity to $\phi = 1$ while keeping the existing interface conditions. Note, that for this procedure one has to ensure that the magnitude of the Darcy and Forchheimer terms does not change.

Even though the suggested modifications significantly improve the results it is not clear whether they really follow physical principles. In order to resolve this problem, dedicated DNS-computations should be consulted. Since such simulations are currently not available, the choice of the correct model remains an open question.

The effect of jump coefficients

The effect of the jump coefficients is shown for the trailing edge made of porous aluminum PA 80-110. The lift curves for various parameter variations of the jump coefficient β and its turbulent counterpart β_t are plotted in figure 6.48. The used parameter ranges are based on the investigations of the channel case CUB in section 6.1.3. The figure shows that the turbulent jump coefficient β_t has no significant effect on the lift coefficient c_l. This is expected since the turbulent kinetic energy is very small at the nonporous-porous interfaces and consequently, the left hand side of equation (3.80) becomes insensitive to β_t.

In contrast, the jump coefficient β appears to have a noticeable effect on the lift coefficient because a negative value of β reduces the velocity at the interface (see the leftmost magnification area of figure 6.49). The smaller velocity at the interface decreases the pressure jump which is discussed in the previous section about the porosity effect leading to a higher mass flow through the porous trailing edge. This

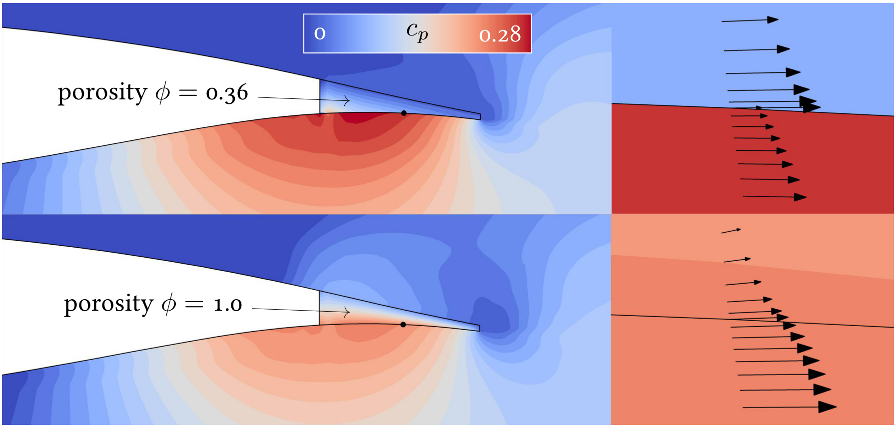

Figure 6.47.: Comparison of pressure coefficient c_p at the trailing edge for the case SBP 120 with the real porosity of $\phi = 0.36$ and an increased porosity of $\phi = 1.0$. The right hand side shows an extremely magnified picture at the location of the black dot of the left hand side. (Angle of attack: $\alpha = 4°$)

is also highlighted in the magnification area in the center of figure 6.49 where the velocity shows higher values for the cases of the more negative jump coefficients. The rightmost magnification area shows that the wake of the cases with more negative jump coefficients is located at a higher position which indicates a reduced circulation and, hence, a reduced lift.

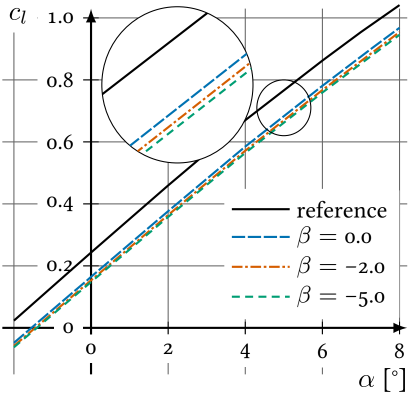

Figure 6.48.: Comparisons of lift curves for different jump coefficients β (left) and different turbulent jump coefficients β_t (right). In the computations the porous media properties of the porous aluminum PA 80-110 were used.

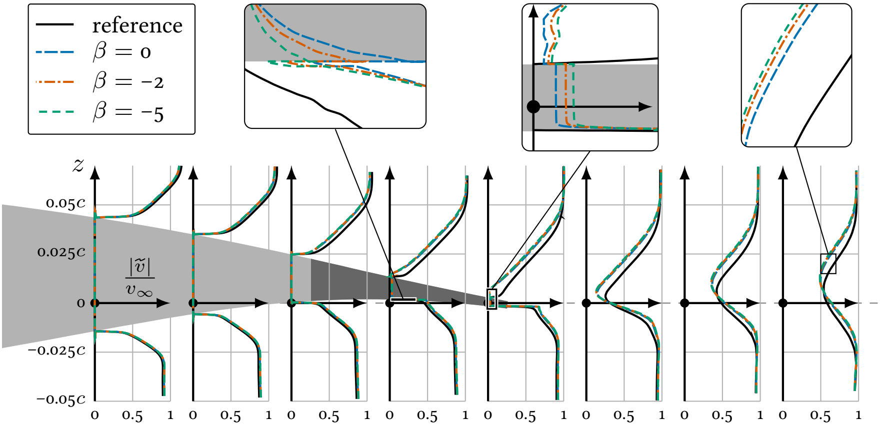

Figure 6.49.: Velocity profiles at the trailing edge of the DLR-F16 airfoil with porous trailing edge (PA 80-110) at different jump coefficients β. (Angle of attack: $\alpha = 6°$)

7. Conclusions and future work

It was mentioned in the introduction that acoustic researchers proved an idea to significantly reduce the trailing edge noise of aircraft wings. The noise reduction is achieved by making the trailing edge permeable. While this demonstrates one case in which porous media are used in context of aerodynamically sensitive surfaces, many more applications exist. There might be other logical positions for porous media like the wing tips or the landing gears and porous media could also damp the noise immission of the engines into the aircraft structure. The latter case could greatly improve the comfort level in civil aviation. While these kinds of investigations are in progress, it is of importance to hold pace with developing tools which can predict the effects of the porous media on the aerodynamic performances. The present work takes a step towards providing such aerodynamic simulation tools.

The challenge for simulating aerodynamic flow over porous media of civil aircraft arise from the high Reynolds numbers and thus, turbulent flow, and also from the extremely fine porous structures compared to the typical length scale like the wing chord length. Besides that, one has to be prepared for Mach numbers which can reach the transonic range. These difficulties are solved by using volume- and time-averaged Navier-Stokes equations which results in a lengthy process of modelling the newly arising unknown terms.

The modelling of the effect that the porous media generate, is based on the Darcy and Forchheimer terms. Turbulence is modelled with the *JHh-v2* turbulence model which is established to simulate transonic flow. The combination of porous media and turbulence leads to, firstly, a much more sophisticated Forchheimer term compared to the commonly used form and, secondly, to a set of adapted transport equations for the turbulence quantities (i.e. the Reynolds stresses and the homogeneous turbulent dissipation-rate).

In addition to the flow inside porous media, special treatment of the outer porous surface is provided. Transformation rules are used for the flow coming through the nonporous region, such that it correctly penetrates into the porous region and vice versa. Caution is taken that the convective mass and energy fluxes are conserved. In order to close the transformation rules, an additional transformation condition is obtained for compressible flows by following entropy conservation. Beside the convective fluxes, the diffusive fluxes are specially treated. Conservation is maintained here at least for the energy fluxes. Since diffusive fluxes are mainly based on the spatial change of flow variables like velocity or Reynolds stresses, relations are defined for these gradients. While the velocity gradient relations of this work rely mainly on the well-known jump conditions of Ochoa-Tapia and Whitaker, the relations for the Reynolds-stress gradients differ substantially from the literature as the turbulent production is now a crucial dependency.

Care is taken to implement the theoretical developments into a finite-volume flow solver. The fact that the code is thoroughly tested with different validation cases provides evidence that this work describes the theoretical fundamentals in a comprehensive manner. This includes details about the Reynolds-stress model, the implementation strategy of the equations into the solver or the computation of the integral forces which act on porous surfaces or the equations of state.

In order to apply the new developments for real-life predictions the model must be validated. This is accounted on two levels. On the one hand, simulations with the new method are conducted and compared to DNS-results of a 1D-channel flow. Thereby, good agreement with velocity and Reynolds stresses is demonstrated. On the other hand, wind-tunnel experiments were performed for a wing with porous trailing edge as it is used by the acoustic researchers for noise reduction purposes. Comparisons of the lift coefficients and the flow field over the trailing edge with the results of the same computation setup also show good agreement to ascertain the quality of the model.

Even though this work is complete by showing its evolution from the theoretical ideas to the development of actual models, the implementation into a flow solver to the validation procedures, many new questions arise which would be interesting to address in future. These are presented here to give an outlook and recommendation for future work.

Anisotropic porous media and porosity gradients

The present work only considers porous media with properties which are independent of the coordinate directions. The porous properties are also maintained constant in space. Since such conditions are only valid for a very limited amount of porous media, the present work should be generalized. Work on these topics is already in progress in the follow-on project of this work.

Improving nonporous-porous interface conditions

Section 6.2.6 showed some shortcomings of the conditions for flows tangential to the interface. The present conditions always predict a pressure jump even if the interface-normal component of the velocity is zero. While this is a direct consequence of both, the energy conservation and the commonly stated condition that the velocity jumps by the factor of the porosity it seems to contradict the experimental experience. At this point it is proposed to depart from the existing literature and change the interface relations given in sections 2.8.1, 2.8.3 and 3.11.1 by replacing the condition of constant velocity direction (equations (2.41), (2.56) and (3.69)) by the condition that the tangential velocity is constant:

$$\langle v_{t,1} \rangle_{\mathcal{F}} = \langle v_{t,2} \rangle_{\mathcal{F}} \quad \text{or} \quad \widetilde{v_{t,1}} = \widetilde{v_{t,2}}$$

where $v_{t,1}$ and $v_{t,2}$ are the velocity components tangential to the interface at the two interface sides (see also appendix B). However, this new development should be supported by new DNS-computations.

Investigate interface conditions of homogeneous dissipation-rate

The end of section 4.2.3 quickly mentions that the current interface conditions seem to under-predict the homogeneous dissipation-rate for the special combination where the porous medium is hardly permeable and the computation mesh is fully resolved. Thus, it might be required to modify this condition by specifying an improved jump condition (equation (3.82)) for the homogeneous dissipation-rate gradients.

Simplified turbulence models

The present work uses a complex Reynolds-stress model for the modelling of turbulence. While this promises high-fidelity results, the simulations are much more expensive if compared to simpler turbulence models (one- or two-equation models). In order to speed up aerodynamic design processes, it is desirable to have access to a variety of turbulence models. Therefore, the theoretical equations and interface conditions in this work should be rewritten and tested to work with other turbulence models.

High Mach number flow

Within this work, special care was taken to write down all models in a way that they are still valid if the flow was compressible. While the given test and validation cases can all be regarded as incompressible, future applications on aircraft require validation at transonic speeds. With all the theoretical groundwork given, compressible validation cases should be set up and tested. It would also be interesting to see how the models perform when the porous surfaces move at supersonic speeds.

Reynolds number sensitivities

No sensitivities of the Reynolds number on the effect of porous media was investigated for this work. Since there exist experimental data on channel flow with a porous bottom at different Reynolds numbers given by Suga et al. [75], it is proposed to use such data for further validations.

Review Darcy and Forchheimer terms in turbulent flow

In this work the effect of porous media on the fluid is modelled by the Darcy and Forchheimer terms. For the turbulence modelling, the Forchheimer term becomes rather complex leading to the problem that even terms inside the Forchheimer term have to be modelled. Such sophisticated modelling procedures can be risky when accurate solutions are desired. Hence, it is proposed to cross-check the Darcy and Forchheimer terms of the momentum and Reynolds-stress equations with DNS-data. Ideally, this should be done by directly computing the surface integral of equation (2.21)

$$\frac{1}{V_\mathrm{f}} \int\limits_{A_\mathrm{fs}} p^{\triangleleft} n_i - \tau_{ij}^{\triangleleft} n_j \, \mathrm{d}A$$

for several time steps in turbulent flow and comparing the averaged values against the Darcy and Forchheimer terms as they appear in equation (3.16). Even more important, the same procedure should be applied for the surface integrals as they appear in the Reynolds-stress equations.

Investigate the large diffusion inside porous media

Section 3.6.3 describes an additional diffusion term in the Reynolds-stress equations which is required to reproduce the high Reynolds stresses inside the porous media. It might be worth investigating, if this diffusion model could be merged with the turbulent diffusion term of the Reynolds-stress model given in equation (3.59). Instead of defining the additional diffusion as done in the present work, only the diffusion coefficient of the turbulent diffusion model would have to be modified. Furthermore, the triple correlation term of the Forchheimer term (3.28) which is modelled with yet another gradient-diffusion model, could be redefined to be directly based on the above mentioned existing turbulent diffusion model of the Reynolds-stress model. In this process, the diffusion coefficient of the turbulent diffusion model could be adopted, leading to one less unknown parameter in the porous models.

Investigations on subfilter stresses

Section 2.5.2 proposed a simple model for the subfilter normal stresses but it did not seem relevant to keep these terms inside this work. However, in future applications the modelling of such a term could become important which would make it interesting to evaluate the term further e.g. for porous ducts.

Heat transfer in porous media

The present work assumed that there is no heat exchange between the fluid and the porous structure. If accurate temperature distributions inside porous media are required, the models would require an update with additional terms. While a first term for such a consideration is presented in section 2.5.1, there exists more literature about modelling heat transport in porous media which could help to further improve the computation of heat fluxes in the present models.

Turbulence in between porous structure

The current work assumed that the local Reynolds number based on the pore size is not very high, so that the local turbulence inside the porous media will always be damped. For high Reynolds numbers this is not strictly the case anymore, as discussed in section 3.1. It might be needed to replace the actual fluid viscosity with an effective viscosity inside the porous media in order to account for such additional turbulence effects. However, this could be continued to arbitrarily higher complexity levels such that small-scale and large-scale turbulence could interact. Such a method is proposed by Kuwata and Suga in [41] where they introduce an additional transport equation which describes the dynamics of the small-scale turbulence.

Gain understanding on the turbulence mechanisms in porous media

This work assumes that the Reynolds-stress model as it is used in nonporous regions can be adapted to porous media by simply introducing new terms. However, it is not clear if the main mechanisms of turbulence are valid any longer inside porous media. Consider, as an example, the production term which strongly relies on the velocity gradients. In this work the volume-averaged velocity gradient field is used in the production term. But note, that the local microscopic velocity gradients inside the porous structure are much higher than the averaged gradients. In addition, the mixing inside the porous medium is strongly enhanced due to the fluctuating movements of the fluid through the irregular porous structure. This might considerably affect the diffusion process. With this in mind, it would be of interest to evaluate DNS-data and examine the main mechanisms how turbulence evolves in different types of porous media. While Breugem shows some information [10], much more detailed evaluations for several different setups would be required.

The proposed points show that a lot of improvements can be made for accurate predictions of turbulent flow over porous media. However, the present state as obtained in this work, already provides many capabilities to support the design process of aerodynamic vehicles which contain porous surfaces.

A. Mathematical Relations

A.1. Averaging a density-weighted average

The intention of this section is to show that

$$\langle\langle\varphi\rangle_{\mathcal{F}}\rangle = \langle\varphi\rangle_{\mathcal{F}} \tag{A.1}$$

is approximately valid. Starting with the definition of the averaging operators (2.6) and (2.9) one can write

$$\langle\langle\varphi\rangle_{\mathcal{F}}\rangle = \frac{1}{V_\mathrm{f}} \int\limits_{V_\mathrm{f}} \langle\varphi\rangle_{\mathcal{F}} \,\mathrm{d}V = \frac{1}{V_\mathrm{f}} \int\limits_{V_\mathrm{f}} \frac{\langle\rho\varphi\rangle}{\langle\rho\rangle} \,\mathrm{d}V \quad . \tag{A.2}$$

Based on the approximation given by equation (2.15), which is assumed valid throughout this whole work, the nominator and denominator of the fraction are spatially constant. Hence, they can be pulled out of the integral,

$$\frac{1}{V_\mathrm{f}} \int\limits_{V_\mathrm{f}} \frac{\langle\rho\varphi\rangle}{\langle\rho\rangle} \,\mathrm{d}V = \frac{1}{V_\mathrm{f}} \frac{\langle\rho\varphi\rangle}{\langle\rho\rangle} \int\limits_{V_\mathrm{f}} \mathrm{d}V = \frac{1}{V_\mathrm{f}} \frac{\langle\rho\varphi\rangle}{\langle\rho\rangle} V_\mathrm{f} = \langle\varphi\rangle_{\mathcal{F}} \quad , \tag{A.3}$$

which gives support that equation (A.1) is valid.

A.2. Flux derivatives of triple correlations of velocity fluctuations

The Jacobians of the implicit parts of the TAU flow solver need the derivatives of the triple correlations of the velocity fluctuations in respect to the Reynolds stresses:

$$\frac{\partial \overline{v'_l v'_m v'_n}}{\partial \overline{v'_i v'_j}} \tag{A.4}$$

The basis for these triple correlations is the model of Hanjalić and Launder given by equation (3.30):

$$\overline{v'_l v'_m v'_n} = -c_t \frac{k}{\varepsilon} \cdot \left(\overline{v'_l v'_k} \frac{\partial \overline{v'_m v'_n}}{\partial x_k} + \overline{v'_m v'_k} \frac{\partial \overline{v'_n v'_l}}{\partial x_k} + \overline{v'_n v'_k} \frac{\partial \overline{v'_l v'_m 1}}{\partial x_k} \right) \tag{A.5}$$

with the turbulent kinetic energy $k = \frac{\overline{v'_k v'_k}}{2}$. The derivative in respect to the Reynolds stress $\overline{v'_i v'_j}$ is reads

$$\begin{aligned}\frac{\partial \overline{v'_l v'_m v'_n}}{\partial \overline{v'_i v'_j}} =& \frac{c_t}{\varepsilon} \cdot \Bigg[\frac{\partial k}{\partial \overline{v'_i v'_j}} \cdot \left(\overline{v'_l v'_k} \frac{\partial \overline{v'_m v'_n}}{\partial x_k} + \overline{v'_m v'_k} \frac{\partial \overline{v'_n v'_l}}{\partial x_k} + \overline{v'_n v'_k} \frac{\partial \overline{v'_l v'_m}}{\partial x_k} \right) \\ & + k \cdot \frac{\partial}{\partial \overline{v'_i v'_j}} \left(\overline{v'_l v'_k} \frac{\partial \overline{v'_m v'_n}}{\partial x_k} + \overline{v'_m v'_k} \frac{\partial \overline{v'_n v'_l}}{\partial x_k} + \overline{v'_n v'_k} \frac{\partial \overline{v'_l v'_m}}{\partial x_k} \right) \Bigg] \ . \end{aligned} \tag{A.6}$$

Therein, the derivative of the kinetic turbulent energy k in respect to the Reynolds stresses is needed,

$$\frac{\partial k}{\partial \overline{v'_i v'_j}} = \begin{cases} \frac{1}{2}, & i = j \\ 0, & i \neq j \end{cases} \ , \tag{A.7}$$

as well as the derivative of the term $\overline{v'_l v'_k} \frac{\partial \overline{v'_m v'_n}}{\partial x_k}$

$$\frac{\partial}{\partial \overline{v'_i v'_j}} \left(\overline{v'_l v'_k} \frac{\partial \overline{v'_m v'_n}}{\partial x_k} \right) = \underbrace{\frac{\partial \overline{v'_l v'_k}}{\partial \overline{v'_i v'_j}}}_{\text{(a)}} \cdot \frac{\partial \overline{v'_m v'_n}}{\partial x_k} + \overline{v'_l v'_k} \underbrace{\frac{\partial^2 \overline{v'_m v'_n}}{\partial \overline{v'_i v'_j} \partial x_k}}_{\text{(b)}} \ . \tag{A.8}$$

The part (a) of this expression reads

$$\frac{\partial \overline{v'_l v'_k}}{\partial \overline{v'_i v'_j}} = \begin{cases} 1, & (l = i \wedge k = j) \vee (l = j \wedge k = i) \\ 0, & \text{else} \end{cases} \tag{A.9}$$

and for part (b) it is

$$\frac{\partial^2 \overline{v'_m v'_n}}{\partial \overline{v'_i v'_j} \partial x_k} = \frac{\partial}{\partial x_k} \left(\frac{\partial \overline{v'_m v'_n}}{\partial \overline{v'_i v'_j}} \right) = 0 \ , \tag{A.10}$$

since $\frac{\partial \overline{v'_m v'_n}}{\partial \overline{v'_i v'_j}}$ is constant. Then, plugging equations (A.10) and (A.9) into (A.8) and (A.7) into (A.6) results in

$$\begin{aligned}\frac{\partial \overline{v'_l v'_m v'_n}}{\partial \overline{v'_i v'_j}} = \frac{c_t}{\varepsilon} \cdot \Bigg[& \underbrace{\frac{1}{2} \left(\overline{v'_l v'_k} \frac{\partial \overline{v'_m v'_n}}{\partial x_k} + \overline{v'_m v'_k} \frac{\partial \overline{v'_n v'_l}}{\partial x_k} + \overline{v'_n v'_k} \frac{\partial \overline{v'_l v'_m}}{\partial x_k} \right)}_{\text{if } i=j} \\ & + k \cdot \left(\underbrace{\frac{\partial \overline{v'_m v'_n}}{\partial x_k}}_{\substack{\text{if} \\ l=i \wedge k=j \\ l=j \wedge k=i}} + \underbrace{\frac{\partial \overline{v'_l v'_n}}{\partial x_k}}_{\substack{\text{if} \\ m=i \wedge k=j \\ m=j \wedge k=i}} + \underbrace{\frac{\partial \overline{v'_l v'_m}}{\partial x_k}}_{\substack{\text{if} \\ n=i \wedge k=j \\ n=j \wedge k=i}} \right) \Bigg] \end{aligned} \tag{A.11}$$

for the index $k \in 1, 2, 3$.

B. Isentropic Flow Change only for Normal Velocity

Section 6.2.6 discusses the fact that the relationships between the flow variables of the two sides of the nonporous-porous interface can lead to biased results. The reason for this is unveiled to be the condition of constant velocity direction given by equation (3.69). This leads to a pressure jump over the interface as soon as the velocity at this point is greater than zero. The experiments on the DLR-F16 airfoil contradict this behaviour. It rather seems that there will only be a pressure jump if the velocity component normal to the interface is not zero. Thus, it is proposed to replace the condition of constant velocity direction by holding the tangential velocity constant (see figure B.1). In combination with the remaining conditions, the pressure jump will not be influenced by the tangential velocity anymore. The present section will quickly describe the newly proposed interface conditions.

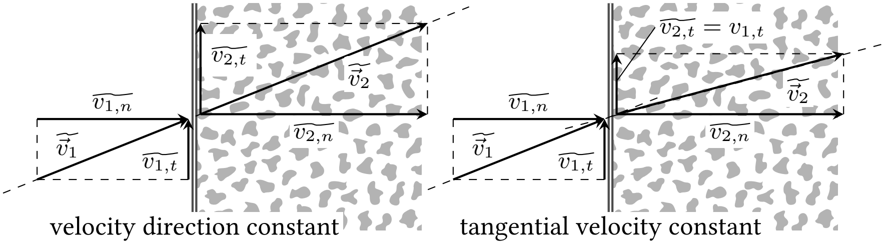

velocity direction constant

tangential velocity constant

Figure B.1.: Velocity relationships over nonporous–porous interface according to the condition (3.69) of constant velocity direction (left) and the proposed improved condition in which the tangential velocity component stays constant.

The flux conservation laws for mass and energy stay unchanged according to equation (3.67):

$$\phi_1\overline{\rho_1}\,\widetilde{v_{n,1}} = \phi_2\overline{\rho_2}\,\widetilde{v_{n,2}} \tag{B.1a}$$

$$\frac{|\widetilde{v_1}|^2}{2} + k_1 + \widetilde{e_1} + \frac{\overline{p_1}}{\rho_1} = \frac{|\widetilde{v_2}|^2}{2} + k_2 + \widetilde{e_2} + \frac{\overline{p_2}}{\rho_2} \tag{B.1b}$$

with

$$\widetilde{e} = \frac{1}{\gamma - 1} \frac{\overline{p}}{\overline{\rho}} \quad . \tag{B.2}$$

Also, the isentropic condition

$$\frac{\overline{p_1}}{\overline{\rho_1}^{\gamma}} = \frac{\overline{p_2}}{\overline{\rho_2}^{\gamma}} \quad , \tag{B.3}$$

and the relationship of the turbulent kinetic energy

$$\phi_1 \overline{\rho_1} k_1 = \phi_2 \overline{\rho_2} k_2 \tag{B.4}$$

are not touched. What is changed is the condition of the constant velocity direction (3.69). It is replaced by the assumption that the velocity component parallel to the boundary is equal on both interface sides. This can be written by

$$\widetilde{v_{t,1}} = \widetilde{v_{t,2}} \qquad \text{or} \qquad |\widetilde{\vec{v}_1}|^2 - \widetilde{v_{n,1}}^2 = |\widetilde{\vec{v}_2}|^2 - \widetilde{v_{n,2}}^2 \quad . \tag{B.5}$$

The constants of the equation system (3.73),

$$\mathrm{a} \cdot (\overline{p_2})^{\mathrm{b}} + \mathrm{c} \cdot (\overline{p_2})^{\mathrm{d}} + \mathrm{e} \cdot (\overline{p_2})^{\mathrm{f}} + \mathrm{g} = 0$$

must then be modified in a way that they read

$$\mathrm{a} = \frac{\gamma}{\gamma - 1} \frac{(\overline{p_1})^{\frac{1}{\gamma}}}{\overline{\rho_1}}; \quad \mathrm{b} = 1 - \frac{1}{\gamma}; \quad \mathrm{c} = \frac{1}{2} \left(|\widetilde{\vec{v}_{n,1}}| (\overline{p_1})^{\frac{1}{\gamma}} \frac{\phi_1}{\phi_2} \right)^2; \quad \mathrm{d} = -\frac{2}{\gamma}$$

$$\mathrm{e} = k_1 (\overline{p_1})^{\frac{1}{\gamma}} \frac{\phi_1}{\phi_2}; \quad \mathrm{f} = -\frac{1}{\gamma}; \quad \mathrm{g} = -\frac{\gamma}{\gamma - 1} \frac{\overline{p_1}}{\overline{\rho_1}} - \frac{|\widetilde{\vec{v}_{n,1}}|^2}{2} - k_1 \quad .$$

After solving the equation system, the velocity vector at the boundary side 2 can be computed with the relation

$$\widetilde{\vec{v}_2} = \widetilde{\vec{v}_1} + \vec{n} \left(\widetilde{v_{n,2}} - \widetilde{v_{n,1}} \right) \tag{B.6}$$

with $\vec{n}$ as the normal vector of the interface.

C. Classification of Flow Through Porous Media

In the following, a short derivation of a typical critical Reynolds number $Re_{\kappa,\mathrm{crit}}$ will be given, telling when turbulence will be maintained solely from the flow through the porous structure. However, before this question can be assessed, a relation between the typical pore diameters d_p and the permeability κ will be derived.

C.1. Relation between pore size d_p and permeability κ

A relation between the typical pore diameter d_p and the permeability κ will be derived on the basis of a quasi-isotropic, simple porous structure as shown in figure C.1. The given structure allows a theoretical development of the relation. The resulting equations are then assumed to be general enough to be applied on more sophisticated porous structures.

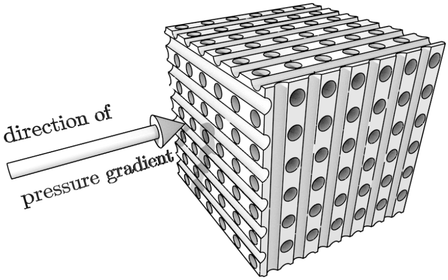

Figure C.1.: Quasi-isotropic porous structure where the pressure gradient is aligned with channels in only one direction.

First, it is assumed that the pressure gradient is aligned with the bunch of holes which point in one direction. This has the consequence that flow will only be forced through this one third of channels while the velocity will stay zero in the rest of the channels. The principal flow setup of the channels which are aligned with the pressure gradient is sketched in figure C.2. It shows that the pore diameter d_p is chosen to be the height of a single channel.

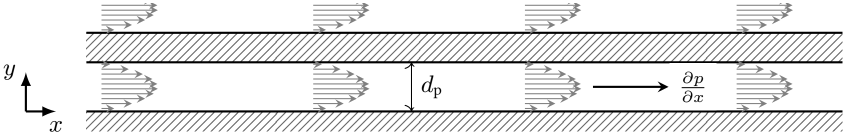

Figure C.2.: Setup of laminar flow through channels.

A relation between the pressure drop and the averaged velocity inside the channel is given by the law of Hagen-Poiseuille (see e.g. [74]):

$$\langle v \rangle_\text{channel} = -\frac{d_\mathrm{p}^2}{32\mu}\frac{\partial p}{\partial x} \tag{C.1}$$

This law is now combined with the law of Darcy

$$\frac{\partial p}{\partial x} = -\phi\frac{\mu}{\kappa}\langle v \rangle \tag{C.2}$$

where the velocity $\langle v \rangle$ depends on the channel velocity $\langle v \rangle_\text{channel}$ by the relationship

$$\langle v \rangle = \frac{1}{3}\langle v \rangle_\text{channel} \quad .$$

The reason for this is that the in two thirds of the channels of the quasi-isotropic porous material, the velocity is zero. The resulting relation between pore diameter d_p and permeability κ is therefore

$$d_\mathrm{p} = \sqrt{96\frac{\kappa}{\phi}} \quad . \tag{C.3}$$

If assumed that a typical value of the porosity ϕ is between 0.1 and 1, one can estimate the pore diameter d_p for a given permeability κ to be

$$d_\mathrm{p} \approx (10\ldots30)\cdot\sqrt{\kappa} \quad \text{or} \quad \sqrt{\kappa} \approx \frac{d_\mathrm{p}}{(10\ldots30)} \quad . \tag{C.4}$$

Anticipated, that these relations can still be applied for random porous structures, it can be stated that the square root of the permeability κ lies between the size of one and one hundredth of the pore diameter d_p.

With this estimation of the pore size d_p based on the permeability κ, one can also classify the flow problem. If the dimensionless Darcy number *Da* is defined,

$$Da = \frac{\kappa}{L^2} \quad , \tag{C.5}$$

with L as a characteristic length scale of the considered flow problem the flow can be classified as follows:

$Da \ll 1 \times 10^{-4}$ → Pore size is much smaller than the dimension of the flow problem

$Da \approx 1 \times 10^{-4} \ldots 1$ → transient region

$Da \gg 1$ → Pore size is much larger that the dimension of the flow problem

The present work only deals with the first case in which the dimension of the flow problem is much larger than the size of the pores.

C.2. Estimation of critical Reynolds number for turbulence living inside pores

The present work does not really consider small-scale turbulence which develops inside the porous structure of porous media. Rather, turbulence is considered which is transported into the porous medium. However, if small-scale turbulence can develop inside the pores due to high local Reynolds numbers

$$Re_\kappa = \frac{\sqrt{\kappa} v \rho}{\mu} \quad ,$$

an increased drag would be expected. In this case, at least the law of Darcy would need adaptions (e.g. by replacing the dynamic viscosity with an effective viscosity). Thus, it is of interest to estimate the critical Reynolds number $Re_{\kappa,\mathrm{crit}}$ which indicates if one would have to expect small-scale turbulence or not.

Inside a channel, flow will turn turbulent if the Reynolds number based on the channel height and the mean velocity exceeds the value of about 2300 (see e.g. [67]). This could be transferred to flow in porous media which have a channel-like porous structure as it is already shown in figure 2.2:

$$Re_{d_\mathrm{p},\mathrm{crit}} = \frac{\rho \left\langle v_\mathrm{p} \right\rangle d_\mathrm{p}}{\mu} \approx 2300 \tag{C.6}$$

Here, $\left\langle v_\mathrm{p} \right\rangle$ is the average velocity inside a channel within the porous structure. However, the rough structure of a porous medium will reduce the critical Reynolds number. Literature (see e.g. [56, 42]) points out that rather small pore Reynolds numbers of about $Re_{d_\mathrm{p},\mathrm{crit}} \approx 300$ are an appropriate value for the critical Reynolds number where flow turns turbulent.

Based on the relation (C.4) one can estimate a value for the critical Reynolds number of about

$$Re_{\kappa,\mathrm{crit}} \approx \frac{300}{10 \ldots 30} \approx 10 \ldots 30 \quad . \tag{C.7}$$

Bibliography

[1] B. Alzami and K. Vafai. “Analysis of fluid flow and heat transfer interfacial conditions between a porous medium and a fluid layer”. In: *International Journal of Heat and Mass Transfer* 44 (2001), pp. 1735–1749.

[2] B. V. Antohe and J. L. Lage. “A general two-equation macroscopic turbulence model for incompressible flow in porous media”. In: *International Journal of Heat and Mass Transfer* 40.13 (1997), pp. 3013–3024.

[3] B. V. Antohe et al. “Experimental Determination of Permeability and Inertia Coefficients of Mechanically Compressed Aluminum Porous Matrices”. In: *Transactions of the ASME* 119 (1997), pp. 404–412.

[4] J. Bear and Y. Bachmat. *Introduction to modeling of transport phenomena in porous media*. Vol. 4. Theory and applications of transport in porous media. Kluwer Academic Publishers, 1990.

[5] Latifa Begum and Mainul Hasan. “3-D CFD simulation of a vertical direct chill slab caster with a submerged nozzle and a porous filter delivery system”. In: *Journal of Heat and Mass Transfer* 73 (2014), pp. 42–58.

[6] J. Blažek. *Computational fluid dynamics: principles and applications*. Second Edition. Elsevier, 2005.

[7] W. P. Breugem and B. J. Boersma. “Direct numerical simulations of turbulent flow over a permeable wall using a direct and a continuum approach”. In: *Physics of Fluids* 17 (2005).

[8] W. P. Breugem, B. J. Boersma, and R. E. Uittenbogaard. “Direct Numerical Simulations of Plane Channel Flow over a 3D Cartesian Grid of Cubes”. In: *Applications of Porous Media: Proceedings of the International Conference on Applications of Porous Media*. Ed. by A. H. Reis and A. F. Miguel. Évora, Portugal: Centro de Geofisica, 2004, pp. 27–35.

[9] W. P. Breugem, B. J. Boersma, and R. E. Uittenbogaard. “The influence of wall permeability on turbulent channel flow”. In: *Journal of Fluid Mechanics* 562 (2006), pp. 35–72.

[10] Wim-Paul Breugem. “The influence of wall permeability on laminar and turbulent flows”. PhD thesis. Technische Universiteit Delft, Jan. 2005.

[11] René-Daniel Cécora et al. “Differential Reynolds Stress Modeling for Aeronautics”. In: *50th AIAA Aerospace Sciences Meeting, AIAA 2012-0465*. Nashville, Tennessee, Jan. 2012.

[12] René-Daniel Cécora et al. “Differential Reynolds-Stress Modeling for Aeronautics”. In: *AIAA Journal* (2014).

[13] H. C. Chan et al. “Macroscopic modeling of turbulent flow over a porous medium”. In: *International Journal of Heat and Fluid Flow* 28 (2007), pp. 1157–1166.

[14] M. Chandesris and D. Jamet. “Boundary conditions at a planar fluid-porous interface for a Poiseuille flow”. In: *International Journal of Heat and Mass Transfer* 49 (2006), pp. 2137–2150.

[15] M. Chandesris and D. Jamet. “Derivation of jump conditions of the turbulence k-ϵ model at fluid/porous interface”. In: *International Journal of Heat and Fluid Flow* 30 (2009), pp. 306–318.

[16] M. Chandesris and D. Jamet. “Jump Conditions and Surface-Excess Quantities at a Fluid/Porous Interface: A Multiscale Approach”. In: *Transport in Porous Media* 78 (2009), pp. 419–438.

[17] M. Chandesris, G. Serre, and P. Sagaut. “A macroscopic turbulence model for flow in porous media suited for channel, pipe and rod bundle flows”. In: *International Journal of Heat and Mass Transfer* 49 (2006), pp. 2739–2750.

[18] T. J. Craft and B. E. Launder. “Principles and Performance of TCL-Based Second-Moment Closures”. In: *Flow, Turbulence and Combustion* 66 (2001), pp. 355–372.

[19] Bart J. Daly and Francis H. Harlow. “Transport Equations in Turbulence”. In: *The Physics of Fluids* 13 (1970), pp. 2534–2649.

[20] H. Darcy and P. Bobeck. *The Public Fountains of the City of Dijon: Exposition and Application of Principles to Follow and Formulas to Use in Questions of Water Distribution.* Kendall/Hunt Publishing Company, 2004.

[21] J. Delfs et al. “SFB 880: aeroacoustic research for low noise take-off and landing”. English. In: *CEAS Aeronautical Journal* 5.4 (2014), pp. 403–417.

[22] Mark Drela. “XFOIL: An Analysis and Design System for Low Reynolds Number Airfoils”. In: *Low Reynolds Number Aerodynamics.* Ed. by Thomas J. Mueller. Vol. 54. Springer Berlin Heidelberg, 1989. Chap. Lecture Notes in Engineering, pp. 1–12.

[23] M. Drouin, Grégoire O., and O. Simonin. “A consistent methodology for the derivation and calibration of a macroscopic turbulence model for flows in porous media”. In: *International Journal of Heat and Mass Transfer* 63 (2013), pp. 401–413.

[24] Richard P. Dwight. “Time-Accurate Navier-Stokes Calculations with Approximately Factored Implicit Schemes”. In: *Computational Fluid Dynamics 2004*. Ed. by Clinton Groth and David W. Zingg. Springer Berlin Heidelberg, 2006, pp. 211–217.

[25] Bernhard Eisfeld. “Reynolds Stress Modelling for Complex Aerodynamic Flows”. In: Lisbon, Portogal, June 2010.

[26] Philipp Forchheimer. “Wasserbewegung durch Boden”. In: *Zeitschrift des Vereins deutscher Ingenieure* 45 (1901), pp. 1781–1788.

[27] Klaus Gersten and Heinz Herwig. *Strömungsmechanik – Grundlagen der Impuls-, Wärme- und Stoffübertragung aus asymptotischer Sicht*. Wiesbaden: Springer Fachmedien, 1992.

[28] D. Getachew, W. J. Minkowycz, and J. L. Lage. “A modified form of the κ-ε model for turbulent flows of an incompressible fluid in porous media”. In: *International Journal of Heat and Mass Transfer* 43 (2000), pp. 2909–2915.

[29] Baoyu Guo et al. “Comparison of Several Turbulence Models Applied to the Simulation of Gas Flow in a Packed Bed”. In: CSIRO, Melbourne, Australia, Dec. 2003.

[30] Jian Hang and Yuguo Li. “Macroscopic simulations of turbulent flows through high-rise building arrays using a porous turbulence model”. In: *Building and Environment* 49 (2012), pp. 41–54.

[31] K. Hanjalić and B. E. Launder. “Contribution towards a Reynolds-stress closure for low-Reynolds-number turbulence”. In: *Journal of Fluid Mechanics* 74 (1976), pp. 593–610.

[32] “Heat Transfer Modeling at an Interface between a Porous Medium and a Free Region”. PhD thesis. L’Ecole Centrale Paris, Nov. 2011.

[33] M. Herr. “Design Criteria for Low-Noise Trailing-Edges”. In: *13th AIAA/CEAS Aeroacoustics Conference*. DLR, German Aerospace Center, 38108 Braunschweig, 2007.

[34] M. Herr et al. “Specification of Porous Materials for Low-Noise Trailing-Edge Applications”. In: *20th AIAA/CEAS Aeroacoustics Conference, AIAA-2014-3041*. Atlanta, Georgia, June 2014.

[35] S. A. Holditch and R. A. Morse. “The Effects of Non-Darcy Flow on the Behaviour Of Hydraulically Fractured Gas Wells”. In: *Journal of Petroleum Technology* (1976), pp. 1169–1179.

[36] S. Jakirlić and K. Hanjalić. “A new approach to modelling near-wall turbulence energy and stress dissipation”. In: *Journal of Fluid Mechanics* 459 (2002), pp. 139–166.

[37] Suad Jakirlić. *A DNS-Based Scrutiny of RANS Approaches and their Potential for Predicting Turbulent Flows.* Habilitationsschrift, Technische Universität Darmstadt. May 2004.

[38] Suad Jakirlić. “Reynolds-Spannungs-Modellierung Komplexer Turbulenter Strömungen”. PhD thesis. Universität Erlangen-Nürnberg, Jan. 1997.

[39] P. Kundu, V. Kumar, and I. M. Mishra. “Numerical modeling of turbulent flow through isotropic porous media”. In: *International Journal of Heat and Mass Transfer* 75 (2014), pp. 40–57.

[40] Y. Kuwata and K. Suga. “Progress in the extension of a second-moment closure for turbulent environmental flows”. In: *International Journal of Heat and Fluid Flow* 51 (2015), pp. 268–284.

[41] Yusuke Kuwata and Kazuhiko Suga. “Modelling turbulence around and inside porous media based on the second moment closure”. In: *International Journal of Heat and Fluid Flow* 43 (2013), pp. 35–51.

[42] Yusuke Kuwata, Kazuhiko Suga, and Yota Sikurai. “Development and application of a multi-scale k-ε model for turbulent porous medium flows”. In: *International Journal of Heat and Fluid Flow* 49 (2014), pp. 135–150.

[43] A. V. Kuznetsov. “Analytical Investigation of the Fluid Flow in the Interface Region between a Porous Medium and a Clear Fluid in Channels Partially Filled with a Porous Medium”. In: *Applied Scientific Research* 56 (1996), pp. 53–67.

[44] B. E. Launder, G. J. Reece, and W. Rodi. “Progress in the development of a Reynolds-stress turbulence closure”. In: *Journal of Fluid Mechanics* 68 (1975), pp. 537–566.

[45] Marcelo J. S. de Lemos and Renato A. Silva. “Turbulent flow over a layer of a highly permeable medium simulated with a diffusion-jump model for the interface”. In: *International Journal of Heat and Mass Transfer* 49 (2006), pp. 546–556.

[46] I. F. Macdonald et al. “Flow through Porous Media – the Ergun Equation Revisited”. In: *Industrial & Engineering Chemical Fundamentals* 18.3 (1979), pp. 199–208.

[47] N. N. Mansour, J. Kim, and P. Moin. “Reynolds-stress and dissipation-rate budgets in a turbulent channel flow”. In: *Journal of Fluid Mechanics* 194 (1988), pp. 15–44.

[48] Dimitri J. Mavriplis, Antony Jameson, and Luigi Martinelli. *Multigrid Solution of the Navier-Stokes Equations on Triangular Meshes.* ICASE Report No. 89-11. Hampton, Virginia 23665: NASA, Feb. 1989.

[49] M. Mößner and R. Radespiel. "Modelling of turbulent flow over porous media using a volume averaging approach and a Reynolds stress model". In: *Computers & Fluids* 108 (2015), pp. 25–42.

[50] Michael Mößner and Rolf Radespiel. "Flow Simulations over Porous Media – Comparisons with Experiments". In: Chengdu, China, July 2014.

[51] A. Nakayama and F. Kuwahara. "A General Macrocopic Turbulence Model for Flows in Packed Beds, Channels, Pipes and Rod Bundles". In: *Journal of Fluids Engineering* 180.10 (2008).

[52] A. Nakayama and F. Kuwahara. "A Macroscopic Turbulence Model for Flow in a Porous Medium". In: *Journal of Fluids Engineering* 121 (1999), pp. 427–433.

[53] Donald A. Nield and Adrian Bejan. *Convection in Porous Media.* 3rd ed. New York: Springer, 2006.

[54] J. Alberto Ochoa-Tapia and Stephen Whitaker. "Momentum Jump Condition at the Boundary Between a Porous Medium and a Homogeneous Fluid: Intertial Effects". In: *Journal of Porous Media* 1.3 (1998), pp. 201–217.

[55] J. Alberto Ochoa-Tapia and Stephen Whitaker. "Momentum transfer at the boundary between a porous medium and a homogeneous fluid – I. Theoretical development". In: *International Journal of Heat and Mass Transfer* 38 (1995), pp. 2635–2646.

[56] Marcos H. J. Pedras and Marcelo J. S. de Lemos. "Macroscopic turbulence modeling for incompressible flow through undeformable porous media". In: *International Journal of Heat and Mass Transfer* 44 (2001), pp. 1081–1093.

[57] C. Peralta, J. Schmidt, and B. Stoevesandt. "The influence of orographic features on wind farm efficiencies". In: *ITM Web of Conferences* 2 (2014).

[58] D. Poulikakos and M. Kazmierczak. "Forced Convection in a Duct Partially Filled With a Porous Material". In: *Journal of Heat Transfer* 109 (1987), pp. 653–662.

[59] Axel Probst. "Reynoldsspannungsmodellierung für das Überziehen in der Flugzeugaerodynamik". PhD thesis. Braunschweig: Technische Universität Braunschweig, Mar. 2013.

[60] Axel Probst and Rolf Radespiel. "Implementation and Extension of a Near-Wall Reynolds-Stress Model for Application to Aerodynamic Flows on Unstructured Meshes". In: *46th AIAA Sciences Meeting and Exhibit, AIAA 2008-770.* Reno, Nevada, 2008.

[61] R. Radespiel and W. Heinze. "SFB880 – Fundamentals of High-Lift for Future Commercial Aircraft". In: *Deutscher Luft- und Raumfahrtkongress.* Stuttgart, 2013.

[62] M. R. Raupach and R. H. Shaw. “Averaging Procedures for Flow within Vegetation Canopies”. In: *Boundary Layer Meteorology* 22 (1982), pp. 79–90.

[63] M. R. Raupach and A. S. Thom. “Turbulence in and above Plant Canopies”. In: *Annual Review of Fluid Mechanics* 13 (1981), pp. 97–129.

[64] Marcelo B. Saito and Marcelo J. S. Lemos. “A macroscopic two-energy equation model for turbulent flow and heat transfer in highly porous media”. In: *International Journal of Heat and Mass Transfer* 53 (2010), pp. 2424–2433.

[65] Marcelo B. Saito and Marcelo J. S. de Lemos. “Laminar heat transfer in a porous channel simulated with a two-energy equation model”. In: *International Communications in Heat and Mass Transfer* 36 (2009), pp. 1002–1007.

[66] S. Sarkar and L. Balakrishnan. *Application of a Reynolds Stress Turbulence Model to the Compressible Shear Layer.* ICASE Report No. 90-18. Hampton, Virginia 23665-5225: Institute for Computer Applications in Science and Engineering, NASA Langley Research Center, Feb. 1990.

[67] H. Schlichting and K. Gersten. *Grenzschicht-Theorie.* 10. überarbeitete Auflage. Springer, 2006. ISBN: 9783540230045.

[68] Dieter Schwamborn, Thomas Gerhold, and Ralf Heinrich. “The DLR TAU-Code: Recent Applications in Research and Industry”. In: *ECCOMAS CFD 06.* Ed. by P. Wesseling, E. Oñate, and J. Périaux. TU Delft, The Netherlands, Sept. 2006.

[69] Renato A. Silva and Marcelo J. S. de Lemos. “Numerical Analysis of the Stress Jump Interface condition for Laminar Flow over a Porous Layer”. In: *Numerical Heat Transfer* 43 (2003), pp. 603–617.

[70] Renato A. Silva and Marcelo J. S. de Lemos. “Turbulent flow in a channel occupied by a porous layer considering the stress jump at the interface”. In: *International Journal of Heat and Mass Transfer* 46 (2003), pp. 5113–5121.

[71] Renato A. Silva and Marcelo J. S. de Lemos. “Turbulent flow in a composite channel”. In: *International Communications in Heat and Mass Transfer* 38 (2011), pp. 1019–1023.

[72] R. M. C. So, T. B. Gatski, and T. P.. Sommer. “Morkovin Hypothesis and the Modeling of Wall-Bounded Compressible Turbulent Flows”. In: *AIAA Journal* 36.9 (1998), pp. 1583–1592.

[73] Charles G. Speziale and Sutanu Sarkar. *Second-Order Closure Models for Supersonic Turbulent Flows.* ICASE Report No. 91-9. Hampton, Virginia: NASA, Jan. 1991.

[74] Joseph H. Spurk and Nuri Aksel. *Strömungslehre – Einführung in die Theorie der Strömungen.* 8. überarbeitete Auflage. Berlin: Springer-Verlag, 2010.

[75] K. Suga et al. “Effects of wall permeability on turbulence”. In: *International Journal of Heat and Fluid Flow* 31 (2010), pp. 974–984.

[76] *TAU-Code User Guide – Release 2013.1.0.* Braunschweig, Mar. 2013.

[77] Federica E. Teruel and Rizwan-uddin. “Numerical computation of macroscopic turbulence quantities in representative elementary volumes of the porous medium”. In: *International Journal of Heat and Mass Transfer* 53 (2010), pp. 5190–5198.

[78] Sonja Uphoff et al. “A Hierarchical Approach to Determining Acoustic Absorption Properties of Porous Media Combining Pore-Resolved and Macroscopic Models”. Accepted for publication in Journal of Porous Media. 2014.

[79] K. Vafai and S. J. Kim. “Fluid mechanics of the interface region between a porous medium and a fluid layer — an exact solution”. In: *International Journal of Heat and Fluid Flow* 11.3 (1990), pp. 254–256.

[80] Stephen Whitaker. “The Forchheimer Equation: A Theoretical Development”. In: *Transport in Porous Media* 25 (1996), pp. 27–91.

[81] David C. Wilcox. *Turbulence Modeling for CFD.* 3rd ed. DCW Industries, 2006.

[82] Jie Wu. “Boundary-layer Instability Experiments in a Tandem Nozzle Supersonic Wind Tunnel”. PhD thesis. Braunschweig: Technische Universität Braunschweig, Mar. 2015.

[83] *XFLR5.* http://www.xflr5.com/xflr5.htm. 2014. URL: `http://www.xflr5.com/xflr5.htm`.

[84] Cai Zhanjun, Kang Weimin, and Li Yabin. “Application of CFD to the Simulation in Aerodynamic Characteristics of Nanofiber Catalytic Converter”. In: *International Journal of Advancements in Computing Technology* 6.6 (2013), pp. 142–150.